FACULDADE DE ENGENHARIA DA UNIVERSIDADE DO PORTO

Detection and Characterization of Defects in Composite Materials Using Thermography

António José Ramos da Silva

Programa Doutoral em Engenharia Mecânica

Supervisor: Prof. Dr. Joaquim Gabriel Magalhães Mendes

Supervisor: Prof. Dr. Mário Augusto Pires Vaz

July, 2016

Abstract

Composite materials are widely used in the transport industry, particularly aeronautics, due to their light weight and enhanced mechanical properties. On the downside, these new materials are less known and their behaviour are unpredictable greatly because of their anisotropic properties, being difficult to simulate and understand their behaviour. To overcome these aspects regular preventive maintenance operations are necessary.

In order to avoid major problems, Non-Destructive Testing (NDT) are a solution to assure the safety without destroying the components. From the vast possibilities available, field image NDT have proved to be fast, precise and easy to interpret. Image technologies usually capture and measure some type of electromagnetic radiation to identify a discontinuity in the radiation pattern that changes due to a component abnormality. Since the natural radiation emitted by objects at the ambient temperature is in the infrared waveband, this is used to create a temperature image, particularly in the middle and far-infrared wavebands. Better results can be obtained when is used a stimulation source to induce a temperature variation, highlighting any defect that a component may have. Two different types of tests can be done with: single or periodic stimulation. When using single stimulation (transient tests), a pulse of energy is applied to the object and observed its recovery to the previous equilibrium state. On the other hand, when performing periodic tests (lock-in), the stimulation is modulated in several cycles, with the amplitude response and phase delay being analysed.

This work aimed to develop a numeric model able to predict the result of an infrared thermal test in carbon fiber reinforced polymers with structural defects. This work is divided in three main parts: field tests, numeric simulation and model validation. Several different field tests were performed with various test samples to identify the settings that produced the best results and give the highest sensitivity to defects detection. These tests were performed using the above refereed techniques, transient and lock-in. During the lock-in tests, it was identified an imperfection in the modulated sinusoidal stimulation, which was quantified and corrected improving the overall results.

The samples used in the laboratory testes where simulated using the finite element technique in Matlab®. This manner it was obtained an internal view of the heat flow inside the component and provided the temperature evolution at the surface of the specimen during an entire test. With the results obtained from the simulations, it is possible to estimate the thermal response obtained with a certain type of test and waveform.

Finally, the model was validated with experimental tests, consisting of samples made of carbon fiber reinforced polymers poly-methyl-meth-acrylate. At the end of this document it is presented a short comparison between the two thermal techniques and shearography.

This page was intentionally left blank.

Resumo

Os materiais compósitos são cada vez mais utilizados em diversas indústrias. A indústria dos transportes, em particular aeronáutica, procura tirar partido de materiais que sejam mais resistentes e leves. Os materiais compósitos possuem propriedades menos conhecidas e o seu comportamento é mais difíceis de modelar. Uma vez que eles são normalmente anisotrópicos são ainda mais imprevisíveis e difíceis de simular. Para contornar estas dificuldades são executadas regularmente operações de manutenção preventiva.

De forma a evitar graves problemas, devem ser utilizados ensaios não destrutivos, garantindo um bom desempenho sem por em causa a integridade do componente. Das diversas técnicas existentes as técnicas de imagem têm-se mostrado rápidas, precisas e fáceis de interpretar. As técnicas de imagem captam e medem uma parte do espectro eletromagnético para identificar uma descontinuidade ou alteração no padrão de radiação alterado devido a um defeito no componente. Uma vez que a radiação emitida pelos objetos à temperatura ambiente está no campo da radiação infravermelha, particularmente infravermelhos médios e os longos, esta é utilizada para criar imagens de temperatura. Os melhores resultados são obtidos quando é utilizada uma fonte de estimulação para induzir uma alteração na temperatura, realçando possíveis defeitos. Estes testes podem ser divididos em duas categorias: estimulação singular ou periódicas. Nos testes com estimulação transiente, esta é aplicada de uma forma uniforme durante um período de tempo e é analisada a evolução da temperatura. Contudo, quando são utilizadas estimulações cíclicas *lock-in*, a estimulação é modulada em vários ciclos e calculada a amplitude e atraso de resposta.

O trabalho pretendia desenvolver um modelo numérico capaz de prever os resultados de ensaios de termografia ativa em componentes de fibra de carbono com defeitos internos. Este trabalho está dividido em três partes: testes laboratoriais, simulações numéricas e validação do modelo. Foram realizados diversos ensaios laboratoriais, com diversas amostras, de forma a identificar as configurações onde eram obtidos os melhores resultados. Estes testes utilizaram as já referidas técnicas de termografia *transient* e *lock-in*. Foi identificada uma imperfeição nas ondas modeladas nos ensaios do tipo *lock-in*, esta foi quantificada e corrigida, melhorando assim a sensibilidade destes ensaios.

As amostras utilizadas nos ensaios laboratoriais foram simuladas utilizando o método dos elementos finitos, com implementação em Matlab®. Desta forma foi obtida uma visão do fluxo de calor no interior das amostras e obtidos os perfis térmicos na superfície da amostra durante o teste. Com os resultados obtidos com as simulações é possível estimar a resposta térmica obtida com um determinado tipo de teste e tipo de onda.

Finalmente os modelos desenvolvidos foram validados com ensaios laboratoriais em amostras de textitpoly-methyl-meth-acrylate e fibra de carbono. No final deste documento é apresentada uma breve comparação entre as técnicas de termografia e xerografia.

This page was intentionally left blank.

Acknowledgments

I would like to thank my supervisors, Prof. Dr. Joaquim Gabriel Magalhães Mendes and Prof. Dr. Mário Augusto Pires Vaz, their support and supervision was of the foremost importance. Either by their extensive knowledge in sensors and instrumentation, as for the experience in the field of non-destructive testing, their contribute for this work was essential.

An important contribution was also given by Dr. Pedro Miguel Guimarães Pires Moreira and Dr. Paulo José da Silva Tavares in the comprehension of the fatigue models and simulations. Despite the fact this was not the main subject of this work, it presented an important role in the understanding of the temperature behaviour during cyclic loading. Alongside these, contributions from other members from the Laboratory of Optics and Experimental Mechanics, INEGI, were also very important. To them, I would also like to leave here a note of gratitude.

I would also like to express my gratitude to my laboratory partners, for their suggestions and support that helped me to achieve my goals.

I would like to thank Porto Biomechanics Laboratory (LABIOMEP) from the University of Porto for the thermal camera used to conduct the laboratory tests.

The support of my family was extremely important, without which this work would not be possible. To them I express here my deepest appreciation. To finish, I would like to thank my friends and co-workers. Although I no longer keep daily contact with some of them, during the last years their help, support and understanding was extremely important.

António José Ramos Silva

This page was intentionally left blank.

"The aim [of education] must be the training of independently acting and thinking individuals who, however see in the service to the community their highest life problem."

Albert Einstein 1936.

to Marco Silva my apologies...

This page was intentionally left blank.

Contents

This page was intentionally left blank.

List of Figures

This page was intentionally left blank.

List of Tables

This page was intentionally left blank.

Symbols

α	Angle between the stimulus radiation and the temperature radiation (rad)
β	Volumetric thermal expansion coefficient $(\,)\frac{1}{K}$
Δ	Gradient of a certain variable (in all direction)
δ	Gradient of a certain variable (in a specific directions)
ε	Emissivity (-)
λ	Wavelength (m)
μ	Dynamic viscosity $(\frac{kg}{s\times m})$
∇	Backward difference operator in a differential operation
ϕ	Generic variable used in differential equation and in this work representative of a generic temperature (K)
ρ	Relative density
σ	*Stefan Boltzmann* constant, $5.67\times10^{-}8$ $(\frac{W}{m^2\times K^4})$
θ	Angle between the stimulus radiation and the measured radiation (rad)
υ	kinematic viscosity $(\frac{m^2}{s})$
ς	Heat capacity $(\frac{J}{K})$
A	Area (m^2)
AS	Amplitude surface (K)
B	Boltzmann constant ($1.38 \times 10^{-23}\frac{J}{K}$)
c	Ratio between the sample remaining thickness and the defect width (-)
c_0	Speed of light $(\frac{m}{s})$
C_p	Specific heat $(\frac{J}{kg\times K})$
CP	Stimulation cycle period p (s)
g	Gravitational acceleration $(\frac{m}{s^2})$
Gr	Grashoff number $(\frac{Ra}{Pr})$
K	Thermal conductivity $(\frac{W}{m\times K})$
l	Sample thickness (mm)

L_c	Characteristic length (m)
m	Mass (kg)
MR	Measured radiation $(\frac{W}{m^2 \times Sr \times nm})$
Nu	Nusselt number (-)
P	Energy radiated by a blackbody according to the Plank law $(\frac{W}{m^2 \times Sr \times nm})$
Pr	Prandtl number (-)
PS	Phase Surface (rad)
Q	Total of energy transferred by heat (J)
Qi	Interior heat source per unitary volume (W)
q	Heat flux (W/m^2)
Ra	Rayleigh number (-)
Re	Reynolds number (-)
S	Energy radiated by a blackbody according to the Stefan–Boltzmann Law $(\frac{J}{W})$
SP	Stimulation Period, *r* on appendix (s)
Sr	Steradians, solid or tridimensional angle (sr)
t	Time (s)
T	Temperature (K)
T_0	Temperature at initial time (K)
T_∞	Temperature at infinite, also called ambient temperature (used 297.15 K)
T_s	Temperature at given surface (K)
TS	Transient surface (K)
TR	Temperature radiation $(\frac{W}{m^2 \times Sr \times nm})$
Tr	Transmittance, capacity of a body to transmit radiation (-)
SR	Stimulus radiation $(\frac{W}{m^2 \times Sr \times nm})$
u	Generic direction (X, Y or Z)
V	Volume (m^3)

Glossary and Abbreviations

AE	**Acoustic Emissions**, sound emission from anomalies existing in a component
AT	**Active Thermography**
ApT	**Apparent Temperature**, the temperature of an object as determined solely from the measured radiance, assuming an emissivity of 1
ASTM	**American Society for Testing and Materials**
ATT	**Active Thermal Testing**
CFRP	**Carbon Fiber Reinforced Polymers**
CMC	**Ceramic Matrix Composites**
CT	**Computed Tomography**, tree dimensional image technique possible through the combination of several X-ray images
DFT	**Discrete Fourier Transform**
DIC	**Digital Image Correlation**
DIRT	**Digital Infrared Thermography**
ESPI	**Electronic Speckle Pattern Interferometry**
FAA	**Federal Aviation Administration**
FDM	**Finite Differences Method**
FEA	**Finite Element Analyzes**
FEM	**Finite Element Method**
FIR	**Far Infrared**
FVM	**Finite Volume Method**
IR	**Infrared**
IRNDT	**Infrared Nondestructive Testing**, is also the name of the commercial program used in this work
IRT	**Infrared Thermography**, indirect temperature measurement (as an image) by measuring infrared radiation
IRTT	**Infrared Thermal Testing**

LDR	**Light Dependent Resistors**
LED	**Light Emitting Diode**
LTT	**Lock-in Thermal Testing**
LWIR	**Long Wave Infrared**
MCT	**Mercury Cadmium Telluride**
MMC	**Metal Matrix Composites**
MWIR	**Middle Wave Infrared**
NDE	**Non Destructive Evaluation**, evaluating a component to access its integrity or determine the extension of a damage without destroying it or further compromise it
NDT	**Non Destructive Testing**, testing a component to access its integrity without destroying it or compromise it
NI	**National Instruments**
NIR	**Near Infrared**
NETD	**Noise Equivalent Temperature Difference**, target-to-background temperature difference between a blackbody target and its blackbody background at which signal-to-noise ratio of a thermal imaging system or scanner is unity
PAN	**Polyacrylonitrile**, method to develop carbon fibers
PAEK	**Polyarylketone**
PDE	**Partial Differential Equations**
PE	**Polyethylene**
PEEK	**Polyetheretherketone**
PID	**Proportional Integral–Derivative** control loop feedback mechanism acting in the feedback signal, its integral and derivative signal
PMC	**Polymeric Matrix Composites**
PMMA	**Poly-methyl-meth-acrylate**
PP	**Polypropylene**
PPS	**Polyphenylene Sulfide**
RT	**Radiographic Testing** Nondestructive testing method using Gamma or Neutron emissions to scan a component
SIF	**Stress Intensity Factor**
SL	**Stimulus Length**, duration of the stimulation in a transient analyses or cycle period in a lock-in test
SR	**Stimulus Radiation**, infrared radiation measured by the infrared thermal camera resulting from an optical stimulation source

ST	**Sample Thickness**, nominal thickness of a sample
SD	**Standard Deviation**
SWIR	**Short Wave Infrared**
TF	**Thermal Fit**, curve fitting to temperature data from active infrared thermal tests
Tr	**Transmittance**
TSA	**Thermal Stress Analyses**, or Thermoelastic, is the determination of the mechanical stress by application of a fast oscillation load and measure its local temperature variation.
TSR	**Thermal Signal Reconstruction** processing algorithm used to obtain better results in infrared thermal tests
TTT	**Transient Thermal Testing**
US	**Ultrasound**, sound waves with frequencies higher than the audible by humans (typically 20 kHz)

This page was intentionally left blank.

Chapter 1

Introduction

1.1 Context

The search for lighter, stronger, and more reliable materials is a daily concern in the majority of the industries. In particular the transport industries can benefit with the discovery of new and better performing materials. This constant evolution led to the creation of composite materials. From the vast number and type of composite materials available today, Carbon Fiber Reinforced Polymers (CFRP) have distinguished themselves as one of the better performing materials. They have very good mechanical properties without having a high manufacturing and processing cost [1]. However, in the transport industries there is a huge concern with security and maintenance operations. An adequate maintenance is essential to guarantee the vehicle safety, and its users, along with a good comfort. This aspect is far more critical in aeronautics, where a failure can result in a catastrophic event.

Non-destructive tests (NDT) are the natural solution when choosing methods to detect and characterize defects during maintenance operations. Over several decades the available techniques have evolved, like mentioned by Jayamangal Prasad and others [2]. Some of these have evolved from single point techniques and those same principles are now used in image techniques. Giving the possibility to scan a component or structure, faster and with the same accuracy. They are usually easier to interpret and the defects are easily identified. Image techniques usually measure a portion of the electromagnetic spectrum to create an image. In particular Infrared Thermography (IRT) has managed to detect anomalies where many others fail, have difficulties or are time consuming. IRT measures the infrared radiation, normally the middle and far sub-bands, that is related with the object temperature.

There are several NDT techniques that use thermography, however active thermography tests (ATT), where a stimulation is applied to the object, are the most effective. During the application of the stimulation to the object or/and some time after its ending, the temperature is monitored and recorded. The processing phase is one of the most critical parts of the thermal analyses. There are

two main types of tests that use thermography as a measurement tool: single stimulation (Transient and Pulse) and cyclic stimulation tests (Lock-in and TSA). Despite being different techniques, Transient and Lock-in thermal testing, they use very often the same type of stimulation source to detect the same type of defect. Although they present some similarities, the methodologies and processing procedure are considerably different. These techniques, require the specification of some parameters: waveform, stimulation or cycle period, instant to analysis, number of cycles, temperature interpolation model used by the software manufacturer, etc.

Being able to extract more information from a thermal test adds more value to a technique that already is extremely used. The improvements in post-processing have the advantage of maintaining the current physical measuring systems, thus preventing added costs to any alteration. Therefore, this work aimed to improve the accuracy in the selection of the parameters used to perform a thermal analyses and provide a guide to the expected results.

1.2 Main Goal

The main goal of this work is to develop a prediction model that provides the ideal parameters and settings to conduct active infrared thermal tests in composite materials with higher sensitivity to defects defection. The development was oriented to detect defects in composite materials, with special emphasis on carbon fiber reinforced polymers. To accomplish this objective, several tasks were defined:

- State of the art review relating non-destructive tests, with special emphasis in thermography techniques;
- Non-destructive thermal tests using thermography, with specimens build specifically to identify and characterize the settings that produce the best results;
- Simulation of thermal tests to increase the comprehension of the heat flow and behaviour during a thermal NDT test;
- Development and validation of a prediction model to perform thermal testing with a higher accuracy and its validation with reference components.

1.3 Structure

This work is divided in seven chapters. The current and first chapter is the introduction to the document. Here are described the main goal and the context of this work.

The second chapter relates the state of the art. This covers two main topics, composite materials and non-destructive testing. The composite materials description is oriented to polymeric

matrix and fiber reinforcements. The sub-chapter referring to non-destructive testing, briefly mentions the most relevant aspects of each NDT technique. A short description of the stimulations sources used in thermal testing is also mentioned.

The third chapter starts by introducing temperature measuring techniques with a main focus in infrared thermography and the several parameters used in the process. Next are presented and discussed the results obtained in laboratory with two main techniques: transient and lock-in tests. In both cases, are compared and discussed the influence of the most important parameters in the tests and in the post-processing. At the end are identified the settings that produced the best results.

The fourth chapter introduces thermal testing using stimulation feedback and with an active controller. The first part uses a light resistive sensor in the system to obtain the optical feedback. The second part, uses that same feedback along with a PID controller to achieve an accurate optical stimulation waveform. At the end of the chapter the three alternatives are compared: the common thermal tests, with feedback and with the controller.

Using the information collected in laboratory tests, finite element simulations were performed to achieve a better understanding of the heat flow during the most relevant tests. In this fifth chapter are presented and described the assumptions, the mathematical models, results and analyses of the simulations. With the results from the simulations, were found several equations that modulate the ideal stimulation parameters and expected results.

The sixth chapter validates the previously described models. Here, the models for the transient and lock-in thermal tests are validated from samples with different geometries and build with different materials, such as CFRP. At the end of this chapter the two techniques analysed in this work and phase shearography are compared.

The final and last chapter has the work conclusion. Here are briefly mentioned the most important comments and results contributions. Some brief notes and recommendations about future steps are also mentioned.

At the end of this document three appendixes are presented. The first is a brief analyses of the Thermoelastic Stress Analyses (TSA), with a special focus in the influence of the load in the thermal and resulting mechanical stress. The second is a resume of the prediction thermal response from the simulations. The third presents technical drawings of the main samples used and analysed in this work.

This page was intentionally left blank.

Chapter 2

State of the Art

This chapter is divided in two main sections, relating composite materials and Non-Destructive Testing (NDT). Both present a global overview of the corresponding field, justifying the importance of carbon fibre reinforced polymers and active infrared thermal testing.

Composite materials can be divided into classes, depending of their composition, structure and manufacturing techniques that will be shortly introduced giving an overall overview to the world of composite materials. The polymeric matrix composites and their reinforcements using fibres are described in a greater detail, since it is a relevant matter to this work.

Currently, several NDT techniques can be used to detect and characterize defects in composite materials. Starting with the most simple one, visual inspection also describing ultrasounds and radiographic, among others, several NDT techniques are mentioned and described. Despite not being the main goal of this work, this provides a better understanding of the alternative techniques to infrared thermography used to perform NDT. Here are reviewed the main and more common NDT technologies, their core principles and characteristics.

2.1 Composite materials

Composite materials are an association of two or more different materials, resulting in combined material with characteristics differing from any of the initial ones. The most common arrangement is the dispersion of the reinforcement in a continuous base (matrix). The reinforcement is usually much stronger than the matrix, but the high properties of a composite, appear when they are combined in an appropriate relative contents, orientations and dispersions [3]. According to their macroscopic structure and reinforcement disposition, composite materials can be divided into four categories [4]:

- **Fibrous Composites** — Composed by a matrix and fibres. These fibres are long and thin (typically 20 μm in diameter), these composites frequently have extremely high mechanical properties in the fibre main direction;
- **Laminated Composites** — Composed by layers of several materials bounded together to form a high performance compound, typically in the form of a plate or shell;
- **Particle Composites** — Composed by small particles dispersed in a matrix. These particles usually have one long dimension and tend to produce a highly isotropic composites;
- **Mixed** — A combination of any of the previously mentioned.

The most common composite materials uses fibres as its main reinforcement. Usually it increases the mechanical properties of the matrix, making the composite very strong in the fibres main direction [5]. In most of the situations the matrix is a resin. Since the composites present very high properties in the direction of the fibres, these can be disperse in a certain configuration to optimize the performance of the composite [6]. The composites reinforced with fibres can be divided in three categories, dependent of the material used in its matrix:

- **Ceramic Matrix Composites (CMC)** — The matrix is composed by a ceramic and the reinforcements are usually fibres (short fibres). They are commonly used in environments with high temperatures;
- **Metal Matrix Composites (MMC)** — These materials use metals for the matrix (aluminum among others) and are reinforced with fibres, the automotive industry is an area where they are more commonly used;
- **Polymeric Matrix Composites (PMC)** — Polymeric based resins are generally used in its matrix and fibres for the reinforcement, they are also referred as fibre reinforced polymers (FRP).

2.1.1 Ceramic matrix composites

Ceramic composites were initially manufactured using ceramic materials in the matrix and in the reinforcements. However, nowadays is also common to use fibres as reinforcement. The highest advantage of ceramic composites is its resistance to high temperatures, therefore they are naturally selected to be used in these environments and conditions, some of these were described by Aldo R. Boccaccini in [7]. The ceramic matrix usually provides high: strength, elastic modulus, hardness and temperature resistance and dimensional stability. The most common type of ceramic composite is by far the glass fibre. The majority of fibres used present an individual diameter of approximately 10 μm. With this small diameters they are capable of flexing, keeping their original stiffness and brittleness, natural of the glass [7]. Being one of the first fibres to be processed industrially, they are still used in a variety of products and components and in some cases, with techniques with several decades [8].

The fibres used in this types of composites can also be cropped in short segments and have them mixed and randomly dispersed in the matrix [9]. If the fibres are short enough, they can be mixed, injected into a mold or even projected onto a surface. This surface could be a mold (a more common situation) or a structural component that is being reinforced, this is explained in more detail by Krishan K. Chawla in [10]. With these materials and manufacturing processes, is possible to produce components with a complex shapes and highly optimized. Here they can have different thicknesses and the mechanical properties can vary in some sections of the component. This type of processing is typically used in large parts like car components and bodies, boats, pressure vessels and pipelines. Most common matrices are chemical inert, these materials are also indicated for corrosive or other damaging environments.

2.1.2 Metal matrix composites

Like suggested by its name, Metal Matrix Composites (MMC) use metals in their matrix, in particular aluminium is widely used in the matrix of MMC. This mainly because of the processing methods developed in the 1970s (foil-fibre-foil method), taking advantage of the low processing temperatures of the aluminium compared to other metals [11]. The result is aluminium composite reinforced with continuous boron fibres and another reinforced with SiC-coated boron fibres. Currently, the MMC based on aluminium can be provided for a direct product application (raw alloys) or to undergo future processes. MMC can posteriorly pass through heat treatments to further improve their properties. Some examples of the research in this area was pioneered by Suganuma and Kainer [12, 13].

Titanium alloys usually present a density of 4300 kg/m^3, being 40% lighter, but with the same strength of the majority of steels. For temperatures up to 300 °C, titanium maintain good structural and mechanical properties, as well as a good resistance to oxidation [14]. Being one of the most

capable metals, its usage in a composite matrix results in one of the most capable materials, usually used in extremely demanding conditions such as the aerospace and aeronautical industries [15].

The reinforcements in MMC may take a discreet arrangement and disposition, leading to a network of individual fibres. As a result, strength and rigidity are improved. Usual reinforcements are nitrides, carbides and oxides, precisely characterized by their strength and rigidity despite the temperature. A short introduction to this matter is performed by Karl Kainer in its book, Metal Matrix Composites [16]. The reinforcements can be short particles or whiskers or long fibres. Despite the short reinforcements, the load is still mainly supported by the fibres while the matrix acts as a restrain for the reinforcements. With the long and continuous or semi-continuous fibres, the supported main load can have higher magnitude, with the matrix still being used to hold the fibres in place and distribute the load.

Some fibres can be coated with an additional reinforcement before the junction with the matrix. The coating usually improves the bounding with the matrix, to achieve cohesive structure, like explained by Kainer [17]. This has a protective role and prevent the fibre diffusion within the matrix, by preventing a direct contact between the two. Alongside these advantages, it is also achieved this way a better distribution of internal thermal and mechanical stresses. The coating also has a protective role during the manipulation and manufacturing processes. There are several manufacturing processes, being the most important:

- Powder blending and consolidation;
- Consolidation diffusion bonding;
- Vapor deposition;
- Squeeze casting and squeeze infiltration;
- Spray deposition;
- Slurry casting;
- Reactive processing.

2.1.3 Polymeric matrix composites - resins

Polymeric matrix composites (PMC) are the most common and used composites in aeronautics industry [18]. Resins are a common material to be used as matrix and will be described here, followed by the fibres. The word *resin*, as described by Anthony Kally, is referred to a polymer that can be described as mixture of various additives or chemical reactive components [19]. Usually the resin determine the final shape of the composite, therefore, its properties define the handling and processing procedure. The main type of resins are:

- Epoxy;
- Polyester;
- Phenolic;
- Thermoplastic materials (Polyimides and silicones);
- Bismaleimide.

An epoxy resin is a polymer characterized by an oxirane structure, a three-member ring with one oxygen and two carbon atoms [20]. They are curable be reacting with acids, amides, amines, alcohols, phenols making them a thermosetting resins [21]. After the curing process they present elevated elastic modulus and strength, excellent adhesion, good chemical resistance, low shrinkage (when compared before the cure process) and are fairly ease to process. The biggest disadvantage is the high brittleness and its sensibility to moisture. The cure process takes place between room temperature and 180°C, being the most common in the range of 120 and 180°C. The cure temperature also influences the resin behaviour and properties after the cure. The curing pressures are low, ranging from vacuum to 700 kPa.

The polyester resins (thermosetting) are economical and fast to process, therefore, they are used for low-cost applications and products. These resins are a combination of polyesters in a monomer solution, generally styrene [22]. This improves the handling of the resin and enables its molding without pressure. Several ancillary products are used to mold the resins, such as:

- **Catalyst** – Start the chemical reaction (cure process), adds an extra substance to the final composition and reduces the energy involved in the process;
- **Accelerator** – Increase the rate of the chemical reaction (cure process) and can be consumed during the process;
- **Addictives**:
  - **Thixotropic** – Improve the resin viscosity behaviour prior to the cure for molding and injection applications;
  - **Pigment** – Add colour to the mixture, mainly for cosmetic purposes;
  - **Filler** – Reduce weight, change specific molding characteristics and reduce costs;
  - **Chemical and/or fire resistance** – Add or increase its impermeability to a certain chemical or increase the fire resistance capabilities.

Phenolic resins, are characterize by having a matrix that is thermal resistance to chemical and smoke. The most common types are resole and novolac, according with their condensation reaction. From their high viscosity and molecular weight, comes their natural capability for unusual conformations or complex shapes. These applications are also enhanced by the capability of curing supporting high temperatures and free-standing post-curing processes. The normal cure of these resins can be performed under pressure or autoclave [23].

Polyamides resins are a family of diverse polymers that contain aromatic circular heterocyclic structure. They can be thermoset or thermoplastic resins, in particular thermoplastic polyimides can be thermoset if a post-cure high temperature is applied, the opposite situation is also possible. Polyimide resins require a cure temperature near 90 °C, and have an operation temperatures range from -150 up to 200 °C. Even at high temperatures they are capable of keep good mechanical properties and are dimensionally stable. Being one of the resins with better properties, their primary use is in circuit boards, hot engine parts and aerospace structures [24].

Another type of resins are thermoplastics. These, can be semi-crystalline or amorphous, with these last corresponding to the majority. Some semi-crystalline thermoplastics are: polyethylene (PE), polypropylene (PP), polyphenylene sulfide (PPS), polyetheretherketone (PEEK) and even polyarylketone (PAEK) [25]. These tend to be very malleable and can be processed into powders, filaments and films. Their usage in primary and secondary structures of aerospace industries is due to the resistance to flames, mechanical properties at high temperatures, after an impact and moisture absorption. Some of the most important amorphous polymers are: polysulfone, polyamide-imide, polyphenylsulfone, polyetherimide, polyether sulfone, polyarylate, polystyrene and polyphenylene sulfide sulfone [26]. These resins are easy and fast to process, their mechanical properties are good, particularly their resistance at impacts and present an excellent hardness [27].

Another type of thermosetting resins are Bismaleimides, resulting from the reaction of a diamine and maleic anhydride. They are generally available as "prepreg" forms, rovings, and sheets of fabrics, among others. Another important characteristic is the extreme adaptability to the reinforcement properties, being dependent of the used reinforcements [28]. The capabilities of bismaleimides are comparable to epoxy with the biggest differences being the glass transition temperature (around 260 to 320°C) and two to three percent higher elongation. This without losing excellent performance at ambient and high temperatures. The processing and resulting products are very similar to epoxy resins [29].

Silicone resins have a three-dimensional structures primarily composed by organosilicon. They can endure temperatures of 350 °C, and with the appropriate fillers, 600 °C could be tolerated. They are one of the resins with higher oxidation resistant, hydrophobic and vapour permeability. The global mechanical properties are also very good, including weathering resistance and their dielectric behaviour is also very good [30].

2.1.4 Polymeric matrix composites - fibres

The most used composite materials are reinforced with fibres and can be very isotropic or highly anisotropic. The fibres are a very important part of the composite and usually are the responsible for the improvement of the matrix properties. The most used types of fibres are:

- Carbon and graphite;
- Aramid;
- Glass;
- Boron;
- Alumina;
- Silicon carbide;
- Quartz.

Carbon and graphite are the most known reinforcement fibres, with great flexibility and a variety of properties that can be adjusted. A polymer reinforced with these fibre will result in a component that is stiff without being brittle. They were used commercially for the first time when Thomas Edison created the incandescent light bulb [31]. The carbon fibres as they are known today were firstly discovered by Roger Bacon, this is also considered the first reference to nanotubes [32]. The carbon fibres are composed of small filaments with 5 to 10 μm in diameter. The fibres can be arranged in three main dispositions depending on their origin: rayon, polyacrylonitrile (PAN) or pitch. The rayon fibres were the first ones to be commercialized (1960), however they have been gradually replaced by the superior PAN type since the 70's [33]. The pitch fibres are able to achieve ultra-high Young modulus and thermal conductivity, being the current choice for critical space and military applications and also very expensive.

Aramid fibres are synthetic fibres that are heat resistant with rigid polymer chains. They are more commonly known as kevlar® or Nomex®. Their most important characteristics are: high strength, resistance to abrasion and organic solvents, non-conductive no melting point, low flammability and good fabric integrity at elevated temperatures [34]. On the downside, they are sensitive to ultraviolet light, being gradated when exposed to sun light. The main and first major application of these fibres is in protective gears like bullet proof vests. Being flame resistant, self-extinguishing and low conductivity, they are a natural choice for wire casing and fire fighting protection equipment [35].

Like many others, glass fibres reinforcements consists in several extremely thin fibres, in this case made out of glass [36]. The most common is the E-glass fibre, they are composed by alumino-borosilicate. The mechanical properties of these fibres are fairly similar to others, even if a little inferior than carbon fibres. Despite a little more ductile and less strong when compared with some types of carbon fibres, their cost is considerable lower, with its brittleness diminished and controlled when used in composites. The fibres can assume an amorphous configuration and be used in building heat insulator or arranged in a textile and introduced in a polymeric matrix. This last application gives origin to strong and relatively lightweight fibre-reinforced polymer with low production costs.

The Boron fibres present an amorphous arrangement of their elements. They are usually manufactured by a deposition reaction on hot tungsten wire which leaves tungsten boride in the core of the fibre. These fibres present a high strength and elastic modulus with small density. They are exclusively available in the filament form or prepreg by epoxy matrix. The boron fibres are considerably expensive (more than carbon fibres), being used in some components in the aerospace and aeronautics industry like F-14/15 stabilizers reconnaissance satellites, and several parts of the space shuttles [37].

Alumina fibres in a polycrystalline form, are ideal to reinforce plastics, ceramics and metals. They can be provided for reinforcements as long or short fibres having good mechanical and chemical resistance. They are good thermal and electrical insulators and their manufacturing cost is comparable to the carbon fibres. Long fibres are ease to align and handling. Over the last years, alumina/epoxy and aramid/epoxy hybrid composites reinforced with alumina and aramid fibres have proved valuable materials in radar transparent structures and high performance electronic circuit boards [38].

Silicon carbide fibres normally possess diameters of 140 μm and present high strength elastic modulus and density. They are oriented to be used as reinforcements of aluminium and titanium alloys, either lengthwise or crosswise. The cure cycles resemble the ones applied in carbon and glass fibres. Being used as reinforcements, their solo properties are not relevant and the composite is highly dependent of the matrix properties [39].

Quartz fibres are used almost in its pure state, with percentages above the 99.9 % fused with silica glass fibres. In the majority of the situations, the fibres are coated with an organic binder, the silane coupling agents endow the fibres with a high compatibility with many resins. Quartz fibres present the highest strength-to-weight ratio, being even higher than the high temperature materials (commercially available). They do not melt or evaporate for temperatures up to 1650 °C and are used in situation were the service temperature is over 1000 °C. The chemical stability and resilience are also very high, with the exception for highly alkaline environments. Despite the high cost these fibres are also used as electrical insulators [40].

2.1.5 Nanotubes and mechanical properties overview

In the past decade, nanotubes have been one of the most studied subjects. Their mechanical and electrical properties have been studied intensively with new applications being constantly discovered. The properties of the carbon nanotubes make them the most appropriate additional reinforcements for specific composite applications. Along with Roger Bacon in 1960 [32], Sumio Iijima in 1991 is considered the father modern carbon nanotubes [41]. Since then, several have reported their high mechanical and physical properties. Namely the modulus, reaching values near the elastic modulus of diamond and strength up to 100 times higher than the better steels,

maintaining a low density. Another important characteristic is their very high thermal conductivity. These properties make them one of the most promising reinforcements to be used in nanocomposite materials. The thermal stability, for temperatures up to 2800 °C, is also very high, along with a capacity to carry electric currents, 1000 times higher than copper [42], [43]. Reinforced with nanotubes, MMC present superior elastic modulus, ultimate tensile strength and yield strength [44]. These composites can have their properties even higher depending on the type of process used (solid or liquid-phase) [45], [46].

Currently are known two types of nanotubes. The first consists in a single sheet of carbon, rolled to a cylindric with a diameter of approximately 1 nm and reaching up to a few centimetres [47]. Nanotubes with multiple walls are formed with several concentric cylinders of carbon sheets. The separation between cylinders is approximately 0.35 nm, which is similar to the distance of planes in graphite [41]. The nanotubes can have diameters ranging from 2 to 100 nm and lengths of some tens of microns. In the present days some researchers have clammed distances of approximately 0.5 meters [48]. In current days, the most common manner of obtaining the nanotubes is by chemical vapour deposition and laser ablation [49], [50]. One of the biggest challenges in the production of composite materials is to achieve an uniform distribution of the nanotubes and consequentially the loads applied to the composite. The load distribution is obtained when exists a dispersion of the carbon nanotubes in the matrix, an optimum blending and the correct alignment of the nanotubes in the matrix.

The unknown behaviour of the newly discovered composite materials makes difficult their usage in production lines or high production rates. Despite the recent discoveries in composite materials, carbon and glass fibres are still the most common. Table 2.1 presents an overview of the main properties of common fibres used in composite materials.

Table 2.1: Fibres main properties

	Tensile modulus (GPa)	**Tensile strength (MPa)**	**Density (kg/m^3)**	**Fibre diameter (μm)**
Carbon [51]	41 - 760	150 - 1000	1600 - 2150	4 - 11
Aramid	135	410	1400	5 - 60
Glass	70 - 12.5	440 - 670	2480 - 2620	30
Boron	400	730 - 1000	2300 - 2600	100 - 200
Alumina	385	1.4	3900	20
Silicon carbide [52]	48 - 66	17 - 170	2.5 - 3.2	7 - 140
Quartz	72	6	2.2	0.9 - 1.1

Very often the matrix main function is to support and maintain the fibres in their respective place, leading to two facts. Firstly, the most part of the structure weight is due to the matrix. Second, the matrix plays the main role in the manufacture procedures. Looking at table 2.1, it is easily observed that carbon fibres present one of the highest tensile strength alongside with Boron fibres. On the the downside, Boron fibres present higher density than carbon fibres. In table 2.2 are exposed the main resins used with carbon fibres. Epoxy resins are low cost and are easy to produce, this made them one of the most used, despite not possessing any particular property that differentiate them from others resins.

Table 2.2: Resins main properties

	Tensile modulus (GPa)	**Tensile strength (MPa)**	**Compressive strength (MPa)**	**Density (kg/m^3)**
Epoxy	10.5	85	190	1100
Polyester [53]	3.4	55 -80	120	1900 - 2000
Phenolic	10	50	—	1400
Polyimides	4.5	152	220	1400
Silicon[54]	2.1	15	—	1000

2.2 Non-destructive testing

Although the surface defects on structures are easier to detect by the naked eye, the inner defects require the use of auxiliary inspection techniques, such as Non-Destructive Testing (NDT) [55, 56]. This way, it is possible to detect and quantify the damage in a structure, or component, without diminish their life span. In this case, the areas to be analysed are stimulated to reveal the presence of discontinuities or changes in structure, usually coincident with defects. The behaviour of the structure in regions of interest are monitored and may also be compared with previous tests or new components.

There are currently various non-destructive inspection methods (NDT) [57]. However, none of the known techniques can fully meet all the needs of NDT in composites. The ultrasound techniques developed over the past decades are one of the most common and reliable techniques. However, the time required to perform the evaluation of an area using ultrasounds is considerably high and require inspections coupling means, water or gel, this fact prevents the inspection of hydrophilic materials. The most commonly used non-destructive tests are:

- Visual inspections;
- Penetrant inspection;
- Electromagnetic testing;
- Radiographic testing;
- Acoustic emission;
- Laser testing;
- Vibration Analysis;
- Ultrasonic Testing;
- Infrared thermography.

For the correct selection of a NDT technique, some considerations are required. The object manufacturing processes and usage conditions, along with the expected defects are some of the most important aspects. Depending on the nature of the expected defects, they can be visible or hidden. To detect a defect, a pass/reject criteria should be defined. Should also be taken in consideration the spatial resolution of the selected technique, along with maximum defect size, supported by the component without compromising its integrity.

2.2.1 Visual inspections

During the first years of aviation, visual inspections were considered to be very subjective and difficult to be re-evaluate or compared since it was not possible to record the data. The operator experience, conditions of the test, cleanness, quality of the optical equipment used and illumination are important aspects of these tests [58]. The evolution of technology leads to the acceptance of visual inspections as a NDT by the American Society for Testing and Materials (ASTM) and Federal Aviation Administration (FAA) to the creation of standards to conduct these tests [59]. Some considerations about this matter is presented in one of the firsts great references in visual inspections by Robert Anderson [60].

Visual inspections can use auxiliary equipment (micrometres and spring loaded depth gauges, among others). For example, when evaluating the corrosion depth on a pipe, appearance and colour of a surface can provide useful indication on the origin and damage extension. Visual inspections are usually used to conduct minimal and fast evaluations, but by using optical equipment it is possible to access defects with a greater detail. The most used equipment's are:

- Borescopes;
- Fibrescopes and Videoscopes;
- Microscopes;
- The Long-Distance Microscope;
- Remote and/or automated Visual Inspection.

Borescopes are optical devices, consist in a long tube, flexible or rigid, with a lenses at one end and a display device at the other. Near the lenses are located an optical fibre and light to illuminate the observation area. Due to its geometry, borescopes are usually used to inspect pipes, tubes, dangerous access zones or other areas difficult to reach like the internal parts of jet engines. Nowadays they are being more and more used in the most divers situations, motivating the development of borescopes that are rigid, extensible, flexible, with micro designs and small amplification capabilities. The diameter, length, rigidity, illumination and amplification are the most important characteristics of these devices and define if a certain model is appropriated for a specific application or to locate a certain type of defect.

The modern fibresopes and videoscopes have overcome many of traditional limitations of the conventional processing and recordings by saving the images in real time. They have become more flexible, thin and reliable. The introduction of optical fibres and electronics, pushed the application range mainly by introducing LED light. The usage of laser lights can provide measuring capacities to visual inspections. Some of the multiple accessories available are: optical adapters (mono and stereo), side viewing optics, wide and extra narrow lenses and remotely controlled flexible cables.

The introduction of the microscope, gave a new insight in non-destructive evaluation. They use visible light and lenses to amplify a certain detail. The observation can be captured by a camera and recorded to future analyses. The main usage is the observation of very small components like jewels polishing, electronic circuits or in the analyses of micro-structure made out of alloys or composite materials.

An alternative to the standard microscope is the long distance microscope and continuously focusable microscope. They are considerable smaller than the standard microscope, but cannot provide the same amplification level. The portability of these devices means they are appropriated to field measurements and applications. In some cases they can have accessories like, illuminations systems, lasers, cameras and others.

One form of increasing visual inspections are known as remote visual inspections. They use a digital video equipment to transmit the visual images to an off-site location, similar to what is described by Lorenz [61]. This type of inspections were initial used in applications were the area of inspection was inaccessible or dangerous. Nowadays, they are also used to centralize the decision making process and as a method to diminishing inspection costs. This type of inspection can use the above mentioned technologies either individually or combined.

Automated inspection uses certain specified parameters to determine the quality and integrity of a component or structure. This inspection method has gain popularity mainly by the evolution of machine vision technologies. Here a specialist defines the criteria of approve or rejection in a determined situation and the images are processed by a computer that access the integrity of

the component. This technology can be easily combined with several others to enable guidance processes (robots and other automated systems), process control or even completely automated inspection.

2.2.2 Dye inspection

Dye or penetrant inspection bases its fundamentals in the usage of a substance that penetrates a crack or discontinuity by capillarity, from the surface to the crack interior. Despite the first mentioned date to 1920s in the steel industry, only in 1941 with the advances of Joseph Switzer, did this type of testing gain noticeable acceptance, witch lead to several patterns along the following years [62–65]. From then until today, the penetrant inspection have evolved continuously, from improved dyes, penetrant, emulsifier among others.

If looking solely at surface discontinuities, the current state of the art liquid penetrant are more accurate and reliable than radiographic tests. The best penetrant substances have a good penetrant capabilities while being able to remain in wide openings, without sacrificing its easiness of removing after the test is completed. A very important characteristic, especially in the case of composite material is the nonexistence of any chemical reaction with the component that can damage or diminish its integrity or even the composite appearance [66].

Due to its main principle, penetrant techniques are restricted to surface defect testing of witch they are very sensible and insensitive to the extension of subsurface defects [67]. On the opposite side, materials with elevated number of cavities and porous, like bronze porous alloys or unglazed ceramics will display an innumerable false defects. The most common of penetrant used are liquids with dye suspensions. Initially they are applied to the surface to be tested. After several minutes (depending on the used liquid type) during which the capillarity effect takes place, the liquid at the surface is removed. If a defect exists, a certain part of the liquid will be expelled and becomes visible, signalizing the presence of a surface discontinuity. In Table 2.3 are described the characteristics of the main types of penetrant liquids [66].

Water washable fluorescent liquids are produced with an oil base and with emulsifiers. Due to the oil base they can be easily removed with water. The designation fluorescent is derived from their ability to reflect a bright yellow light (usually) when illuminated with a black light. If a quantitative evaluation is desirable, it can be performed with a spectrometer sensible to ultraviolet light. Temperature changes the liquids viscosity, making them hard do appear in shallow defects (high temperatures) or harder to remove after inspection (low temperatures).

Post-Emulsification Fluorescent liquids are also produced with an oil base and a brilliant fluorescent additive. However these cannot be removed with plain water due to the missing emulsifiers. The emulsifiers are added after the liquid by pulverization or spaying, in a manner to

Table 2.3: Main dye penetrant characteristics

Variable	**Water washable fluorescent**	**Post emulsification fluorescent**	**Water emulsification visible**	**Solvent clean visible**
Sensitivity		×	×	
Visibility	×	×		
Fast test	×	×		
Retest		×		×
Portability			×	×
Shallow defects		×		
Big components			×	×
Black light	×	×		
Examiner influence			×	×
Rough surfaces performance	×			

obtain a uniform layer, allowing the removing of the excessive liquid. They are sensible than water washable fluorescent and are the easiest ones to reuse. Since they are easy to clean using water, they are recommended for components that have rough surfaces, like parts obtained by casting. Due to the high sensibility of these liquids, it is recommended the usage of black light not only to analyse the component but also for cleaning processes, prior to the examination.

Water emulsifiables penetrant liquids, require the application of a developer to the surface after the excess liquid is removed, usually with a white colour thus providing an even higher contrast to the test by contrasting with the coloured dye particles, increasing its sensibility. In some cases the marks are left visible after the test, to facilitate repair operations. Since they are oil-free liquids, anti-corrosion, coating, or welding operations can be performed after a simple clean process [68].

Solvent clean visible liquids are characterized mainly by being highly portable and therefore are largely used in field inspections since water or post-emulsification agent is not required. It is also a preferred liquid when, the usage of black light is a major difficulty. On the downside, it requires the existence of clean surfaces, free of oil, carbon, rust, grease, paint, or other coatings and impurities. These impurities may lead to false positives (false defects) indications. These types of liquids are applied direct from the containing aerosol recipient. The dwelling time depends of the required sensitivity, nature of the defect and surface conditions. The temperature is the major influence in the liquid viscosity and its capability to detect and highlight some defects [69].

2.2.3 Electromagnetic testing

Non-destructive testing using electromagnetic principles can be divides into three main topics, Eddy currents, leakage flux and magneto-elastic tests.

Eddy current testing uses an alternating magnetic field, created by passing an alternated current through a coil. When the magnetic field approaches an electric conductive material it generates continuous Eddy currents. The induced Eddy currents penetrate in the material and are reflected to the coil. These reflected currents are inverse to the initially created ones and, will diminish the generated magnetic fields. When a defect exists in the component, this deviates the magnetic flux and consequentially the reflected eddy currents will change and diminish. Increasing the coil impedance, thus indicating a discontinuity or defect [70].

Since Eddy current testing uses the secondary, or reflected, magnetic flux to measure the material conductivity (smaller in the presence of a flaw), the material conductivity has a large influence in the technique sensitivity. Since the air has little magnetic conductivity, the distance and its variation to the surface is also extremely important. For very small distances and for small distance variations, the changes in the magnetic flux is linear. This distance variations can be measured in order to calculate the coil impedance for a zero distance between the coil and the object surface. The magnitude of the frequency influence is in the same order of the magnetic conductivity. Thus is possible to select a certain frequency that will result in a favourable operating point that maximizes the detection of defects with predefined characteristics.

The majority of tests that use Eddy currents do not require the precise measurement of the flux. In most situations the goal is to define a reference value for an area and then inspect the rest of the component surface, searching for flux variations that correspond to a defect.

If a testing prob with a single coil is used, the test will be greatly affected by the distance variation between the test piece and the prob surface. The probe will be affected by the component superficial rugosity and natural vibrations from the manipulation process. These difficulties can be overcome by using a coil with differential configuration. The movements affect both coils and therefore they compensate each-other minimizing these variations. In the presence of a defect, it will be sensed firstly by one then by the other coil. The comparison of the same defect measured by the two coils increases the system sensibility. The design of the coils shields may be used to shape the field and/or increase sensitivity and resolution [71].

Magnetic flux leakage testing uses the lines created in a component when a ferromagnetic material is magnetized. The existence of defect deviate and disrupts the flux lines enabling their detection by using leakage flux. With some limitations, is possible to characterize the extend of the defect by measuring the intensity of this flux [72]. These tests use magnetic sensors to detect

and measure variations in the flux leakage. They are not restricted to planar surfaces and can be used in round components with diameters ranging from 10 over 600 millimetres. In the center of a surface these flux lines are undetectable.

The sensors themselves should be extremely small if short and small defects are to be detected. This small size enables the stacking of several sensors in a single sensing prob tip, increasing the scanning speed. The sensors consist in inductive coils or solid-stat Hall sensors. In magnetic flux leakage testing these probes present the following advantages:

- Long-life solid-state devices;
- Direct or alternating current according with the magnetic field;
- High-speed switches, they provide bounce-free, contact-free logic level voltage transfer;
- They have a wide range of operating temperatures (-40 to +150°C) and high repeatability.

During the manufacturing and life cycle, loads applied to metallic components instigating residual stress, difficult to predict. Magnetoelastic tests are used to characterize the residual stress in magnetic materials using the Barkhausen noise principle [73].

The application of a magnetic field to a metallic component will magnetize and also elongate it, in the direction of the induced field. The reverse phenomenon also occurs. This principle is valid for tensile and compressive loads. If the two (force and field) vectors are perpendicular nothing will be measured. When an unaligned magnetic field, resulting from a residual stress, is subjected to a magnetic field is going to align with this, creating a measurable Barkhausen noise. These equipment's are usually lightweight and easy to manage, simplifying field measures [74].

2.2.4 Radiographic testing

Radiographic Testing (RT) methods are used in NDT to accessing components defects, in this case by using a type of radiation that can penetrate the material under analyses. The main aspect defining this type of techniques is the usage of an ionizing radiation.

Radiographic tests can be performed through several principles, being the most effective denominated as single wall exposure, or single view. This technique is extremely useful in planar components, were the radiation can pass through a surface and the amount of radiation that penetrates the objects is measured on the opposite side and gives information on its insights. Depending on the dimension of the component, other modalities can be used such as double wall exposure single view technique or double wall exposure double view technique. Overall these systems are extremely inefficient, with only around 1 to 4% of the energy being used to create X-ray (the remaining is converted into heat) [70].

The first to record radiographic images, was by using a radiographic films. These films were composed by several layers of individual films crystals, being divided into classes depending on the type of image and test being performed [75]. Nowadays a variation of this technology is CT (computerized tomography). In this case, several sequential X-ray images, perpendicular to a main axis, are acquired and digitally stored. It is imperative that the images are captured digitally to permit the reconstruction of tree-dimensional image.

Another types of radiations are Gamma and Neutrons. They complement one another, with Gamma radiation being used for denser materials and neutron for lighter ones. Neutron testing uses the capacity of some materials to absorb neutrons. The majority of plastics and hydrocarbon foams with a petrochemical basis are transparent to Gamma rays but have a great absorption coefficient to Neutron radiation [76]. In general, Gamma rays are used in metals and organic lead. If the component is thick, neutron radiation can also be used in metals. As a resume, the main advantages and disadvantages of radiographic image testing are presented in table 2.4.

Table 2.4: Radiographic testing main characteristics

Advantages	**Limitations**
Provides an extremely accurate and permanent record	There are safety hazards with the use of radiation devices
Is very versatile and can be used to examine many shapes and sizes	RT has thickness limitations, based on material density and energy used
Is quite sensitive, assuming the discontinuity causes a reasonable reduction of cross section thickness	RT requires extensive experience and training of the personnel taking the radiographs and during the interpretation
Permits discontinuity characterization	RT is very costly in initial equipment and expendable materials
Is widely used and time-proven	It is also very dependent on discontinuity orientation
Is a volumetric NDT method	RT can be time-consuming

2.2.5 Acoustic emission

Acoustic Emission (AE) testing uses the natural forces applied to a structural component. The stress resulting from the working loads produce deformations, cracks, friction, that eventually lead to AE. These emissions can also result from the plane dislocations that occur at an atomic

level when a plastic deformation takes place. Inside a metallic alloy there are several non-metallic particles that are usually brittle than the metallic matrix and tend to break easier. When one of these breaks occur a sonic wave is created in the metal, that is then used to identify and characterize as a possible crack. In the presence or initiation of a crack, this phenomenon is even greater, being one of the highest sound amplitudes in acoustic emissions. This is also one of the most dangerous types of defects in metallic structures. In the crack area, namely in the opening faces there is friction (as the crack opens and closes) this is also an acoustic emission source [77]. The appearance of corrosion in the tip of the crack enhances the acoustic emission in the crack area. The energy source of AE is the elastic deformation that is released in a short pulse and sends waves through the component and structure. After several years of research and optimization it was found that the best results are obtained for frequency between 100 and 500 kHz. The theory of AE says that the amplitude of the emission is proportional to the new created area and that a slow growing crack leads to a smaller amplitudes than the creation of a new crack. Another accepted fact is that the AE amplitude is also proportional to the crack growth rate [77].

The AE propagates through the material and then is captured by an adequate probe (sensor). Generally the signals are analysed taking in consideration the existing frequencies and amplitudes. The sensors can be of two types: narrow or broadband. The broader sensors capture a wider and a more realistic signals. However, the narrow band sensors are universally cheaper and more sensitive. Capturing a narrow band also enable the refined tunning and rejection of background noise. These narrow-band probes are far more used and common.

The wave propagation through the structure tend to diminish the signal amplitude, this is called attenuation. The structure geometry is the main responsible for the wave propagation and its attenuation. This is extremely important when positioning the probes to monitoring a structure continuously. The probes should be positioned in the most critical areas and where the cracks and corrosion can induce higher damage but also where the prob is subjected to less external noise [78].

Due to the frequencies used in AE, the sensor probes contain a piezoelectric sensor. It is imperative a good acoustic contact between the sensor and the test specimen. which requires a coupling agent like an adhesive or grease [79].

The AE systems can be composed of several sensors. This means that an event can be detected in several sensors thus, helping the detection and diagnose of the possible defect with higher accuracy. The time difference between several sensors can be used to pinpoint the location of an event more precisely [78]. AE techniques can be used to identify and analyse crack initiation and growth, unwanted friction, component failure, impacts, dislocations and corrosions.

2.2.6 Laser testing

Laser testing defines a group of techniques used in non-destructive testing. These are characterized by using laser and therefore do not require any contact with the structure. The non-existing contact facilitates the examination of complex and curved surfaces. They can be used in macro or micro scale increasing this way its applicability. The main NDT techniques that use lasers are ESPI, shearography, holography and profilometry.

The acronym of Light Amplification of Stimulation Emission Radiation (LASER), gave origin to the word laser. A laser is characterized by emitting light that is intense, single wave-length, plane polarized and extremely stable. The first laser was a ruby laser made with a ruby crystal. This consisted in crystal inside a tube where an intense light was discharged. At the end of the tube are positioned two mirrors, one completely flat and the other semi-transparent [80].

The majority of lasers can be divided into four classes. Class 1 lasers are harmful, due to its radiation levels, therefore are used for simple measurements, pointers, among others. The class 2 emits radiation in the visible waveband of the electromagnetic spectrum. The class 3A does not create permanent injuries to the eyes if viewed with naked-eye and for just brief instances. Class 3B can in turn damage the human eye and consist of laser up to 500 mW of radiant power. Lasers of class 4 are dangerous for humans, not only the eyes but also the skin. In the recent years this last class has grown exponentially.

With the invention of a monochromatic coherent light source in 1960 reappeared a technique called holographic interferometry. Here the light is divided in two separated beams, one that goes directly to the camera (reference) and the second that is projected in to the object. The two beams are oriented to be superimposed on a photodetector; film or photopolymer. The image is then analysed as a common photography. With the illumination of the film with the reference beam the light is diffracted to the original form and recreates the object wavefront. Therefore any alteration in the object can be easily seen. Nowadays the most known and used setup is called Electronic Speckle Pattern Interferometry (ESPI) [81]. The main applications are:

- Vibrational modes characterization of moving objects;
- Measuring deformations in structural elements;
- Measure mechanical Strain/stress and thermal strain/stress;
- Crack detection in steel plates;
- Bonding evaluation in composite materials.

Illuminating a surface with a coherent light will result in a stochastic interference pattern (speckle). Shearography differs from ESPI and holography since the comparison is performed with the test object as a reference. Since the image is divided (sheared), into two images the method

is more sensitive to external vibration and noise.The application of a small loads deforms the component or structure, as a result a non-uniform deformation leads to a new speckle pattern that when compared with the reference image reveals the non-uniformity in the component behaviour. The ESPI method is sensitive to two out of phase beams resulting from displacements of 10 nm maximum. This limitation can be overcome by combining it with white light techniques. Here the entire surface is analysed and processed afterword's. The resolution of these systems can range from 60 nm up to some millimetres [82].

In the last years, the advances in tridimensional Digital Image Correlation (DIC) make this technique complement ESPI [83]. This is due to the ability of the DIC testing method to measure large deformations and, with the same equipment, reach resolutions of less than one micron [84].

A laser can also be used to inspect the surface of a certain component, this is called profilometry. This is of extreme importance in surfaces where some movement will occur, like roller bearings, machined parts, insulators layers of electronics. The optical profilometers overcome the main disadvantage o stylus profilometers like the resolution and especially the lateral resolution. The most commons are ESPI using coherent light and white light interferometry that uses white or low coherent light.

2.2.7 Vibration analysis

The majority of machines has a set of moving parts, resulting some sort of vibration. Each machine or component has a set of small acceptable imperfections that leads to a certain vibration signature. If a bearing or roller bearing develops a small imperfection that may lead to a failure, it will present a "tell-tale" variation. This behaviour is also observed in a unbalanced component (subjected to corrosion), misalignments among others [85].

Since the analyses of vibrations does not require the removal of components from a machine, it is becoming a preferable diagnostic technique in preventive maintenance operations. Enabling, this way, the early diagnostic of imperfections in components before the development of defects or complete failure. With this technique, regular tests are performed in a periodicity so that small alteration can be identified. Over time all the measures are compared to trace the vibration profile and evolution. The failure consequences and costs usually define the periodicity that the component is evaluated or tested [86].The measuring equipment probes can composed of four different types of sensor [87]:

- Triaxial accelerometers (axis perpendicular among themselves), used with high frequencies;
- Velocity sensors, these sensors are mainly used in handheld equipment;
- Displacement sensors, use Eddy currents and are used for low frequencies;
- Can scan almost any substance, opaque or transparent, composites and metals among others.

The ideal situation is when the transducer is permanently in the machine structure so that the data is collected always exactly in the same manner. The majorities of the software for vibration analyses uses the vibrations historic to determine the pass/fail parameters. The basic analyses observes the main natural frequencies of a component thus evaluating the component mass, rigidity and damping coefficient. This is possible through the combination of experimental and numerical data. The modal analyses can and is usually used to optimize the sensor location in the component or structure [88]. The software can identify loads, damage detection, location, characterization and quantification, in some cases exam life prediction. In the last years the application of statistical pattern recognition. Machine learning techniques, artificial neural networks have proved powerful methodologies in the early detection of defects [89, 90].

2.2.8 Ultrasound testing

The ultrasounds (US) are created by applying electrical pulses at a piezoelectric crystal that vibrate at resonance frequency, transmitting vibrations to the material or component being tested. The ultrasound technique bases the evaluation in the density measurements. The existence of a discontinuity, density variation, rigidity alteration or any other that changes the vibrations, will reflect some part of the wave back to crystal (echo). This echo is then converted by the piezoelectric crystal into an electrical signal. This procedure can be repeated from 60 to 1000 times per second, according to the probe an acquisition system. The tests can be performed in a immersion tank (usually water). Immersing the test sample and the ultrasound probe increases the transmissibility and therefore the technique sensitivity [91].

The common ultrasound waves, even if not audible, have the same behaviour of the audible sound waves. They propagate easily in solid materials or liquids with low viscosities, being attenuated by gases [92]. Ultrasounds are attenuated by variations in the elasticity, Young's modulus, grain size among other properties. Ultrasounds are exceptionally useful in the detection and evaluation of corrosion. Since this technique does not involve ionizing radiation, it can be safely used in pressure vessels and pipelines or in the chemical and petrochemical industries.

The size of the transducers is related with the frequency band and can range from 1 up more than 75 millimetres. The sensors used in rigid elements (up to 25 millimetres) generate great pressures (acoustic) thus transmitting up to 2 MHz waves. Variations in the air temperature, pressure and humidity influence the non-contact ultrasound measures and should be compensated. The most relevant characteristics of ultrasound waves are:

- Well defined and characterized beams;
- Constant velocity for uniform materials;
- Long distance propagation in solids;
- Reflection in locations where the mechanical properties change.

US tests use ultrasound waves and measures the density of solids, liquids and gases permitting:

- Evaluation of mechanical properties and its micro-structures;
- Microscopy structure analyses;
- Portability and economically efficient;
- Can analyze almost any substance.

The domain of the measures can be in time, frequency, attenuation, and images. The detection of defects with this technique is performed by looking at the variations in thickness, density, elasticity and several other mechanical properties. The frequency sensors quantify ultrasound wave attenuation, acting as a spectroscopy. Their main applications are at the micro scale like micro-structure analysis, pores detection [93].

Ultrasound waves have four different travel modes: Longitudinal (compression), Transverse (shear), Rayleigh (surface) and Lamb (plate). The first mode is similar to the propagation of sound and are similar to the ones generated by the crystal. This type of waves is the only that propagates in liquids. Transverse waves are characterized by the vibration of the particles having an angle to the wave. There are two critical angles, 27.5 and 57 degrees. 90 degrees waves tend to propagate along the material surface and transform itself in a surface wave. Surface waves, possess very small attenuation in the main direction (wave direction) but are strongly attenuated in other directions and do not exist in immersion test. Lamb waves have multiple velocities. The velocity depends on the thickness of the sample and the frequency of the oscillator. Among the multiple modes, the most usual travel modes are symmetrical and asymmetrical like illustrated in figure 2.1 [94].

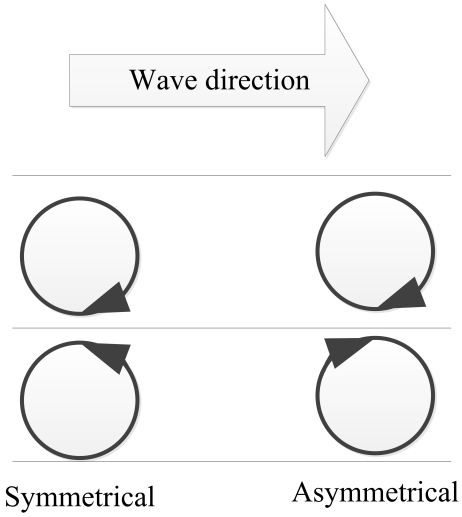

Figure 2.1: Symmetric and asymmetric particle movement

The current US equipment allows 2D and 3D characterization of the most diverse objects in industries like medical, petrochemical, pharmaceutical, automotive, aeronautics and aerospace. In the last years US imaging has proven a valid replacement for the ionizing X-Ray's. One of the major limitation in conventional field applications is its limitation to a waveband from 500 kHz to 5MHz, meaning high attenuation in the air and therefore requiring a transmission mean such as water.

One of the most important NDT techniques in present days is Infrared Thermal Testing (IRTT) [95–97]. This work focus on the usage of thermography to detect and characterize defects, thus a more detail overview of this technique is presented in the next chapter.

Has final overview of the main NDT are presented in table 2.5 the main characteristics of the referenced techniques.

Table 2.5: Main characteristics of the refereed NDT techniques

	Advantages	**Limitations**
Visual Inspections	rapid, minimal evaluations, easy to automate	mainly superficial defects, require adequate illumination, the evaluations are relative
Dye inspection	detect subsurface defects, can be used in a wide range of materials, low cost	require preparation, time consuming, limited to small areas
Electromagnetic testing	subsurface defects, rapid, low cost	can only be used in magnetic materials, single point measures, penetration depth
Radiographic testing	subsurface defect, metallic and non metallic materials, penetration depth	"limited" to laboratory usage, ionizing radiation, component size
Acoustic emission	low cost, continuous monitoring, fatigue failure prediction	mainly in metallic structures, inaccurate location of failure, materials damping properties
Laser testing	full field image technique, scanning area, can be used in several materials	requires high power lasers, expensive, high stable mounting setup
Vibration analyses	low cost, global analysis, fast testing	dependant of the material stiffness, require contact with object, require preparation
Ultrasound testing	penetration depth, low cost, accuracy	"single point" measure, "require" contact with the object, only for components with simple shape

2.3 Conclusion

The composite material have proved to have unique and very interesting characteristics. High strength, corrosion resistant, capable of assuming complex shapes and light are some of the most usual and important characteristics.

Among the vast range of composite materials available today, due to the processing cost and mechanical properties, polymeric matrix composites are by far the most commonly utilized. From the vast possible combinations carbon and glass fibre reinforced polymers represent a considerable percentage of polymeric composites. This increases the demand in the quality control and analyses techniques, either during manufacturing processes, or in maintenance operations.

The research for diagnostic tools and techniques started several decades ago. Over the years many technologies have appeared. Currently are commercially available several NDT techniques with renowned results in several fields. Naturally, each technique can achieve good results in some fields and fails to detect and characterize others, thus the correct selection is essential. Radiographic testing is one of the most complete, but requires a closed environment and uses ionizing radiation. Ultrasound testing is also extremely reliable, however the result is a single transverse profile making it hard to interpret and to scan large areas. The vibration techniques require the use of a dynamic mechanical load thus is difficult to use in field applications. In the case of lasers, it requires the use of a bulk laser that is difficult to transport. These last techniques also require very particular and stable conditions to operate in perfect conditions.

Chapter 3

Infrared Thermography and Thermal Tests

This chapter will deal with infrared thermography and thermal testing like recommended by commercial manufacturers. The data here presented will serve as reference to the work presented in the following chapters. This chapter presents two examples of thermal tests that use infrared thermography: transient and lock-in thermal testing.

The first sub-chapter deals with the most relevant matter in this work, thermography. Starting by explaining the core principles of the technique up to the main developments in commercial equipment, mentioning also historical evolution of infrared thermography. The technique main characteristics and accessories (stimulation sources) used in NDT tests are also presented.

The second sub-chapter deals with the simplest thermal tests, Transient Thermal Testing (TTT). Overall, the equipment and processing steps are considerably fast and straight forward. In this sub-chapter are performed several analyses and a comparison of the most relevant parameters used in this test.

The third sub-chapter presents the tests that use a lock-in approach, also known as Lock-in Thermal Tests (LTT). These use a continuously controlled stimulation source to access defects in components. Here the effect of several parameters is also discussed and analysed, in order to identify the one that produces the best results.

3.1 Infrared thermography

3.1.1 Temperature measurements

One of the first instruments to measure temperature was developed by Galileo Galilei [98] and is known as the thermometer. This name is still used today referring to temperature sensor. Actually, to measure temperature there are several types of sensors. These are described in further detailed by Stephenson in the sixth section of Webster's book [99]. In table 3.1 are indicated the main types of temperature sensors.

Table 3.1: Temperature sensors

Sensor type	**Principle**
Bimaterial	Two plates with different expansion coefficients
Resistive	Electric resistance that varies with the temperature (metallic semiconductors
Thermistor	Electric resistance that varies with the temperature (ceramic semiconductors)
Thermocouple	Two metals with different thermoelectricity (Seeback effect)
Semiconductor Junction	PN junction with connected to a transistor
Pyroelectric	Electric current generation with the heat flow (crystal element)
Liquid-in-Glass	Liquid expansion (without pressure variation)
Manometric	Gas, volumetric variation
Fiber-Optic	Thermal expansion and phase variation in the coherent light
Infrared	Electromagnetic radiation measurement (Stefan–Boltzmann Law)

The majority of the referred sensors performs the temperature measuring in a single point, or small area, and gives one single reading or average temperature value. From all of these, the pyroelectric sensors stand apart for being extremely fast even if losing in precision. This principle is also used in infrared thermography, which is also very fast at measurements, though with pour precision. For these reasons some of the sensors referred in table 3.1 are used as a reference in the calibration procedures of infrared cameras.

The word thermography is a combination of two Greek words: *thermós* standing for hot [100] and *graphia* meaning of representation [101]. This word has a meaning that stands for the

representation of heat, this stands true even today. Currently this word is synonym of a technology very resemble with photography, however the recorded data is used to represent, for each pixel, the temperature calculated through the captured infrared radiation.

Infrared thermography presents one big advantage over other measurement technologies since it does not need to be in contact with the object and can measure different areas simultaneously. There are two types of thermography: liquid crystal and infrared thermography. Liquid crystal thermography uses small liquid crystals in the form of paint to assess, temperature on top of a coated black paint. Depending on the temperature of the object below the paint, the liquid crystals will react and change their colour. Then, a visible photography is taken, recording a colour pattern related to temperature distribution [102]. This type of thermography is gradually being disuse [103] due to its low precision, preparation procedures and time required to acquire one image. However, currently is still the best manner of measuring the temperature distribution in water and other fluids. Contrary to infrared thermography, this does not present errors due to reflection, pour emissivity definition, transmissibility among several others.

Infrared Thermography (IRT) is the most commonly used type of thermography. IRT uses the fact that all objects above the absolute zero emit electromagnetic radiation. Therefore, by measuring the infrared radiation is possible to estimate the temperature of an object.

3.1.2 Infrared thermography principles

One of the first contributors to thermography was John Herschel with his thermogram [104]. Another great contribution to thermography came from Wilhelm Wien, this researcher stated that the radiation peak emitted from a blackbody is proportional to its superficial temperature [105]. The Stefan–Boltzmann Law (equation 3.1) states that the total energy radiated by blackbody per second and square meter per steradians (S) is directly proportional to the fourth power of the blackbody temperature. Here, σ is the Stefan–Boltzmann constant calculated according to equation 3.2. The final piece was developed by Max Planck (Planck law) and describes the energy radiated from a given area of a blackbody (P) according to its temperature at a certain wavelength (equation 3.3).

$$S = \sigma \times T^4 \tag{3.1}$$

$$\sigma = \frac{2\pi^5 B^4}{15c^2h^3} \tag{3.2}$$

$$P = \frac{2hc^2}{\lambda^5} \times \frac{1}{e^{\frac{hc}{\lambda BT}} - 1} \tag{3.3}$$

Where:

σ	Stefan–Boltzmann constant, 5.67E-8 $(\frac{W}{m^2 \times K^4})$
T	Temperature (K)
B	Boltzmann constant, 1.38 E-23 $(\frac{J}{K})$
c	Speed of light, 2.99 E+8 $(\frac{m}{s})$
h	Planck constant, 6.626 E-34 $(J \times s)$
λ	Radiation wavelength (m)
S	Energy radiated by a blackbody according to the Stefan–Boltzmann Law $(\frac{J}{W})$
P	Energy radiated by a blackbody according to the Plank law $(\frac{W}{m^2 \times Sr \times nm})$

By applying equation 3.3 to a given temperature, the radiation distribution of a blackbody and the irradiated energy is obtained, as described by Breitenstein in its book [106]. This information is extremely important in order to develop the mathematical models for thermography. The radiation distribution, function of the wavelength for some temperatures are represented in figure 3.1. It is also possible to observe the exponential increase in the radiation stated by the Stefan–Boltzmann Law in equation 3.1.

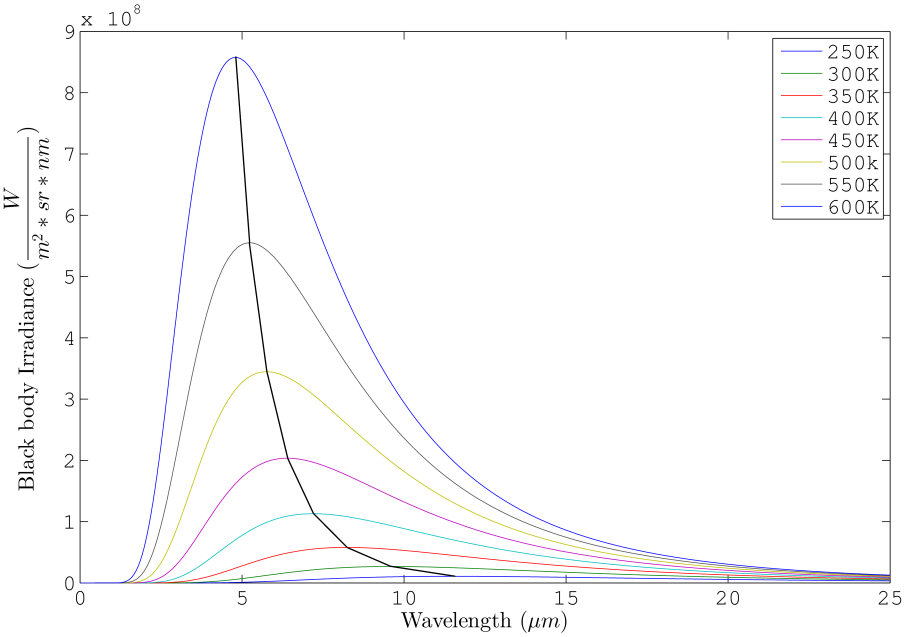

Figure 3.1: Planck's law for six different temperatures

Up until today it is impossible to measure the complete spectrum radiated by a radiation source. This difficulty is overcome by using several sensors like what is performed within a spectrometer. Spectroscopy quantifies the radiation intensity through the wavelength [107]. Since sensors used in thermography are not capable of measure the entire wavelength emitted by a blackbody at a given temperature, the infrared spectrum was divided into 5 different areas or sub-bands like presented in table 3.2 [108]. This subdivision may vary depending on the authors or field. In a thermal camera, by applying a bandpass optical filter, only the radiation with a certain wavelength will reach the sensor. This subdivision and filtering restriction leads to an easier calibration procedure and precise measurement system. This manner, it is possible to accurately calculate the temperature of an object just by measuring the intensity of the captured infrared radiation. The most used wave bands are Long Wave Infrared (LWIR) and Middle Wave Infrared (MWIR). Usually, uncooled cameras measure LWIR and cooled cameras MWIR radiation. Each camera presents properties that make them more appropriate for certain applications. The sensors used in these cameras change their electric resistance when the intensity of the infrared radiation changes. In the band of MWIR, the most common used sensors are Mercury Cadmium Telluride (MCT) and in the LWIR the usual is to use VOx Microbolometer. There are several technologies, usually using bimetallic pairing, to measure the radiation, however these are not so common in commercial equipments or applications [109].

Table 3.2: Infrared wave sub-bands

Abbreviation	**Name**	**Wavelength (μm)**
NIR	Near Infrared	0.75 - 1.4
SWIR	Short Wave Infrared	1.4 - 3.0
MWIR	Middle Wave Infrared	3.0 - 8
LWIR	Long Wave Infrared	8.0 - 15
FIR	Far Infrared	15-1000

3.1.3 Infrared thermography measuring parameters

The temperature of an object is far more accurately measured when there is direct contact between the sensor and the object. To reach a temperature value by measuring its emitted radiation (without contact) some error can occur. To minimize and compensate some radiometric phenomena, several parameters can be added to the mathematical models. These models are combined with calibration parameters to compensate the non-ideal conditions (real situations) and make temperature measures to be more reliable and accurate. Being several the sources of radiation that can influence the thermal measurements, they can be divided into groups similar to what is explained by FLIR® [110]. Some of the most important parameters when using infrared thermography are:

- Object;
  - Emissivity;
  - Reflected temperature;
  - Distance;
  - Transmissibility;
- Ambient
  - Ambient temperature;
  - Relative humidity;
  - Transmissibility;
- Optics;
  - Temperature;
  - Transmissibility.

Emissivity is a dimensionless parameter representing the ratio between the amount of energy emitted by an object due to its temperature and the total amount of energy leaving the object (figure 3.2). An ideal object where all the energy leaving it is only due to its temperature is called a blackbody and have an emissivity of 1. Thus, no object can emit more radiation for solid angle than a blackbody. This means that part of the emitted radiation by an object is proportional to its temperature, thus its temperature can be measures using thermography [111, 112]. Another property of the blackbody is its directional spectral emissivity. Here, the "emissivity" is always 1, despite the observation angle, a blackbody is a 100% diffuse emitter.

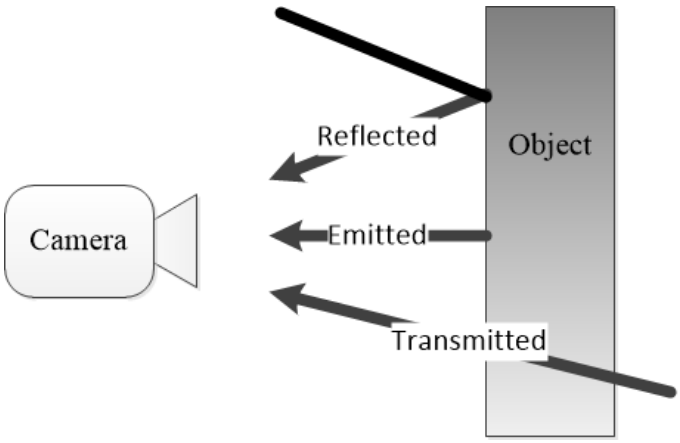

Figure 3.2: Different sources of radiation that reach the thermal camera

If an object is placed in a completely dark room (no radiation source) at an ambient temperature of 24 °C (297.1 K) and an object in thermal equilibrium with the room, the value of the emissivity is irrelevant. If the object is subject to a temperature variation and its emissivity is not 1, the radiation leaving the object surface is a mixture between: the radiation emitted by the body and the radiation reflected by its surface. The radiation captured by a thermal camera will have both

"radiations". When defining the other radiation sources and conditions, the software creates a reference value (in a digital form). If an object has an emissivity lower than 1, for situations where it is cooler than the environment, it will appear hotter than actually is. The opposing is also true for situations where the object is warmer than the ambient [97]. This occurs because the radiation that the thermal camera receives will be naturally emitted by its temperature, added to the radiation reflected. This reflected radiation will be more intense if the other sources are hotter or, less intense if they are cooler. The weight of the emissivity (ε) for several temperatures is displayed in figure 3.3. Here the amount of radiation received by the camera was kept constant and the temperature was calculated by changing the object emissivity, in the software. It is clear that for higher emissivity, the errors in temperature measures due to an erroneous definition of the emissivity are small [113]. Contrary, for small values of emissivity are expected higher errors in the temperature calculation due to an incorrect emissivity specification [105]. The relationship between the emissivity and an object temperature for a certain radiation is illustrated in the equation presented in figure 3.3. Here the ε represents an emissivity value and T the resulting temperature, reaching an R^2 for the correlation between the experimental data and the regression of 0.988. Like observed in figure 3.3, the reflected radiation has a great influence in the calculus of the temperature values.

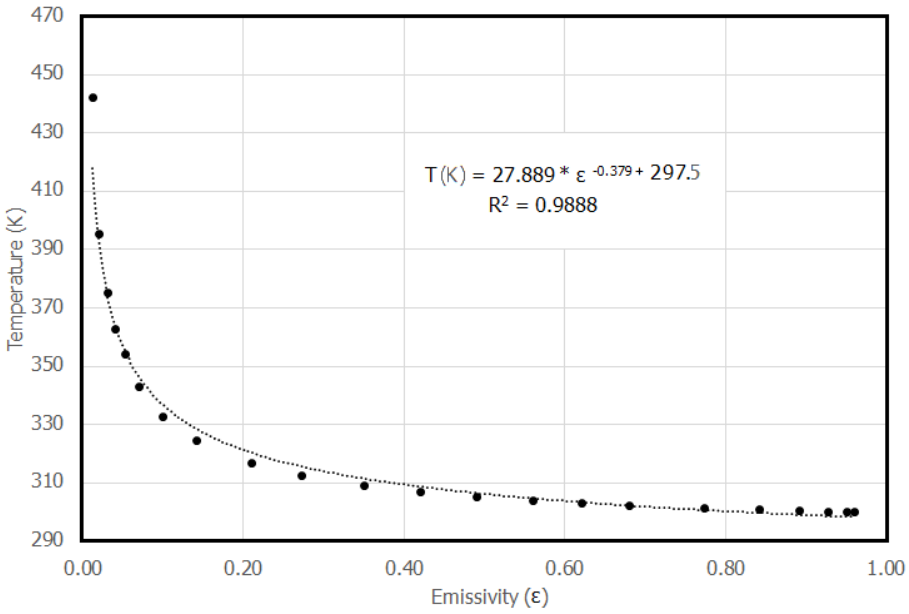

Figure 3.3: Temperature variation for different emissivities

Complementary, reflected temperature also has a great impact in the temperature measurements (a detailed explanation is given by Henke [114]). In figure 3.3 the reflected temperature was kept at 297.1 K, while in figure 3.4 the emissivity was set to 0.8 and the reflected temperature is varied from 273.1 up to 393.1 K (object at 304 K). From figure 3.4 is observed that, for reflected temperatures near the object temperature, the final temperature variations will be small. This is

also observed in the regression also displayed in figure 3.4 were x is the reflected temperature and T the resulting temperature. In commercial software, the total of reflected temperature is sub divided in two different parameters. The ambient temperature is used to compensate the radiation emitted by the background that then is reflected by the object surfaces from all directions. This is generally uniform and constant in the entire object. The reflected temperature, refers to any punctual and considerably hot or cold sources, like explained by Dominique Guilhema [115]. In these situations the object is small, compared with the area being observed, and has a temperature that greatly differs from the measured temperature. This reflected temperature is usually applied to a section of the image.

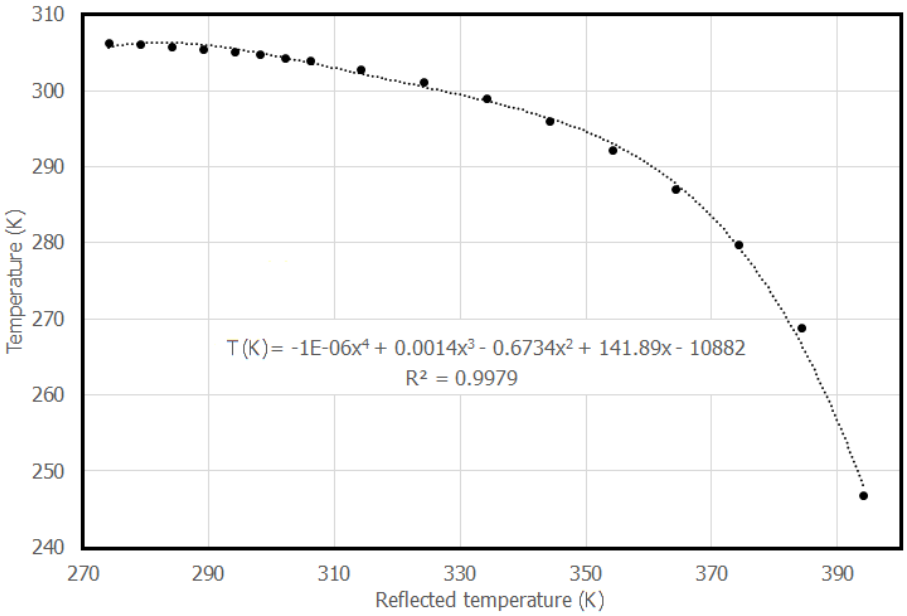

Figure 3.4: Temperature variation for different reflected temperatures

The majority of the gases like H_2O, CO_2, O_2, N_2O among several others, filter the radiation in a narrow band [116]. Thus, the mixture of several gases results in several cuts in the atmospheric transmissibility throughout the electromagnetic spectrum (figure 3.5). For the last 70 years this property (also called transmittance Tr) has been studied by several groups [117, 118]. Today the main reference is the ASTM G173-03 standard that presents a table with standard values for reference solar spectral irradiances [119] for a vast part of infrared spectrum. This table is plotted in figure 3.5a. Since the radiation of an object follows the Plank law, by overlapping the two sets of data, results a more realistic radiation distribution represented in figure 3.5b. A detailed observation of figure 3.5b reveals two considerable radiation bands, the band from 3 to 5.3 μm and the band from approximately 7 to 14 μm. The first band is notoriously uniform with very small cuts and is located near the radiation peak. The second band is located in an area where the radiation variation per degree is higher, resulting in technologies with greater sensibility [120]. This is another reason for the constant research in infrared cameras in these wavebands.

A variation in the atmospheric gases like O_2, H_2O and CO_2 may result in significant measure variation. For this important aspect is imperative that the thermal cameras are calibrated near the temperature that they will operate.

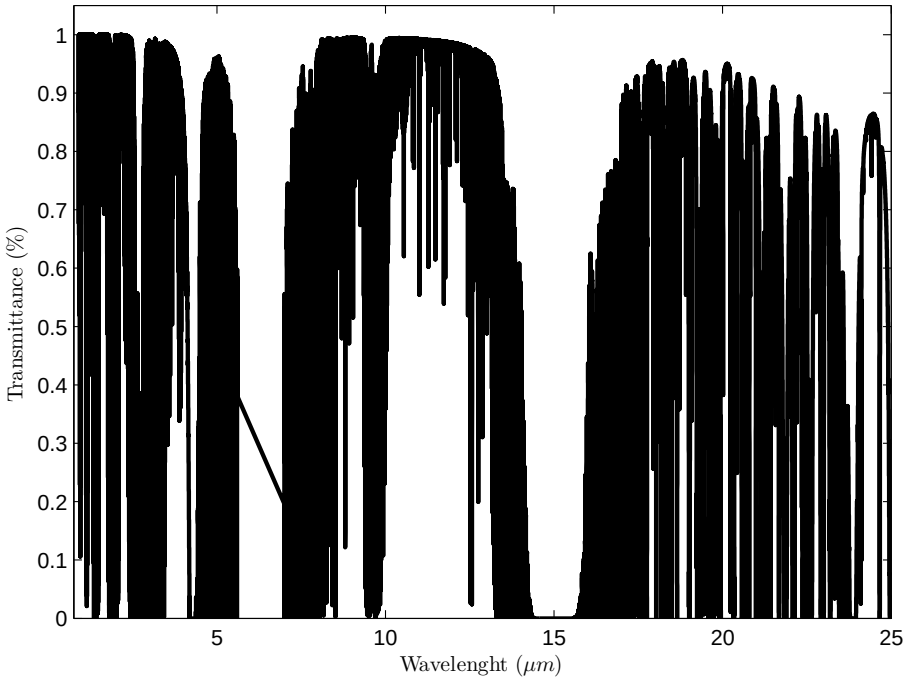

(a) Atmospheric transmittance

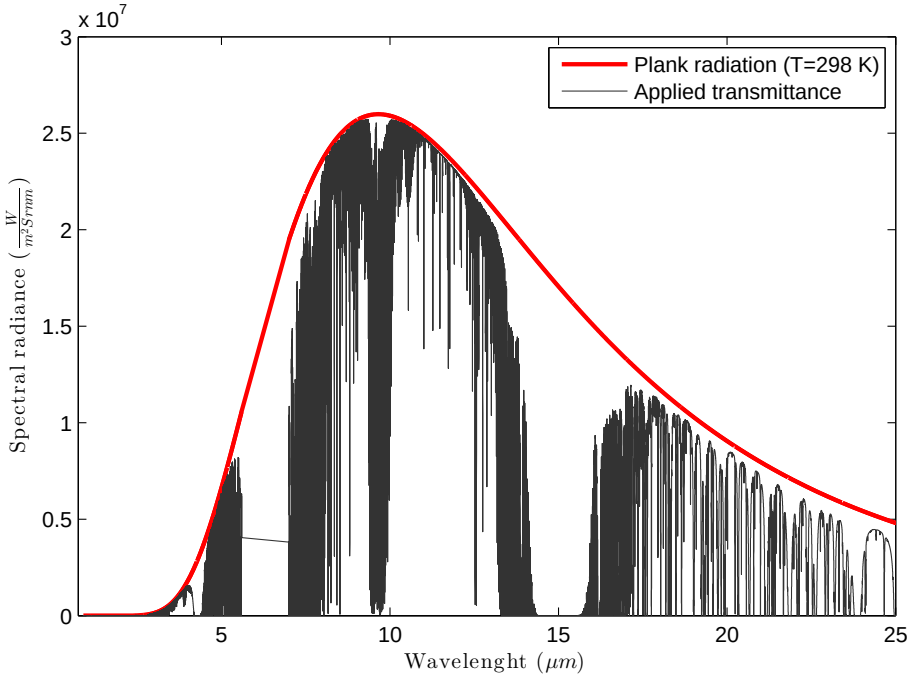

(b) Radiation of a blackbody

Figure 3.5: Radiation in the infrared waveband

Gases are characterized by their low density and in its vast majority indistinguishable with the human eye. The low density of gases implies that their absorption of radiation (infrared or other) is considerable small. Further information in this matter can be found in Dumoulin work [121]. The effect of the absorption is significant if the distance between the object and the camera is very high. This is particularly important in applications of night vision where the object being observed can be at some kilometres [122]. In temperature measurements the distances used in NDT are very small. However very often the temperature variations in NDT applications are extremely small, thus in some cases this can have a great impact in the results, making distance an essential parameter.

Similar to what occurs with the reflected temperature and ambient temperature, the influence of the gases in the atmosphere can also be divided. Water has a considerable cutting band in the infrared spectrum. Furthermore the water concentration in the air is extremely variable. Therefore the mathematical models use the distance, humidity and ambient temperature to compensate their combined attenuation in the measurements like demonstrated by Grinzato [123]. The attenuation in the radiation due to the water is then a combination of ambient temperature, the relative humidity and the distance. These last two quantify the "number of layers" of water that the radiation has to pierce to reach the thermal camera.

Similar to what happens in photography, in digital infrared thermography (DIRT) it is also necessary to focus the radiation in the sensor to create a planar image in this one. Again, like in photography, here is also used one or various lenses (optics). The optics (or pair of lenses) used are not completely transparent to the radiation being measured, explains Minkina [124]. This aspect can also be compensated. In a situation where the optics is not transparent, it will emit radiation that will be captured by the sensor and cut other part of the radiation that is emitted by the object. The conjunction of the optics temperature (dependent of the location and situation) and transmissibility (optics intrinsic characteristics) quantify the amount of radiation that is received and it is derived from the area being observed. For this compensation to be accurate, the optics temperature has to be known.

The aspect that cannot be compensated in commercial software is the viewing angle. Like mentioned previously, the radiation of a blackbody can be calculated by the Stefan-Boltzmann law and has the same density regardless the observation angle. This means a blackbody irradiates energy with equal intensity, regardless the direction. In reality such body does not exist, therefore the emitted radiation of the surface being measured is usually more intense perpendicular to the surface and starts to decrease as the viewing angle becomes parallel to the surface. Some research has been performed in this field to accurately incorporate this parameter in the NTD, namely by Pech-May and Junyan [125, 126]. For this reason the thermal cameras are calibrated with reference objects (commercial blackbodies) and are positioned perpendicular to the reference temperature. Thus, all the measures should be taken perpendicular to the measured surface [127–129].

3.1.4 Thermography in NDT applications

Infrared thermography (IRT) have been used in the most diverse fields like, health [130, 131], maintenance [132], early diagnostic [133, 134] and energy efficiency [135, 136]. The use of infrared thermal imaging in non-destructive testing has shown significant improvements in the past years due to the evolution in the infrared sensors and correspondent electronic. The usage of thermal patterns in NDT presents a great versatility when combined with the different stimulus.

NDT techniques using thermography can be divided in two distinct categories: active and passive techniques. The passive technique capture an infrared image of the object exactly as it is and, the entire analyses is performed based on a single image. In these analyses the usage of several images is only performed to have different perspectives of the object. Since the objects tend to an equilibrium with the environment, this type of tests does not provided much information. These tests are more directed to equipments malfunction, diagnostics and quality controls.

In active thermography a stimulation is applied to the object, this can be either one single stimulus or multi-stimulus (usually cyclic) [137]. Single stimulus techniques can be characterized by a single application of energy. The duration of the stimulation can range from milliseconds for materials with high thermal conductivity up to a full day like described by Zhi Zeng and Angeliki Kylili [138, 139]. In these cases, the stimulation creates or increases the thermal unbalance with the environment. This manner, any discontinuity that changes the component thermal properties will create local temperature variation in the object. In the analyses, one image at the beginning of the test can be compared with an image after the stimulation and use the differences to detect the defect. A more complex approach is to capture a sequence of images during or/and after the stimulation being applied. The images can then be processed with complex mathematical models to highlight certain aspects of the temperature evolution for each pixel and created a final image were the possible defects are easily identified.

A cyclic stimulation is defined by the application of several stimulations during one test. The stimulation wave can have several profiles: square, triangular, sawtooth or sinusoidal. The sinusoidal waves are by far the most frequently used. The algorithms used to process these images vary, depending on the stimulation type (single or multiple frequencies) and the type of wave (sinusoidal, triangular, square, etc...). Here the usual is to perform the evaluation and analyses based in the amplitude and phase delay response of each pixel, when compared with the reference signal. This type of analyses was initially developed to evaluate electric circuits and is called lock-in approach.

The correct correspondence between the stimulation source and analyses is also very important. Transient and pulsed IRNDT are very similar, however the duration of the stimulus is different as

well the technologies used in the stimulation [140, 141]. Pulsed thermography is a terminology usually applied in situations where the stimulation is very fast (a few milliseconds). Transient analyses is associated with a single stimulation but with longer time periods (several seconds). Despite their differences at the equipment level, the analyses procedure is very often equal. The analyse possibilities will be discussed in the next section.

Lock-in Thermal Testing (LTT) and thermal stress analyses (TSA) are the most common tests that use cyclic stimulation. Along with the examples presented in this document (chapter 3.3 and appendix A) other can be found in the literature from other groups, namely by Breitenstein and Proulx [142, 143]. LTT use several types of stimulations, synchronous with image acquisition throughout several cycles. In TSA a cyclical mechanical load is the most common stimulation. These two approaches share the analyses algorithm. In the lock-in tests the results are the phase and amplitude images, while in the TSA the thermoelastic parameter is applied to the amplitude image to obtain a mechanical stress image.

According to several properties in the materials being analysed, namely: emissivity, thermal conductivity, geometry among others, not all the stimulation sources can be used in every situation like explained by Maldague [144]. Materials such as metals or metal based composites have a high conductivity therefore, their stimulation should be fast. In order to accomplish a proper test, the stimulation and its analyses should be selected taking in account the type of defect to detect or characterize. Very often the name of a test starts with the stimulation source, followed by the type of analyses. For example Microwave lock-in thermography, uses microwaves as a stimulation source, modulated in a cyclic manner and analysed with a lock-in approach and, uses thermography as measure mechanism.

3.1.5 Stimulation sources for IRNDT

There are several combinations between the type of test (experimental protocol), stimulation, and analyses. Usually the type of component and its main function give some indications on the type of defect that may appear during its usage. This is a great contribution to the selection of the correct type of test to conduct and its corresponding stimulation source.

The simplest type of stimulation consists of applying some energy to a component and observe its temperature variations. Several types of energy can be used for this purpose. One of the most used and versatile is radiation, typically visible light. Using light to apply a uniform radiation can assume two denominations, transient or pulse thermography. Highly conductive materials, like metals or metal based composites, rapidly dissipate energy, thus the stimulation has to be very intense and for a short period of time (some milliseconds). For materials with lower thermal conductivity like carbon fibers and other resign based materials, polymers or plastics, the stimulation has to be longer. This is required in order for the temperature variations the reach the full thickness

of a component (back side). In the presence of a defect, the heat flow will change due to the variation in the geometry and thermal resistance, thus the temperature at its surface will present different patterns.

The most common type of analyses consists in observing the temperature evolution during the cooling phase. Due to the nature of the stimulation (radiation) its reflection is usually captured by the thermal camera since the objects are not perfect blackbodies. In the cooling phase the reflected radiation is reduced or even null, resulting in accurate temperature measurements. Since the cooling normally occurs mainly by convection, the temperature evolution in the cooling phase is also slower, leading to higher contrasts.

Several technologies can be used to produce a light stimulation. The faster and more intense are usually flash lights. The slower and less powerful, are common halogen lamps. Due to the decrease in their price, LEDs are becoming an option as an optical stimulation source. Their downside is the narrower waveband emission. Table 3.3 enunciates the most relevant properties of transient optical stimulations and figure 3.6 is an example of an image resulting from the corrosion detection with flash thermography from FLIR® [145].

Table 3.3: Main characteristics of transient light stimulation

Advantages	**Limitations**
No contact with the object	Danger for the human eyes
Simple power units	Limitations for thicker components
Simple processing algorithms	High precision cameras
Low price	Influence of the stimulation period in the results
Test duration	

One of the most used alternatives to transient stimulations is their modulation in a waveform. These are most commonly modulated in a sinusoidal wave. Sinusoidal waves can be applied using light, microwaves, ultrasounds, mechanical forces, or other means that produce heat. From the several types of stimulation that can be used cyclically, light is the most common.

In the cyclic stimulations, the temperature images can reveal important defects. The analyses in the frequency domain presents accurate results meaning that the temperature evolution recorded in each pixel is compared with the stimulation signal and calculated the amplitude and phase response. The data in each pixel is combined in order to build the images, one corresponding to the amplitude and another to the phase. The cyclic sinusoidal stimulations typically called lock-in tests. The analyses of these tests is done usually in the frequency domain and only

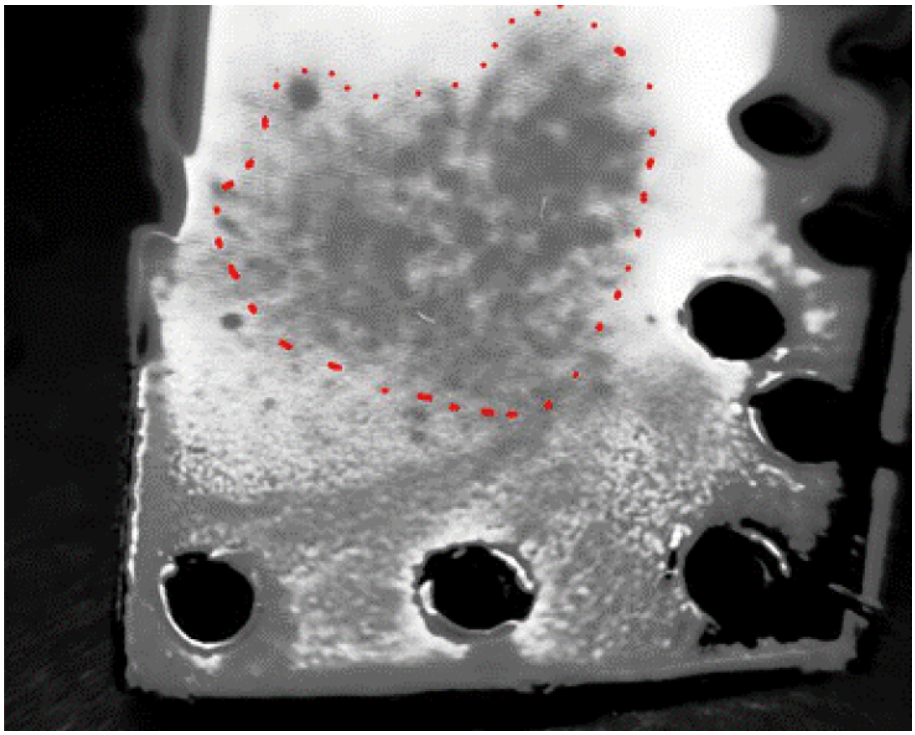

Figure 3.6: Detection of corrosion (red line) underneath the painting of an aluminium plate [145]

are observed variations with the same frequency of the stimulation, thus they are insensitive to punctual reflections and offsets (zero frequency) in the thermal images. which is one of the biggest advantages when comparing them to transient stimulations.

The usage of radiation modulated as a sinusoidal waveform presents important characteristics. The most important ones are referred in table 3.4 and an example is presented in figure 3.7 [146].

Table 3.4: Main characteristics of light modulated stimulations

Advantages	**Limitations**
No contact with the object	Danger for the human eyes if viewed directly
Insensitive to temperature offsets	Material has to be opaque
High detectability	Synchronization between the stimulation and image acquisition
Materials with high and low thermal conductivity	Longer test periods (when compared to transient analyses)
Metal based and polymeric materials	

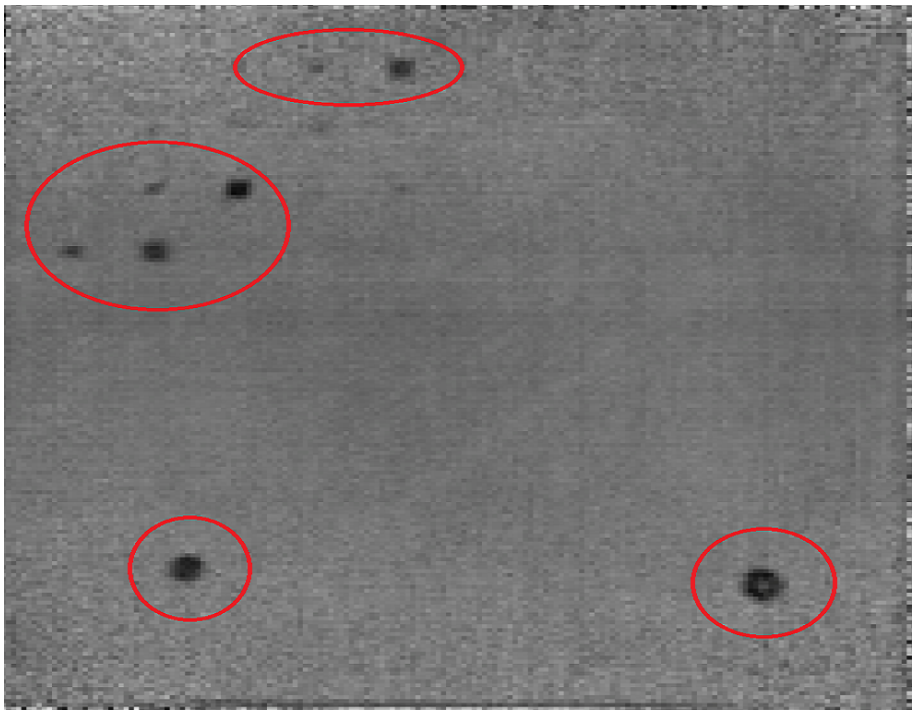

Figure 3.7: Detection of dis-bound (red delimitation) in square honeycomb composite [146]

Microwaves can also be used to deliver energy to a structure. This way, taking in consideration some aspects, these waves can be used to change the temperature of objects and help to detect some defects. These waves are usually referred as comprised between the 300 MHz and 300 GHz like presented by Roberto Sorrentino in its book [147]. Overall, the dry air is permeable to the majority of the microwaves, with some small attenuations for certain frequencies [148]. However, the small part of radiation that is absorbed is due to the presence of water. Thus existence of water rapidly increases its temperature.

With the appearance of cracks, delamination, corrosion and other defects, it is possible that water will start to accumulate. With temperature variations the water will contract and expand, increasing the defect. Selecting the proper frequency for the microwaves increases the local temperature of objects. This will highlight the presence of any excess of water or humidity condensation inside the components.

The usage of microwaves may be conditioned by the material being examined. However, if a material in permeable to microwaves and water is being accumulated inside it will be detected. While this can also be accomplished with other types of stimulations, microwaves can reveal the existence of humidity in deeper and thicker components. Table 3.5 presents the most relevant characteristics of microwave stimulations used in NDT with thermography and figure 3.8 [149] presents an example of these images.

Table 3.5: Main characteristics of microwaves used as stimulation

Advantages	**Limitations**
No false positives	Requires contact with the object
The phase is proportional to the defect depth	Poor performance in materials with low attenuation
No reflections from the stimulation	Can induce or increase cracks
Detection of defects perpendicular to the surface	Difficult use with rigid materials
Easy to use in composites like CFRP	

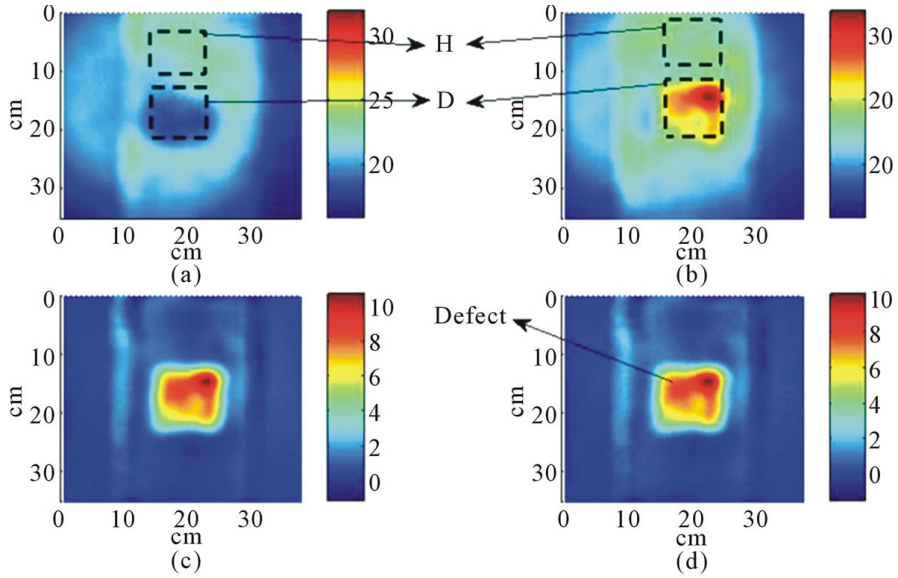

Figure 3.8: Detection of a defect in CFRP with microwave stimulation [149]

In ultrasound IRNDT, an infrared thermal camera is used to monitor the temperature variations resulting from the application of energy by ultrasounds. The application of ultrasounds to a component creates waves that will travel throughout all the directions. A crack, debonding or other defects may originate local friction. This will result in the generation of heat from the local friction and viscoelastic properties of the material. As a result, local temperature patterns will become visible. In most cases the defects tend to appear with higher temperatures.

For the application of an ultrasound stimulation, this should be modulated in several forms depending of the object being analysed, these should be able to easily propagate in the sample. The easiest form of stimulation is to modulate the ultrasounds into a square wave with a period of some milliseconds inducing several frequencies in the component. Here, the usage of Fourier type analyses can help to evaluate the depth of a defect.

The stimulation of the components can also be modulated in a more continuous manner. The most common case is for the ultrasounds to be modulated in amplitude in a sinusoidal wave. Frequency modulated waves are not common, however can also be used, particularly in components with low thermal conductivity. The thermal images should be acquired synchronously with the stimulation. Here the processing is similar to the performed in lock-in thermography previously referred. Ultrasound stimulations present several characteristics, their main advantage and disadvantages are illustrated in table 3.6. In figure 3.9 are presented example of images obtained by R. Plum [150] using ultrasound stimulation.

Table 3.6: Characteristics ultrasounds used as stimulation

Advantages	**Limitations**
No false positives	Requires contact with the object
The phase is proportional to the defect depth	Poor performance in materials with low attenuation
No reflections from the stimulation	Difficult use with rigid materials
Detection of defects perpendicular to the surface	Components resonance frequency
Easy to use in composites like CFRP	

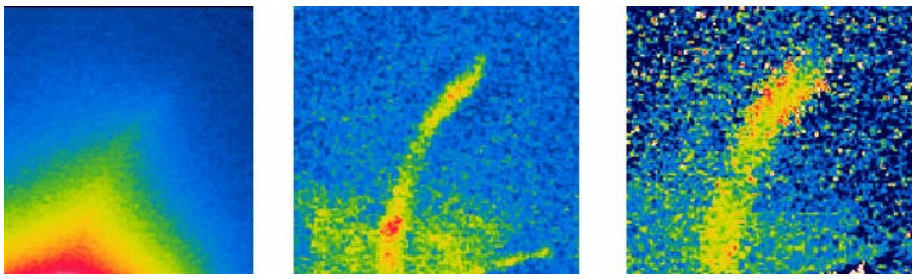

Figure 3.9: Detection of a defect in CFRP with ultrasound stimulation [150]

The thermal tests where a mechanical stimulation is used is mainly for the detection and characterization of cracks in components, usually resulting from manufacture errors or fatigue mechanisms. This test uses the thermal-elasticity property of materials. Due to this property, the materials increase their temperature when rapidly compresses and vice-versa. This behaviour only occurs in adiabatic situations and the temperature variation in an area is proportional to the mechanical stress in that same area (exemple presented in appendix A.

The thermal elasticity in most materials is very low. As result, for a high mechanical stress, the temperature varies a few milikelvin. To increase the sensitivity the tests, they are performed in a cyclic manner. At the end of the test (post-processing) the temperature data is processed similar to

the procedure in lock-in thermography. To calculate a stress image, are determined the amplitude response in each pixel. The amplitude response is then multiplied by the thermoelastic coefficient of the material under analyses. An example of the resulting stress image is illustrated in figure 3.10 with its main characteristices presented in table 3.7. This subject is presented in detail in appendix A.

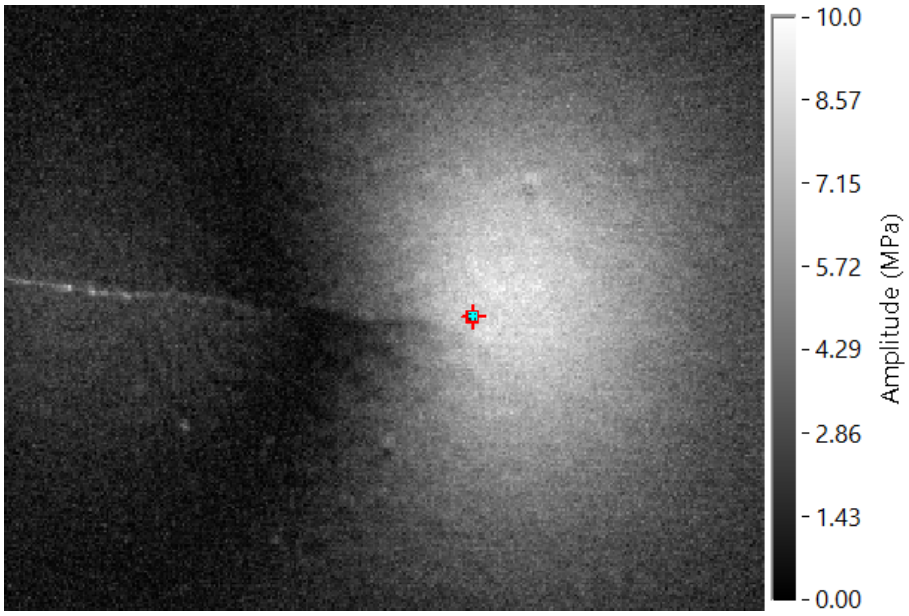

Figure 3.10: Stress in an aluminium sheet at the tip of a crack

Table 3.7: Characteristics mechanical loads used as stimulation

Advantages	**Limitations**
Measure mechanical stress contact-less	Controlled mechanical loading system
Quantitative and immediate measures	Low temperature variations
Components with complex shapes	Influence of reflections
Usage in metallic, metallic based and polymeric materials	Errors in components with low emissivity

There are several possibilities to combine a type of test, with a certain stimulation. Depending on the modulation of the stimulation source, several analyses can be performed. The appropriate selection of all these variables also has to take in consideration the type of defect and local conditions. Despite almost all combinations may be used, some produce better results thus, are more common and recommended. In figure 3.11 are presented the main stimulation sources, tests and types of analyses, according to the main references in this field [95, 151–157].

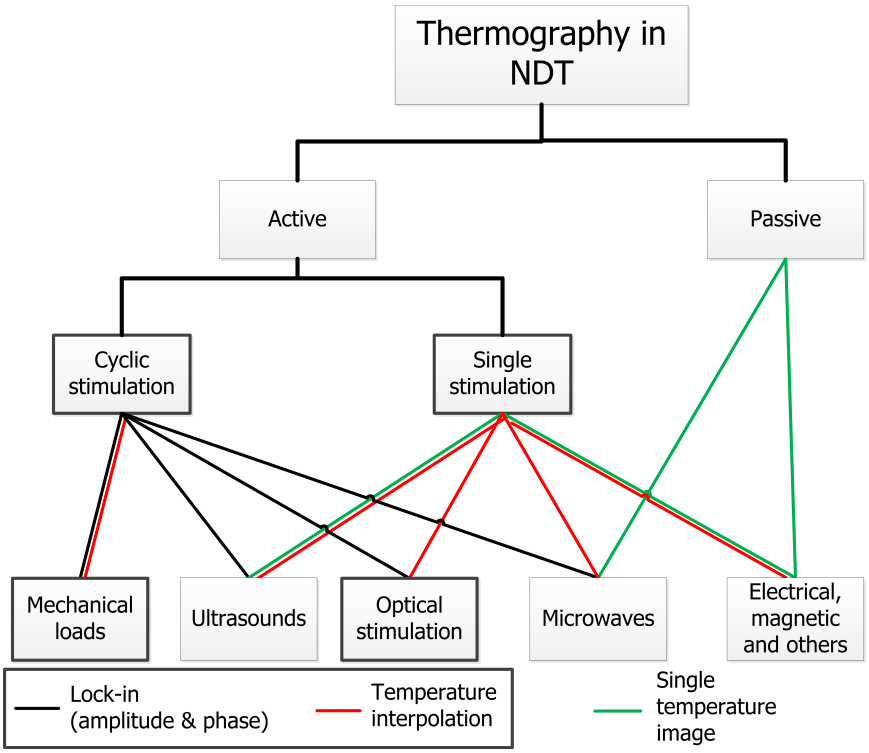

Figure 3.11: Correlation between type of thermal test, stimulation, and possible analyses

3.2 Transient thermal testing

3.2.1 Overview

Every object surface emits some kind of radiation which frequency increases with the temperature (Plank's law). Depending on the temperature of the object, the majority of the radiation emitted, may be located in the infrared bandwidth. This permits the estimation of the temperature at a given surface region by measuring the infrared radiation and finally computing the temperature images from this data [158]. This way, infrared thermography is an image technique that measures infrared radiation and uses it to assess the temperature of the objects surface.

This section deals with the Transient Thermal Testing (TTT) and analyses technique, also called pulse thermography by some authors [140]. In this case the stimulation is in the form of a transient stimulation (single pulse). Non-destructive transient testing and analyses using thermography can be very accurate and precise. Indeed, Abidin and Zeng were able to estimate a defect geometry and depth only by reading the temperature on surface [159–161]. In this tests the thermal analyse is usually performed for temperature variations and not for the absolute temperature values [162].

These tests have two phases: the active phase where, when the stimulation is applied and the recovery phase, when the heat flows inside the specimen and to the environment change until

the equilibrium is reached. Since only one stimulation is applied to the test object, its correct specification is a critical aspect of the test efficacy. The transient pulse duration (stimulation period) corresponding to the active phase of the test is one of the most important parameter, since usually determines the amount of energy that is applied to the object. Another important aspect is the instant (during the entire test) at which the thermal analyses is performed, like for example: right before the stimulation, after the stimulation (preventing interference from the stimulator) or even some time after the end of the stimulation. Besides the basic thermal and stimulation parameters, the type of image processing and post processing also plays a major role in the precision of the technique. The correct analyses can make a difference between a conclusive or inconclusive test.

Until now, the test parameters were normally defined by technician experience (empirically) or by trial and error. Hence the main goal of this work is to access the influence of the test and analyses parameters in the detectability of a defect and its precision. For this purpose were conducted several tests with different stimulation periods and applied to four different test samples. With the data obtained from the experimental tests using several parameters and settings, it was compared its influence in the final results of the TTT.

3.2.2 Experimental setup

The samples used in these tests, four rectangular sample plates, were made from Polymethyl Methacrylate (PMMA) with a 4.5 thickness and 210 by 160 millimetres wide. The replacement of Carbon Fiber Reinforced Polymer (CFRP) by PMMA assured a higher uniformity and isotropy of the test plates, essential for the purpose of this work and that was previously performed by others [159, 163–166]. To simulate a defect, several slots were machined in the test samples backside (figure 3.12a. Each sample possessed slots with different widths: 5, 7.5, 10, and 12.5 millimetres, and with the corresponding depth of 0.5, 1.5, 2.5 and 3.5 mm. An example of one of the samples is presented in detail in appendix C.1

The samples were individually placed in a vertical position without any support underneath like illustrated in figure 3.12b, as recommended by several authors [163, 167, 168]. This kept constant the natural convection conditions and prevented any temperature flux by conduction from the plate boundaries during the warming-up or cooling-down phases of the test [159, 166]. The thermal camera used was the FLIR® 7500, middle wavelength infrared camera with less than 25 mK of noise equivalent differential temperature (NEDT). The camera was positioned observing the samples front-side (reflective mode) at 1.0 ± 0.01 meters from the specimen and aligned at 90 $\pm$11.5 degrees with the specimen centre.

The stimulation source was mounted over the thermal camera (approximately 0.8 meters). In order to minimize the external radiation and noise, all the tests were conducted during the

evening (no solar light or other considerable radiation sources in the neighbourhood). The indoor lights were shut down and the person conducting the tests was at approximately 1.5 meter from the specimen and placed parallel to its surface, thus preventing reflections. The stimulation source was one halogen lamp from Hedler® type H25s with a maximum power of 2500 W. The power controller was from Automation & Technology (PowerBox model) connected to a computer through a NI USB-6251 Module. The program IRNDT (version 1.7 2008), also from Automation & Technology, controlled the entire equipment and was used to record the data and for the first part of the processing procedure. The samples, thermal camera and stimulation source were positioned in reflection mode since it is the common situation in industrial applications, like mentioned by Maierhofer [163].

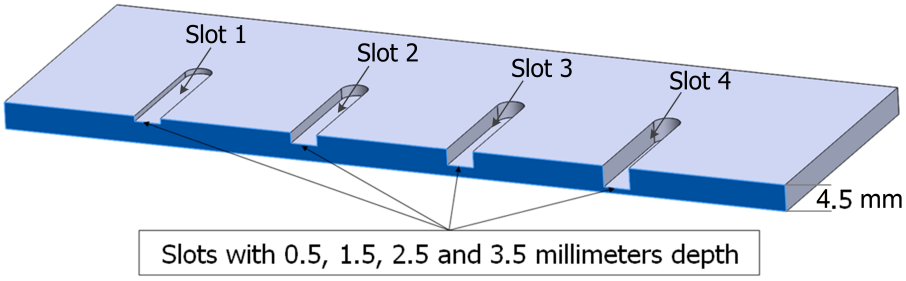

(a) Example of a test specimen used in the thermal tests (symmetry plan)

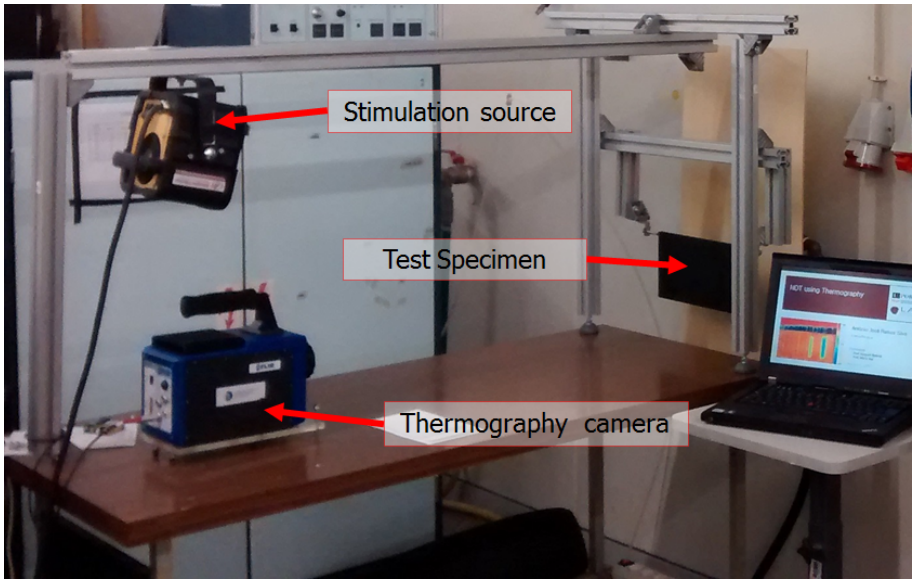

(b) Experimental setup

Figure 3.12: Laboratory tests setup and sample section view

3.2.3 Experimental protocol

In order to maintain and adjust the geometrical position between the three main components (stimulation, thermal camera and test sample), a support structure was build using conventional

Bosch® aluminium framing profiles. The test specimens were aligned with the thermal camera and were hold vertically by its top side corners using two pins. The holding pins have threads to adjust the position and tightening force to position the samples as represented in figure 3.12b. The thermal camera was mounted on a flat base that possessing adjusting screws so it could be perfectly levelled and aligned perpendicular to the sample surface.

Since the majority of the tests were performed sequentially, in the beginning of every section, a 5 second stimulus was applied. This stimulation acted as a startup stimulation. After a test (including the cool down phase) two criteria were used to define the waiting time before the next test. The first was a 20-minute waiting period and the second was the temperature difference at a reference area. The reference area consisted of a rectangular area in the centre of the plate with approximately 100 pixels, with the entire image having 320 $\times$ 256 pixels. For this reference area, the temperature should not differ more than 0.5K when compared with the beginning of the test. The thermal camera frequency was set in order to acquire 300 frames during the stimulation phase (*sampling frequency* = 300/*stimulation period*) but the camera integration time was held in the value for which it was calibrated. After the stimulation phase, the plate temperature was recorded during nine times the stimulation period. At the end of the test, the entire sequence (3000 thermal images) was recorded so it could be processed and analysed afterwards. After recording, all the tests were checked for abnormalities such as image movements, unwanted and unpredicted reflections, plate's misalignment, and errors in image sequence etc. If any of these was observed the test was repeated.

3.2.4 Data processing

The data was analysed using two different approaches: the commercial IRNDT from Automation & Technology^{TM} and by using a script developed in LabVIEW®. IRNDT internal processing algorithm is based in the thermal signal reconstruction (TSR) principle similar to the one described by Junyan [153]. This methodology has been mainly developed by Steven M. Shepard and patented in 2005 [169]. The two main processing methodologies available in IRNDT for analyses of the recorded thermal images are the root model and the e-model reconstruction. Both processes find the best curve fit solution for each pixel during the cooling phase. The root model uses a polynomial fitting with a root approach, while the e-model uses an exponential equation to model the temperature curve. When analysing the data, this can be performed in the fitted curves or in its derivative, here, all the calculus are performed using the fitted curves, either root or e-model. This is executed to overcome the limitations of the detections mainly by the diffusion process, further readings can be found in [170, 171]. This procedure greatly diminishes the noise in the thermal sequence and from of the images to be analysed. In all sequences, eight different recorded instants were analysed, corresponding to a certain test time. These instances were corresponding to the end of the stimulation period, i.e. the images with the index 300, 310, 350, 400, 500, 1000, 2000 and 2999. For each of these instants, five different images were exported: reconstruction, the 1st,

2nd, 3rd derivative and the residual. The residual image corresponds to the difference between the real data and the interpolated curve and only served as a control parameter). These images where then processed in a custom application developed with LabVIEW®.

The first step in the LabVIEW® script is cropping the image to concentrate the analysis in the area of interest, using an edge detection algorithm. In some situations, the defined parameters for the edge detection were not capable of effectively detect the edges leading to a null image. In these situations, the images were manually cropped. Since all the samples have the same geometry, the slots location and their boundary are known. A set of 30 pixels aligned with the longest dimension of the slots was average for each area under study (the four slots, three central references and two side references) calculated along with its standard deviation (SD), like illustrated in figure 3.13. Finally, the results were recorded to an external file and analysed, combining for all the possibilities presented in table 3.8. The values of the c parameter that existed in the tested samples is presented in table 3.9

Table 3.8: Resume of all the parameters that can be combined among themselves

Slot width (mm)	**Stimulus period (s)**	**Image index**	**Analyses**
5, 7.5, 10 and 12.5	2, 3, 4, 5, 7, 10, 15, 20, 25, 30, 35, 40, 50, 60 and 80	300, 310, 350, 400, 500, 1000, 2000 and 2999	Reconstruction, 1st derivative, 2nd derivative, 3rd derivative and residual

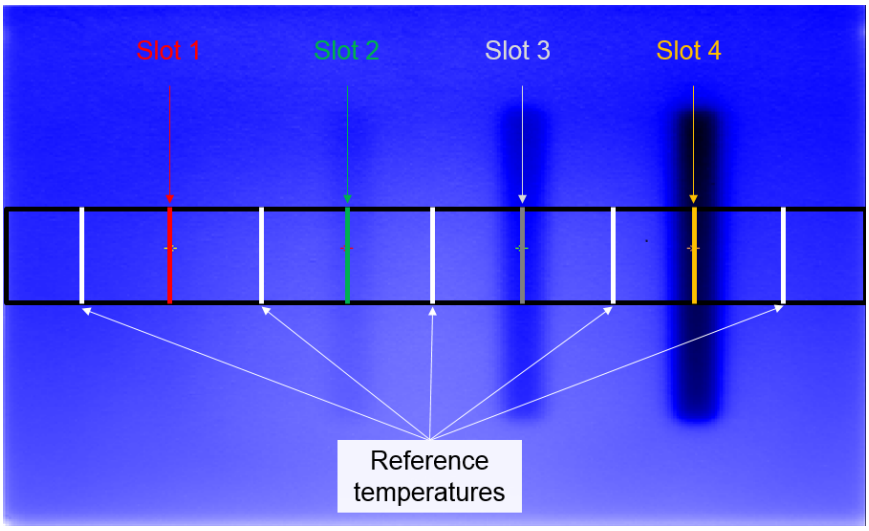

Figure 3.13: Example of thermal (12.5 millimetres width) image and measurement locations

Table 3.9: Values of the c parameter in the used samples

		Slot width (mm)			
		5.0	**7.5**	**10.0**	**12.5**
Thickness in defect area (mm)	**1.0**	5.0	7.50	10.00	12.50
	2.0	2.5	3.75	5.00	6.25
	3.0	1.67	2.5	3.33	4.17
	4.0	1.25	1.88	2.50	3.13

3.2.5 Results

The commercial software uses the TSR method. Since this is applied to the raw bit data and not the temperature curves, the result is a curve, fitted the raw bit data. This way, the temperature data of these analyses is described as Thermal Fit (TF).

The stimulation period, as expected, was the most influential parameter during a transient thermal test, therefore this was the first parameter examined. Figure 3.14 presents the temperature for the above referred stimulation period for the samples with slots width of 5 and 12.5 mm. The temperature and thermal patterns among the samples did not differ significantly, however the temperature amplitude varies (figure 3.14a and 3.14b). This is visible when comparing the temperature for the sample with 5 mm (Figure 3.14a) and 12.5 mm (Figure 3.14b). These slots data clearly indicates the influence of the defect width.

It is referred in the IRNTD user manual that the detectability of a defect is proportional to the parameter c (equation 3.4) and the minimum value for this dimensionless parameter is 2 [172]. This means the defect width has to be at least the double of the remaining thickness. Thus in the sample with the 5 mm slots, slots 1 and 2 should not be visible (figure 3.12a) since its c is 1.25 and 1.67 respectively (other values presented in table 3.9). If one assumes an error of at least two standard deviations for the limit of detectability, then, slot 2 is clearly detected and the recorded tendency shows an increasing in the "detectability" for slot 1 (figure 3.14) even if not immediately visible [153].

$$c = \frac{defect\ width}{thickness\ in\ defect\ area} \tag{3.4}$$

The slots with less thickness, namely slot 4 that has a thickness of 1 mm, reached considerable higher temperatures than its sound area. For higher stimulation periods (50 seconds or more), the temperatures are higher and tend to increase for higher stimulation periods, but the difference

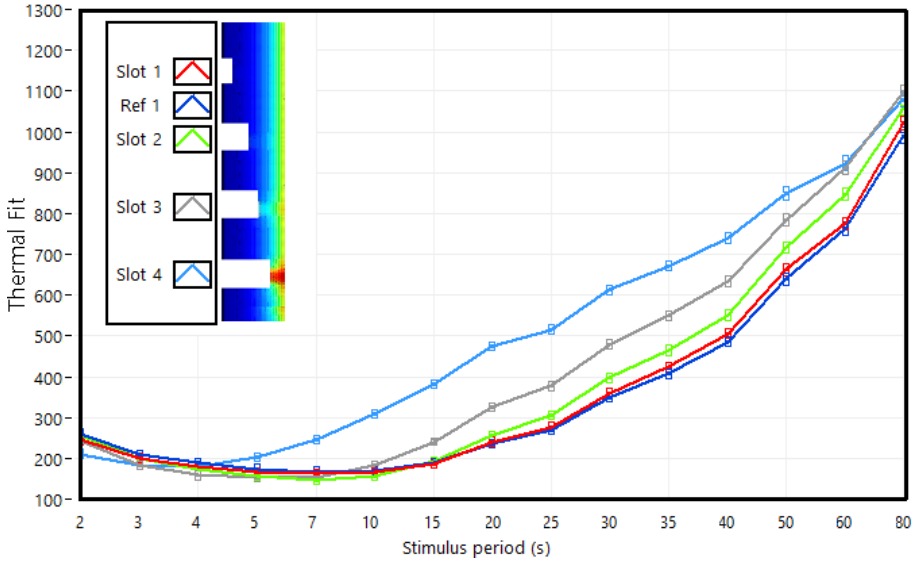

(a) Slots with 5 mm width

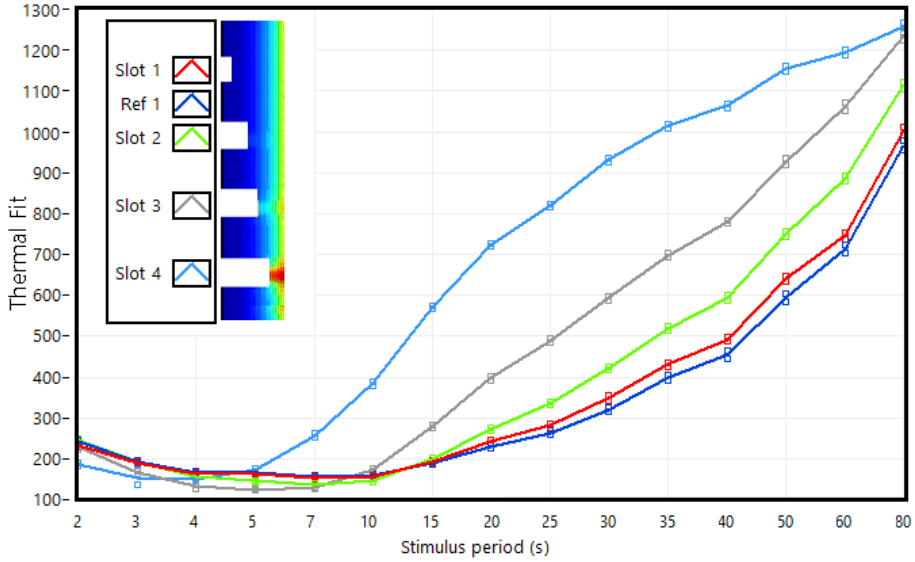

(b) Slots with 12.5 mm width

Figure 3.14: Temperature response for several stimulus durations for samples with different widths

between the slot central temperature and the temperature of the surrounding areas decreases, this is even more evident in figure 3.15.

This behaviour was observed throughout all the test plates, as illustrated in figure 3.14a and 3.14b, as well as, in table 3.10. With the slots depth decrease, the time at which the maximum difference for the adjacent areas occurred (maximum detectability) also increased (figure 3.15). This clearly indicates that for a certain defect, here represented by a machined slot, exists a determined optimum stimulation period. Consequentially, increasing the stimulation may even diminish the thermal contrast and overall test effectiveness.

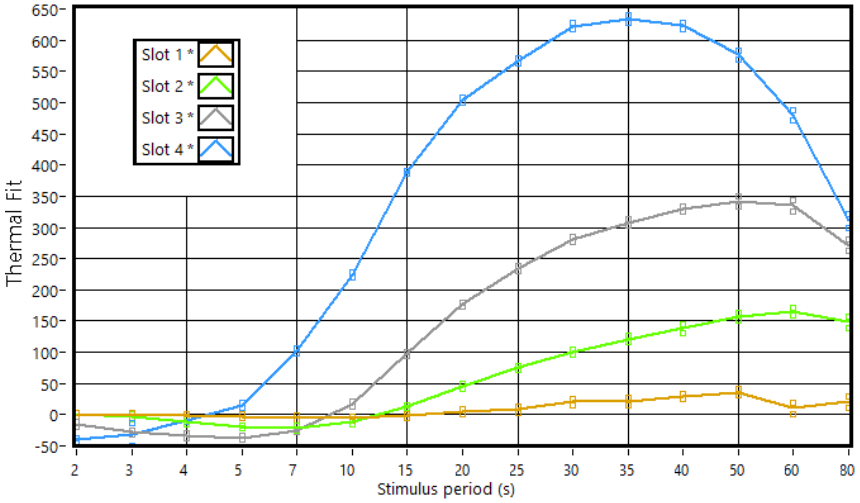

Figure 3.15: Difference between the temperatures and the adjacent reference temperatures for the plate with the 12.5 mm slots

By analysing figure 3.15 it can be observed an inversion in the temperature response from stimulations of 5 seconds to the longer ones. The temperatures in the deeper slots, for the smaller stimulation periods (5 seconds or lower) are lower than for the surrounding area. This temperature response passes for a transition phase in the stimulations of 5, 7 and 10 seconds (figure 3.14b), depending of the slot. The transition point varies with the slot depth. For smaller depths, the time for which the inversion occurs increased and vice versa (figure 3.15). For higher stimulation periods, the slots temperatures are higher than their surroundings and the temperature continuous to increase in all the points. It is important to highlight that the temperature increase for longer time periods is far greater than the decrease in shorter periods. This result means that higher temperatures are expected for higher stimulation periods, however only signify a higher average temperature and not a higher detectability (figure 3.14a). These thermal patterns and behaviour were recorded for all the test plates. It was expected that the reference temperatures were equal among themselves. However, this was not observed due to the natural offset error in thermography measurements. This aspect is not relevant, although was diminished by calculating the difference between the average slot temperature and the adjacent reference temperatures (figure 3.15).

By observing table 3.10, it can be said that for a higher TF difference between a sound area and slot thickness, one will achieve a higher thermal contrast. The stimulation period for which slot 1 maximum contrast was not expected. This result is not relevant due to the low detectability coefficient. Even so, this finding is concluded by looking at the tendency and evolution of the stimulation period for the other slots. Furthermore, comparing the readings for slot 1 maximum contrast (MAX in table 3.10) and the corresponding Standard Deviation (SD), it can be conclude that these are considerably close. A complete pattern is observed in all readings, deeper and wider slots lead to higher thermal contrast.

Table 3.10: Thermal difference limits for all plates

Slot width		Slot 1	Slot 2	Slot 3	Slot 4
5 mm	Maximum	18.4	82.4	167.3	285.5
	Standard deviation	10.6	7.3	7.4	5.4
7.5 mm	Maximum	22.7	114.1	229.6	413.1
	Standard deviation	4.7	9.3	6.9	4.2
10 mm	Maximum	14.8	142.6	300	538.9
	Standard deviation	5.8	7.2	6.4	4.4
12.5 mm	Maximum	36.1	165.5	341.8	633.8
	Standard deviation	5.9	6.4	7.4	5.4

For this analyse, the cooling time was divided in 8 instants proportional to the stimulation duration. Thus, minimizing the influence of the different stimulation periods. All tests recorded 3000 images, this analyses was conducted by observing eight different images from each of the sequences corresponding to eight image with the same indexes (images 300, 310, 350, 400, 500, 1000, 2000 and 2999). These are presented in figure 3.16, whit the vertical axis in auto-scale.

The 3 seconds stimulation (figure 3.16a) reveals smaller variations for the deeper slots and lower temperatures for the slots when compared with the reference temperature. This corroborates the findings for the different stimulation periods since slot 4 kept a lower temperature for most of the test. Naturally after the stimulation period, the global temperature tends to balance itself with the ambient temperature and so the temperatures start to decrease. The faster increasing rates for warming up phase are also the faster decreasing rates during the cooling phase. For the deeper slot (slot 4) there is an equilibrium instant near the index 1000 image (temperature of slot equal to its reference), corresponding to an instant of approximately 3.3 times the stimulation period.

Like referred previously, the 7 seconds stimulation period represented in figure 3.16b is a transition phase and for that it is clear the higher overall temperature is achieved for the deepest slot, while for the remaining slots this behaviour was not yet observed. This is also visible in the previous stimulation analyses. The temperature difference between slot 4 and its surrounding area is considerably higher for the test in which it reached a higher temperature.

For the 30 seconds stimulation period (figure 3.16c) it is observed the higher temperature contrast for slot 4 and lower for the smaller one. This stimulation period presented the higher detectability values in the previous analyses. Naturally, the areas at higher temperature will have a faster cooling process. This evolution results in an equal and locally uniform temperature for slot 4 at the image 2000, when compared with the reference temperature, making this slot at this stage impossible to detect. This evolution is mimicked by all other slots, however due to an increasing

thermal damper coefficient (described in chapter 5), with the decreasing of the slot depth, the time at which this occurs is different.

For the higher stimulation period (80 seconds) illustrated in figure 3.16d and looking with a closer attention is possible to see that slot 4 equals the reference temperature earlier than slot 3. For slots 3 and 4 begin the cooling phase with very similar temperatures, it is visible that a faster cooling rate is obtained for slot 4 due to its small thermal damper coefficient. The temperature at image 300 (ending of the warming phase) is similar for the two referred slots. This clearly evidence the importance of the correct choice of the stimulation duration.

Even if the plots in figure 3.16 are referent to the analyses of the plate with slots of 7.5 mm width, the behaviour and above comments were verified for all the test plates. It is important to highlight the "evenly" distribution of temperatures in the four slots for the 30 seconds stimulation, like observed in the stimulation analyses. Looking at the recorded data and performed analyses, this is negligible. It can be concluded that the detectability right before or after the stimulation period is similar. However after a certain period, the detectability starts to decrease and for higher periods of cooling may lead to erroneous analyses due to the temperature pattern inversion. However, if the stimulation period is not adequate, different defects can produce the similar temperature variation (80 seconds stimulation) and the difference can only be observed near a thermal equilibrium. Therefore, it is recommend the usage of images right after the stimulation, maintaining a great detectability and preventing any artefacts (reflection) from the optical stimulus.

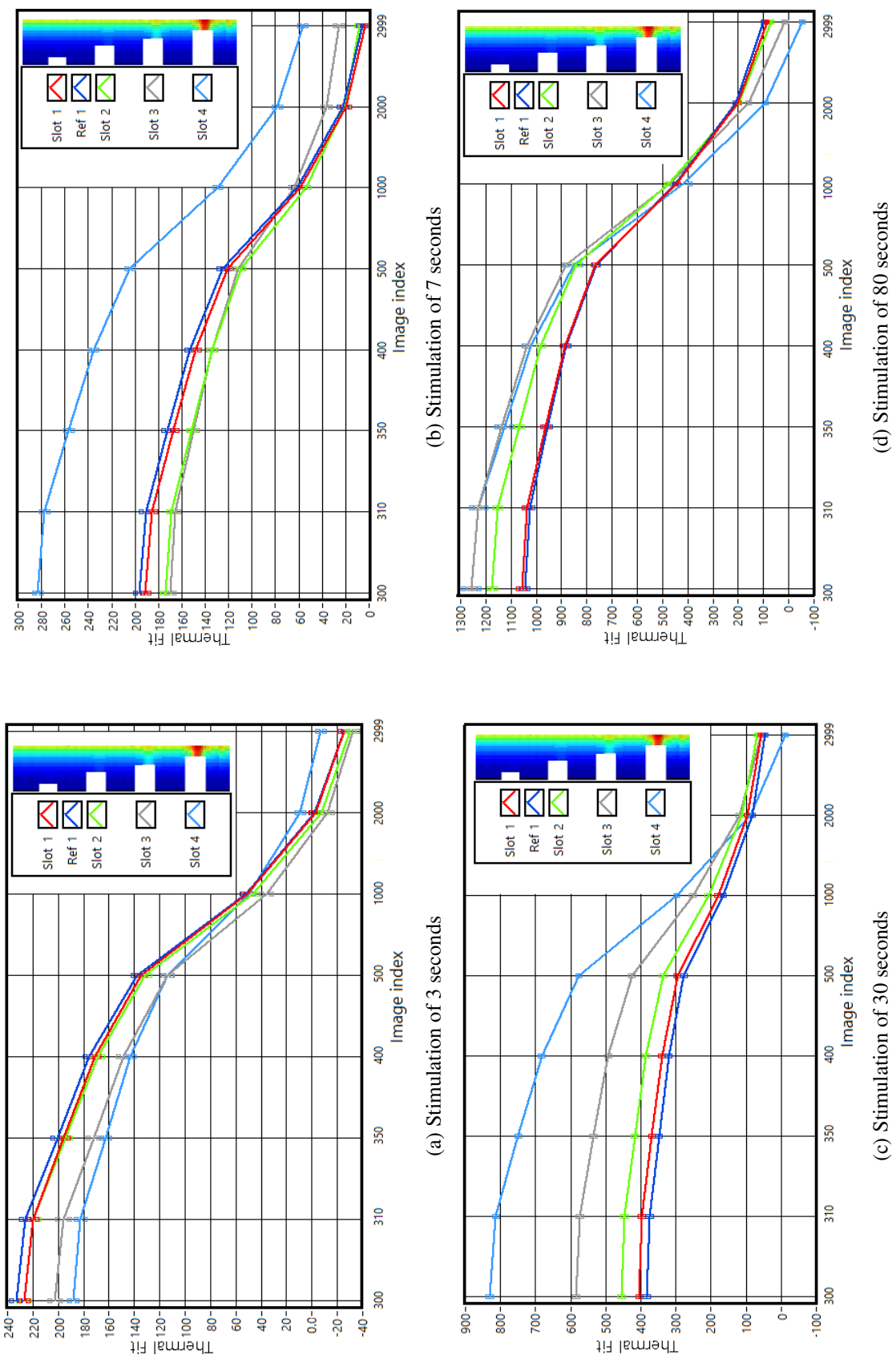

(a) Stimulation of 3 seconds (b) Stimulation of 7 seconds

(c) Stimulation of 30 seconds (d) Stimulation of 80 seconds

Figure 3.16: Slot's temperature for different stimulation durations, slots with 7.5 millimetres

From the literature, it is referred that the material defect width versus thickness should be bigger than 2 [153] (comparison among plates). Even so, it is easily observed that the wider and deeper the slot is, the higher the temperature difference to the reference is, this correlation is almost a linear relation. With the exception of the smallest slot (slot 1 with 0.5 millimetre and slot 2 with 1.5 millimetre) all the others presented considerable differences for their reference signals, figure 3.17. Although even the slot 1, when compared the correspondent standard deviation values (Figure 3.17 and table 3.10) with the measured data, the detectability limit of two standard deviations, was overpassed, for the 12.5 millimetres width for different stimulation periods or index of image being analysed.

With four different widths and four different depths, it was possible to detect "defects" with a ratio for the defect width *vs* thickness which is lower than 2. However for a correct and precise evaluation of this aspect, samples with smaller ratio should be tested. Also, it should be taken into account the relation between the thickness in the defect area and the thickness in the reference area, combined with different widths. It is worth noticing that the tests were performed in different days due to the necessity of a temperature normalization period. As a result, some variations in the reference temperatures (smaller than 1 K), may occur and create some deviations.

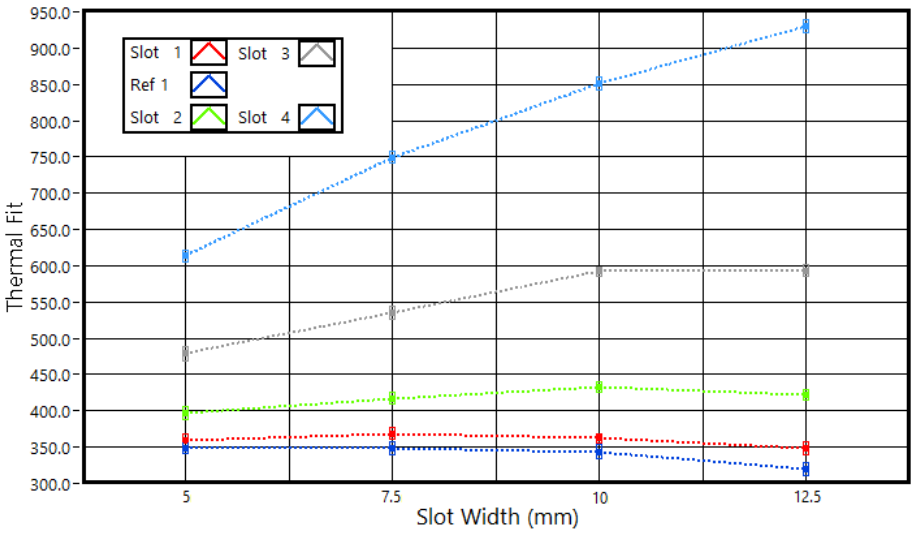

Figure 3.17: Slot width comparison for the 30 seconds stimulation period and image index 350

The image analyses process described previously uses the temperature reconstruction curves, 1, 2, 3 derivative and residual images. Each and every one of these images presented less noise than the raw temperature images, validating the value of the TSR technique. Due to the difference in the magnitude of the different images, the signals in figure 3.18 were normalized for the value correspondent of slot 4. Thus, the sensibility between the different analyses is accessed by comparing the standard deviation values. Since the higher temperature is always recorded for the deepest slots (slots 3 and 4), another point for evaluation may be the amplitude measured for the second slot. Apart from small apparent differences in the images, the data comparison does

not provide any indication of a higher sensibility for any of the types of analyse (figure 3.18). However, it was apparent a higher contour definition for the reconstruction and to the 3rd order derivative image (figure 3.19a and 3.19b respectively). The reconstruction, 2nd order derivative and residual curves have a fairly resemble profile, however the residual value for slot 3 is smaller than the 2nd order derivative, which in turn is smaller than the reconstruction signal. Looking at the temperature evolution, naturally the image index at which the temperature derivative presented a maximum contrast was at the location where the temperature for the slots was equal to the adjacent references curves.

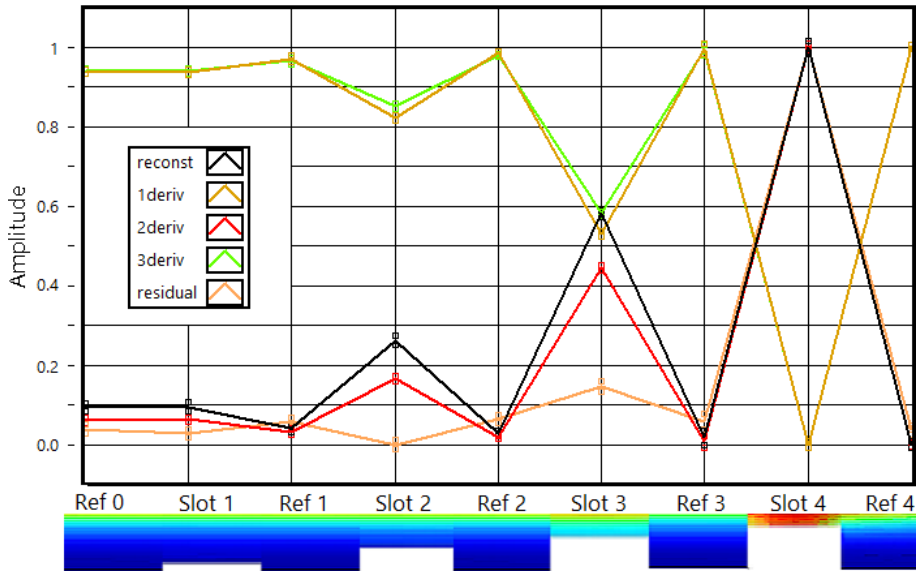

Figure 3.18: Comparison of the different types of analyses

3.2.6 Transient Thermal Tests conclusion

The parameter with the higher influence and impact in the analyses is the stimulation period. This was expected since it determines the amount of energy transferred during the test. The variation of the stimulation period also revealed the somewhat unexpected data, the slot temperature variations for the smaller stimulation periods. The smaller temperatures in the thinner areas may result from the smaller thermal resistance and therefore the higher heat transference to the air, while the thicker areas may not let the temperature reach the back of the plate in order to release heat by natural convection. For the slot 4, the maximum difference (maximum detectability) was observed for a stimulation of approximately 35 seconds. The second thinner slot presented a peak for approximately 50 seconds, while slot 2 roughly at the 60 seconds. This indicates a clear increasing tendency for the maximum detectability. On the contrary, with the increase of the stimulation duration may even happen that slot 3 presents a higher thermal amplitude than a deeper

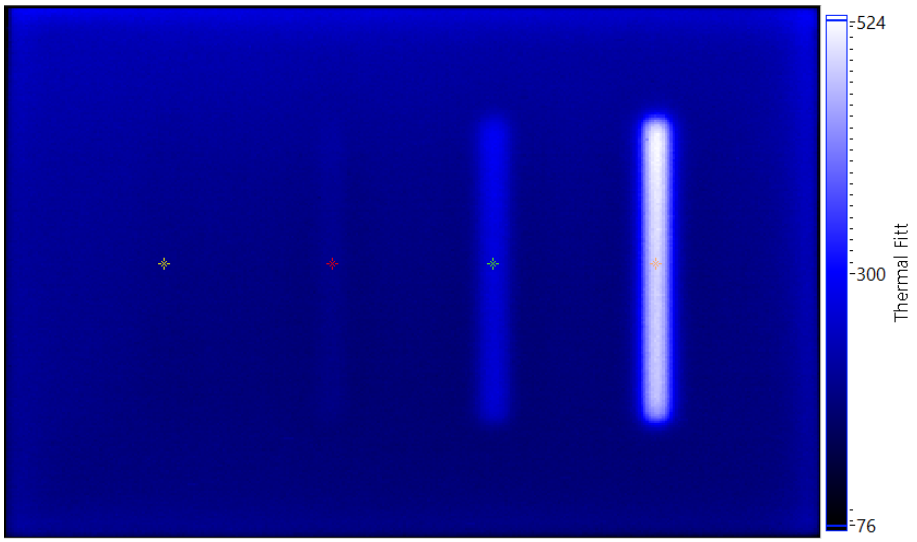

(a) Reconstruction image

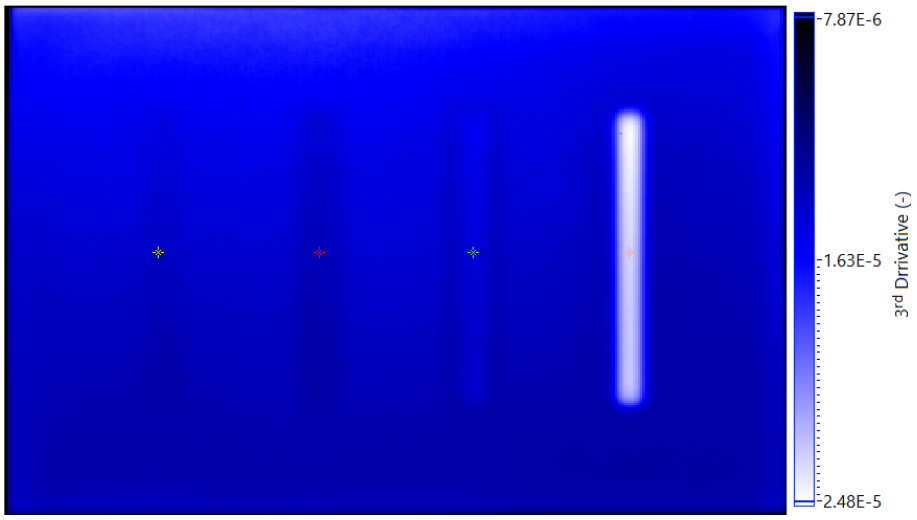

(b) Third derivative image

Figure 3.19: Images for the plate with 7.5 millimetres slots, stimulation of 15 seconds and image index 350

one, like slot 4. The thicker slot thermal response was small and therefore is difficult to reach a precise conclusion about the thermal behaviour when compared with the reference temperatures. This may be explained since for the longer stimulation tests, the higher temperatures result in an increase of the natural convection in both sides and therefore the thinner areas start to present hotter areas since they receive more energy for millimetre.

For a sample with a thickness of 4.5 mm, the appropriate test is with a stimulation between 30 and 60 seconds (depending on the defect to detect). The tendency of the maximum detectability observed in figure 3.15 reveals a proportionality although the thermal conductivity of the material has not been taken into account and it is difficult to present any objective extrapolation. However,

higher thermal conductivities will result in higher internal heat flux thus, the temperature variations should be faster and the maximum detectability should be observed for smaller stimulus periods.

The best time to conduct a thermal analyses is right after the end of the stimulation in order to have the maximum contrast in the thermal imeags and to minimize the artefacts. This way the thermal contrast is maximized and the defects will be detected and quantified, preventing thermal equilibrium situations similar to the ones observed in figure 3.16.

The state of the art indicates the material defect width *vs* thickness should be larger than 2. However, the tests conducted for this work indicate that it can be lower (1.6 approximately). This means that the detectability of the current NDTs techniques using thermography is considerably higher than observed in the past.

Currently the commercial software allows the TSR and provide the temperature reconstruction image and its derivatives. The extra information in each of these images is not relevant, but combining this information, come errors like the equilibrium instants in the cooling phases here discussed may be prevented. Due to the difference in the used technique, equipment and test parameters, the limitation of 2 millimetres found by D. Bates was surpassed, being now comprised between a thickness of 3 to 4 millimetres [173] .

3.3 Lock-in thermal testing

This section describes the principles, methodologies, analysis and results relating Lock-in Thermal Tests (LTT). The experimental tests presented in the following pages were performed to identify the best settings to perform LTT.

3.3.1 Overview

Active thermography testing (ATT) can be used for non-destructive testing with stimulations more complex than a simple transient. One of the alternatives is to define a wave with a certain profile and loop it for several cycles. In general, these types of tests are called Lock-in Thermal Tests (LTT). Lock-in thermal testing uses a stimulation to vary the temperature of an object, at each cycle. In these tests, the stimulation is applied in a cyclic manner, generally with repetition of a sinusoidal wave [174]. A correct lock-in thermal test amplifies the temperatures differences (when compared with one cycle) in areas with different thermal properties. The most common form of analysing the temperature data is to calculate the amplitude response and phase delay [175, 176]. The presence of areas with different thermal or optical properties that may result from cracks, delamination and deboundings, thickness variations, unwanted insertions or production defects. Applying energy to the object under analyses can be achieved by using several different sources

like: ultrasounds, halogen lamps, electric current, microwaves among others [175, 177–179].

One of the most important requirements in these tests is the synchronization between the stimulation source and the infrared thermal image acquisition. With this, the thermal images should be acquired at a constant frame rate. This procedure permits the calculation of several parameters by comparing the temperature evolution of each pixel with the reference (during the stimulation). There are several ways to calculate these parameters for thermal image sequences, being the most common developed in the middle of the 80's and 90's by Beaudoin et al [180–182].

The main goal of this work is to increase detectability of the defects and their characterization. Very often, with defects located in the interior of a component, it is possible to identify the depth at which they are located [177]. The main theories until now use one of several correlations to estimate the size and depth a defect, usually based in the phase contrast method. The blind frequency method, analyses the temperature evolution for a frequency the presents a zero phase delay (blind frequency) [183]. The blind frequency method tends to give better results in the pulse phase method however, it can also be used in the lock-in method [184, 185]. In the phase method, it was observed that the defect depth is proportional to the phase delay [186, 187] that is locked with the acquisition process. The stimulation is modulated using a wave (mainly sinusoidal waves). The stimulation is modulated so that the temperature of the object increases and decreases at each cycle. Thus increasing the temperature variations in the object under analysis and the resulting sensibility.

3.3.2 Procedure and processing

Like stated in chapter 3.2, to simulate a sample with a known defect it was used PMMA samples with four machined slots each. Similar to the transient thermal tests four samples were used, with slots of 5, 7.5, 10 and 12.5 millimetre width with remaining thickness of 1, 2, 3 and 4 millimetres respectively. The camera and sample position, stimulation equipment, setup layout and software used are the same described for the TTT. The LTT were also conducted in the reflection mode [163, 188].

Each test also was performed sequentially with a startup cyclic test with a stimulation of 10 cycles with 5 seconds each. The cool-down phase after the startup test and after each test was the same, also consisting in two criteria.

The test samples, were tested each with a different cycle period. The stimulation periods used for each cycle were: 3, 4, 5, 7, 10, 15, 20, 25, 30, 35, 40, 50, 60 and 80 seconds. The thermal camera integration time was kept constant and was the value used to calibrate the camera by FLIR®. The acquisition frame-rate was defined in order to maintain a constant number of frames (300 frames) for each cycle, for a total of 15 cycles in a single test.

Analysing the data was a process divided into two steps. Firstly the data was processed using the program IRNDT from Automation and Technology^{TM}. Here it was used the already mentioned thermal signal reconstruction (TSR) method [153, 169]. The most useful recognized analyses in lock-in thermography are the calculus of images corresponding to the phase delay and amplitude response. The conducted tests were performed in order to access the influence of several parameters in the results of the lock-in thermal tests, table 3.11.

Table 3.11: Resume of all the parameters that can be combined among themselves

Slots width	**Slot depth**	**Cycle period**	**Number of cycles**	**Interpolation method**	**Image type**
5, 7.5, 10 and 12.5 mm	0.5, 1.5, 2.5 and 3.5 mm	3, 4, 5, 7, 10, 15, 20, 25, 30, 35, 40, 50, 60 and 80 (s)	1, 2, 3, 4, 5, 6, 7, 8, 9, 10, 11, 12, 13, 14 and 15	Harmonic or DFT	Amplitude or phase

The influence of the first three parameters (slots width, depth and stimulus duration) were accessed by performing several tests. All the plates have four slots with the same width and different depths thus varying the slot depth. The stimulation duration was accessed by performing several tests, each with its own stimulation time, for each plate. The influence of the remaining parameters were evaluated by changing the parameters in the software at the post processing phase. To access the influence of the number of cycles each test and the correspondent image sequence was truncated for the desired number of cycles. During the post-processing, several resulting images were exported each corresponding to a different analyses. For each situation two images were taken into consideration and exported, the phase and amplitude response, thus taken into consideration the type of analyses. The remaining and previously mentioned configurations resulted in four different images, depending on the interpolation method and the resulting parameter being used (image type). The software uses the temperature to calculate the best fitting to the data and applies one of the following methods:

- **Harmonic** - This evaluation method the measured signal in each pixel is first approximated by an analytical function ;
- **DFT** - calculates the phase and amplitude responses using a discrete Fourier transform.

The temperature measurements of each pixel was compared to the reference signal, normalized stimulation. By performing this comparison for all the pixels, it are created images corresponding to the amplitude response and phase delay. All the images were exported and analysed afterwards using custom scripts implemented in LabVIEW®. Here the first steps are equal to the ones described for the TTT.

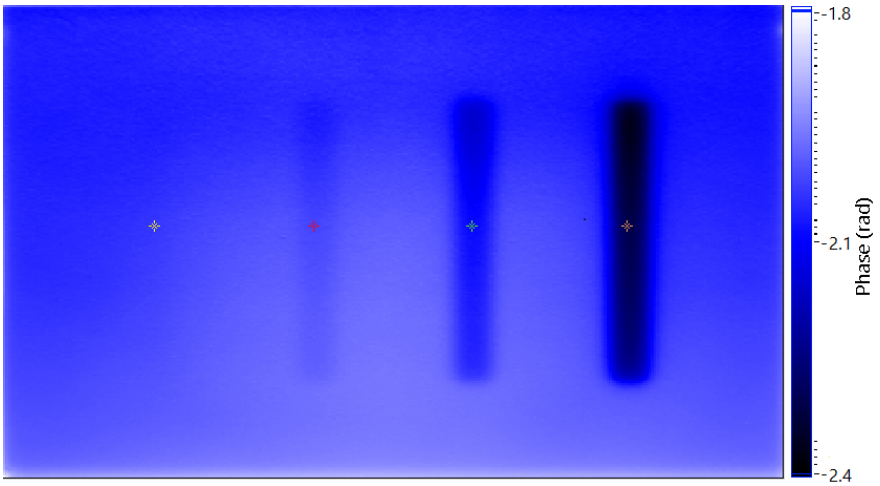

Figure 3.20: Example of an image from the analyses of a sample with 12.5 millimetres (phase)

In the analyses of the LTT were also used 30 average cross section profiles since the vertical variations are very small like illustrated in figure 3.20, this corresponding to the sample with slots of 12.5 millimetres width. From analysing figure 3.21 is observed a tendency in the vertical profiles, however this variation is linear like observed in figure 3.21. Another extremely important aspect is the amplitude of the noise, present in this data. Looking at the central values, is observed that the amplitude of the existing noise is in the same range of the variation for approximately 30 points. Thus 30 profiles were used to average in order to achieve an average profile reducing the existing noise and give origin to a superficial profile that is more representative of a general cross-section.

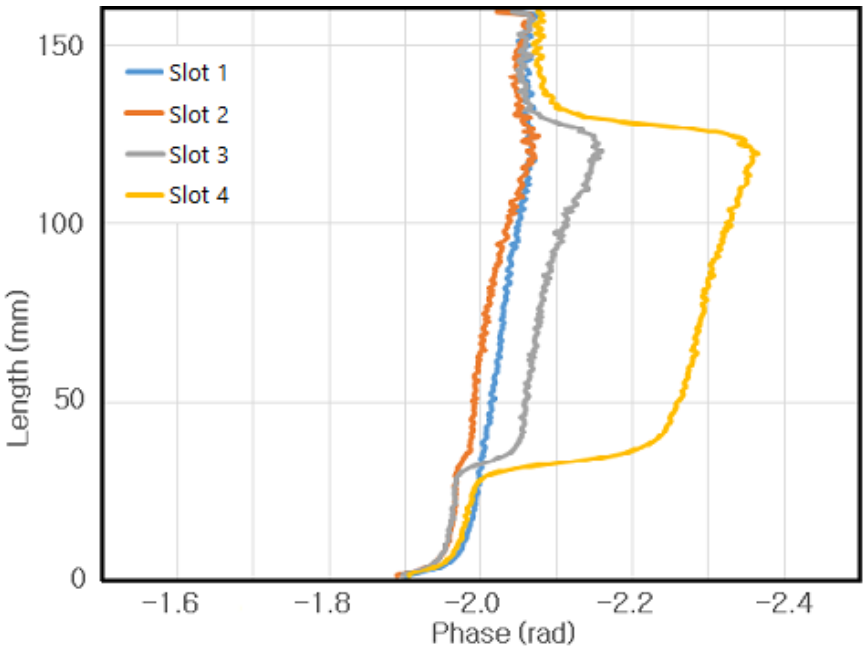

Figure 3.21: Vertical profiles of figure 3.20

A global overview of all the steps performed in the laboratory tests is presented in figure 3.22. This is divided in three main phases: The test and acquisition of the temperature data, the processing with the software IRNDT were several types of data can be obtained and the last phase with the custom scripts built with LabVIEW®.

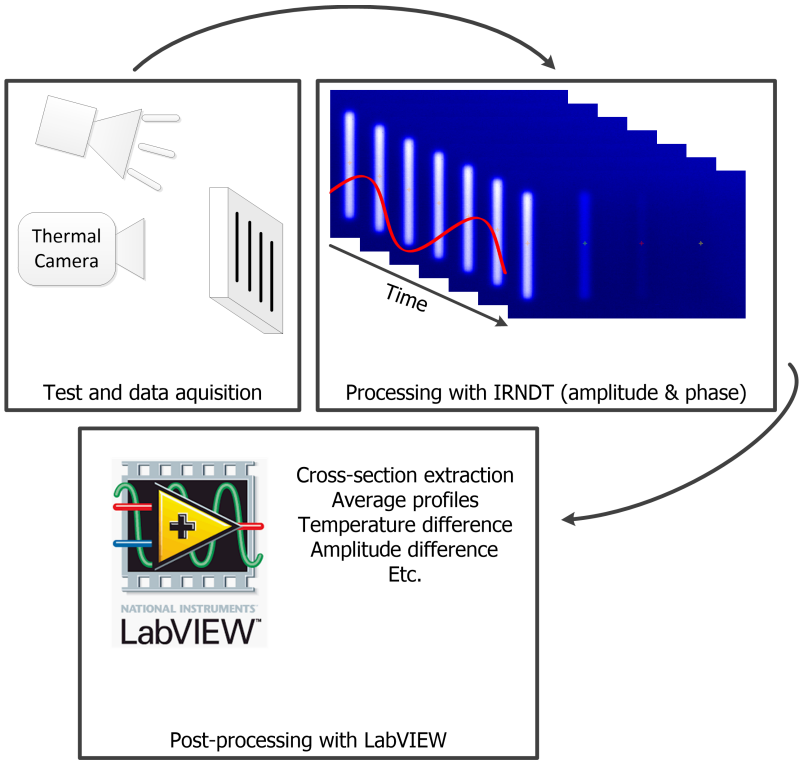

Figure 3.22: Schematic of the steps performed in a lock-in test.

3.3.3 Results

The first and most obvious results are the ones accessed by software in the post processing phase. These can be changed in the commercial software and produce different images with the same raw data. This way the comparison of its influence in the results is very precise.

Most authors use infrared thermal data to calculate the amplitude response and the phase delay at each pixel during a test. Naturally this information has to be identified and correlated with a possible or known defect [187, 189]. Phase data have the advantage of being slightly independent of the material emissivity and insensitive to some superficial imperfections. On the downside, suffers from the existence blind frequencies [183]. As the component frequency response is synchronous with the stimulation and therefore is not detected neither visible in the phase image. One major difficulty in using the phase image is therefore the presence of blind frequencies. Despite this being a big concern in the laboratory lock-in infrared thermal tests, this

subject will be addressed in chapter 5.

The phase image represent the delay of a full cycle, and present values between -3.14 and 3.14 radians. The amplitude can be expressed in temperature, a normalized image, or as raw data like bits. To compare the two types of data they have to be in the same order of magnitude. Therefore, the amplitude and phase delay average cross-sections were normalized like illustrated in figure 3.23. The phase average cross-section profile presented a considerably higher response for the deepest slot and a very resemble level of noise. For this sub section the phase data will be considered as a reference. This aspect will be further discussed in chapter 5.

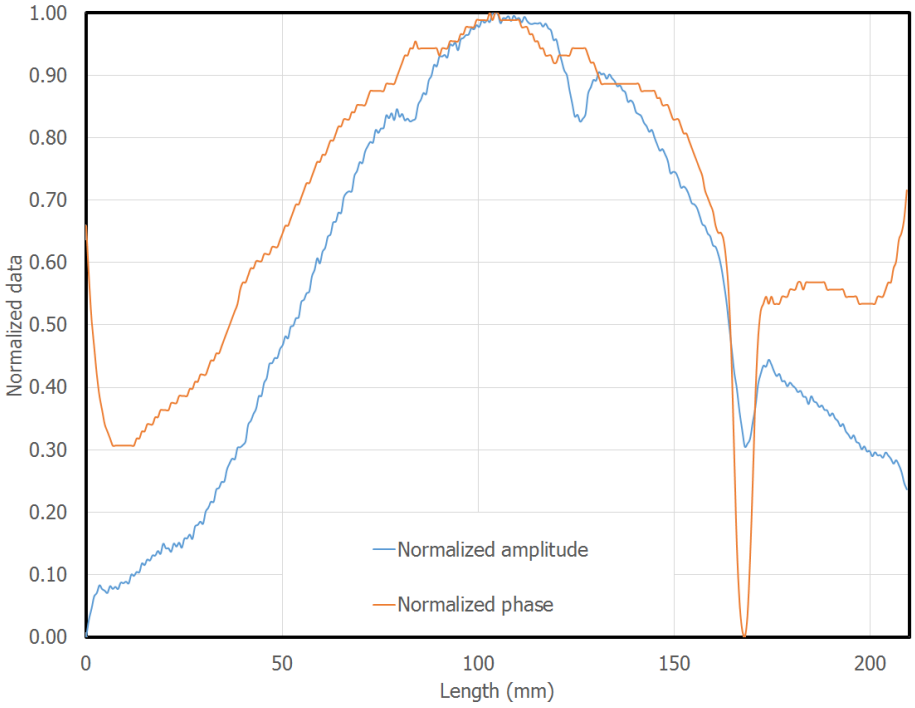

Figure 3.23: Normalized phase and amplitude response

Another important comparison is between the two interpolation methods. In figure 3.24 are represented two average cross-section profiles obtained by a harmonic approximation and another using a single DFT. Figure 3.24 presents the amplitude for the two interpolation methods, displaying a very high similarity among the two profiles. In the analyses it was not observed any relevant difference in the amplitude profiles calculated with the two methods.

The phase cross-section average profiles were also compared and are illustrated in figure 3.25. In the phase profiles the difference in the cross-section profiles is more evident. In the phase profiles it is easy to find a match of the phase profiles and the slots, when compared with the amplitude profiles. To easily compare the two available methods to calculate the phase delay a third profiles was created. By multiplying the single DFT profile by 1.063 it was achieved an

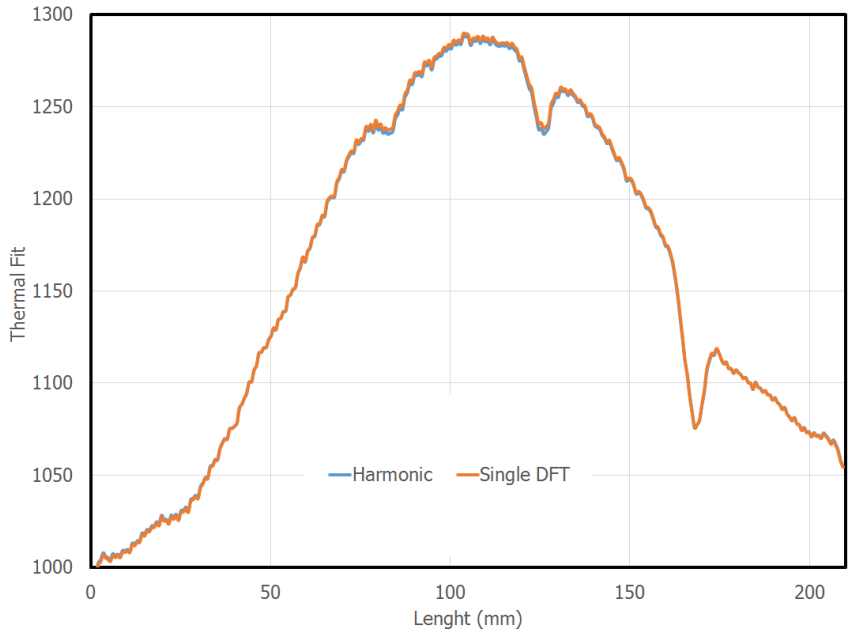

Figure 3.24: Comparison of the two interpolation methods, harmonic and DFT

almost perfect match between the two profiles. Observing at the lightly higher profile in second deepest slot, the single DFT method will be used to present the rest of the results.

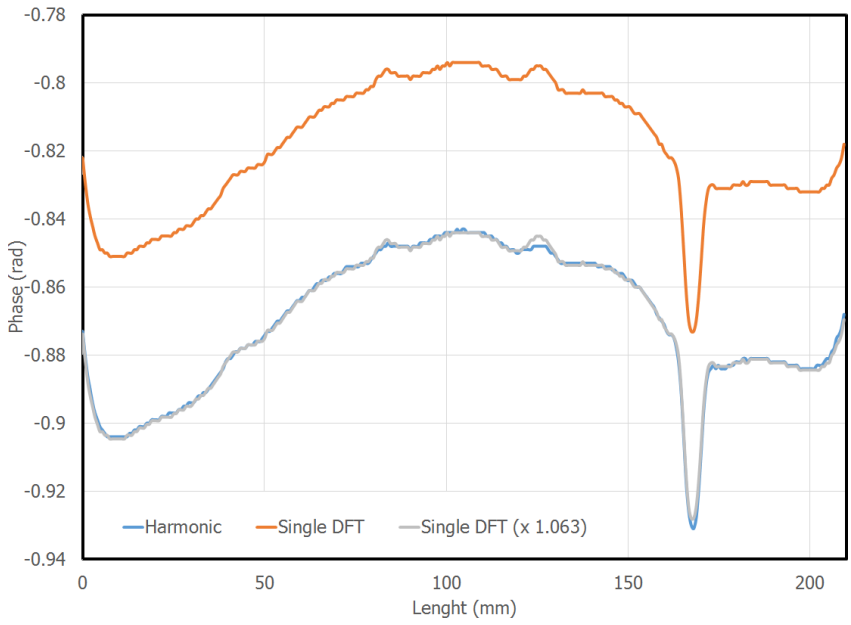

Figure 3.25: Average phase cross-section profiles

The last parameter to be accessed was the number of cycles. Figure 3.26 presents the variation of the mean response at the centre of the slots for the various number of cycles (Y axis in auto--scale). By analysing figure 3.26a is visible the low variation of the amplitude response, despite

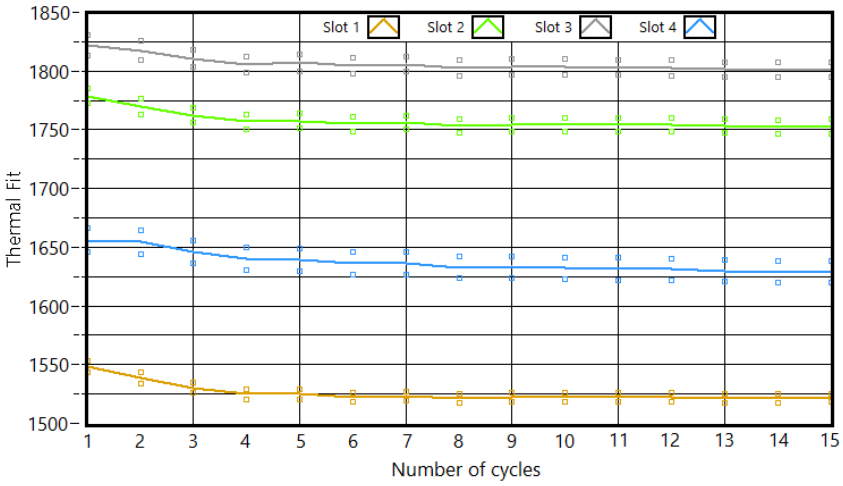

(a) Amplitude data

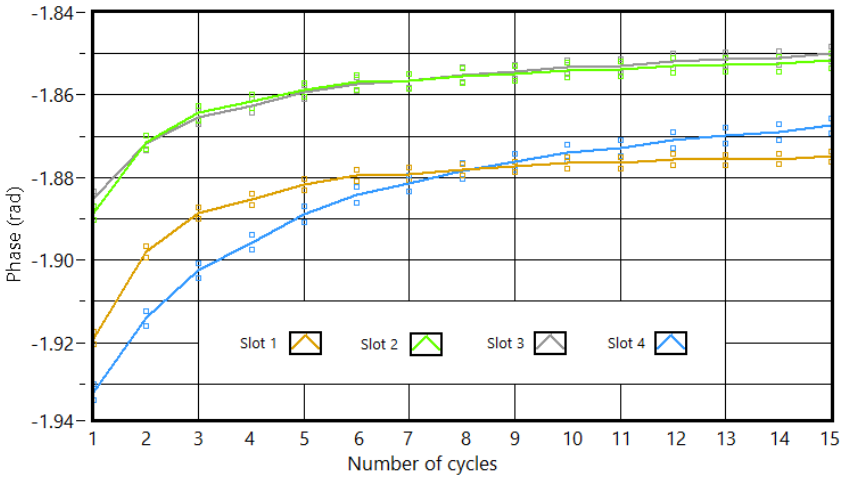

(b) Phase data

Figure 3.26: Variation of the slots data for several number of cycles in the stimulation

using one or all available 15 cycles. In all the slots the variation is near the standard deviation. On the contrary, in the calculus of the phase delay, the number of cycles has a great influence. Like illustrated in figure 3.26b, the phase variation presents a logarithmic decay. This decay is higher for deeper slots. For tests with more than 8 cycles, the variation is extremely small.

From the several parameters accessed during the lock-in tests, the time per cycle is the most important with these results presented in figure 3.27. Due to the existence of the already referred blind frequencies, are represented the results for the amplitude response and for the phase delay.

From the amplitude response for the stimulations with shorter cycles periods (figure 3.27a) it is clearly visible the higher response of the sound area. This is observed in all the cross-section profiles in the same quantity, similar to an offset. In stimulations having cycles of 3, 4, 5, 7 and 10 seconds it is not visible any variation in the profiles that indicates the presence of a defect

(figure 3.27a). The stimulations of 15 seconds reveal a small local drop in the location of the deepest slot, without any indication of the other slots. The stimulation of 20 seconds per cycle leaved no doubt the presence of slot 3 and 4, the stimulation of 25 seconds presented a small alteration at the location of slot 2. The longer stimulations presented a decreasing in the amplitude response at the location of the slots (figure 3.27b), similar to what was observed for the shorter stimulations. From the various responses in the area corresponding to slot 4, it was observed that the maximum response was registered for the cycle of 25 seconds. For longer stimulations the amplitude response tends to diminish and inverts to the stimulation of 80 seconds. For slots 2 and 3 it was observed a crescendo in the amplitude response with an increasing of the stimulation time. More precisely, slot 3 becomes visible with a stimulation of 25 seconds and slot 2 with a stimulation of 40 seconds.

Like already mentioned, the phase analyses is considerably more sensitive than the amplitude. The phase cross-sections present a small curvature at the centre of the image, smaller but similar to the observed in the amplitude profiles and images. This curvature, along with the average values of the phase delay increase for longer stimulations. Even for a stimulation extremely short, like in the 3 second test, slot 4 is identifiable 3.27c. The smallest slot (slot 1) is not visible in none of the phase profiles. Slot 3 (the second deepest) becomes traceable with cycles of 5 seconds and slot 2 for cycles of 25 seconds. For the longer tests, the phase delay increases of the deepest slot (may also be seen as the test detectability) increases with the increment of the cycle duration. The same behaviour is observed in slot 3. For slot 2 the "detectability" is very low and a test with longer cycles leads to a less differentiability in the phase image 3.27d.

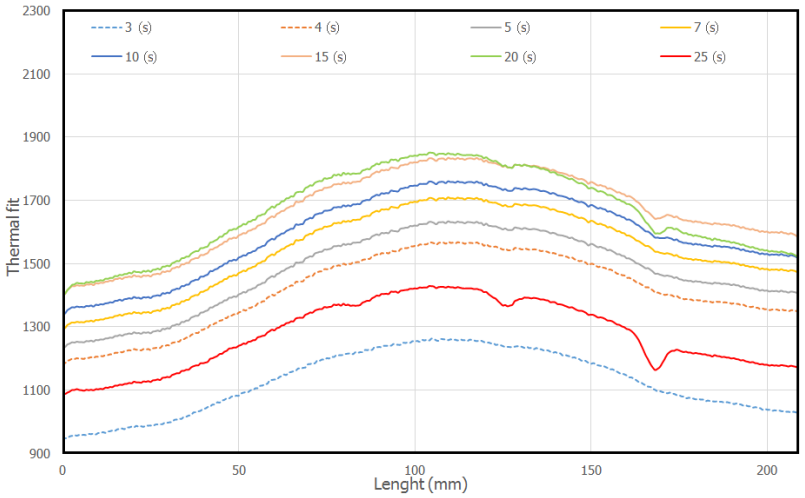

(a) Amplitude cross-section for stimulations of 3 - 25 seconds

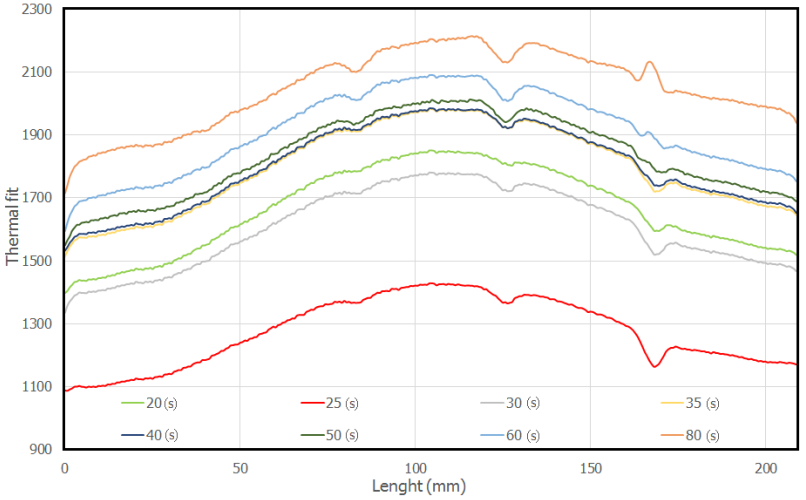

(b) Amplitude cross-section for stimulations of 20 - 80 seconds

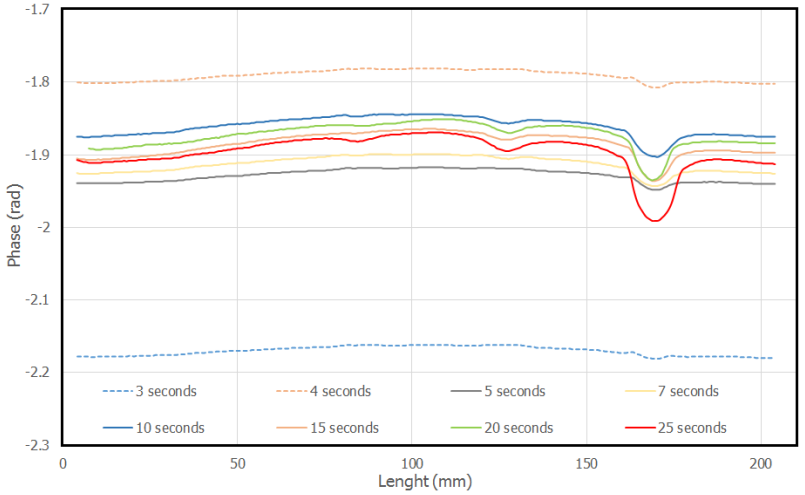

(c) Phase cross-section for stimulations of 3 - 25 seconds

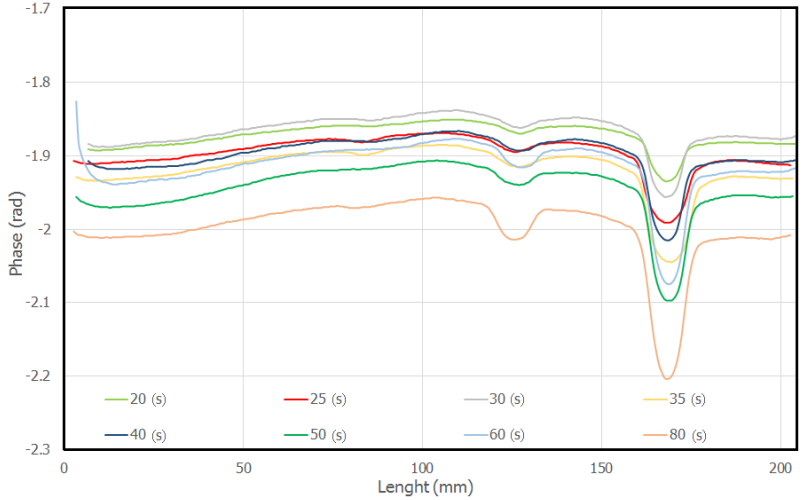

(d) Phase cross-section for stimulations of 20 - 80 seconds

Figure 3.27: Average amplitude and phase cross-sections

Like expected, the deeper slots are easily visible than the smaller ones. This was observed in the already presented results and is resumed in figure 3.28. In both analyses, amplitude and phase delay, wider slots presented higher amplitude and higher phase responses.

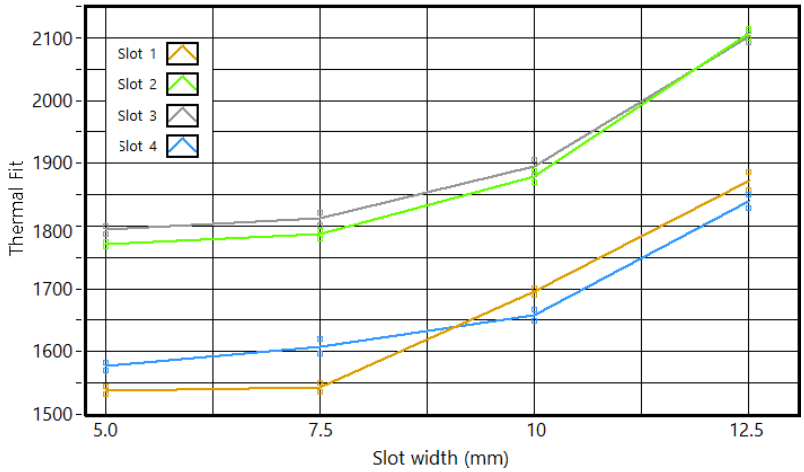

(a) Amplitude results

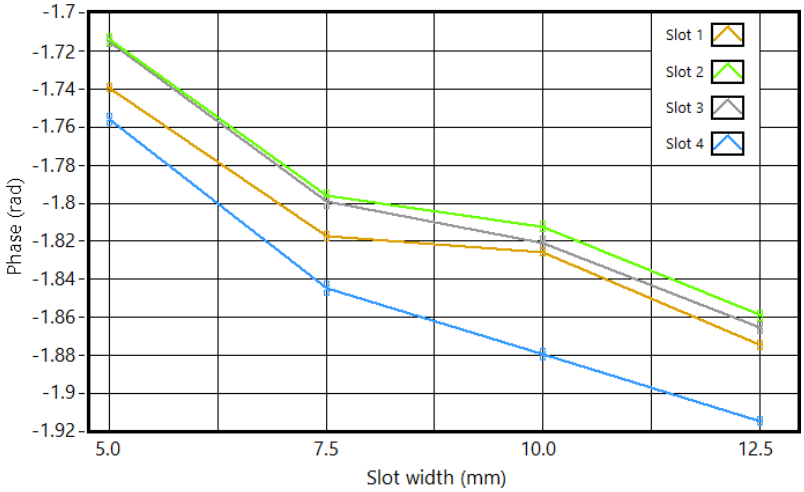

(b) Phase results

Figure 3.28: Results for slots with different width and depths

3.3.4 Analyses of lock-in thermal tests

The majority of the studies relating infrared thermal testing in NDT applications uses the phase image to identify the defects and in some cases to estimate the defect depth. Therefore, it was expected a higher sensitivity in the phase images and consequently its cross-section profiles. Figure 3.23 clearly indicates this, despite the higher values at the centre of the profile. Along with figure 3.23, figure 3.27d illustrates the clear differences in both, phase and amplitude. In figure 3.27d slot 2 is only observed in the phase cross-sections with 25, 30 and 35 seconds. Contrary, in the amplitude data slot 2 is considerably more visible for stimulations with longer cycles. The

amplitude profiles clearly reveal the existence of this slot. Another negative aspect of amplitude data is the level of noise. Figures 3.27a and 3.27b profiles show a higher level of noise, when compared with the profiles presented in figures 3.27c and 3.27d. The downside of using phase data is the blind frequencies where is indicated a zero phase delay. Therefore the best and most accurately analyses for a lock-in test should focus mainly in the phase response and observe the amplitude to confirm the results and prevent bad analyses due to blind frequencies.

The results of the thermal analyses can be accessed by two different forms, single DFT and harmonic interpolation. Both methods calculate the same parameters, the pixel amplitude response and its phase delay, both parameters compared with the normalized reference signal. Like represented in figure 3.29, the difference between the two methods is very small, the difference among the two is at the logic bit level, approximately 3 bits. At first impression this profile could be used to detect and identify the defects. However this curve was obtained calculating the average of 30 cross-section profiles. Using a single profile to access the difference between the harmonic and single DFT methods would result in a similar curve with a resolution of 1 and no differences would be noticed. Thus this method cannot be used with raw temperature or logical bit data. In conclusion, currently this difference is inherent to calculus method and does not represent any significant difference between the two. Looking at the phase data, the two methods revealed some differences in their results. The example presented in figure 3.25 indicates the single DFT method calculates lower phase values. These calculations are performed with the program IRNDT from Automation & technology^{TM}. The software and its provider does not indicate the equations used. This prevents the exact comparison of the two processing methodologies. Even so, multiplying the single DFT average profile by 1.063, results in an almost exact match with the harmonic interpolation. This last profile (Single DFTx1.063 in figure 3.25) indicates a little higher detectability for slot 3 and a lower one for slot 4. Here the differences are so small that is irrelevant the usage of one method over the other, therefore it was adopted the harmonic method.

Another important aspect is the number of cycles used in a single thermal test. The number of cycles used in a LTT is proportional to the time necessary to conduct a thermal analyses. Therefore, using more cycles that don't improve the technique sensitivity and defect detectability is a major step-back. By varying the number of cycles the amplitude variation observed in figure 3.26a in considerably small. The variation is fairly consistent and equal for all the slots. The steepest decrease in the amplitude response is observed in the first four cycles. After eight cycles it was not observed any significant change in the amplitude response for any slot. Using a higher number of cycles does not contributes for a better analyses, either for the amplitude or its noise. The phase response (figure 3.26b) revealed a small difference when the number of cycles varies. It is observed a significant drop in the phase response when the stimulation uses just a few cycles. This variation tends to stabilize for stimulations with more than eight cycles. In the case of slots 1, 2 and 3 this is extremely clear. However, for slot 4 this situation is not observed. Here, a decrease in the phase do not indicate a trend to a certain phase value.

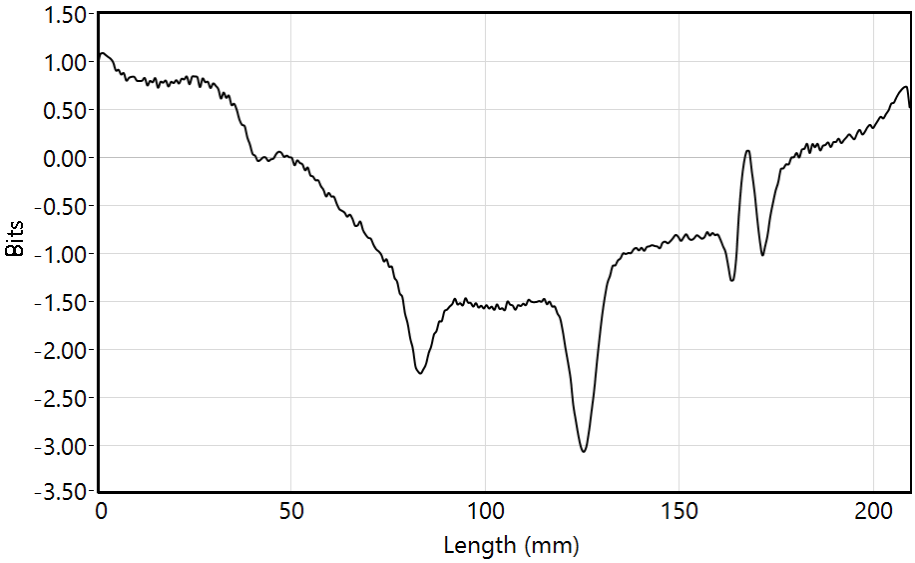

Figure 3.29: Difference between the amplitude averaged profiles, using Harmonic and single DFT

The lock-in tests start with the samples in equilibrium with the environment, At the beginning of the second stimulation, the samples (due to the stimulus and thermal conductivity) are at a higher temperature than the one at the beginning of the first cycle. The temperature evolution presents an exponential evolution. With the successive cycles the specimen temperature will increase up to an equilibrium situation. This equilibrium is reached when the energy absorbed during a cycle is equal to the energy released by convection and radiation. Since slot 4 has a smaller thickness, its temperature is easily changed, thus its higher sensitivity to the number of cycles applied during a test. Despite the results for slot 4, is irrelevant to perform more than 7 cycles in a lock-in thermal test.

Along with the number of cycles, the time per cycle used in a lock-in thermal test is the most important parameters and cannot be altered in the post processing phase and therefore, a wrong specification of requires the repetition of the test. The stimulation has to be sufficiently longer for the specimen to change its temperature and reveal a temperature pattern that indicates the presence of the discontinuity and/or variation in the thermal properties. Like is observed in figure 3.27a, the shorter cycles do not reveal any temperature variation. The PMMA has a thermal conductivity of approximately 0.2 W/mK, at ambient temperature [190]. With a thermal conductivity as low as this, the cycles of 3 and 4 seconds do not permit the specimen to a significantly change its temperature. Another important aspect within this type of analyses, is the emissivity. Since the conducted test uses a radiometric stimulation, its reflection will also be added in the temperature response. The only situation where this is not observed is in the presence of a perfect blackbody. The high intensity lights, the small thermal conductivity of the samples and an emissivity lower than 1.0, results in an amplitude response different from zero, due to the reflected radiation, and fairly uniform in the entire specimen. For stimulation cycles shorter than 10 seconds it was not

observe any alteration in the slots. The same did not occur in the phase data. Like already mentioned, the phase data reveal to be more sensitive to the presence of the slots. Since in the phase analyses, the main aspect that is evaluated is the delay in the temperature variation, the amplitude of the variation has low impact. The phase delay will be the combination of two "sinusoidal" waves. The first with a higher amplitude (at least for shorter cycles) is due to the reflected radiation. The second is the temperature response of the material. Since the first wave is mainly uniform in the entire plate, an offset is observed in the phase data. This delay is visible, even in short cycles.

For longer cycles, the amplitude response corresponding to slot 4, suffers an alteration in its response profile. From cycles of 25 seconds on, it is observed a decrease in the amplitude response of slot 4. In a cycle of 60 seconds the amplitude response at slot 4 is, however, the borders of the slots is visible. This occurs for all the four slots, despite the width. Slot 3 presents an amplitude response of the same magnitude for cycles with 60 and 80 seconds. This behaviour was observed in slot 4, but occurs for a cycle considerably longer. This is only visible for cycles considerably longer than what is desired in real situations. The remaining slots present an increasing amplitude with the increasing of the time per cycle. For the longer cycles, it was observed an increasing tendency in the phase profiles (increasing phase). Along with this increase, the response at the slot location was getting wider.

It has already been mentioned the influence of depth of the slots. A deeper slot correspond to a section with a smaller thickness. Therefore, the thickness decrease results in an area with a smaller thermal resistance. The heat will reach the side opposing the stimulation easily and thus be subjected to a higher thermal convection. This helps to comprehend the lower amplitude responses in the areas of the slots. Since have less material to warm-up, they will reach higher temperatures. Natural convection is responsible for the cooling, thus the decrease of the temperature during a longer periods will lead to a higher delay in their global temperature response. These behaviours are visible in almost all figures presented in section 3.3.3

The local change in the temperature due to the thickness variations are higher for wider slots. The slots are a transient variation in the samples thickness profiles. Therefore, local temperature gradients will appear and consequentially, changes occurs in the vertical convective flow. Each slot has two transient variation in its thickness and thus a wider slot means that each one will be further apart. Since neither the amplitude or phase profiles reach a horizontal and stable profile, reveals that the geometry did not reach a stable and uniform temperature variation similar to what occurs in sound area in the middle of the slots. With the separation of the boundaries, the profiles would develop up until a stable temperature profile.

3.3.5 Lock-in conclusion

In lock-in thermal tests, the parameter with higher influence in the results was the cycle period. The energy applied to sample is determined by the stimulation period and the number of periods. According with the literature, the most accurate analyses method is the phase delay. This was clearly observed, despite the blind frequencies. For this reason the amplitude response should always be taken into the analyses. In the suspicious of the existence of blind frequencies, the amplitude images and raw temperature images should also be analysed. The number of cycles did not revealed a big influence in the results, especially in the amplitude data. The phase results reveal higher phase differences for smaller number of cycles. However using just one cycle can lead to false conclusions. This is due to the starting process that occurs in the lock-in cycles. However this aspect will be discussed in more detail in chapter 5.

There are two common methods used to determine the amplitude and phase delay response. In the amplitude responses it was not found any significantly difference in the two methods. The phase delay revealed some differences, manly a proportional difference between both. Since the equation used by the commercial software are unknown, it was not possible to determine which is the most accurate method.

The phase data was found to be less noise and higher "detectability" when compared with the amplitude. Even so the possible usage of a frequency that correspond to a blind frequency and thus preventing the detection of some defects makes the amplitude images vital.

The geometry of the slots revealed a significant influence in the temperature patterns. Deeper slots, mean less thickness and therefore a lower thermal resistance. The deeper slots presented higher temperatures but lower amplitude variations. A slot that is wider also presents a higher temperature and a higher amplitude variation. These aspects will be analysed again in chapter 5.

3.4 Conclusion

IRT presents some unique characteristics when compared with other temperature measurement techniques. The versatility of IRT in NDT applications and being a contact-less technique, make it a preferable technology in defect analyses for several materials. Being an image technique, and with certain conditions, very sensitive measurements are achieved (near the millikelvin), resulted in its regular use in maintenance operations in aeronautics. The easiness of analyses and interpretation of the results in composite materials have greatly contributed to the technique evolution and widespread. The usage of a stimulation sources provides great improvements over traditional analyses. These may use ultrasounds, microwaves, radiation or even mechanical loads. These can be modulated as a single stimulation or a cyclic, giving several test alternatives. The research in this field has tried to develop technologies, techniques and protocols which maximize the detectability of Infrared Non-destructive Testing (IRNDT).

Transient thermal test is one of the most used single stimulation tests. In this case, the stimulation period is the most important parameter in the test settings. Short stimulations do not induce significant temperature alterations and patterns and longer stimulations lead to more uniform temperature images. The optimum duration varies on the defect to be identified. Ideally the analyses should be performed after the end of the stimulation and right after the stimulation is completely shutdown.

Lock-in thermal tests use cyclic stimulations to identify defects. There are two typical results used in these tests: amplitude response and phase delay. The amplitude usually presents less sensitive images compared with the phase images. On the downside the phase data and images may suffer from blind frequencies. Here, the defects will be synchronous with the stimulation and will not be visible in the phase images. Similar to what happens in the TTT, the stimulation period is the most important parameter when performing these tests.

Chapter 4

New Lock-in Thermal Tests

The commercial test system used to obtain the results showed in the previous chapter, permits the usage of stimulations with different types of signals: square, sinusoidal, triangular, among others. However, the produced stimulation is not equal to the one specified in the software. In this chapter are presented the system characterization and the results obtained with two different approaches.

In the first sub-chapter is presented the dynamic characterization performed to the optical stimulation system (along with power unit) used in this work. Here are described the various stimulation waves in the time an frequency domain.

The second sub-chapter presents the results of lock-in thermal tests and analyses when an optical sensor was introduced in the system. The data of the sensor is captured during the tests and used as a reference in the calculus of the amplitude response and phase delay.

The third sub-chapter introduces an alteration in the modulate waves used in the lock-in tests. Using the feedback sensor, a PID controller was implemented in order to create a stimulation wave near the desired one.

A comparison is also performed in order to quantify the difference of these new results when compared with the previous tests.

4.1 Stimulus characterization

4.1.1 Laboratory tests setup

The main goal of these tests was: the characterization of the dynamic response of the halogen lamps and power unit. The power unit is manufactured by Automation & Technology and the stimulation by HEDLER like mentioned previously. The software used to conduct thermal tests and analyses was developed in LabVIEW®. This permits the selection of several types of waves with constant or variable frequencies.

To fully characterize the real stimulation and quantity any difference between the desired and real stimulation produced by the power source, it was necessary to use a feedback sensor. The sensor used to measure the light was a photocell, CdS model GL55. This photocell is a light-dependent resistors (LDR). This means, its electrical resistance will change with the received light. In this case the electrical resistance varies from 1MΩ (no light) to 10kΩ (maximum light). The sensor was connected to an electric circuit recommended by the manufacture, consisting in a voltage divider. On top of the light entrance (figure 4.1) it was positioned a fabric in order to diminish the amount of light reaching the sensor. This was necessary because of the amount of light that reaches the sensor when the stimulation was at its maximum, preventing the sensor saturation. This procedure is also recommended by the sensor manufacture. To apply a gain and offset to the sensor, it was performed a characterization. The characterization consisted in the definition of the voltage output for the extreme situations, with the light at its minimum and maximum. The minimum and maximum light were set with a stable reference during 10 seconds for each situation.

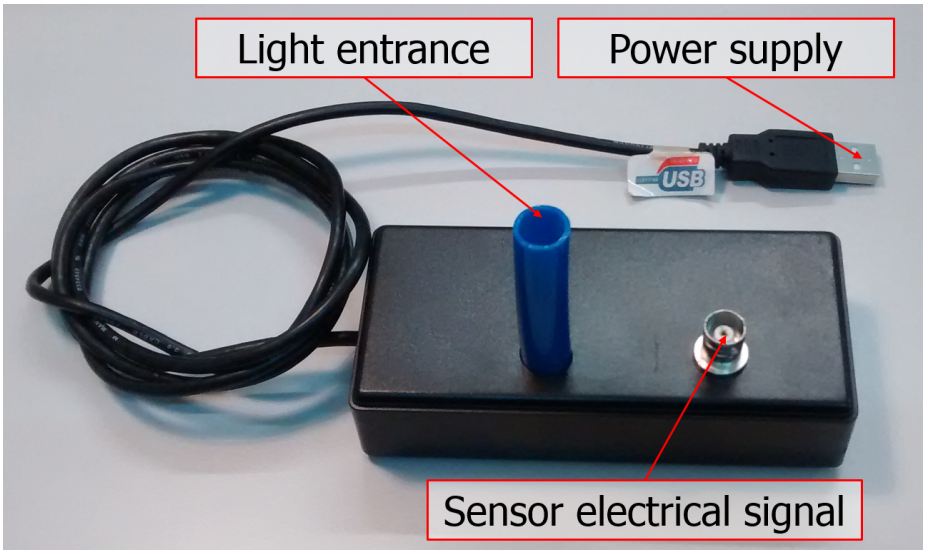

Figure 4.1: Light sensor box and physical connections

To conduct the characterization, the sensor was firmly positioned in the structure previously described, to perform the thermal tests. The sensor position and angle was approximately the same as the test sample. The output signal was connected to a data acquisition system from National Instruments^{TM}. The generated reference signal was inserted in a parallel analogue channel (figure 4.2), thus the feedback and electrical reference signal were used as reference signal in the analyses, thus preventing any delay between the signals.

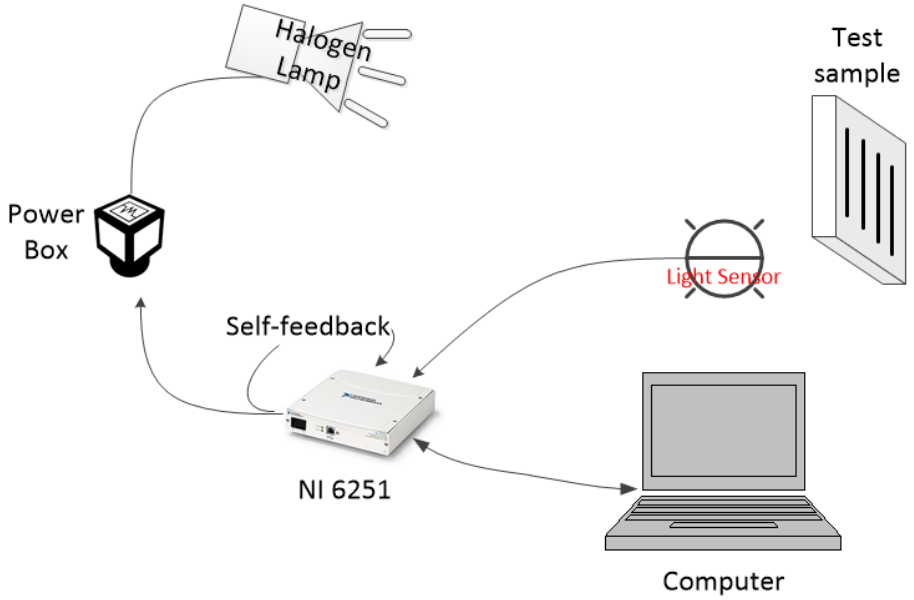

Figure 4.2: Schematic of the stimulation characterization with the light sensor test.

To perform a good characterization, the reference signal should have a varying frequency. To achieve this, a custom application was developed and implemented in LabVIEW®. In this application it is possible to define the period of the first and last cycle. The intermediate cycles are created with an even spacing period accordingly with the number of specified cycles. The generated signals started with a delay of $\frac{\pi}{2}$ so it started with a value of zero. This also ensured that the signal has a continuity since its derivative (between each cycle) is null. The periods vary from 20 to 0.5 seconds for a total of 50 cycles, all starting with a delay of $\frac{\pi}{2}$. The generated signal was reproduced by the NI module and consequentially by the power unit, at a sampling frequency of 1000 samples per second. The electrical signal of the NI module ranges from 0 to 10 Volt. The output voltage of the sensor was tested with a minimum and maximum light resulting in 1.2 and 4.5 V respectively. Due to the difference in the amplitudes, both signals were scaled so they ranged from 0 to 1.

4.1.2 Stimulation dynamic characterization

The stimulation sources used in this work were halogen lamps. Therefore, it was not expected a complete response, particularly at high frequencies. In figure 4.3 are presented the normalized reference and sensor signal, by its observation it is visible difficulty of the system to respond at high and low frequencies. Here, are visible the lack of proportionality between the reference signals and the produced stimulations. Even if the electrical power created to the reference may be proportional to the reference signal, the created light signal is not. This may be due to the variation of the electrical resistance of the tungsten filament of the lamp with the temperature.

When creating a sinusoidal reference signal with low frequency 4.3a the resulting stimulation is approximated to a square wave. It is noticed a small inertia in the system for small reference values. After the simulation reaches 50%, the opposite behaviour occurs. In figure 4.3b is visible the difficulty of the system to follow high frequencies. Here is also clear the delay in the system response.

The triangular wave is a continuum stimulus, while its derivative has discontinuities points. Naturally at these points the system was not expected to follow the reference. However the magnitude of the error encountered for the high and low frequencies was far above the expected (figures 4.3c and 4.3d). Actually, when compared the response to a sinusoidal reference the two responses are similar.

The sawtooth wave is characterized for having a constant derivative and a discontinuity point in its derivative and signal. For the lower frequencies (figure 4.3e) is easy to visualize a similar behaviour to the already mentioned signals. However, the transient instances present a much faster response. For the higher frequencies (figure 4.3f), the system continues to have difficulties to follow the reference and displays a delay.

Finally the square signal is defined by a uniform signal with two transient instances. Compared with the previous signals, the error for this reference is extremely small for low frequencies, like illustrated in figure 4.3g. For higher frequencies (figure 4.3h) is noticed a difficulty in the amplitude response.

The overall behaviour of the stimulation was very poor. For lower frequencies the system demonstrated difficulty in accurately represent the middle values. One aspect that was observed in the response to all types of stimulations was the difficulty in higher frequencies, with a better response for increasing references when compared to decreasing values.

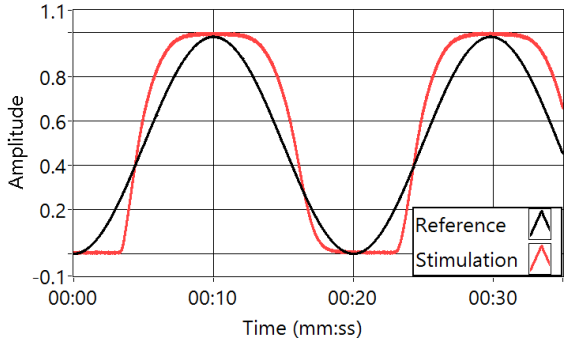

(a) Sinusoidal signals at the beginning of the test

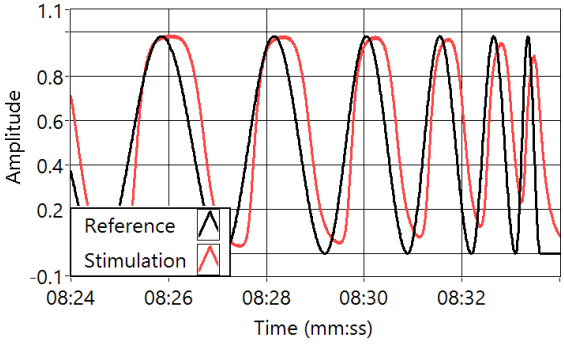

(b) Sinusoidal signals at the end of the test

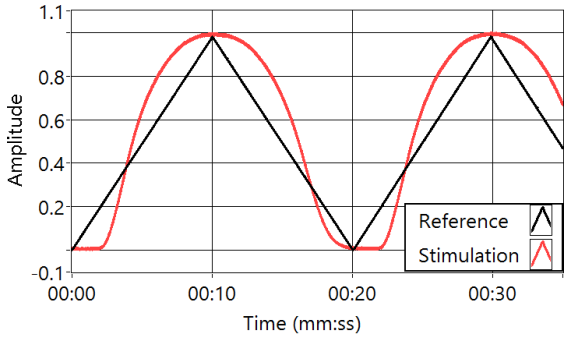

(c) Triangular signals at the beginning of the test

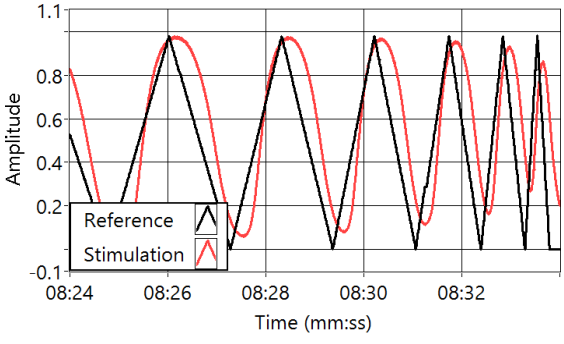

(d) Triangular signals at the end of the test

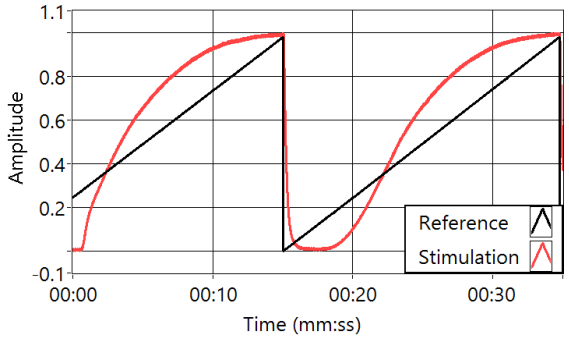

(e) Sawtooth signals at the beginning of the test

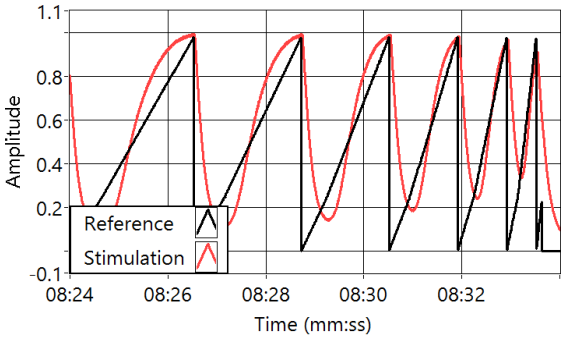

(f) Sawtooth signals at the end of the test

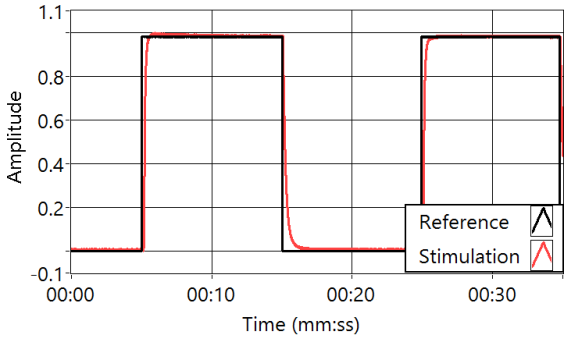

(g) Square signals at the beginning of the test

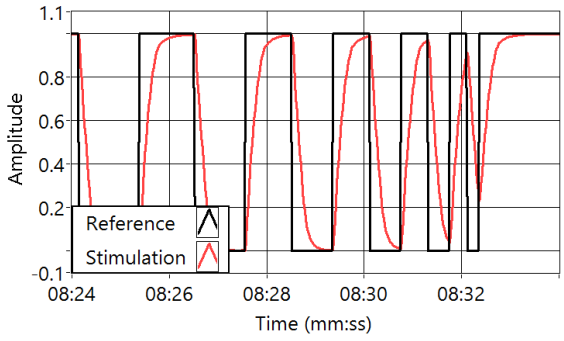

(h) Square signals at the beginning of the test

Figure 4.3: Reference signals and correspondent stimulations at the beginning and end of the characterization tests

4.1.3 Stimulation with PID controller

To improve the dynamic response of the stimulation system it was implemented controller with a Proportional an Integral and a Derivative action (PID), without alter the physical layout (apart from the feedback sensor). The previously developed application to create the stimulation was redesigned to include a digital PID controller. The parameters were set using an auto-tuning controller for stimulations from five to 90 seconds. By looking at figures 4.4 is immediately observed a significant improvement in the stimulation.

For the sinusoidal wave, at low frequencies (figure 4.4a), it is clearly visible the decrease in the stimulation error when compared to the reference curve. The two curves are overlapping each other, even in the maximum and minimum values. For higher frequencies (figure 4.4b), the system cannot achieve a complete response. However, the stimulation is similar to a sinusoidal, presenting a small delay and amplitude attenuation when compared with the reference.

The triangular waves for low frequencies are also well defined by the stimulation, like is presented in figure 4.4c. Here, is observed a small delay, similar to what was observed in the sinusoidal wave (figure 4.4a). In the wave extremities (figure 4.4d) is observed some inertia in the system. For higher frequencies the stimulation continuous to present some difficulties to precisely reproduce the reference wave.

The sawtooth wave is observed in figures 4.4e and 4.4f. Similar to what was observed in the other stimulation waves, the sawtooth wave was now very well defined for low frequencies. Once again, for the higher frequency the stimulation was not able to follow the desired reference. The difficulty in defining the inversion of the signal and the rounding of the peaks is also visible and is clear in higher frequencies.

The square wave, without the PID controller, was already well defined. It was not observed a significant improvement in the square stimulation at low frequencies (figure 4.4g). For higher frequencies was observed a similar behaviour, being this represented in figure 4.4h). This different variation was expected, since the controller is reproducing the reference signal almost without any interference.

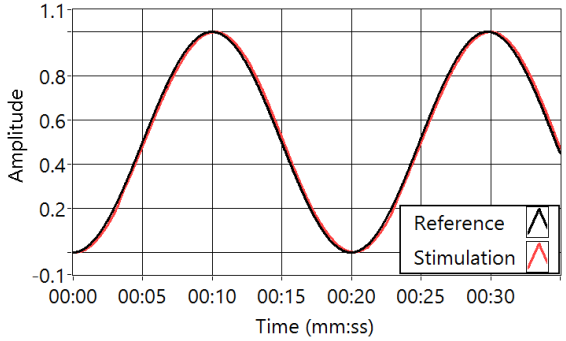

(a) Sinusoidal signals at the beginning of the test

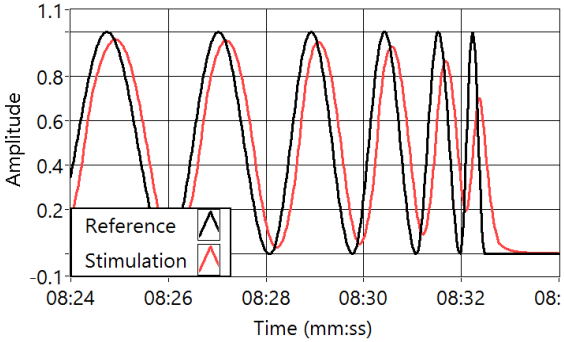

(b) Sinusoidal signals at the end of the test

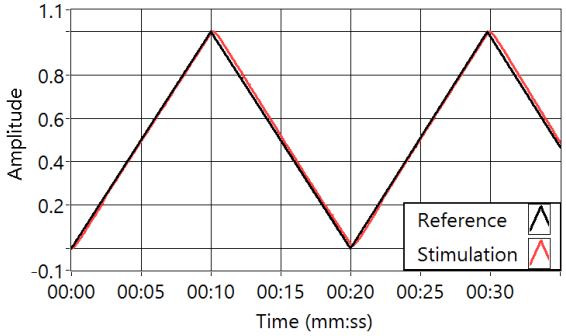

(c) Triangular signals at the beginning of the test

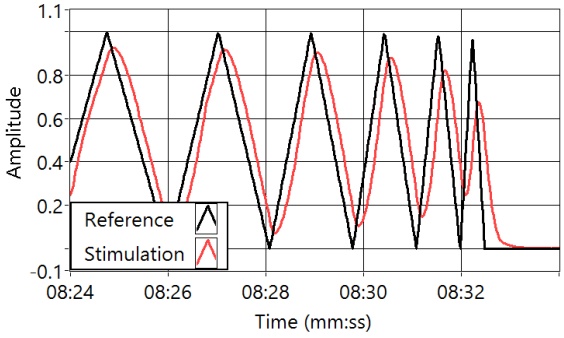

(d) Triangular signals at the end of the test

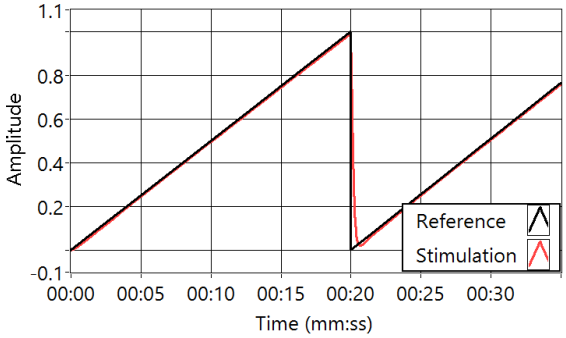

(e) Sawtooth signals at the beginning of the test

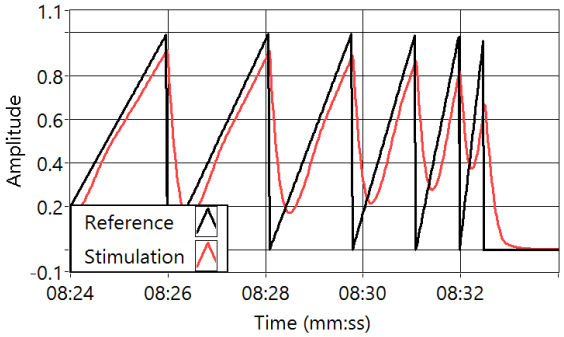

(f) Sawtooth signals at the end of the test

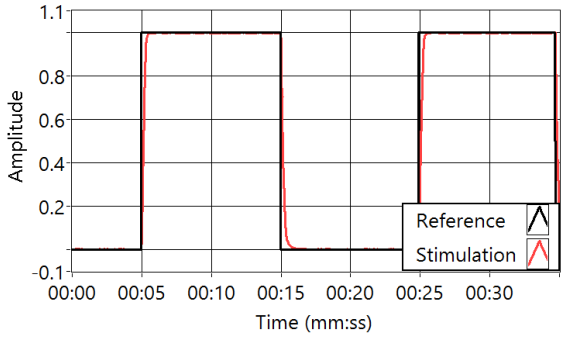

(g) Square signals at the beginning of the test

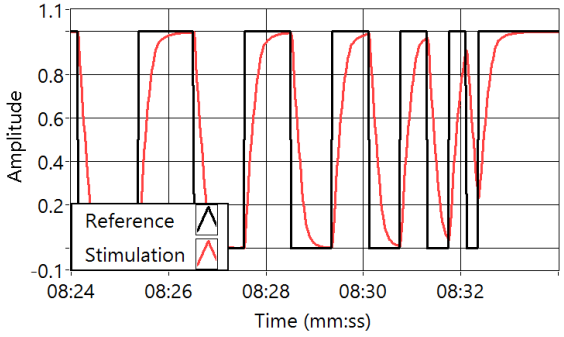

(h) Square signals at the beginning of the test

Figure 4.4: Reference signals and correspondent stimulations at the beginning and end of the characterization tests

4.1.4 Stimulation response analyses

The most accurate manner to analyse the dynamic response of a system is to calculate the system response and plot the results in a Bode plot (figure 4.5). Here are represented the amplitude and phase delay for the two previously described situations, original system and with the introduction of a PID controller.

In figure 4.5a is displayed the magnitude response of both signal. The first aspect to notice is the 1 dB gain of the original system. This values is constant for frequencies up to 0.028 Hz. Contrary, the implementation of the PID controller corrected the response to a 0 dB gain, for frequencies up to 0.17 Hz. A magnitude response of -3 dB is usually considered to be an acceptable limit magnitude response, when a system is being dynamically characterized [191]. The original system reached this mark at approximately 0.27 Hz, while system with the PID controller implemented the -3 dB were reached at 1.17 Hz.

The magnitude response of the system with the controller implemented, revealed an inversion point at approximately 4.55 Hz. The system was set to run (acquisition and controller) at 50 Hz. This frequency was measured during the test and presented a variation of $\pm$ 23 μs, centred in a zero delay. A frequency of 50 Hz has a corresponding Nyquist frequency of 25 Hz, which is far from the referred inversion point. Therefore this inversion in the magnitude response is most likely due to the discretization of the PID controller and some noise in the derivative feedback. This could be overcome by implementing a filter. This interpretation is reinforced by the increase in the upper and lower limits of the characterization (accuracy of 99.9 %). This area is the only situation were the upper and lower limits are not overlapped by the response curves. However, how it was observed in the previous chapter 3.3, that the best results were obtained for frequencies far inferior than 4.55 Hz, thereby this inversion point is not relevant.

In figure 4.5b are represented the phase delays for both setup, with and without PID controller. Like mentioned previously, the original system revealed a poor frequency response. Parallel to an earlier magnitude decay, it also presents a higher phase delay for smaller frequencies. The original system presented a smooth inversion in the phase delay at approximately 0.44 Hz (phase delay of 40.2°). For this frequency the delay for the system with the controller was 26.5°. The two systems intersect each other at approximately 0.8 Hz. The crescendo in the delay of the system with controller could be greatly diminished if the controller was implemented at higher frequencies. For this, the NI hardware and feedback sensor had to be replaced. Once again, since these situations occur for frequencies far from the ideal (like mentioned in chapter 3.3) there was not the necessity to overcome them. With smaller practical influences and considerable costs, the improvements in the system response were not implemented. Since the amplitude and phase response were calculated from experimental data, in figure 4.5 are also represented the upper and lower limits, being overlapped by the main response curves.

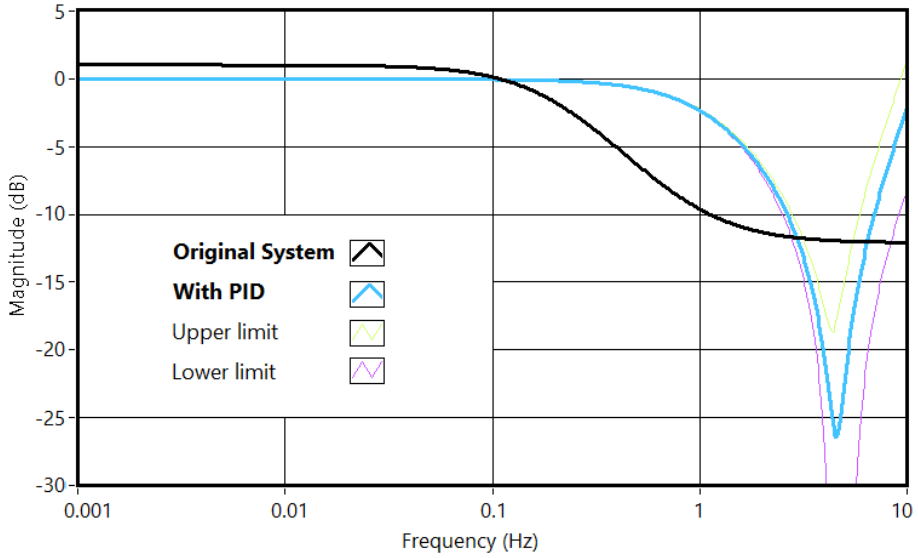

(a) Magnitude response of the stimulation

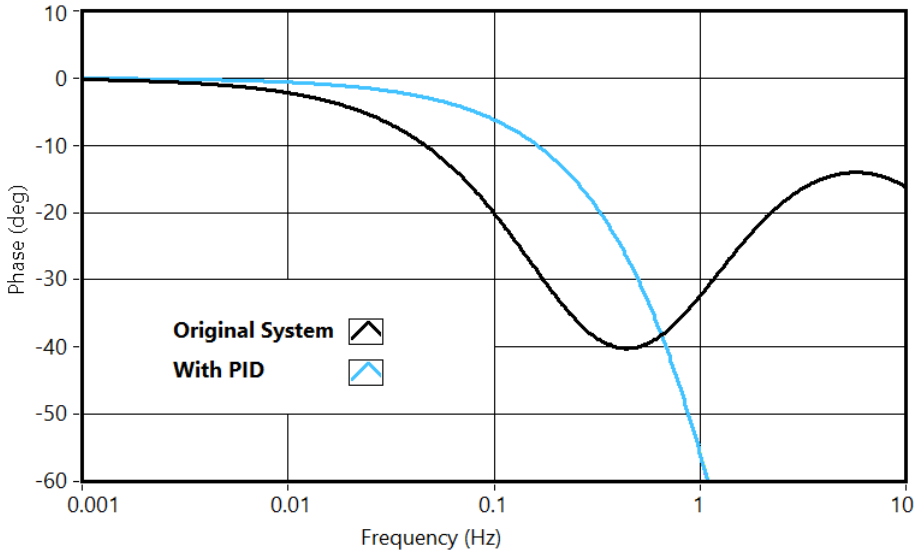

(b) Phase response of the stimulation

Figure 4.5: Stimulation dynamic response (Bode plot)

The frequency response was performed with a confidence level of 99.9%. In both cases the difference between the magnitudes and the upper and lower limits were extremely small and are not visible. The only situation where this is not verified is in the magnitude response of the PID system near the inversion peak. This reinforces the suggested hypotheses that this inversion is due to noise, probably in the calculated derivative signal.

4.2 Feedback modulated tests

After a detailed characterization of the optical stimulation used in the thermal tests, it is necessary to understand its impact in the IRNDT. During the analyses it was assumed a sinusoidal stimulation. Using a feedback sensor it is possible to determine the correct and real stimulation curve. Here will be presented the results and analyses of lock-in tests that used the measured stimulation as a reference instead of a perfect sinusoidal wave.

4.2.1 Setup and settings

In this section will be presented and analysed the thermal tests performed using a feedback sensor to determine the real stimulation. The reference curves are used as a comparison for all the pixels temperature curves to calculate the amplitude response and phase delay. Naturally any uncertainty or deviation in the reference, changes the results of the thermal tests. Consequentially, a wrong or inaccurate stimulation used as a reference can result in a failed analyses.

The main goal of these tests were to quantify the influence of the reference (ideally equal to the stimulation) curve. In these tests were used two of the already analysed samples, more precisely the plates with 5 and 10 millimetres slots. The setup followed the same layout previously presented in figure 4.2. The test sample, stimulation source and thermal camera maintained the disposition presented in chapter 3. Thus, it is possible to perform a direct comparison with the already performed tests.

4.2.2 Results of thermal tests with feedback

The temperature profiles obtained for each pixel were fairly equal to the ones obtained for the tests described in chapter 3.3. In figure 4.6 are presented examples of four temperature profiles obtained in two different tests. The feedback curves (Ref) correspond to the data measured with the feedback sensor for two different cycles. The sound temperatures correspond to the temperature evolution during the entire test, at the centre of the image, which correspond the sound area.

While any reference is automatically normalized by the software, the feedback signal is not. Here the feedback is represented in relation to the complete scale available for the NI module ($\pm$ 10 V). The recorded feedback during a lock-in test with a 10 seconds cycle is represented in figure 4.6a (Ref). Here is observed a small start-up phase that lasts for approximately two cycles. This startup phase is almost non-existing in the 30 seconds stimulation.

For the example (figure 4.6a), are presented two temperature profiles, one corresponding to the temperature observed in the middle of slot 4 and another of the sound area. In both are observed similar temperature evolutions, both with two wave components. The first component

is approximated to a sinusoidal signal corresponding to the stimulation. The second is a signal with a very low frequency that presents an exponential decay. The second test presented (figure 4.6b), refers to a LTT with a 30 seconds per cycle. Here, the temperature responses also present responses with two distinct dynamics.

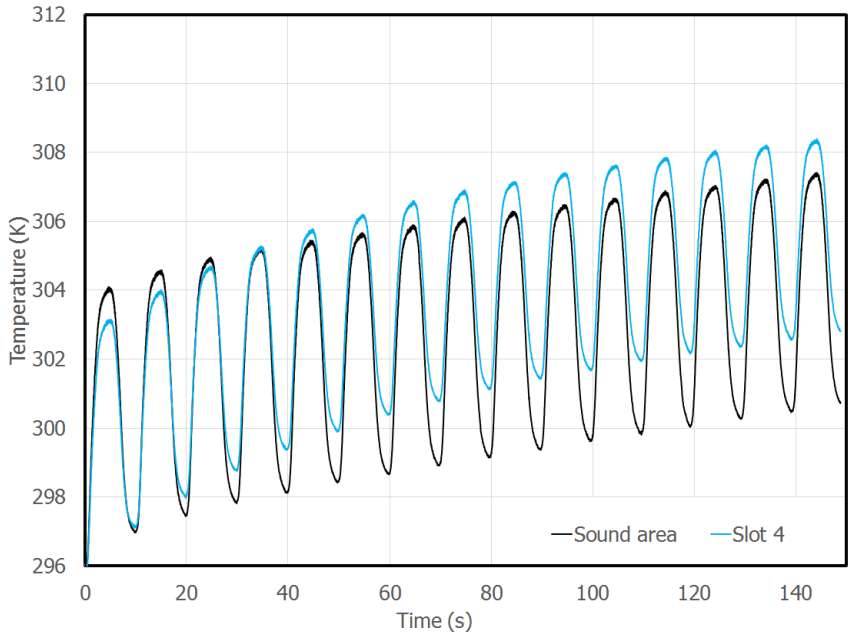

(a) Feedback and sound temperature for 10 second cycle period

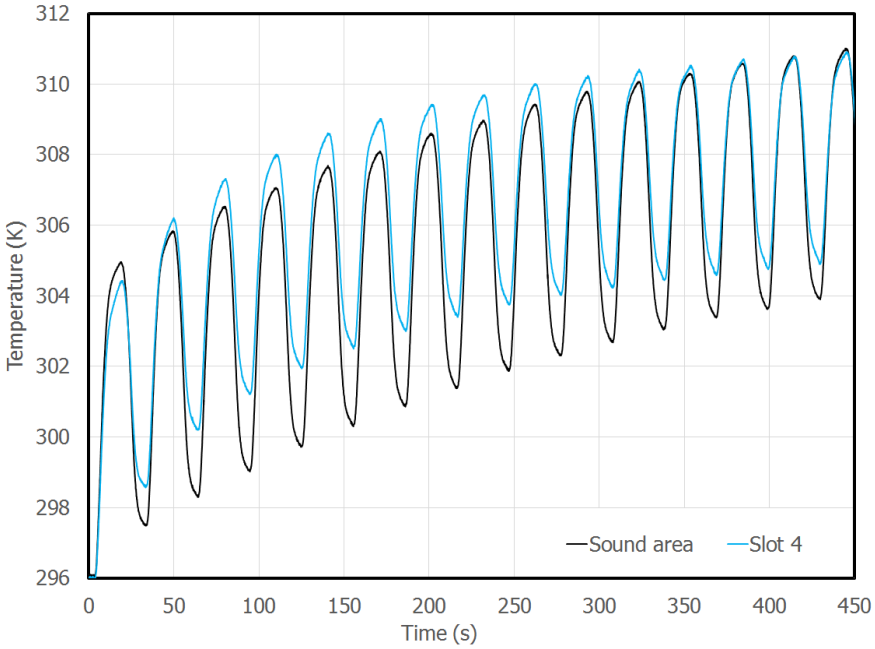

(b) Feedback and sound temperatures for 30 second cycle period

Figure 4.6: Example of temperature curves during the thermal tests with optical feedback with 15 cycles

When comparing the lowest respond of the two curves presented in figure 4.6a, they are considerably different. Looking at slot 4, this presented lower maximum temperatures until the fourth cycle, with the sound area revealing a more stable temperature. Looking at the higher frequencies, the sound area revealed a higher amplitude variation for all the cycles, being expected a higher amplitude response.

When comparing the lowest respond of the two curves presented in figure 4.6a, they are considerably different. From the start of the test until four cycle the slot 4 temperature was lower then the sound are, then it reverts. The temperature amplitude in the sound area was larger than in the slot 4.

The comparison of results can be accomplished using averaged cross section profiles, instead of the resulting images. This permits a more objective and precise comparison of the results. In these feedback tests, the temperature variation is equal to the lock-in tests. However the reference curve is different, like presented in the sub-chapter 4.1. Since the sensor output ranged from 0 to 5 Volt, scaled the curve used as a reference by the IRNDT software was considerably small. As a consequence the temperature amplitude response was considerably higher (figure 4.7).

Like observed in chapter 3.3 the amplitude responses tend to be higher at the centre of the sample. In the location of the slots, the amplitude response is smaller than the near sound areas. Therefore the slots are identified with a lower amplitude response. The IRNDT software used in this work did not enable the usage of the acquired feedback curve to obtain the phase image, it was only possible to obtain the amplitude response.

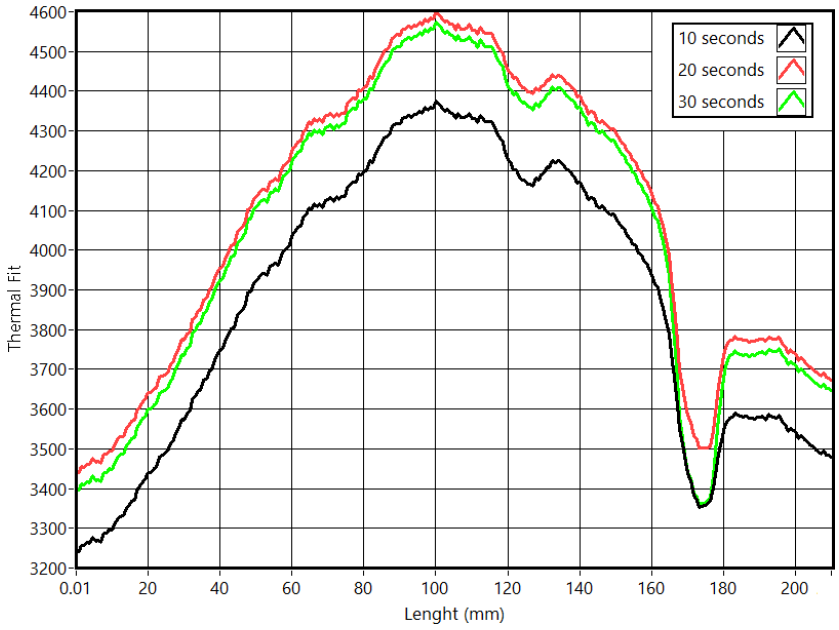

Figure 4.7: Thermal fitting results for the lock-in tests using the optical feedback

4.2.3 Feedback tests analyses

One important aspect when analysing the example temperatures presented in figure 4.6 is to comprehend the causes of the different responses. The sound areas present a thicker area than the slot areas thus, a different thermal dynamic behaviour. The expected result is a slower temperature evolution over time. While this explains why the maximum temperature in the slot was increasing rapidly than the maximum temperature in the sound area. The fact that the temperature variation in on cycle is lower for the slot than the variation in the thicker areas is not obvious. This evolution can also be explained by the thermal resistance in the slot. A higher thermal resistance also means that the heat will have more difficulty to disperse, thus reducing any heat transfer occurred by convection. With a smaller thickness, the temperature in the opposite side of the slot will be higher than the temperature of sound area. Thus the heat removal rate of the slot is higher than in the sound are, resulting in a smaller amplitude variation.

Looking at the slower temperature evolution the heat transfer phenomena act in the same manner, even if is not immediately obvious. A thicker area naturally has a higher thermal resistance thus a higher thermal inertia to transmit and disperse any temperature difference. Looking only to the lower frequency temperature variation, lead to a slower temperature evolution compared to the slot area. This behaviour is even more obvious in the test with a lower frequency. Here is clearly visible the rapid evolution (again looking only to the slower temperature evolution) in the slot temperature. The sound temperature evolves considerably slower, but reaches the same maximum temperature in the last cycle. In the last cycles of the longer stimulus is also clear the smaller amplitude response of the slot which is confirmed in the averaged cross section in figure 4.7.

In figure 4.7 three temperature amplitude responses are represented using the reference signal. Since the output of the sensor varied from 0 to 5V and the NI module has a range of 20 V ($\pm$10V) it was expected an amplitude response four times higher due the four times smaller reference. This is easily confirmed when compared the amplitude values of these curves with the results illustrated in chapter 3.3. To facilitate the comprehension, in figure 4.8 are plot the already mentioned amplitude curves and the amplitude curve obtained with the common LTT with a 10, 20 and 30 seconds cycle period. To establish an overall comparison, the four amplitude responses were normalized. It is easily observed the higher sensitivity of the fourth slot of the feedback profiles, compared with the 20 seconds lock-in test. Here, the third slot is slightly visible, while in the cross-section profiles obtained with feedback, this leaves no margin for doubt. The second slot might be identifiable in the feedback data, even if with a small response. Thus, the feedback data not only gives a higher signal to noise ratio in the higher defects, but also is able to detect defects not visible with the common LTT. While not very obvious, the level of noise present in the common lock-in test is higher than the noise existing in the feedback curves.

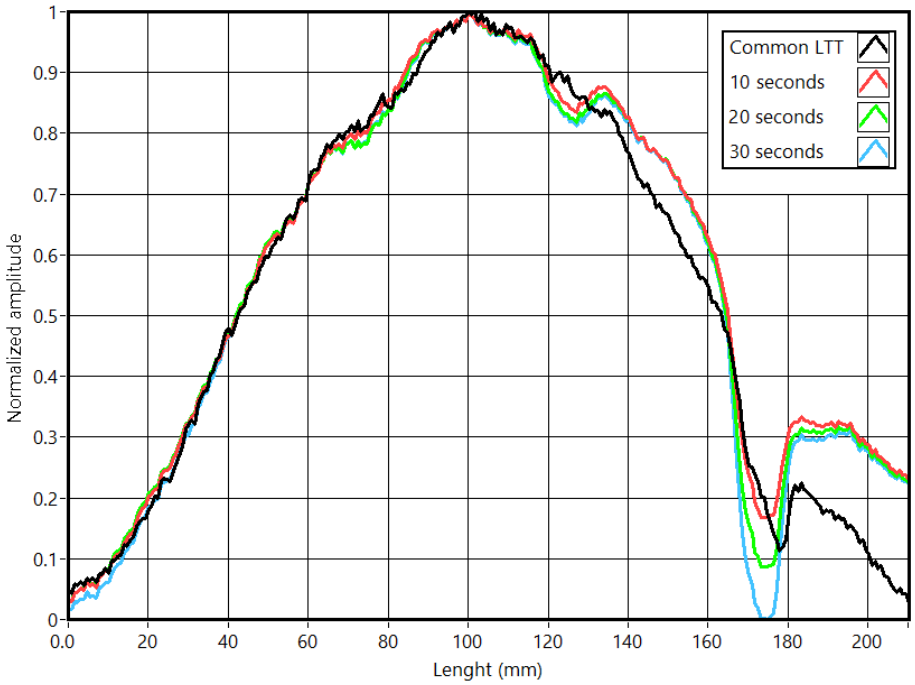

Figure 4.8: Amplitude average profiles obtained with the optical feedback

Since the real feedback curve is not a sinusoidal wave, like presented previously, differences between the feedback thermal testing and the common LT were expected. Therefore, during the analyses, the reference will undergo the same processing. This will increase the similarity between the two signals and consequentially the system sensibility. It is important to notice that the temperature measures that are important to the amplitude response are the ones with similar profiles of the stimulation. This manner the slower temperature evolutions (exponential decay) are not taken into consideration in this analyses.

Like all measurement equipment, the thermal camera has to be calibrated. This calibration consists in the application of a gain and offset value for each pixel. Therefore is extremely difficult to achieve a calibration to the condition of these tests. This adds small errors to the temperature measurements. The main observe errors due to this aspect is an offset in the temperature in the form of a higher temperature in the centre of the images. Another contribution to the amplitude responses at the middle is due to the reflections of the stimulation. The temperature readings are the combination of the infrared radiation emitted by the object and also reflected by it. Since the stimulation source is located in the centre of the sample and above the thermal camera, the stimulation reflections are higher at the centre. This justifies the higher amplitude responses at the centre of the profiles. If it was possible to remove this, the result may be similar to the data presented in figure 4.9. Here, it was applied a high pass filter in order to remove the curvature in the profiles, remaining only the corresponding noise and slots. It was applied a gain to the common LTT, so they were all with the same magnitude. The gain was defined so the noise in all the profiles had the same magnitude. In all the analyses, the detectability that use the optical

feedback is even more visible. Since the results for the samples with slots of 5 and 10 millimetres were so similar, only the results for the 10 slots are presented.

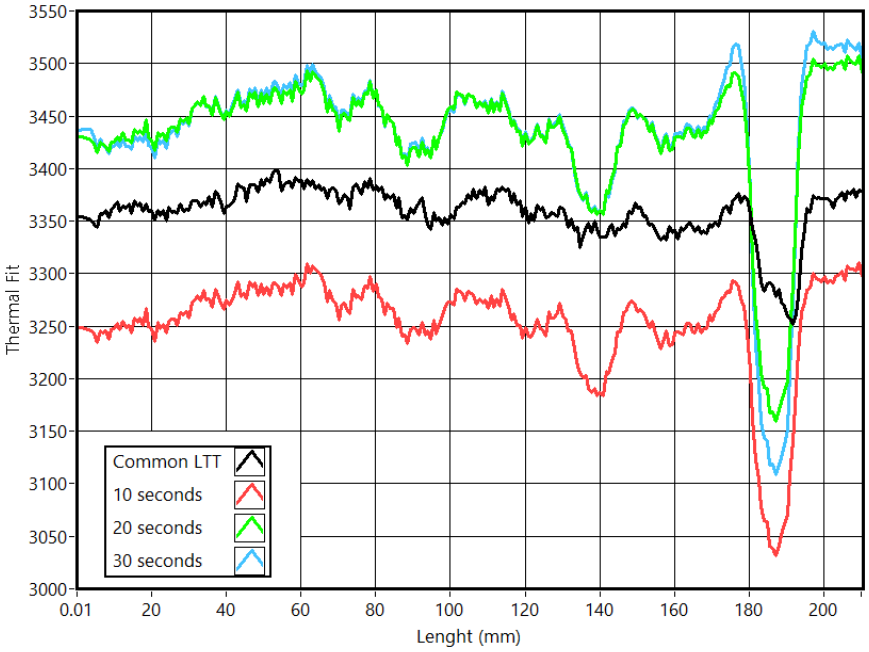

Figure 4.9: Averaged cross-section profiles for common and feedback LTT

4.3 Stimulation with PID controller

Like previously mentioned, the stimulation applied during the lock-in tests does not follow a sinusoidal profile like desired. After introducing a sensor to access the real curve of the stimulation and its impact in the results, the next logical step is the introduction of a controller that ensure the stimulation will have the desired profile. In this sub-chapter will be presented the setup, results and analyses of this implementation.

4.3.1 Setup and PID settings

The implementation of the PID controller required some alterations. Introducing a PID controller, implied a direct control of the NI module. Since the software IRNDT required the connection to the referred module, a second module was installed. This way, the NI 6251 (2) module presented in figure 4.10 acts as a dummy for the IRNDT software. Simultaneously a custom LabVIEW™ script controls the module NI 6251 (1). This script receives the light sensor signal and calculates the correct output using a PID controller implemented in the software. The thermal camera is directly connected to the computer and the power box is connected to the module NI 6251 (1). The characteristics and dynamic response of the system has already been presented.

Similar to the other tests, here the sample and stimulation were maintained in place using an aluminium structure and the sample was held in a vertical position. In these tests were analysed the same two samples presented in the previous section. Here, the tests also consisted in three different stimulations, with cycles of 10, 20 and 30 seconds. The main goal of these tests was to study the influence of a real sinusoidal wave in lock-in thermal testing.

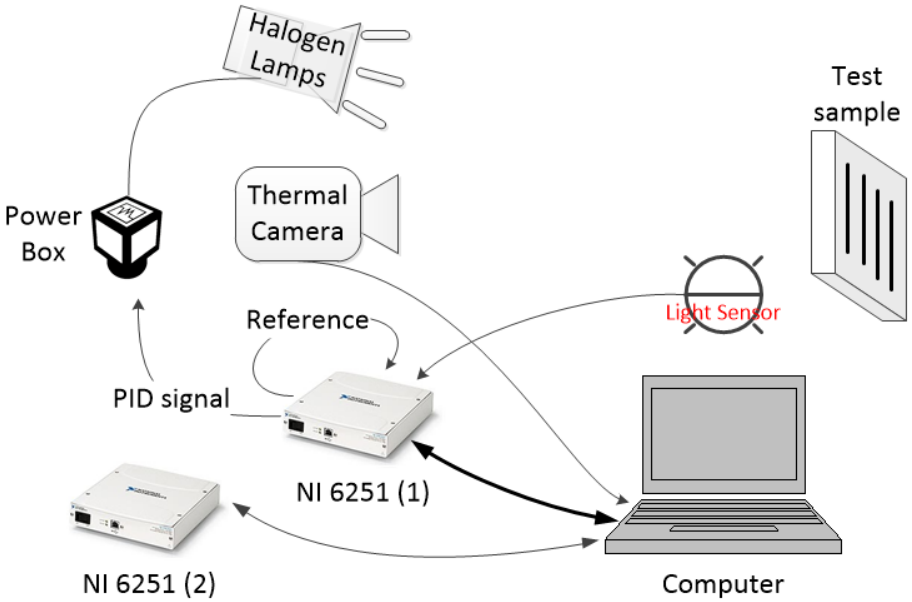

Figure 4.10: Setup of the thermal tests using the PID controller

4.3.2 Temperature results

At the first impressions the temperature readings and the amplitude responses were considerably similar. Like observed previously, the temperature responses can be divide into two frequencies, one corresponding to the stimulation cycles and the other to a exponential decay. Once again the temperature at the slots revealed a lower amplitude due to the stimulation, when compared with a sound area (figure 4.11a). The readings at the slot area revealed a lower amplitude, but a higher dynamic response from cycle to cycle. This was also observed in the feedback tests.

For the test of 30 seconds per cycle (figure 4.11b) the temperatures during a test were also very similar to the ones obtained with feedback. In the slots were observed smaller temperature variations and a rapid evolution of the global temperature. The thicker sound area presented as smaller thermal response to the global test, even if with higher temperature variations inside a single cycle. The temperature in the slot evolved faster than in the sound area. At the end of the test the maximum temperature in both points was similar. The thermal profiles at each cycle had a response that was not completely a sinusoidal wave. They evolved rapidly from the minimum temperature and right afterwards their evolution was very low, until they reached the maximum.

In the exponential decay evolution the same behaviour was observed however, the rapid variation was longer and the slower evolution shorter in time. This temperature evolution during a cycle was observed in the cycles of 10 and 30 seconds (figure 4.11).

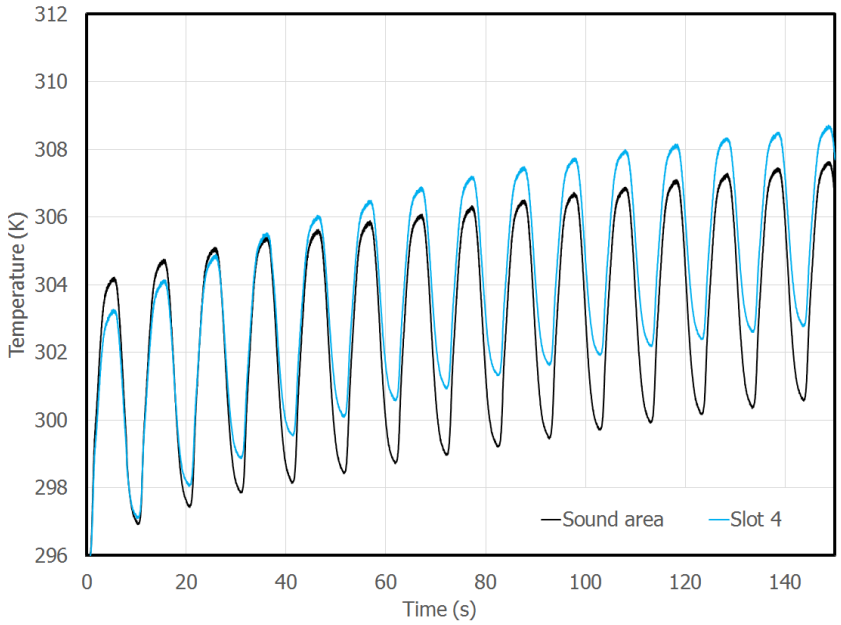

(a) Temperatures for PID test with a 10 seconds stimulation per cycle

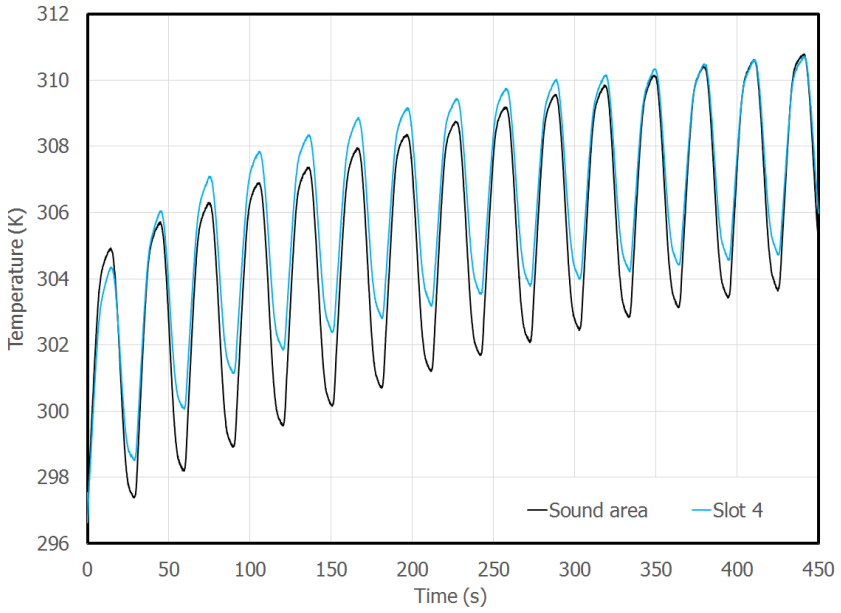

(b) Temperatures for PID test with a 30 seconds stimulation per cycle

Figure 4.11: Example of temperature curves during the thermal tests with PID controller

4.4 Comparison

Until this point three types of thermal tests were performed and analyses using optical cyclic stimulation: Common LTT, LTT with feedback and LTT with a PID controller. In the first two

types, a test with certain parameters results in the same stimulation, therefore the temperature curves will be the same. In the LTT with a PID controller, the stimulation is slightly different, being near a perfect sinusoidal wave. In this section some of the results obtained with the different types of LTT will be quantitatively compared.

4.4.1 Comparison results

The first aspect to highlight is the high similarity between the temperature profiles obtained with LTT with feedback and, the LTT with PID controller. Despite the differences in the stimulation profiles observed in subsection 4.1, in both situation the slot temperature profiles presented smaller amplitudes than the sound area, both for the same reason already mentioned. Being extremely similar, the feedback curves presented slightly lower temperatures, compared to the PID tests. Even observing in detail the temperature curves at the beginning of the tests, is difficult to identify any significant difference (figure 4.12a). In figure 4.12b is presented the temperature curves for the entire tests with a 10 second stimulation cycle. While not visible in the beginning of the test, the temperature evolution is slightly different. At the end of the test, the temperature obtained with the PID stimulation were higher than the obtained with the feedback tests (figure 4.12b). This small difference, for the slot 4, reached approximately 0.5 K, in the maximum and minimum temperature at the last cycle. In the sound area this difference was smaller reaching values of approximately 0.3 K and also presented a constant evolution during the entire test.

For the test with 30 seconds per cycle (figures 4.12c and to 4.12d) the temperature profiles were still very similar. At the beginning of the tests (first cycle), the maximum and minimum temperatures (local peaks) were the same however, the profile revealed small differences. The feedback tests presented a faster evolution than the tests with the PID. At $\frac{1}{4}$ of the period the temperature evolution presented a higher values for the feedback tests, with the temperature of the PID being almost equal at approximately $\frac{1}{2}$ of the stimulation period. Here, the temperatures reached for one cycle did not present a significant difference. This thermal response was similar in both, the slot 4 and the sound area (figure 4.12d). Even more important is to notice that the feedback profiles reached higher peaks, despite the same values in the valleys. This is present in the slot 4 and sound area temperature curves. Once again, the peaks were slightly higher in the slot 4 than in the sound area. These were the main difference between the two stimulations resulting from correction of the sinusoidal stimulation curve.

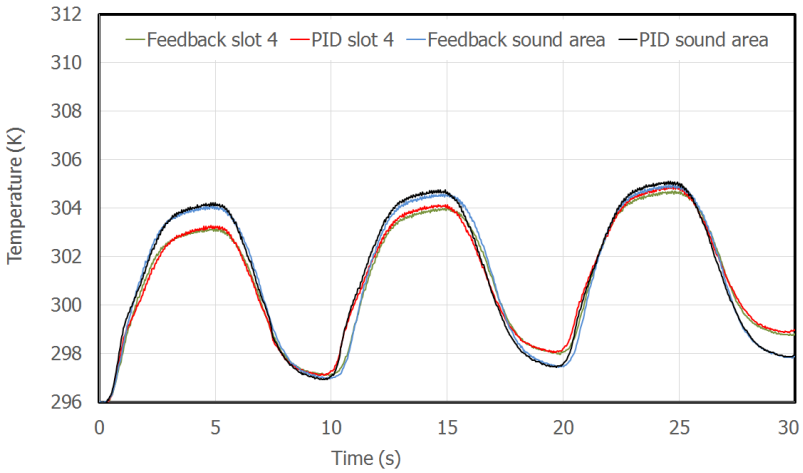

(a) Temperatures at the beginning of a 10 second cycle period

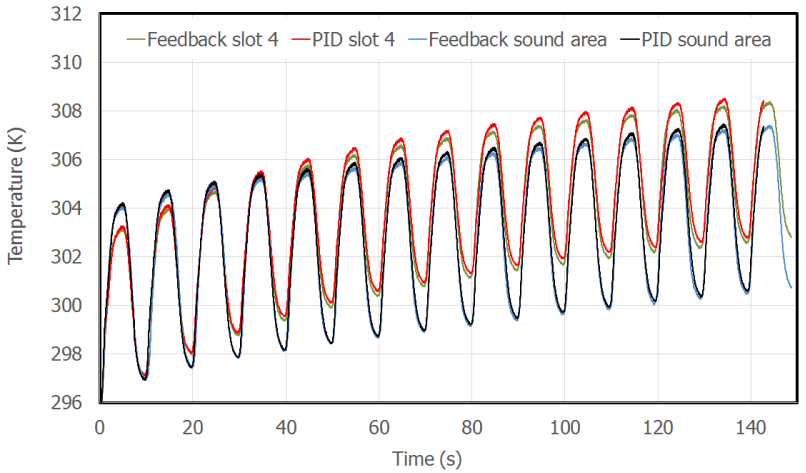

(b) Temperatures during a 10 second cycle period

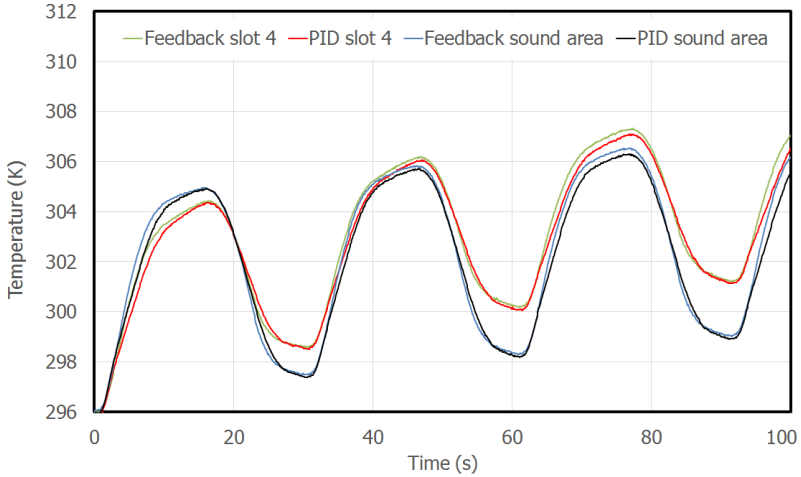

(c) Temperatures at the beginning of a 30 second cycle period

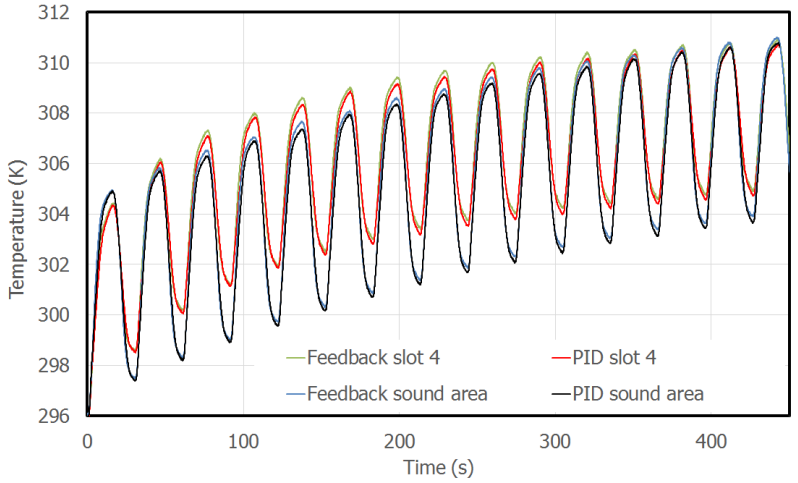

(d) Temperatures during a 30 second cycle period

Figure 4.12: Temperature of sound area and at slot 4 for a feedback and PID LTT, during the 10 and 30 second cycle period

To an easier comparison of the two tests, could be analysed only the peaks and valleys of the temperature responses, these are represented in 4.13. Like mentioned, the similarity between the feedback and PID is very great. Looking to the difference between the slot 4 and the sound area, it is observed a higher difference in the valleys when compared with the peaks. At the end of the tests, these differences tend to decay. The peaks reach an equilibrium at the end of the test (after 14 peaks). The valleys presented a similar behaviour however, the slot 4 and sound temperature did not reach an equilibrium after 15 cycles. Looking at the curves tendency, approximately 20 to 22 cycles would be required to reach an equilibrium point. In figure 4.13 the four upper curves represent the peaks and the lower the valleys.

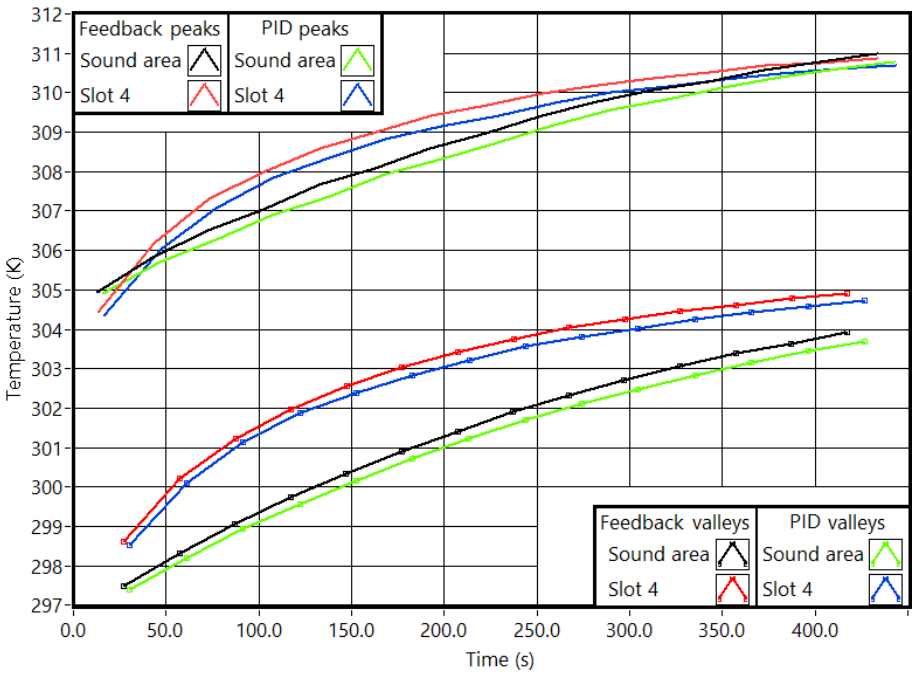

Figure 4.13: Peaks and valleys observed during the tests

Similar to the observed previously, the common LTT do not present amplitude values of the same magnitude, when compared to the tests that use feedback or the PID controller. To compare the three test among themselves, the three main average profiles were normalized (figure 4.14). Here are presented the normalized curves for the Common LTT, feedback LTT and LTT with PID, all for cycles of 20 seconds. Like expected after the observing the temperature profiles of the slot and sound area, the feedback LTT and the LTT with the PID controller, present average profiles almost identical. Apart from a small offset in the LTT with PID, the two profiles are almost overlapping each other. Again, the common LTT present smaller variations in the slot areas. More precisely, the third slot is almost imperceptible, despite being the amplitude averaged profiles. The second slot, while completely imperceptible in the common LTT, is lightly visible in both the feedback LTT and in the PID-LTT

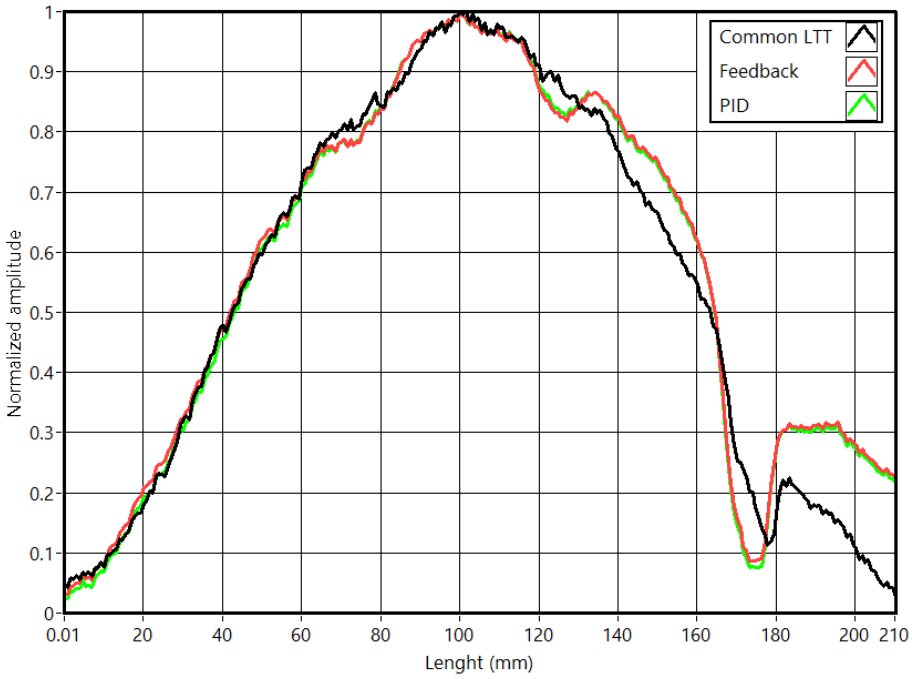

Figure 4.14: Common LTT, feedback LTT and LTT with PID normalized profiles (cycle period of 20 seconds)

Another comparison could be made by multiplying all the curves for a value in order so that the noise was equal in all the curves, like previously performed in 4.9 and also in the following figure 4.15. Here, the low frequencies present in the images were also removed. This result is presented in figure 4.15. The lower sensitivity of the common LTT was already mentioned, but here, once again the other two tests revealed a high similarity. In figure 4.15, the detection of the third slot is evident, with the second being slightly visible, contrary to what happens in the common LTT. To quantitatively compare the three methods, a high-pass filter was applied to the three curves presented in 4.14, being the result presented in figure 4.15. The high similarity between the feedback LTT and LTT with PID is evident and the lower response of the common LTT is here even more evident.

4.4.2 Comparison analyses

Like mentioned previously, using halogen lamps to apply a sinusoidal wave may result in a different stimulation waveform. This means that the recorded infrared thermal data will be the component response to undetermined wave and not the sinusoidal wave used as reference. Thus, when conducting a lock-in thermal analyses, the reference wave used to calculate the amplitude response and the phase delay will be different from the one that actually was applied. For this reason it was expected and confirmed by the results an inferior sensibility by the common LTT.

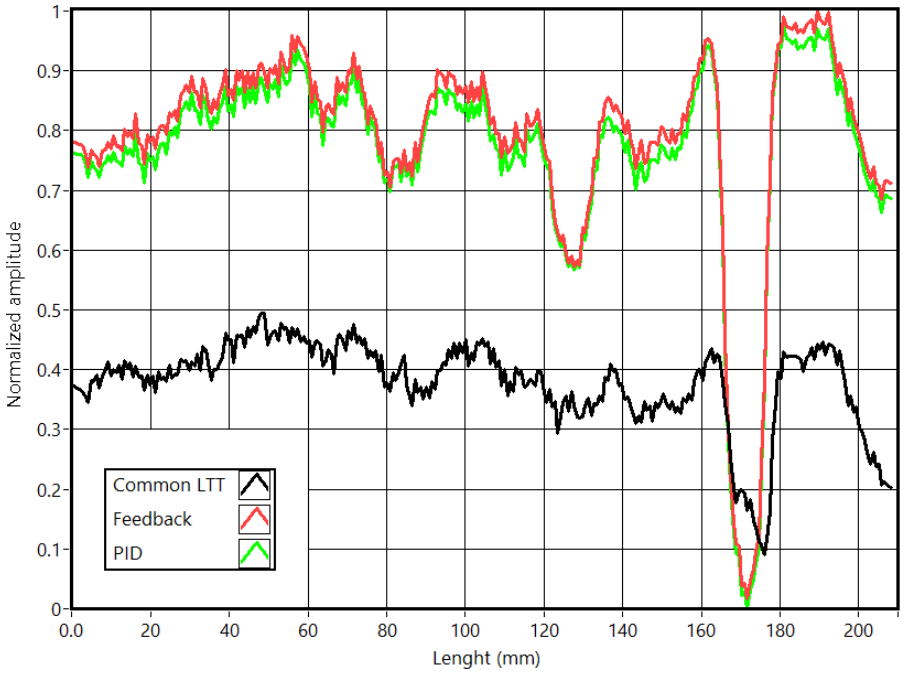

Figure 4.15: Common, feedback and LTT with PID, normalized profiles with high-pass filter

To objectively compare the three methods it were compared the response (amplitude) in the slot 4 area. The maximum, minimum and amplitude data corresponding to the slot 4 presented in figure 4.15 are presented in table 4.1. The amplitude is the difference between the maximum and minimum values of the refereed sections. To quantitatively compare the three tests, the amplitude of each test was divided by the amplitude of the common LTT (table 4.1, sensibility ratio). Although other methods may exist to access the sensibility of an infrared thermal analyses, like the ones used by Terumi Inagaki or others refereed by Minkina, this gives a rapid and considerably objective comparison between the three tests [124, 133]. The tests using the feedback signal and with the PID controller revealed a sensitivity gain of 2.4 times over the common LTT. Following the proximity and similarity of the temperature curves in the feedback and PID tests, the relative sensitivity gain was expected to be very similar, like it was observed.

Table 4.1: Values of the several normalized LTT, for slot 4

Type of LTT	Maximum	Minimum	Amplitude	Sensibility ratio
Common LTT	0.479	0.108	0.371	1.00
Feedback LTT	0.961	0.049	0.912	2.46
LTT with PID	0.945	0.041	0.904	2.44

Since the program IRNDT does not allow the calculus of the image corresponding with the phase delay using an external wave, it was not possible to compare the phase data of the three test.

The phase image, accessible in feedback test, uses the same method applied in the common LTT, this comparison is irrelevant. On the contrary, the LTT with a PID uses a different stimulation, far more resemble to a sinusoidal wave. This manner, the usage of an ideal sinusoidal wave as a reference (in the calculus process of the IRNDT program) introduces less errors than in the common LTT. In figure 4.16 is represented the phase averaged cross-sections for the common LTT and LTT with PID. At the LTT with PID was applied a gain so the existing noise was equal in both phase images. An offset was applied, so the two phase profiles would have beginning, in this case zero. This was performed only to have a direct comparison of the two averaged phase profiles and access its sensibility. The slot 4 was once again the most easy to identify, observed in both phase profiles but, clearly more visible in the LTT with PID. Again the third and second slot are well identified in the LTT with PID, contrary to what happens in the common LTT phase profile. In the LTT with PID, the valleys, located at the slot positions, present an amplitude proportional to the slot depth. This profile also presents far less oscillations than the common LTT.

Since the commercial software did not permitted the determination of the phase delay image using a feedback signal, an important question remains unanswered. Does the phase delay in the feedback tests presents the same level of improvement observed in the LTT with PID test. Observing the similarity in the temperature response of the feedback LTT and the LTT with PID, it is expected very similar phase responses from the two tests. This idea is enhanced by resemblance of the amplitude results of both tests, despite being independent and performed in separate occasions.

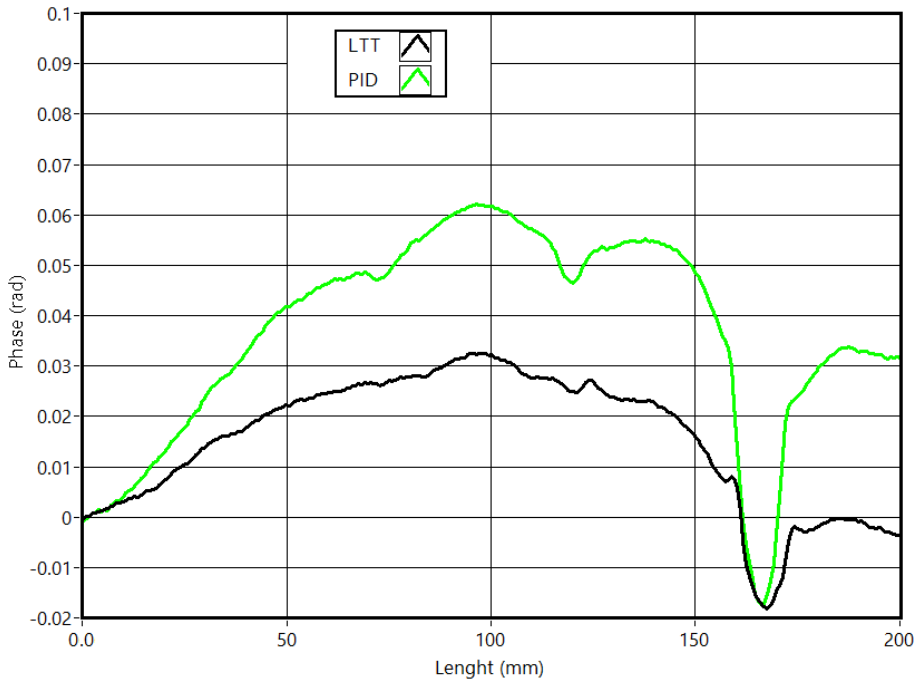

Figure 4.16: Comparison of the phase average profiles

4.5 Conclusions

In this chapter the optical stimulation was characterized. This was necessary and important because no literature have been found in the field of lock-in thermography referring to this matter. Despite only one system have been tested, most certainly, the other commercial systems present similar dynamic responses.

The used optical stimulation revealed difficulties is providing sinusoidal stimulations with frequencies higher than 0.27 Hz, corresponding to a period of approximately 3.7 seconds. In situations that presented a transient variation, it was necessary near one second to reach the desired value. Overall the stimulation presented higher responses to step-up than to step-down signals.

Since a desired stimulation did not correspond to the real stimulation being applied to the objects under analyses, it was necessary correct this aspect. Two approaches were implemented: the usage of the real stimulation (measured by the feedback sensor) in the analyses and the creation of a stimulation that is closer to the desired waveform. These two approaches were tested using sinusoidal waves.

The local temperatures of slot and sound area, despite of their different thermal resistance, reached similar temperature values after approximately 7 minutes, like was observed in the cycles of 30 seconds. The usage of the real stimulation in the analyses processing revealed excellent results. The slots sensibility was greatly improved and some slots that were not visible with the common LTT were identified in the amplitude responses.

After the improvements with the introduction of the feedback signal, it were expected bigger improvements in the sensibility by using a PID controller to create a real sinusoidal wave. This was not observed and the variations in the controller parameters did not alter the results. The temperature variations and consequentially the amplitude response in each pixel were extremely similar to the ones observed with the feedback system. Consequentially the sensibility of this new implementation was very similar to the obtained with the feedback LTT.

Unfortunately, using the commercial software it was only possible to calculate the phase delay images. Therefore, it was impossible to calculate the phase delay and access any improvement provided by these two alterations to the system. In conclusion, the usage of a real sinusoidal wave may be irrelevant. On the contrary, a correct and exact correspondence between the stimulation applied to the object under analyses and the wave used as reference used by the software is imperative.

Chapter 5

Thermal Tests Simulation

In this chapter it will be presented the numerical simulations of the thermal tests. The simulations follow the rules existing in heat transfer models used with the Finite Element Method (FEM). The numeric simulations described where performed through the implemented of several routines in Matlab® to solve the Partial Differential Equations (PDE).

The first section presents assumptions and approximation to the laboratory tests. The mesh used and some parameter settings are also described here. A brief comparison of some different meshes, and its simulation results are also illustrated and analysed.

In the second section are presented the simulations of the transient thermal testing. Here several simulations are presented to evaluate the stimulation periods influence in the temperature results. At the end of this subsection is presented a polynomial regression, providing the influence of the stimulation period for a generic sample, despite its thickness.

The third and last subsection follows the procedure and analyses methodology executed in the TTT, however here is relating the LTT. The main focus of this subsection was the influence of the cycle period in the amplitude and phase profiles and consequently their corresponding images. At the end, equations are presented to predict the results for a LTT for a sample with a thickness up to 10 millimetres.

5.1 Mathematical models

5.1.1 System governing equations

The simulations performed and described in this chapter intended to create the bases to develop a model that mimics laboratory tests. The objects under analyses were the samples used in tests, previous described in chapters 3.2, 3.3 and also presented in higher detail in appendix B. In figure 5.1a is presented a 3D model of a generic sample used in the simulations[1].

The main goal of the simulations was to obtain the temperature variations in the sample front surface to its interior. With the slots having a uniform geometry, vertically oriented and with the sample being isotropic, this vertical dimension may be discarded (Z dimension in figure 5.1a). As a result, the sample may be simplified into a two dimensional shape corresponding to a cross section, similar to the one resulting from the section cut in figure 5.1a and illustrated in more detail in figure 5.1b.

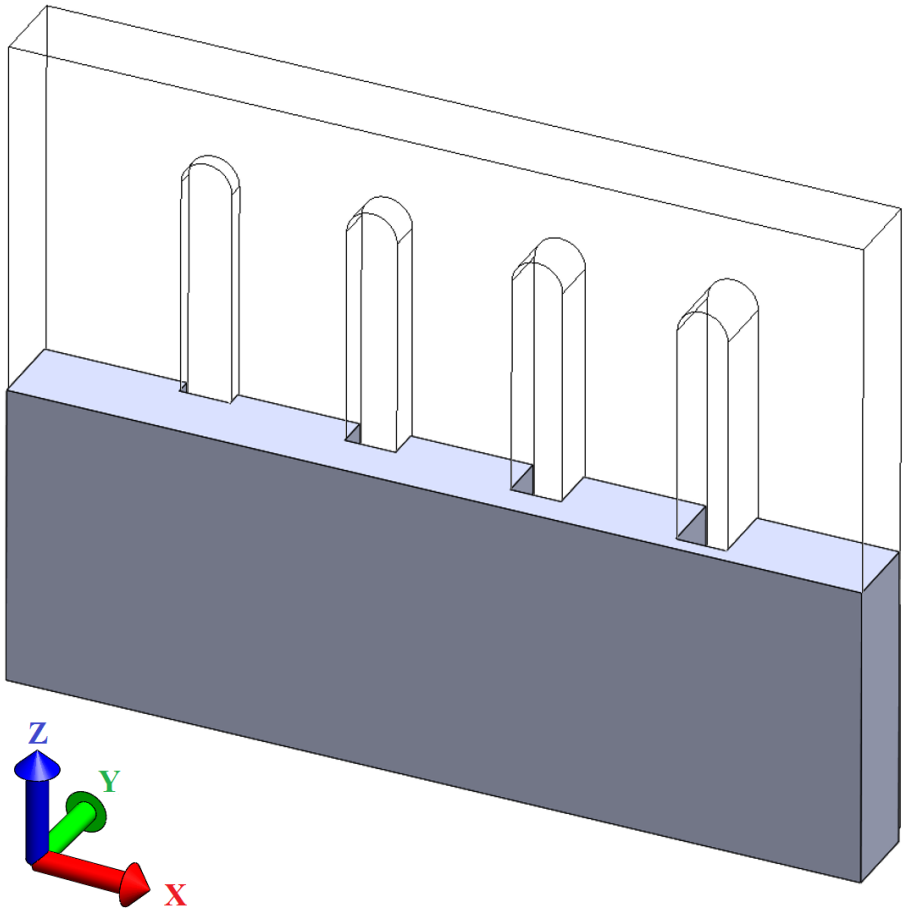

(a) Cross section of the sample

[1] sample thickness and slot width increased to improve visualization

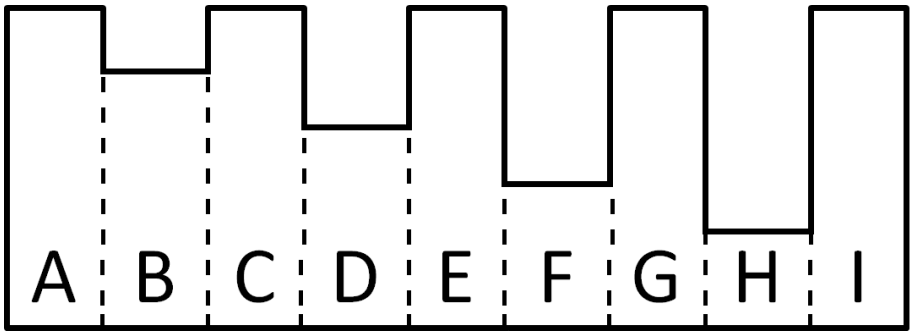

(b) Scheme corresponding to the sample division in sections

Figure 5.1: Sample to be simulated

To assure this approximation is accurate, is necessary to analyse the heat transfer involved during a sample thermal test. As the sample is warming, appears a vertical air flow due to the natural convection. Analysing the Rayleigh number (Ra) is possible of identify the type of convection occurring (laminar or turbulent) and if the dominant heat transfer is by convection or conduction. This may be calculated by multiplying the Grashof number by the Prandtl number. In the case of a simple vertical plate, herein discussed, they can be calculated using equations 5.1 and 5.2 respectively. With these results is obtained a Ra of 3.84E+6, thus is inside the limits of a significant laminar flow (10^1 and 10^9). This means the air flow during a thermal test is significant, like expected with the results obtained in the third chapter, more precisely visible in figure 3.21.

$$Gr = \frac{g\beta(T_s - T_\infty){L_c}^3}{\upsilon^2} \quad \Rightarrow \quad Gr = 5.39E6 \tag{5.1}$$

$$Pr = \frac{C_p \mu}{K} \quad \Rightarrow \quad Pr = 0.71 \tag{5.2}$$

Where:

υ	Kinematic viscosity, 15.68E-6 $(\frac{m^2}{s})$
T_s	Temperature at the sample surface, 306.5 (K)
T_∞	Ambient temperature, 296.5 (K)
β	Volumetric thermal expansion coefficient, 3.3E-3 $(\frac{1}{K})$
L_c	Characteristic length, 0.16 (m)
C_p	C_p is the specific heat, 1005 $(\frac{J}{kg \times K})$
μ	Viscosity, 1.857E-5 $(\frac{kg}{s \times m})$
K	Thermal conductivity, 0.0262 $(\frac{W}{m \times K})$

An accurate model to calculate the heat transfer coefficient was proposed by Churchill and Chu in 1975 [192]. This model requires the previous calculation of the Rayleigh number (Ra) and the Prandtl number (Pr) and is calculated as illustrated in equation 5.3. From the study of the free convection, if the Biot number is less than 0.1 the temperature gradients inside the sample due to the convection heat transfer are irrelevant (equation 5.4).

$$h = \frac{K}{L_c}\left[0.68 + \frac{0.67 \times Ra^{1/4}}{\left[1 + (0.492/Pr)^{9/16}\right]^{4/9}}\right] \quad \Rightarrow \quad h = 3.84\,(\frac{W}{m^2K}) \tag{5.3}$$

Thus is obtained a Biot number of:

$$Bi = \frac{hl}{K_{PMMA}} \Rightarrow \quad Bi = 0.08 \tag{5.4}$$

Where:

l	Sample thickness, 4.5E-3 (m)
K_{PMMA}	Thermal conductivity, 0.21 $(\frac{W}{m \times K})$

As expected, with the convection heat transfer coefficient h, is calculated a Biot of 0.08, thus being less than the established limit of 0.1. This guaranties the vertical temperature gradients inside the sample due to the natural convection are insignificant and any temperature patterns are a direct result from a defect or slot. Therefore the simplification of using a two dimension horizontal surface is a good and correct approximation. This section is illustrated in figure 5.1a where it was selected the cross section passing in the middle of the sample. The cross-section was chosen to maximize the distance from the boundaries reducing any influence from slot boundaries.

5.1.2 Finite element method

Numeric simulations predict the behaviour of structures or components under certain conditions [193]. These are particularly useful in situations where exact solutions are unknown or are complex to obtain. Another alternative to study processes is to build prototypes and testing them. Apart from the cost, this process can also be time consuming. Simulations can also give an inside look of the components or structures, not easy in real testing processes.

The most common numeric simulation uses one of three methodologies: finite differences method (FDM), finite elements method (FEM) or finite volume method (FVM) [194]. Due to their mathematical approach these are also called the classic choices to solve Partial Differential

Equations (PDE's). The FDM uses local Taylor expansion as an approximation of the differential equations. This method present some difficulties in complex geometries [195]. In the FVM the equations are integrated in each volume, assuming a linear variation of the variables. This may lead to errors in tetrahedral meshes or in the disproportional elements [196]. In most cases, the FEM uses the weighted Galerkin's method. These are well suited and deal easily with most geometric shapes. The development of the FEM in the last years made them the most common choice in commercial simulation software [197]. Due to the robust formulation of the FEM and its flexibility for a certain given mesh, this was the selected method in this work.

The FEM bases the derivative of the equations in the following principle: the flux of u (x, t) for a certain volume V, plus the flux of u at a given frontier A, is equal to the rate of S (u, x, t) [198].

To analyse the evolution and distribution of the temperature in the samples, it should be use the Fourier's First law of heat conduction (equation 5.5). Here, q is the heat flux that enters a certain surface, K is thermal conductivity of the material, x is the distance transversal to the surface and T represents the temperature.

$$q = -K\frac{dT}{dx} \tag{5.5}$$

The simulation of a transient response is a common situation and is well described in the literature. The application of a sinusoidal stimulation (lock-in tests) could be discretized as several and different transient stimulations. Equation 5.5 is presented in its basic form and has to be expanded to match the tested sample geometries and the PDE. Considering the simplification into a two dimensional shape, is possible to describe the temperature evolution in the axis X and Y, lime presented in equation 5.6. Similar to what succeed in the laboratory tests, the temperature is dependent of the time and space. Since the vertical direction was discarded (Z axis), the geometry will be defined in the X, and Y coordinates along with time (t), this by expanding the PDE commonly use in the finite elements approximation, the final and governing equation is represented in equation 5.6. Here Q_i is the interior heat source per unitary area (stimulation), K_X and K_Y are the conductivity coefficients in the X an Y directions respectively, ρ is the material relative density and ς the heat capacity ($\frac{J}{K}$). The simulations were implemented in Matlab® and follow the methodologies described by Erik Thompson [199]. In this case, the X varies from [0-210], Y from [0-l] and t from zero seconds until the end of test, ten times the stimulation length for the TTT and fifteen times the cycle period for the LTT. At the beginning of the simulations all temperatures are equal to the ambient temperature (296.5 K).

$$\frac{\partial}{\partial x}\left[K_x\frac{\partial T}{\partial x}\right] + \frac{\partial}{\partial y}\left[K_y\frac{\partial T}{\partial y}\right] + Q_i = \rho \times C_P\frac{\partial T}{\partial t} \tag{5.6}$$

The simulated area required the definition of the boundaries conditions that mimicked the laboratory tests. Thus, was applied a natural convection coefficient to the external contour of the simulated sample. Along with the natural convection (energy output) it was required to simulate the stimulation (energy input). Corresponding the used surface (figure 5.1b) with the laboratory tests, the heat was applied in the lower line of the global contour, in these nodes it was defined a heat generation (Q_i) coefficient. Due to the uncertainty in the determining the eat applied by the halogen lamps, the natural convection and heat parameters were determined by fitting the temperature curves to the laboratory data (the results are presented in the next section). Despite the variation of the thermal conductivity for different temperatures, this variation was assumed to be vary small, this taking in consideration the temperature measured during the laboratory tests.

5.1.3 Adopted mesh

In most numeric methods, the mesh is a critical aspect of the simulation. The meshing process is responsible to divide the geometry under analyses in several elements (segments, surfaces or volumes). This can be seen as a discretization of the complete and continuous segment, surface or volume.

The creation of a mesh starts by applying a grid of points, in the case of the cross-section, the surface will be divided in quadrilateral shapes with one nodal point at each corner. The nodal points should be positioned as uniformly as possible to provide a uniform mesh. A constant spacing in the nodal points distribution will lead to an equilateral and balanced element, preventing significant errors and singularities in the shape functions. To accurately simulate any geometric variations, the elements and nodal spacing should be very small. The disadvantage of, using smaller elements is the increase in the number of nodal points and consequentially the number of equations to solve, and thus, the computational payload. In order to have a good mesh, this should be detailed for steep geometrical variations or areas that require higher precision. Areas and locations that present uniform geometries, properties and loads should have bigger elements. The study to obtain the best simplified geometry can make a difference between a good and a bad simulation and has been actively studied in the last years for several types of simulations including for surfaces and for volumes meshes [200, 201].

In this work the geometry was very simple and mainly composed by straight lines and flat surfaces. This immensely facilitated the discretization of the surface under analyses (figure 5.1a) not requiring a local mesh refinement. Thus, it was only necessary to define the number of elements and its corresponding size in each section. The cross section geometry was divided in nine different sections, like illustrated in figure 5.1b. The sections B, D, F and H are the internal areas of slots 1, 2, 3 and 4 respectively. Being critical and important areas, these require a higher detail in the simulation, analyses and corresponding mesh. Sections A, C, E, G and I separate the slots from the environment and from neighbour slots, located at the sample extremities, sections A and I are equal among themselves and a little wider than section C, E and G. These samples present

the same geometric dimensions of the sample with 10 millimetres slots (appendix C.1), changing only the thickness. The slots depth is proportional to the sample thickness. The dimensions of the sections represented in figure 5.1b are displayed in figure 5.2.

An example of the created mesh is illustrated in figure 5.2. The horizontal dimensions (*L, a, b* and *d*) were kept constants and in agreement with the test sample. The meshes were created with uniform spacing in the sample thickness (*l* and *c*). The nodal spacing in this direction is one of the critical aspects in the mesh, to obtain an accurate approximation of the temperature variation along the sample depth. Since these areas are considerably longer (dimensions *a, b* and *d* in figure 5.2), the number of elements used was defined to balance the corresponding shape functions.

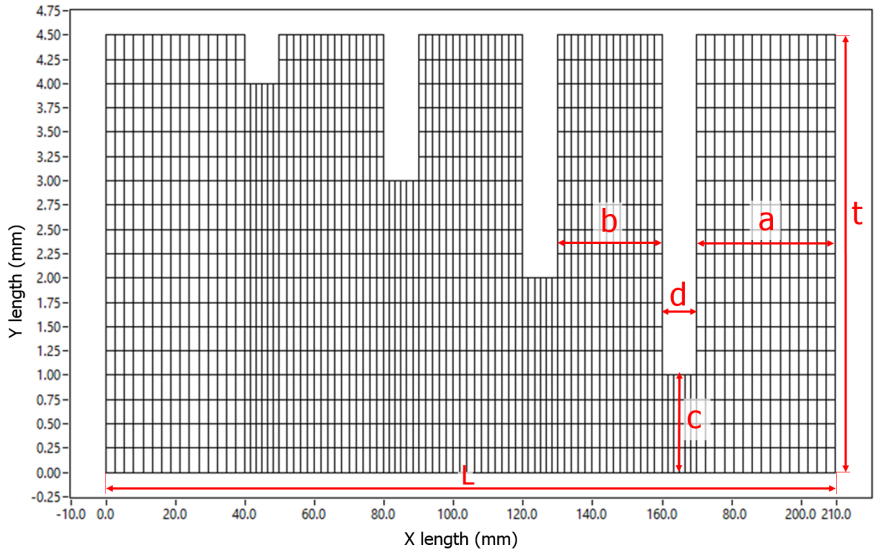

Figure 5.2: Example of mesh used in the numeric simulation with slots of 10 millimetres

Despite the number and size of the element being discussed (2D quadrilateral elements with four nodes), all of them where quadrilateral with four nodes each. To access the temperature variations in the results, resulting from number of elements, were performed several simulations, each with a different mesh. In this first analyses, all the meshes had twenty elements in width *a, b* and *d* varying in the number of elements of the length *c* and consequentially *l*. The result from these tests are visible in figure 5.3.

5.1.4 Evaluating mesh settings

In this section will be presented the results obtained by changing the number of elements in the key locations, maintaining the dimensions corresponding to the sample with slots of 10 mm in width. The temperature profiles were obtained by simulating a transient stimulation of forty seconds to all the nodes located at the X axis, and will be explained in greater detail in the next section.

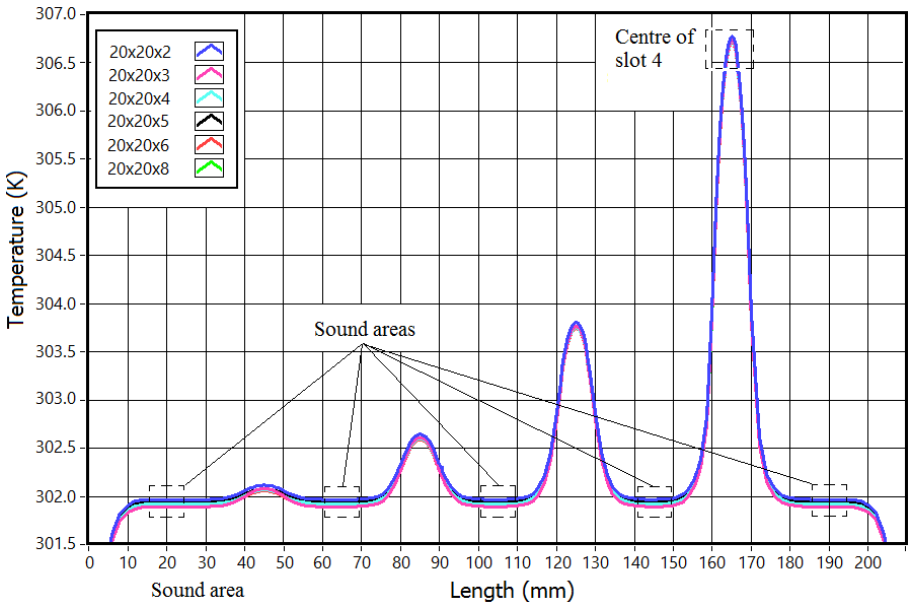

Figure 5.3: Temperature profiles in the sample, for different number of elements in the Y direction

Figure 5.3 presents an overview of the simulations results for several different meshes. The used meshes had twenty elements in sections corresponding to lengths *a, b* and *d*, thus they were named 20x20xXX. The last index (XX) of each mesh referred to the number of vertical elements used in the thinnest area (slot 4). The vertical spacing was keep constant in all sections. Some small temperature differences are observed, mainly in the centre of slot 4 and the sound areas. Naturally for deeper slots, higher temperatures are observed and vice-versa. In figure 5.3 are also highlighted the centre of the slot four and the sound area that are referred in figures 5.5 to 5.6.

In figure 5.4 the same temperature profiles are presented, but with a greater detail in the sound areas. Here, it is possible to note small differences in the mean distance between slots. The mesh using eight vertical elements is naturally the most detailed, and therefore is used to establish a comparison. The meshes using two and five vertical elements presented comparatively higher temperatures. Using three and six elements resulted in lower temperatures. Using only four elements, produces results very similar to the ones obtained with eight elements. This may be due to a higher balance elements and thus better shape functions.

In figure 5.5 are presented the same temperature profiles, zoomed at the centre of slot 4, for different number of elements in the dimension *c*. Here, the mesh with two vertical elements was also the one that reached values with the higher differences. The mesh with six elements was the one that reached temperatures near the reference. However the mesh with four elements was also very close. Observing the results from all the meshes, it can be concluded that the four elements mesh produces here results very similar to the one with eight elements. With this information, it were used four elements in the vertical dimension, corresponding to the thickness of slot 4. This way, is avoided an exponential increase in the calculus time, when compared with usage of eight

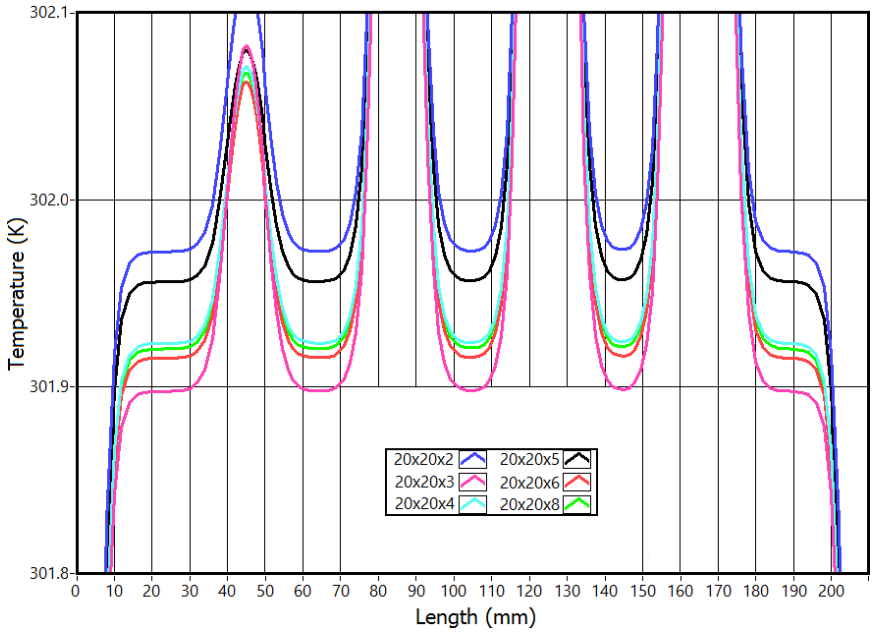

Figure 5.4: Base area temperature profiles, for different number of elements in the Y direction

nodes, without losing accuracy. The other sections had multiple vertical elements, maintaining constant the height of the elements.

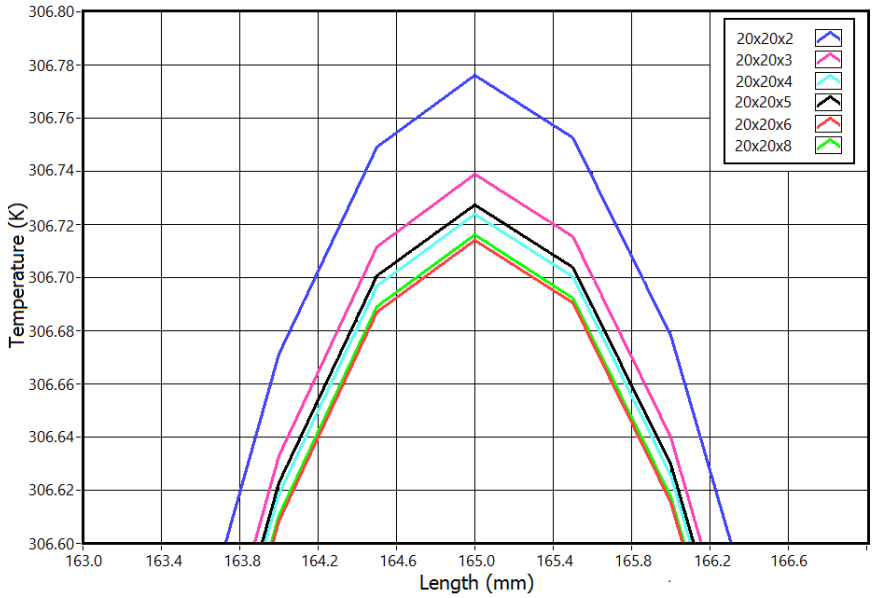

Figure 5.5: Temperature profiles for different number of elements in the centre of slot 4

It was necessary to define the number of elements to use in sections A, C, E, G and I along the horizontal direction (figure 5.1b). Here, it were performed several simulations to determine the convergence temperature and the number of elements that could lead to that value. However, the temperature differences were extremely small. This aspect can be justified by the higher thermal

resistance in the sound area. Even when observing the results with a very small temperature variations (figure 5.6), no significant variations are observed. It was then decided to use 20 elements. This way, the elements had a maximum ratio of 10 between the height and length of the element.

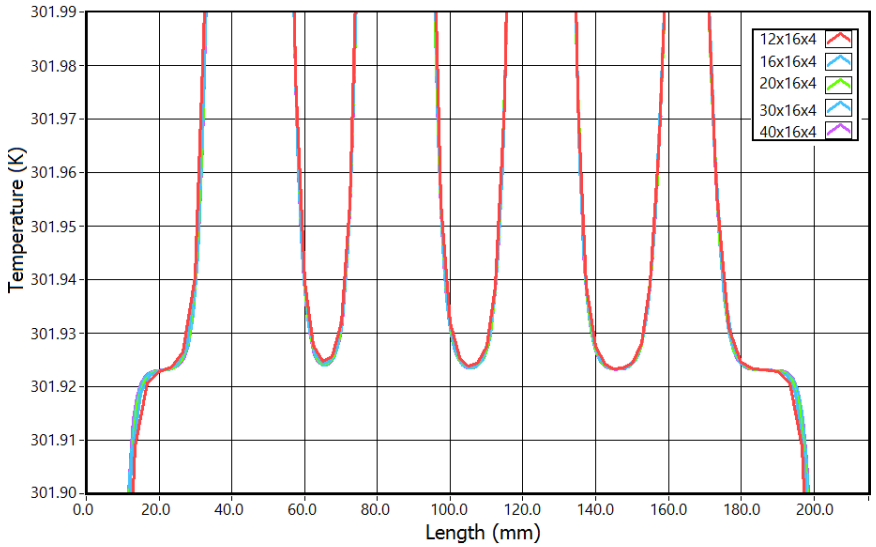

Figure 5.6: Temperature profiles for different mesh in the area between slots

The next step was to evaluate the influence of the number of elements in the horizontal direction (dimension d in the X axis) of sections B, D, F and H. Here the number of elements along the Y direction was maintained at four elements. Figure 5.7 shows the results at the centre of slot 4. For these simulations the difference among the several meshes was a little higher than previously observed. Additionally, the temperature at the centre of the slot decreased with the increasing number of elements. This requires a detailed observation of the temperatures. The temperatures of each mesh were compared with a simulation that use 40 elements in the referred areas. It can be observed that this temperature converges to the value of 306.7 K. The temperature variation from meshes 16 to 20 is considerably smaller than from meshes 12 to 16. This variation indicates a convergence in the temperature results for the mesh with 16 elements or higher. Thus, the number of elements that will be used in the simulations along the slot length is 16 elements.

In the third chapter were analysed two tests, Transient and Lock-in thermal tests. The next two main sections present the simulations relating these two approaches. The first simulation relating IR NDT technique presented is the TTT (chapter 5.2) followed by the simulations of LTT 5.3.

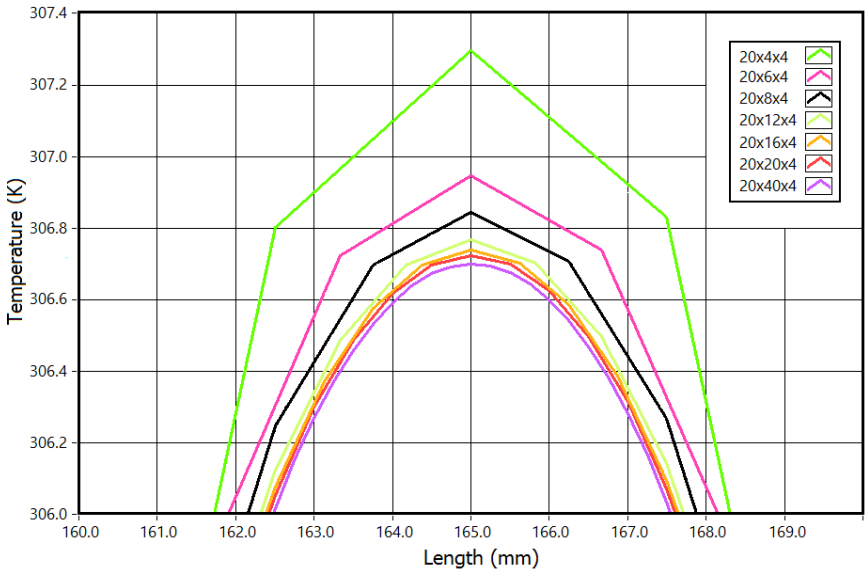

Figure 5.7: Temperature profiles for different meshes in the mean area of slot 4

5.2 Transient test simulation

5.2.1 Introduction to the simulation

The simulation of the TTT followed the procedure and mathematical model described in the previous section. Similar to the stimulation used in the experimental tests, the stimulation started with a maximum value that was maintained during a certain period of time (stimulation period). The simulations lasted for ten times the stimulus period, similar to the performed in the laboratory tests. Thus ensuring that the sampled had time to recover and all of the most relevant information was recorded and analysed.

In the laboratory tests measured the temperature distribution at the entire surface of the samples (reflection mode) and the analysis were performed mainly observing averaged horizontal profiles along the X axis. In the stimulations it was evaluated the temperature distribution through the sample, from the stimulation surface to the opposite side. Then, the only common zone in the two geometries, is the stimulation boundary, where the stimulation was applied. To validate the simulation settings, the results where compared with the laboratory tests previously analysed. In figure 5.8 it is represented an example of two temperature evolution, the black corresponds to the simulation and red to the laboratory (real) tests. These curves correspond to the centre of slot 4 from a TTT with a stimulation that lasted for 20 seconds. Similar to all the simulations, the end of the stimulation correspond to frame 3000 (visible in figure 5.10).

Like previously mentioned (chapter 3.2), the phase during which the simulation is being applied, introduces a considerable amount of reflected radiation. Thus, the analyses is only performed during the cooling phase. The higher temperature difference between the real and

simulation curve is observed at frame 300, which is exactly the first image after the end of the stimulation, thus is already considered the cooling phase. Due to the low dynamic of the stimulation source, some stimulation (reflected radiation) is still observed in the cooling phase. This justifies that higher temperatures maybe measured in some frames immediately after the image 300. The remaining temperatures are extremely similar, namely after frame 340. For stimulations with other stimulation periods and sample frequencies, small changes can be observed. As it can be observed, the simulation results match very well with the laboratory data.

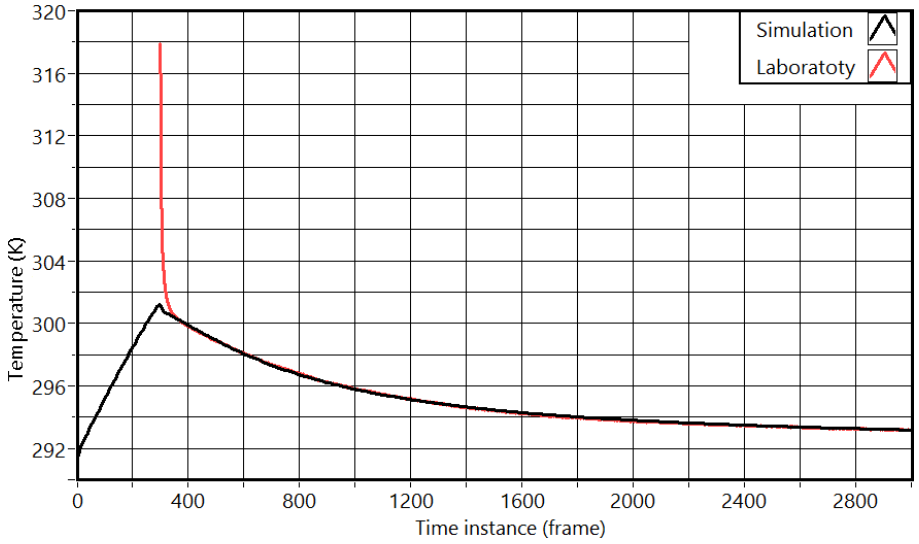

Figure 5.8: Temperature obtained in laboratory and by simulation, for a stimulation of 20 seconds in the central point of slot 4

In figure 5.9 are illustrated two temperature profiles at the stimulation boundary, obtained from a transient test of twenty seconds (average cross-section temperature profile of a laboratory test and the temperature profile of the corresponding simulation). These where obtained from frame 350, that corresponds to approximately 3.5 seconds after the stimulation end, when stimulation is completely off [2]. This assures the temperature measurements were not influenced by any reflected radiation. The alignment of the two profiles was accomplished by cropping the temperature image (similar to the described in chapter 3.2) and scaling its length (in pixels) to 210 millimetres corresponding to the real measures. This procedure was described in the previous chapter 3. Through the entire length of the profiles, it is observed a great similarity between them. The simulation presented a fairly uniform temperature throughout the entire sound areas. In the laboratory profile is observed a slightly smaller temperature at the extremities of the sample. This is a common situation in infrared thermal imaging due to some imperfections in the calibration, mainly in the offset matrix. Naturally, these are not observed in the simulation profiles.

[2]This aspect can be easily observed in figure 4.4h

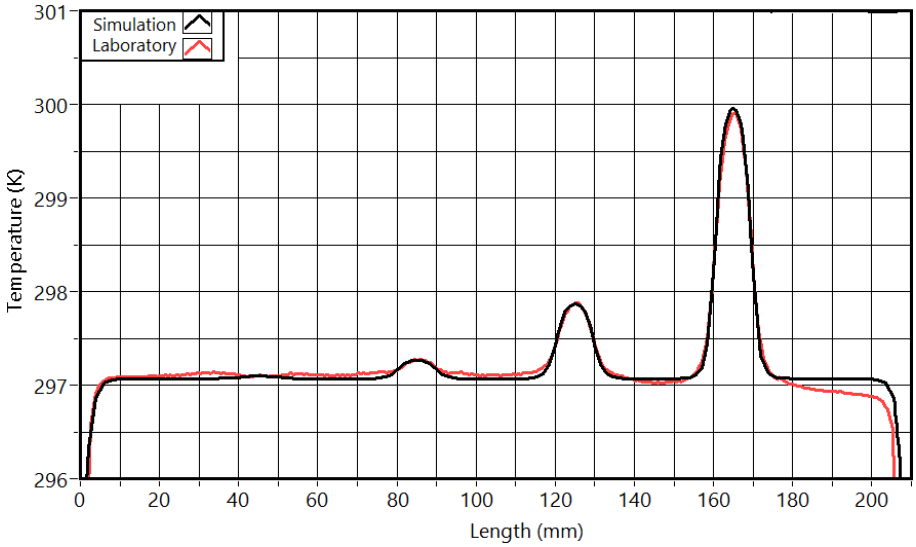

Figure 5.9: Temperature profiles at frame 350 for the stimulation of 20 seconds

5.2.2 Results

The temperature response at a transient stimulation is a well-known situation for several materials and some simple geometries, therefore some of the obtained results were expected. The equations governing the temperature were presented at the beginning of this chapter, and from these, a negative exponential can be predicted (equation 5.6). This temperature evolution should be present in the warming and cooling phase, as it was observed. The magnitude of the decay at each point should produce different thermal patterns at the stimulation area. The difficulty was to predict the result of the temperature profiles at the stimulation surface during the cooling phase.

Figure 5.10 presents the temperature evolution obtained by simulation, corresponding to the temperatures at the centre of slot 4. In the sub-figures, the vertical axis is presented in auto-scale to improve visualization. The application of the stimulation creates an increase in the temperature of the sample, which will continue to raise until the end of the stimulation. The first and most obvious observation is that, a longer stimulation results in a higher maximum temperature. The maximum temperature is naturally observed at the end of the stimulation, corresponding to frame 299 in all the tests. This is observed for all the stimulations, ranging from 0.03 to 90 seconds. At the end of the stimulation, the temperature of the sample starts to decrease. This is due to the natural convection flow resulting from the temperature difference between the sample and the environment. This heat transfer will stop when the sample reaches a stable temperature and an equilibrium with the environment.

Shorter stimulations deliver less energy to the samples (figure 5.10a), this results in a smaller temperature range and minor convective flow, thus smaller temperature gradients over time. As the stimulation period increases the maximum temperature also increases, like is easily observed in figure 5.10, and particularly 5.10b. This intensified the convective heat flux at the beginning

of the cooling phase. At shorter periods and lower temperatures, the exponential decay is fairly identified. As the stimulation time increases, the temperature evolution also suffer some small modifications. After the end of the stimulation (frame 299), a fast temperature drop (longer stimulus in figure 5.10c - a quick drop is observed). After some frames, a change in the temperature decay is observed, becoming smaller. For the longer stimulations (figure 5.10d), the variations are gradually diminishing.

In figure 5.10 some curves that reach higher temperatures intercept curves where its maximum temperature is lower. This succeeds because the time step in each curve is different and does not mean that the temperature variation is higher. This aspect is particular easily observed in figure 5.10c and 5.10d where all the curves intercept each other at frames 700 and 450 respectively.

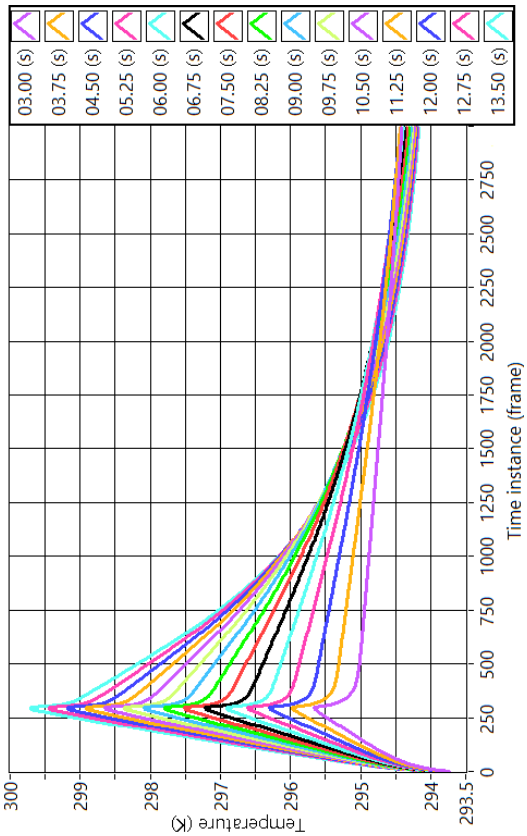

(b) Temperature for stimulations of 3 to 13.5 seconds per cycle

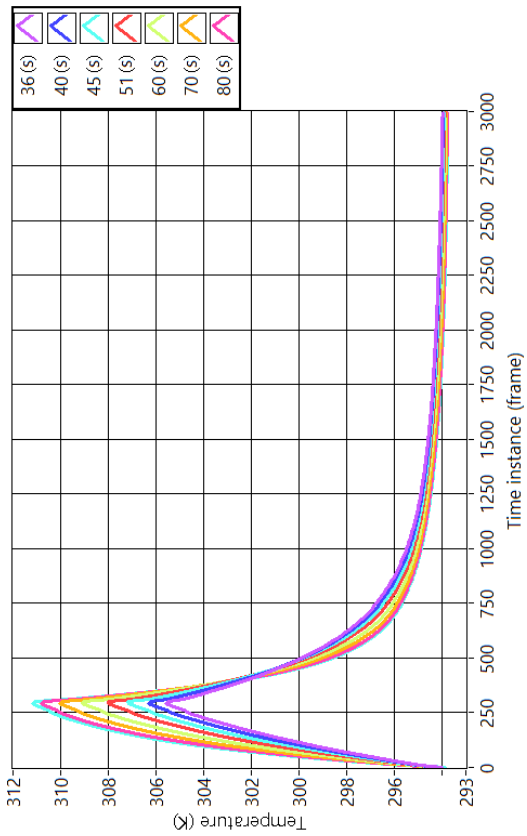

(d) Temperature for stimulations of 36 to 80 seconds per cycle

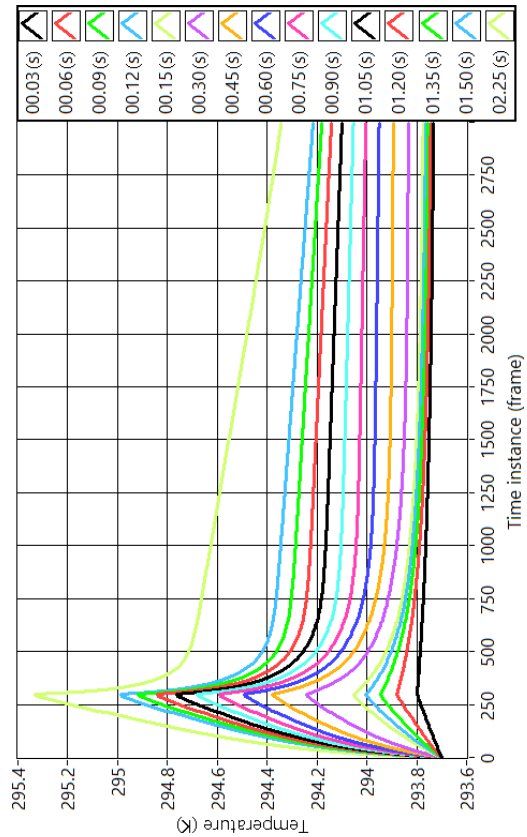

(a) Temperatures for stimulations of 0.02 to 2.25 seconds per cycle

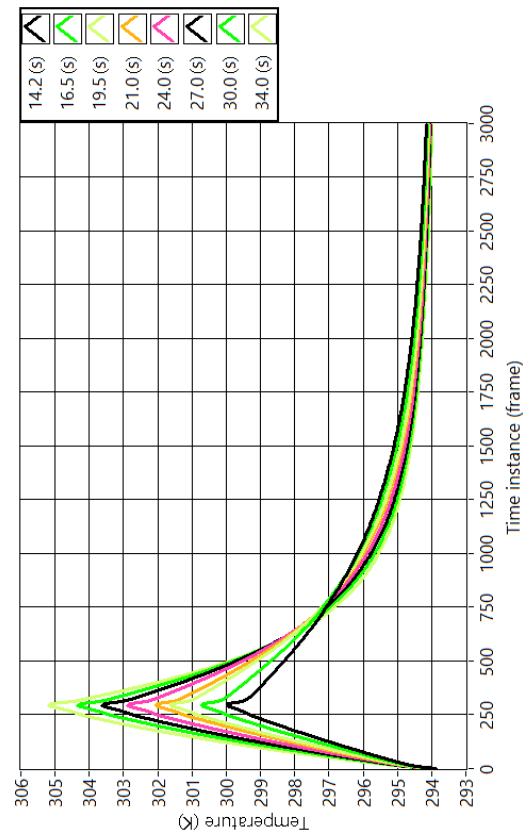

(c) Temperature for stimulations of 14.2 to 34 seconds per cycle

Figure 5.10: Temperature evolution at the centre of slot 4 for different stimulus duration

The maximum temperature observed during the tests is extremely important. In the laboratory tests, best results were obtained at the beginning of the cooling phase, thus preventing any reflection from the stimulation source. This temperature can represent the effect of the stimulation period. In figure 5.11 are presented the maximum temperatures for several stimulus periods, referred to slots 1, 2, 3, 4 and sound area (Ref in figure 5.11). Here two main aspect should be analysed. Firstly, the maximum temperature is constantly increasing, despite being attenuated. The second is a stabilization in the temperature difference between the slots and the reference. This difference is almost keep constant for stimulations longer than forty seconds. This maximum temperature difference for stimulations with forty seconds was also observed in the laboratory tests.

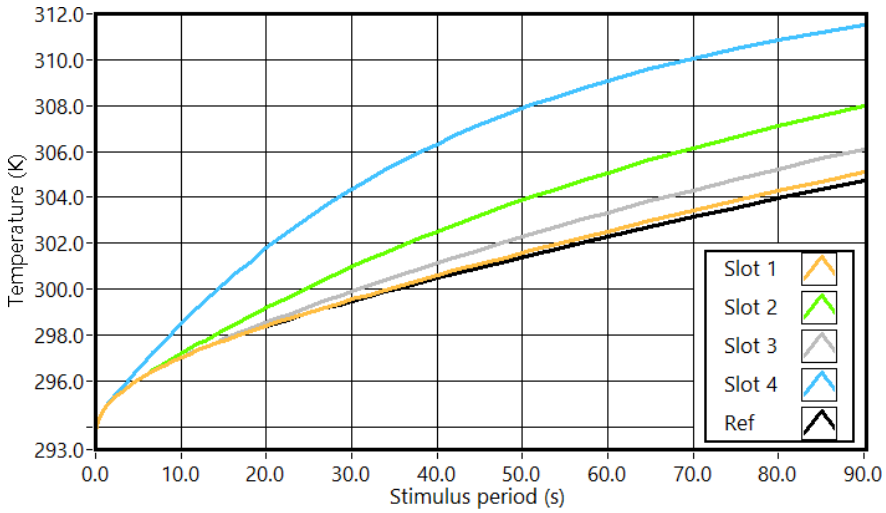

Figure 5.11: Temperature at the end of the stimulation in the centre of the four slots

One of the most important data are the temperature profiles in the surface where the stimulation in being applied, corresponding to the average cross-section profiles. These are illustrated and also divided is four groups (figure 5.12), each with a different scale in the vertical axis for a better visualization. As the stimulation period becomes longer, the temperature in the slots areas is higher. Naturally the first slot to be detected is slot 4, with a stimulation of 1.2 seconds (figure 5.12a) and slots 1, 2 and 3 with stimulations of 15, 8.25 and 3.75 seconds, respectively (figure 5.12b). With the increase of the stimulus period, the temperature differences also increased. In figure 5.12c, is clear that these are the best temperature profiles, providing a good temperature difference for the slots with good boundary definition. Increasing the stimulus duration, the temperature profiles also became less accurate in the boundaries, thus less resemble with the geometry profile. This is particularly visible in figure 5.12d, where the boundaries between the slots and the sound areas are "soften" becoming very difficult to distinguish the boundary location and even less to characterize it. With these stimulations, the temperature profiles are softer and rounder near the slot areas. The constant temperature profile at slot 4 is observed for stimulations shorter than 9 seconds. For this stimulation the third and fourth slots are fully visible. The first and second slot are fully visible with stimulations of 65 and 34 seconds respectively.

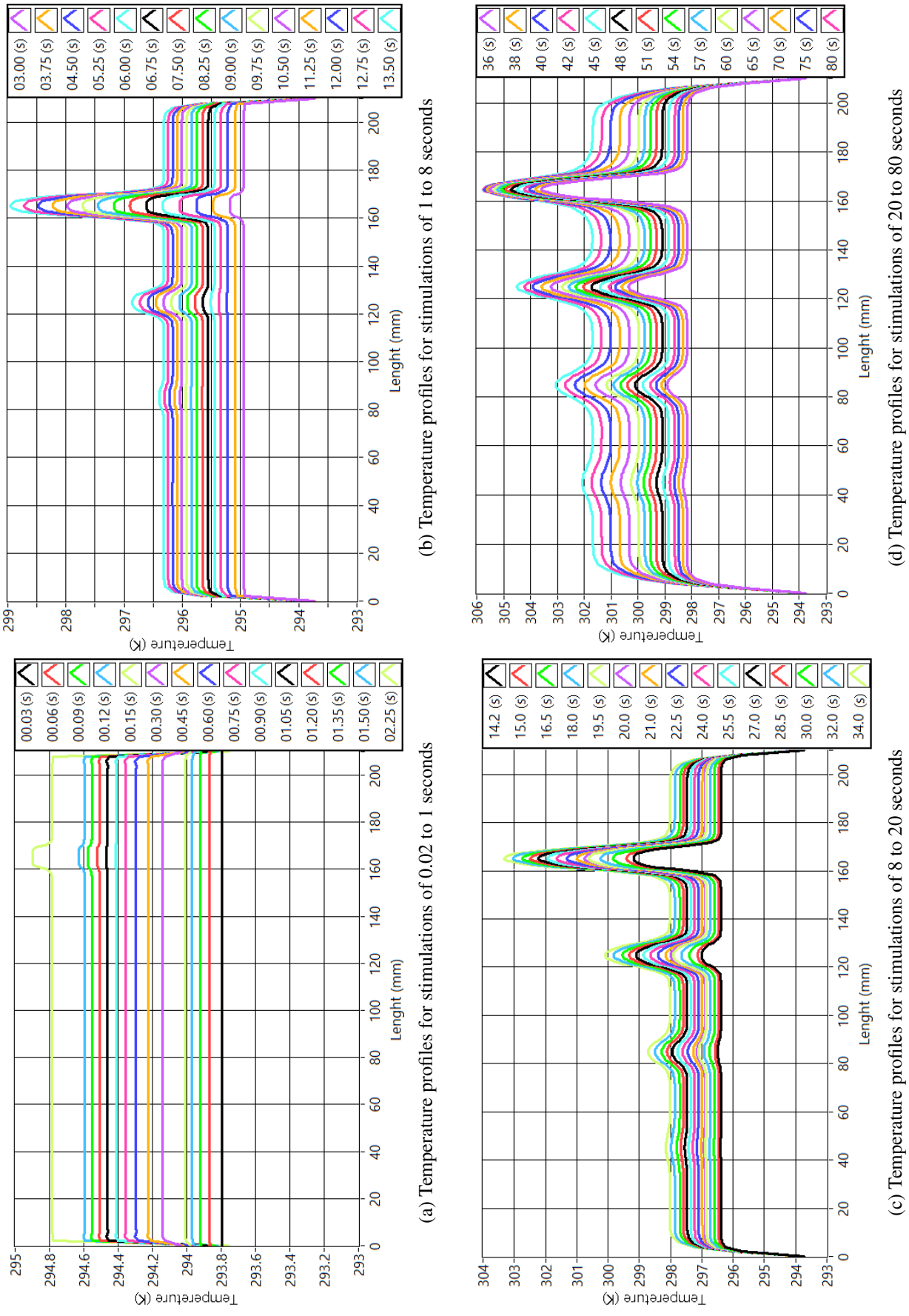

(a) Temperature profiles for stimulations of 0.02 to 1 seconds

(b) Temperature profiles for stimulations of 1 to 8 seconds

(c) Temperature profiles for stimulations of 8 to 20 seconds

(d) Temperature profiles for stimulations of 20 to 80 seconds

Figure 5.12: Temperature profiles in the stimulation boundary

5.2.3 Simulation analyses

The similarity obtained between the simulated and laboratory temperature profiles was very good (figures 5.8 and 5.9). The temperature evolution over time followed the predicted exponential decay, with the exception of the faster temperature drop exactly after the end of the optical stimulation (laboratory tests), resulting from the stimulation light slow power off.

During the stimulation phase, there is a heat flow from the surface to the entire sample. At the stimulation end, the sample will be warmer than the environment, and thus the heat flow will change from inside the sample into the environment. This will reduce the global temperature of the sample. Since the sample surface receive heat from inside, this will lead to a delay in its cooling curve, a situation not observed prior to the stimulation end, when the flux is in the opposite direction.

An area with a higher thickness results in a higher thermal resistance and consequentially in a slower temperature evolution. Globally, this evolution follows an exponential function. With the stimulation active, the temperature will increase and thus a heat flow will appear, increasing the temperature of the sample. During the stimulation phase, the energy received flows in order to reach this equilibrium temperature; at this temperature, the energy received by the sample will be equal to the loss of energy by convection and radiation. Since the deepest slots have a lower thermal resistance, it reaches the equilibrium faster. As the thermal resistance increases, the time required to reach this also increases. The equilibrium is affected by the environment temperature, the sample emissivity and the stimulation intensity. The ideal test should provide the highest temperature difference between locations with different thermal resistances, this can be achieved with the correct stimulation period.

Usually the rate at which the temperature increases in the stimulation phase is higher than the rate that the temperature decreases in the cooling phase. This means the energy applied by radiation is more intense than the heat released by radiation and convection in the cooling phase. Thus, the temperature variation and its differences will be slower in the cooling phase, thus they will be easily observed. With the increase of the stimulation period, the slots differentiation will increase until a certain point, after which will decrease. However this does not mean that a maximum difference is the optimum stimulation time period. This because in most real situations the defects do not present a boundary so well defined as the slots. Thus, the identification of the defect boundaries is also very important. Looking at figure 5.12 is easily observed that longer stimulations lead to a poor identification of the boundaries, despite a decrease in the differentiation not being observed (figure 5.11). Comparing the temperature profiles in figure 5.12d is observed that the benefits of using a stimulation longer than 40 seconds are very small. Indeed the boundaries will become difficult to identify, like suggested by the results of longer stimulations in figure 5.12d.

In figure 5.13 the temperatures are illustrated at the surface for six different stimulations. Shorter stimulations (figures 5.13a and 5.13b) originate lower temperature differences between the slots and the surrounding areas. Particularly figure 5.13a presents almost no differences at the end of the stimulation (stimulus of 1.5 seconds). The temperature of slots also presents a very small decay over time, even when compared with the stimulation of 4.5 seconds. This is not related to material thermal conductivity, is due to the small heat transfer by convection. Along with this, the temperature response of the second slot is very small, being very difficult to identify and even to delimit its surroundings, even if slightly easier with a stimulation of 4.5 seconds.

Figures 5.13c and 5.13d present two similarities, the temperature increase (from the beginning of the test) of the sound area is roughly half of the temperature increase of the fourth slot and the temperature profiles at the end of the tests revealed lower temperature for the slots. In particular the stimulation of 30 seconds (figure 5.13d) presented one of the highest ratios between the temperature increase at the centre of the slots and the sound areas. After a detailed observation of all the performed simulations, this was coincident with the best obtained results (and can be observed easly in figure 5.12). The existence of an instance where the temperature profile is fairly uniform and the slots are almost undetectable was also observed in the experimental tests. At the end of each of these two tests, the temperature in the slots was lower than for the sound area. At the test end, the temperature differences were considerably smaller than at the end of the stimulation. Thus, the usage of these profiles, would not produce a temperature profile that would result in a better result. The lower temperature of the slots is a clear evidence of their higher thermal dynamics and lower resistivity, compared with the sound areas.

The last two tests (figures 5.13e and 5.13f) refer to those used with long stimulations. Here is observed a blur in the temperature profiles, despite the instant being analysed. This blur in the thermal images and profiles is an evidence that the stimulation was too long and the temperature differences were starting to fade. This results from the appearance of significant heat flows, located in the slots boundaries, parallel to the stimulation surface (X axis). Another aspect to be noticed was the temperature profiles at the end of the tests. Comparing to the sound areas, the slot present higher temperatures at the end of the stimulation, lower temperatures after a certain period and an almost complete equilibrium at the end of the stimulation. In these simulations, the final temperatures were almost equal to the initial temperatures, particularly in the stimulation of 90 seconds.

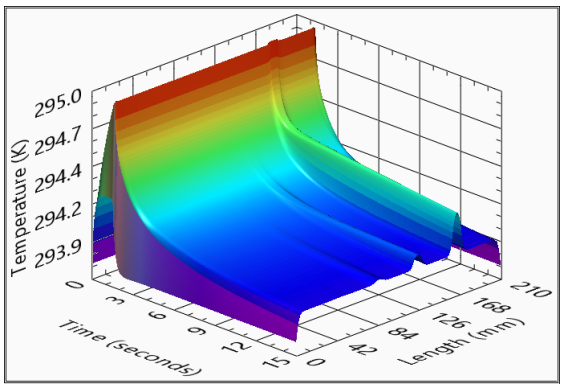

(a) Temperature profiles for stimulation of 1.5 (s)

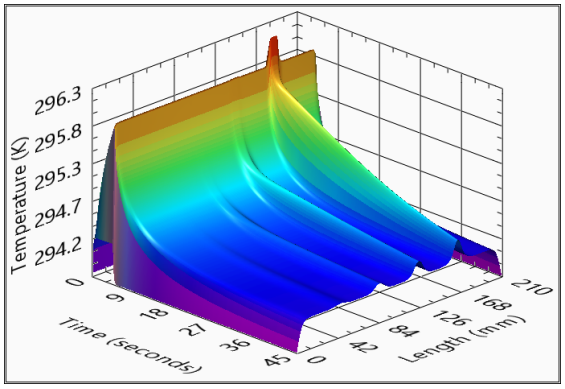

(b) Temperature profiles for stimulation of 4.5 (s)

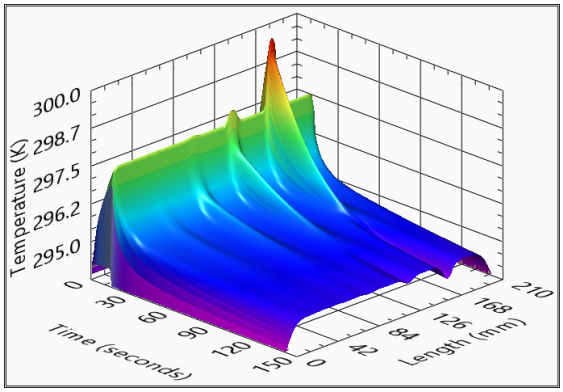

(c) Temperature profiles for stimulation of 15 (s)

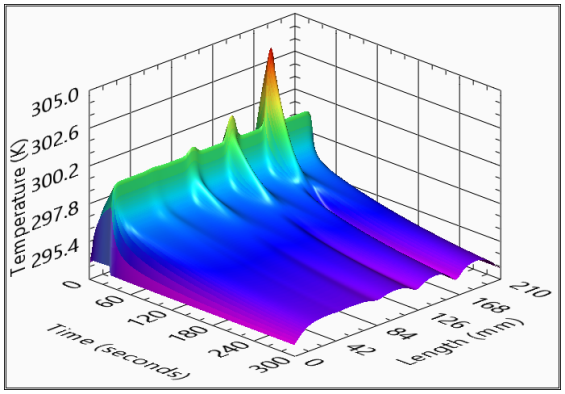

(d) Temperature profiles for stimulation of 30 (s)

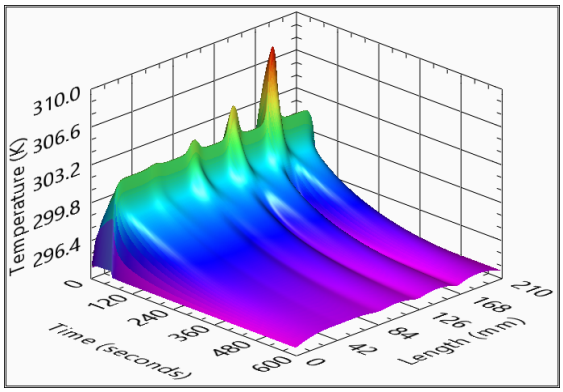

(e) Temperature profiles for stimulation of 60 (s)

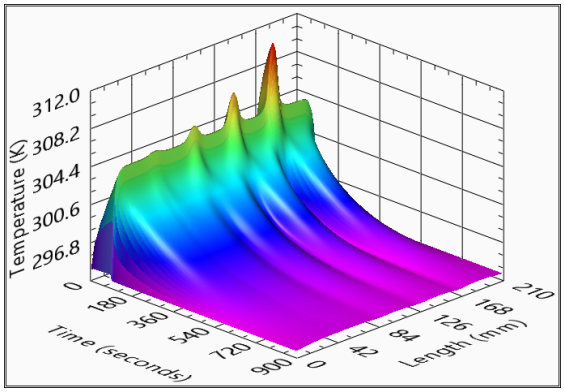

(f) Temperature profiles for stimulation of 90 (s)

Figure 5.13: Temperature evolution where the stimulus is being applied

The temperature difference between the slots and their surroundings along with the blurring at the boundaries, establishes the technique sensibility. In figure 5.14 are represented the temperature differences for the four slots as a function of the stimulus length and the frame being observed. Similar to the laboratory tests and simulations, the stimulus lasted from frame 0 up to the 299th. After a certain period, the difference between the temperature at the slots and the sound area is almost zero and in the case of the fourth slot it tends to diminish. Here is also observed the negative difference between the slot and sound area. This is clearly smaller than the observed at the end of the stimulation, and does not provide any information that could significantly improve the analysis. Like already mentioned and visible in figure 5.14, the usage of stimulations longer than a certain value is not positive for the analysis, regardless of the slot being analysed.

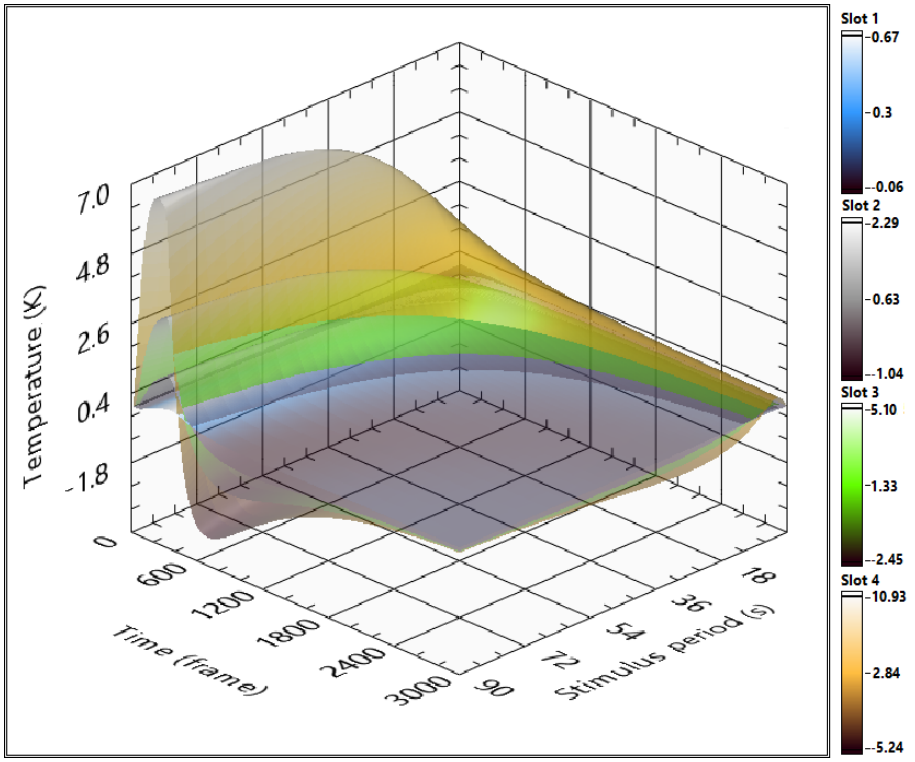

Figure 5.14: Temperature difference between slots and its surrounding areas function of stimulus period and instance being analysed

It is worth noticing that a lower thermal resistance results in a lower thermal dynamics for the sample, and vice-versa. Like observed in the previous chapter, the halogen lamps used as stimulation do not have a high dynamics. For these reasons the transient analyses in highly conductive materials, such as, metals or metal based composites, have to be performed with LED stimulations, flash lamps or other highly dynamic systems.

5.2.4 Optimum settings

The numeric simulations were capable of accurately represent the laboratory tests previously described. The usage of the numeric results assured a higher understanding of the temperature evolution during a NDT with an optical stimulation, particularly by enabling the observation of the temperature variations inside the sample. The next step is to use the numeric simulations to precisely identify the ideal parameters to conduct a TTT.

A NDT thermal test should produce results which allows the accurate characterization and detection of a defect. From what was observed in the laboratory tests and in the simulations, it is possible to detect the smallest slot (slot 1). However, its characterization, boundary definition among other aspects, are difficult to define and the accuracy is usually low. Overall, with the present methodology, it is possible to define the second slot as the characterization limit of infrared thermography using optical transient stimulations. Therefore, the ideal parameters will be selected for this slot.

Like it was mentioned in chapter 3.2, one of the most important parameters in a thermal analyses is the parameter c [187, 202], which is obtained by dividing the slot width by its thickness (equation 3.4 page 52). The variation of this parameter might be accomplished by changing the slot thickness, slot width or both. In these simulations it was changed the global thickness with the slot thickness being proportional to this. This keeps the relation between the thickness in the slot area and its surroundings. This way the best stimulation period will be determined for a slot with 10 millimetres width and several global thicknesses (thickness in the sound area), ranging from 0.5, 1.0, 1.5, 2.0 and 3.0 ... up to 10 millimetres. The evaluation of the test sensibility was accomplished by comparing the temperature shortly after the end of the stimulation (the equivalent to frame 350). This was performed at the centre of the referred slot and at the centre of the sound area. The obtained results are presented in figure 5.15.

In the performed simulations the shortest stimulation used was 2 seconds. The most obvious and expected result was that a thicker sample required a longer stimulation to reach the similar temperature difference. While not being a direct proportional, a certain proportionality is observed. In figure 5.15 are also represented a green and a red group of points, the red group representing the location of the maximum temperature difference for a sample with a certain thickness. Since the differentiation decreases for stimulation periods longer than the ones indicated by the red points, this should be viewed as the maximum stimulation period. Using equation B.2 is possible to obtain the stimulation period for which the maximum temperature difference can be obtained.

Like already mentioned, the maximum temperature difference may not be the best result. When the boundary of a defect already started to become blurred. The alternative is to use a stimulation that produces a similar temperature differences, however, slightly smaller so the

boundaries are easier to identify. This can be accomplished by analysing the space derivative of the temperature difference for a certain thickness. The green group of points represents the location where the derivative of the curves is smaller than 0.14. With equation 5.7 is obtained the stimulus period that will lead to the best global results for a given sample thickness. In these equations, the sample thickness should be higher than 0.2 and less than 10 millimetres. In the equations (B.1 to B.3), l is the sample thickness in millimetres and the stimulus period is obtained in seconds.

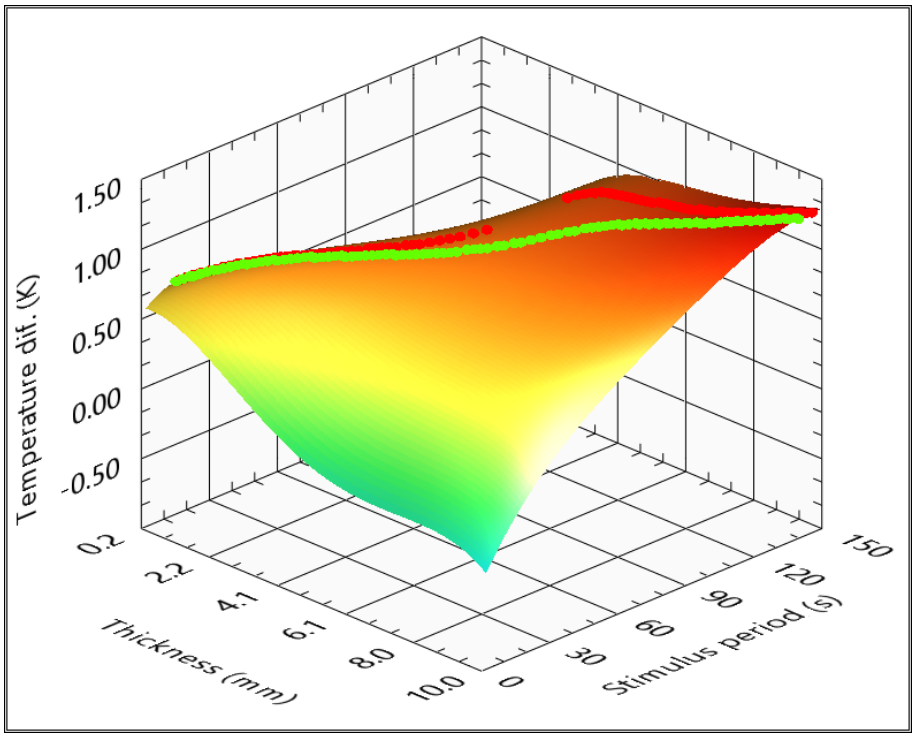

Figure 5.15: Temperature difference function of the PMMA sample thickness and stimulation period, red and green dots represent the maximum and recommended stimulation period

$$Stimulus\,Period_{recommended}(s) = 17.74 + 3.52 \times l + 2.93 \times l^2 - 0.21 \times l^3 \tag{5.7}$$

After the analyses and understanding of the results obtained with the samples made of PMMA, the next step is to analyse samples made of composite materials. In the second chapter several types of composite materials and their compounds (reinforcements and matrix) were described. Among the composite materials, polymers reinforced with glass fibers or carbon fibers are the most used. Of these two, carbon fibers tend to be used in structures and components where safety is a major demanding. Thus, several simulations were performed to evaluate the temperature variation of samples with several thicknesses, the same approach as described previously, and with various stimulations periods. However in this case the simulated samples were made from CFRP.

The carbon fibers can be combined with polymeric resins in various ratios. The deposition of resin on a fabric made of carbon fibers makes the composite highly anisotropic, from the thermal properties perspective [203]. Changing the fiber orientation and resin concentration have a great influence in the composite mechanical properties [204, 205]. Naturally this will lead also to different thermal properties, namely thermal conductivity. The manufacturing process also plays an important role in the thermal properties [206]. In recent years, some new approaches have improved the global mechanical properties by reinforce the carbon fibers with nanotubes, also changing the thermal conductivity of the CFRP [207]. In the simulations relating a CFRP sample, it was used different thermal conductivity in the X and Y directions. It was assumed that the fibers are disposed parallel to the surface receiving the stimulation, thus, the thermal conductivity in the X axis was 6.3 and 0.6 in the Y axis, like indicated by Tian Tian [203] (figure 5.1a).

The temperature difference between the slots and the sound area indicates the sensibility of TTT to a slot in the CFRP. The results for these simulations are represented in figure 5.16 and its function is represented in equation B.4. It is detected a change of the temperature behaviour when comparing the simulation results from the PMMA with the CFRP sample (figure 5.15 and 5.16). In this case, the maximum temperature difference is obtained with the thinner samples. For thicker structures (over 5 millimetres) the maximum temperature difference is almost constant, despite the stimulation period required to reach that same maximum. These variations are due to the highly anisotropic characteristics of the CFRP and the difference in the thermal conductivity. It is observed that longer stimulations always lead to worse results, despite the maximum stimulation length being only 90 seconds, contrary to the 150 of the PMMA sample. The red and green curves represented in figure 5.16 also represent the maximum (equation B.5) and ideal stimulation periods (equation 5.8). Equation B.5 gives the stimulation period that should be applied to a given sample (thickness l in millimetres) to obtain the maximum temperature difference, while equation 5.8 is the ideal stimulation period.

$$Stimulation\,Period_{recommended}(s) = 34.39 - 1.17 \times l - 0.46 \times l^2 + 0.056 \times l^3 \tag{5.8}$$

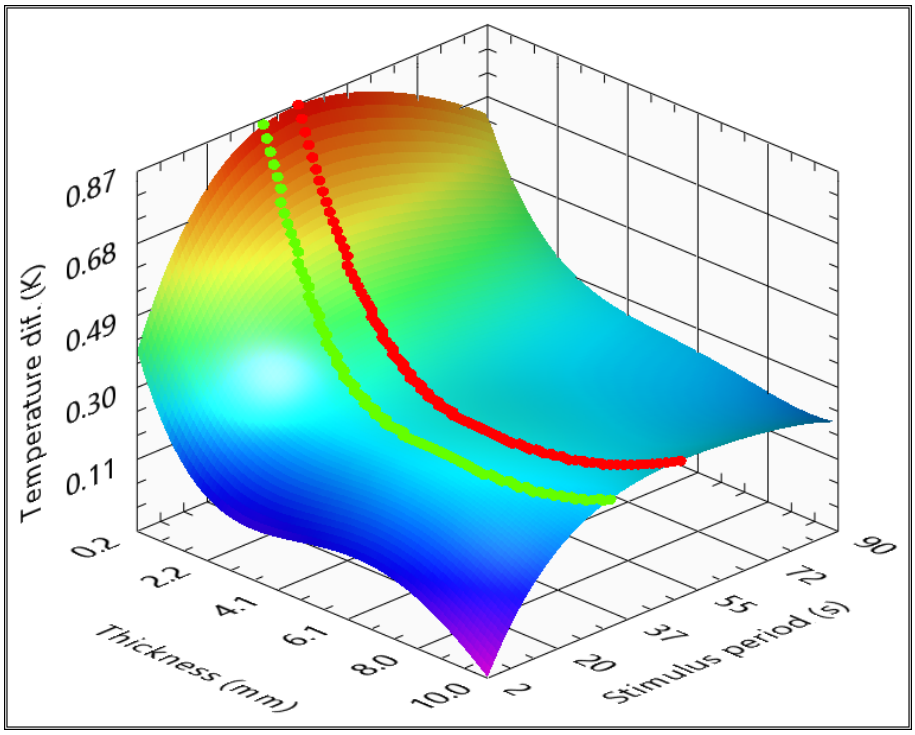

Figure 5.16: Temperature difference function of the CFRP sample thickness and stimulation period

5.3 Lock-in test simulation

The lock-in thermal tests are characterized by applying a sinusoidal stimulation. Therefore the results and observations of the transient analyses cannot be translated to a cyclic stimulation. This manner, the next section presents and analyses the stimulations relating the IR-LTT.

5.3.1 Introduction to the simulation

The lock-in thermal tests were simulated accordingly to the procedures and results presented in chapter 3.3. The mathematical equations are the same that were presented in the beginning of this chapter. The major difference between the LTT and the already presented TTT is the stimulation wave. In the transient tests, the stimulation is a single square impulse. In LTT it is used a stimulation with the same amplitude of the TTT, however is modulated as a sinusoidal wave.

In the laboratory tests, the temperature distribution was measured at the entire surface of the test samples. In the simulations, the temperature distribution through the sample was evaluated, from the stimulation surface to the opposite side. Then, the only common zone in the two geometries is the stimulation boundary, where the stimulation is applied. Thus, to compare and validate the simulation settings the results for this zone will be analysed. In figure 5.17 is presented the temperature in the centre of slot 4. Corresponding to a test with 20 seconds per cycle with slots

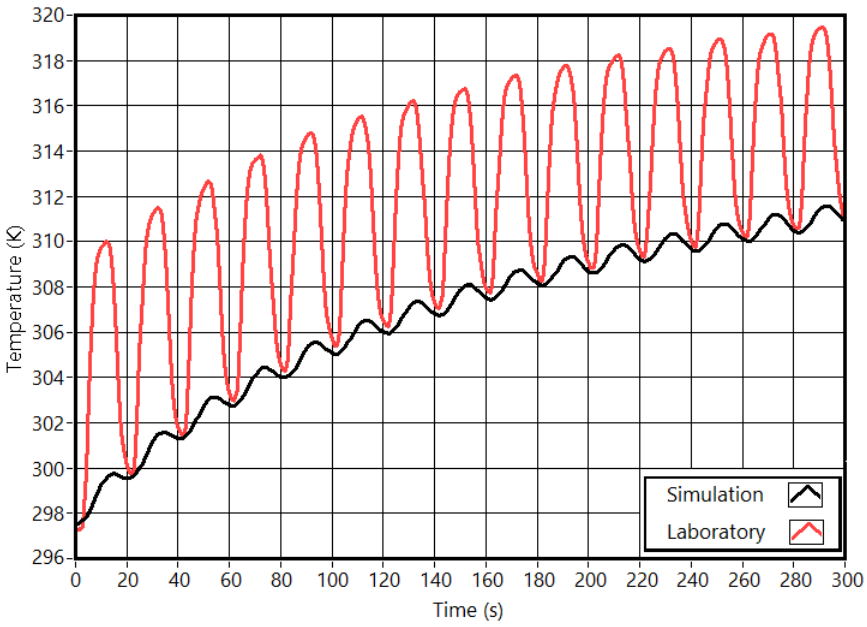

Figure 5.17: Temperature obtained in laboratory and simulation in the centre of slot 4

of 10 millimetres width. Figure 5.18 presents the temperature profiles after 15 cycles (last frame of this test).

The temperature evolutions, despite the stimulus period being used, is very similar to the ones presented in figure 5.17. Here are clearly visible the existence of two frequency responses. The temperature from laboratory tests and the simulated ones are considerably different. This is occurs because of the disturbance caused by the radiation from the stimulation source. This increment in the temperature is proportional to the stimulation amplitude. Thus, as the amplitude increases, the difference between laboratory and simulated temperatures is higher, and vice-versa. The small differences observed at the lower part of the temperature waves are due to the stimulation dynamics. Like observed in chapter 4, the stimulation waveform is not a perfect sinusoidal. Therefore, when is desired a stimulation of zero (without any light), this is not accomplished existing some light and consequentially some reflected radiation. However, in the lower stimulation instances (valleys), the reflected radiation is also smaller, making the temperatures in the laboratory tests and simulation very close.

The observation of the last frame of the tests (figure 5.18) assures that if any incorrect definition of the stimulation parameters occurred, this would be visible. The laboratory profiles was obtain from one of the tests presented in chapter 3. This is assured due to the cumulative effect of applying a cyclic stimulation. The biggest difference observed, when compared the real and simulated curves, is in the area of slot 1. Due to the overall warm up of the sample and mainly the higher temperatures in the deepest slots, the natural convection will be influenced by the surrounding temperatures. Although in the simulation, the heat loss by convection is proportional to the node

temperature. The influence of the neighbour nodes is discarded for the convection effect. Since all the other temperatures were very similar, and the profile obtained in laboratory was an average profile with very low temperatures variations for this slot, this difference was not considered to be significant.

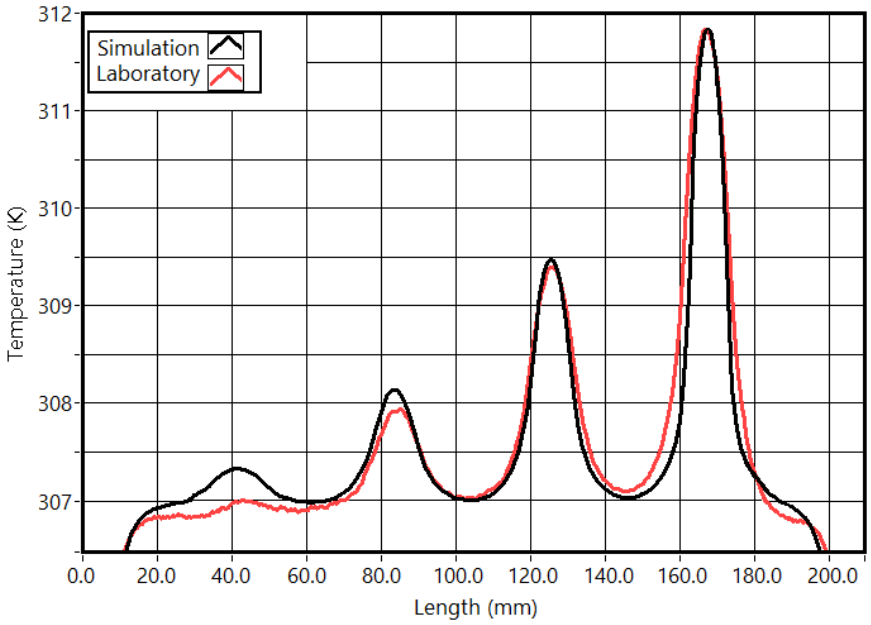

Figure 5.18: Temperature profiles at the end of the test in the stimulation surface (20 seconds)

5.3.2 Results

Figure 5.19 presents the temperature evolution of the central node located in slot 4. Similar to the performed previously, these sub-figures are presented in auto-scale in the vertical axis. As expected from a lower thermal resistance, any temperature variation due to the alteration in the test parameters would be firstly visible here. In figure 5.19a are represented the temperature evolutions for stimulations of 0.02 to 1 second per cycle. Here is visible that the temperature evolutions are mainly affected by the stimulation cyclic variation. Even in the longest test, the complete duration is 15 seconds. Here is clear the predominance effect of the stimulation similar to the faster frequency already mentioned in other thermal tests (chapter 3.3).

Figure 5.19b presents the temperature evolution for tests with 1 to 8 seconds per cycle. In this group, apart from the sinusoidal temperature evolution, this start to present a negative exponential, similar to what was observed in the previous section. Here it is not possible to evaluate the influence of the two responses or the impact of each in the results. An important aspect is the decreasing difference among tests as the time per cycle increases.

The third set of tests is observed in figure 5.19c, these represent cyclic tests with stimulations ranging from 8 to 20 seconds per cycle. Apart from the first three cycles, and an offset in the temperatures, it was not observed any significant differences between the tests. Thus the main temperature variation presents a superposition of two curves, a sinusoidal stimulation and a negative exponential.

The temperature evolution for cycles of 20 to 80 seconds is represented in figure 5.19d. In this last set of results the curves present a higher response for the negative exponential temperature. Here are visible higher temperature variations corresponding to a stimulus frequency and an exponential decay. These bigger variation in the slot temperature occur in the first 3/4 cycles. After these, the slot temperature evolution is only due to the sinusoidal stimulation. The sinusoidal temperature variation in the entire profile is fairly equal. Among the several simulations, the temperature variations in the centre of the deepest slot, are considerably small when compared with the temperature variations during the entire test.

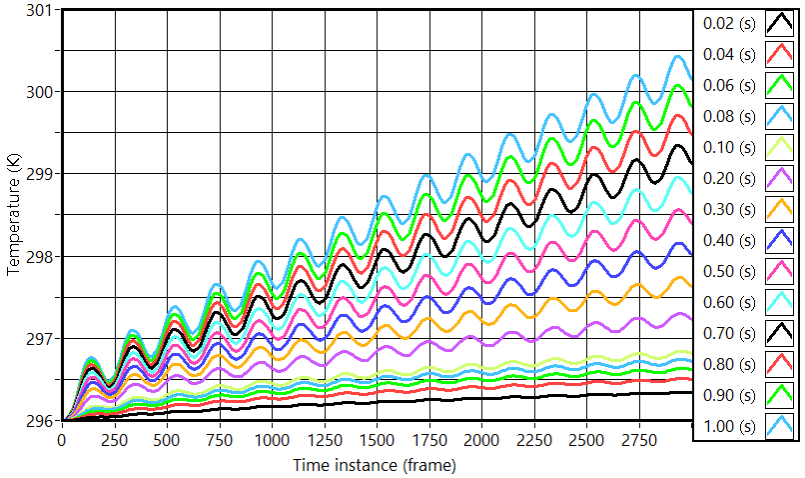

(a) Temperatures for stimulations of 0.02 to 1 seconds per cycle

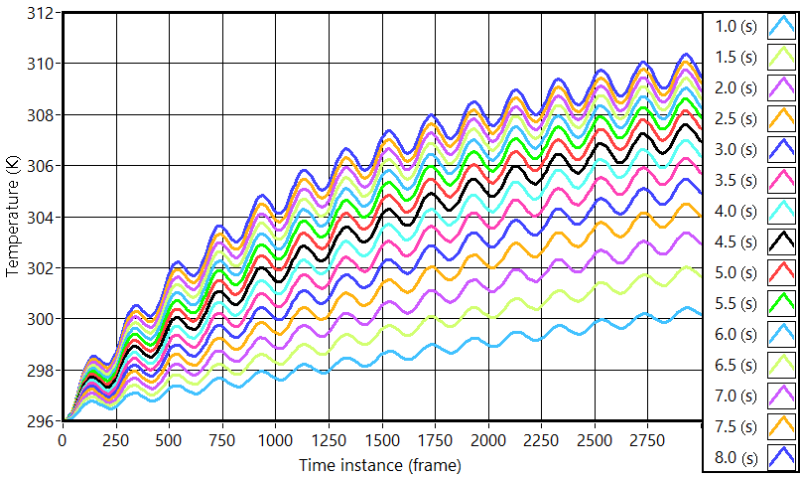

(b) Temperature for stimulations of 1 to 8 seconds per cycle

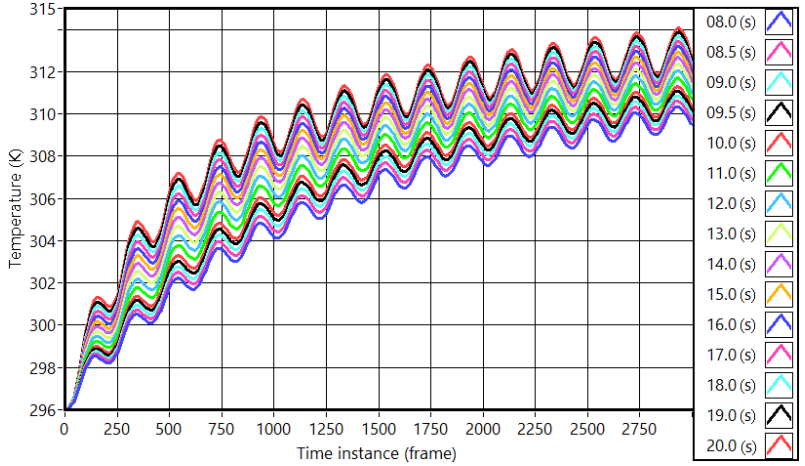

(c) Temperature for stimulations of 8 to 20 seconds per cycle

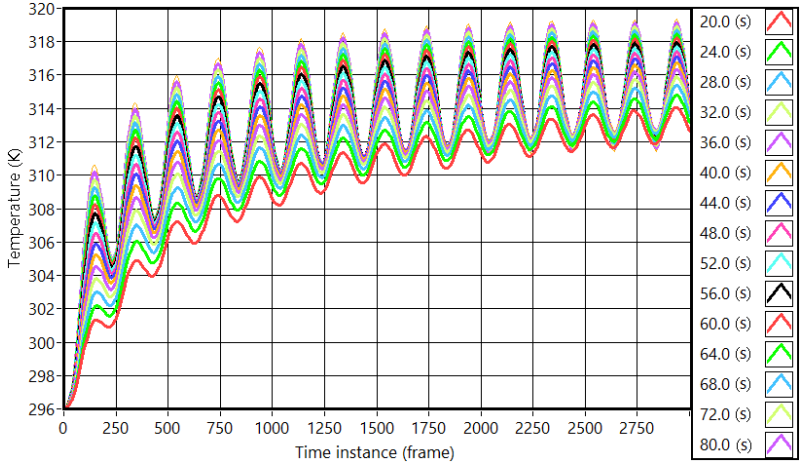

(d) Temperature for stimulations of 20 to 80 seconds per cycle

Figure 5.19: Temperature evolution at the centre of slot 4

One of the main principles behind the use of the amplitude analyses is that any slightly difference will be amplified (cumulative effect) through each cycle. Thus the observation of the temperature distribution after a certain number of cycles can be used to identify thermal patterns. In figure 5.20 the temperatures are presented at the surface after 15 cycles, due to the great temperature differences the vertical axis is in auto-scale. These were obtained with cyclic stimulations with 0.02 to 80 seconds per cycle. It was expected that the deepest slot (slot 4) present a higher temperature response. Despite the existence of small variations in all simulations, like observed in figure 5.20a, they are only significant for stimulations longer than 0.1 seconds. This referring only to slot 4. Slot 3, 2 and 1 are visible for stimulations longer than 0.2, 0.7 and 2, respectively. Here, the temperature difference for the boundaries increases with the increasing of the time period and the slot boundaries are considerably easy to identify.

Figure 5.20b illustrates the temperature profiles after 15 cycles, for stimulations from 1 to 8 seconds per cycle. It is clearly an increase in the temperatures at the slots location, when compared to its surroundings. Here the maximum temperature increases for all the stimulations. As the slots present higher temperatures, the temperature profiles also become "rounder", indicating an attenuation in the temperature distribution. In the third set of profiles (figure 5.20c), it is observed an inversion on the temperature responses. Here the maximum temperature at the centre of the slot 4 is decreasing with the increasing of the time period. In the boundaries of slot 4 inversions appear on the temperature response. They are clear in the boundaries of the 20 seconds simulation, where are visible local valleys in the boundaries locations. It can also be mentioned that increasing the cycle period, makes the boundaries becoming harder to identify.

In figure 5.20d are presented the temperature profiles corresponding to simulations for time periods ranging from 20 to 80 seconds. The higher temperature profile is observed in the boundaries of slot 4 for shorter stimulations.

In the longer stimulations (longer than 36 seconds), the temperatures observed for the centre of slots 3 and 4 are lower than the observed for the surrounding areas. Here is also visible an increment in the temperatures between the slots. In the longer stimulations the forth slot loses its characteristic thermal profiles and becomes invisible.

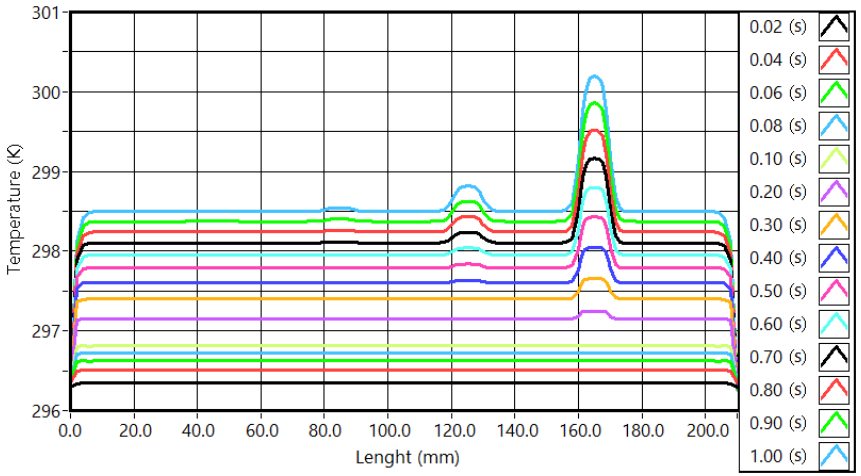

(a) Temperature for stimulations from 0.02 to 1 seconds per cycle

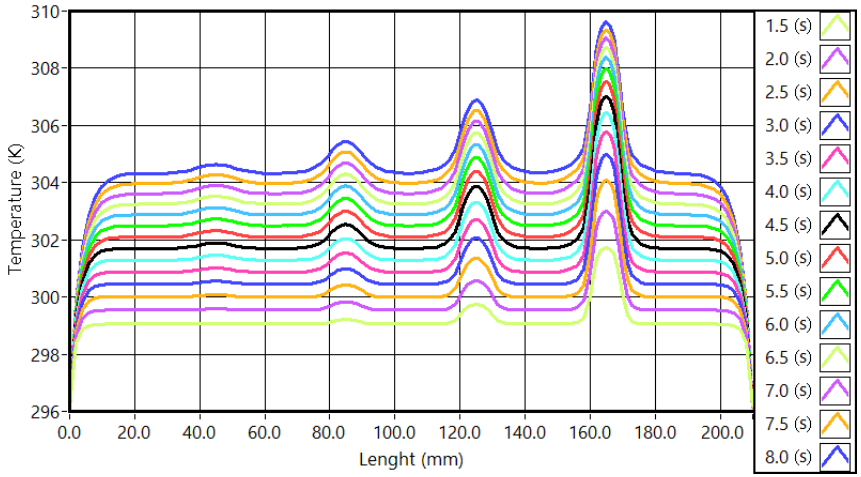

(b) Temperature for stimulations of 1 to 8 seconds per cycle

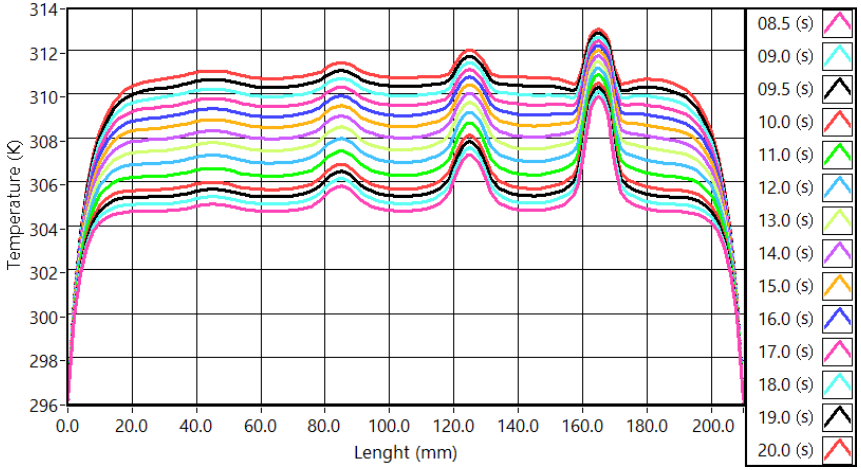

(c) Temperature for stimulations of 8 to 20 seconds per cycle

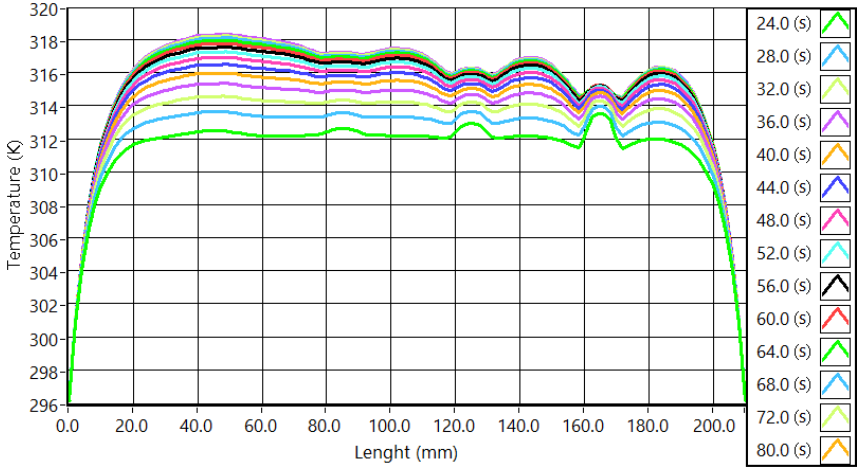

(d) Temperature for stimulations of 24 to 80 seconds per cycle

Figure 5.20: Temperature profiles in the stimulation surface after 15 cycles

Sequentially to the observation of the temperature profiles after several cycles, is necessary to analyse the frequency response for each node. Therefore to access the amplitude and phase delay, it was necessary to use an DFT and extract the relative gain and phase from the temperature signals. This was performed through the development of an application in LabVIEW®. Figure 5.21 illustrates the amplitude profiles in the area where the stimulation is being applied, for stimulation ranging from 0.02 to 80 seconds per cycle.

Following the observations of the temperature profiles, it was expected that the temperature variations were very small for the shorter stimulations and higher for stimulations near the 30 seconds per cycle. In figure 5.21a are represented the amplitude results for the stimulations ranging from 0.02 to 1 second. The first amplitude variations appear for the stimulation of 0.2 seconds per cycle. The small amplitude variation was observed at the location of slot 4. There are small variations in the amplitude, for the stimulation with 0.4 seconds at the location of the third slot. For stimulations up-to 1 seconds it is not possible to identify the first and second slot.

The identification of slots 1 and 2 is only possible in figure 5.21b. Here are present the amplitude results for the tests with 1 to 8 seconds of period. More precisely, slot 2 is visible in the stimulation of 2 seconds per cycle and slot 1 in the stimulation of 5.5 seconds. However this last detection is very difficult. The profiles in the area of slot 4 present an inversion in the amplitude, with a maximum detectability approximately in the stimulation of 3 seconds. This behaviour is similar in slot 3, however this is observed for the stimulation of 7 seconds.

Figure 5.21c illustrates the amplitude results for stimulations with periods of 8 to 20 seconds. In slot 4, the amplitude response stabilizes for stimulations near 15 seconds, starting to increase for longer stimulations. The small temperature decays observed at the boundaries of the slot become visible for stimulations longer than 11 seconds. A similar amplitude behaviour is also observed in slot 3, however the profile variations are softer and tend to appear for slightly longer stimulations. The major difference between slot 4 and 3 is the complete inversion of the amplitude profile at the slot 3 location, passing for a near zero identification for the stimulation of 14 seconds. The thermal response of slot 1 is still very difficult.

Finally, figure 5.21d presents the amplitude results for stimulations between 20 and 80 seconds. For these stimulations, the temperature responses of slot 4 increases considerably, especially for the longer cycle periods. Here the increase of the stimulation increases the amplitude response and the small decays in the slot boundaries tend to disappear. An inversion of the amplitude response is also observed for slot 3. Here, in the centre of the slot is observed a transition from a decay in the amplitude to a peak, passing for a neutral response in the stimulation of 52 seconds. Slot 2 presents the same behaviour, however is not observed the complete inversion in the amplitude response.

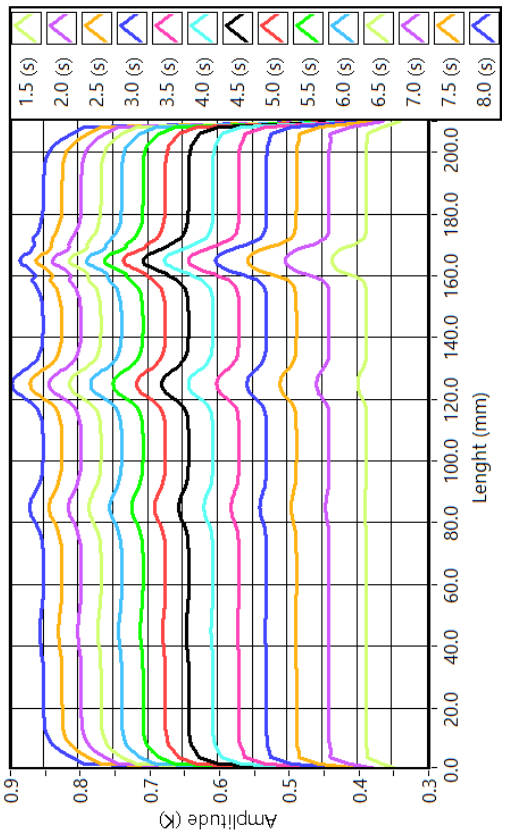

(b) Amplitude response for stimulations of 1 to 8 seconds per cycle

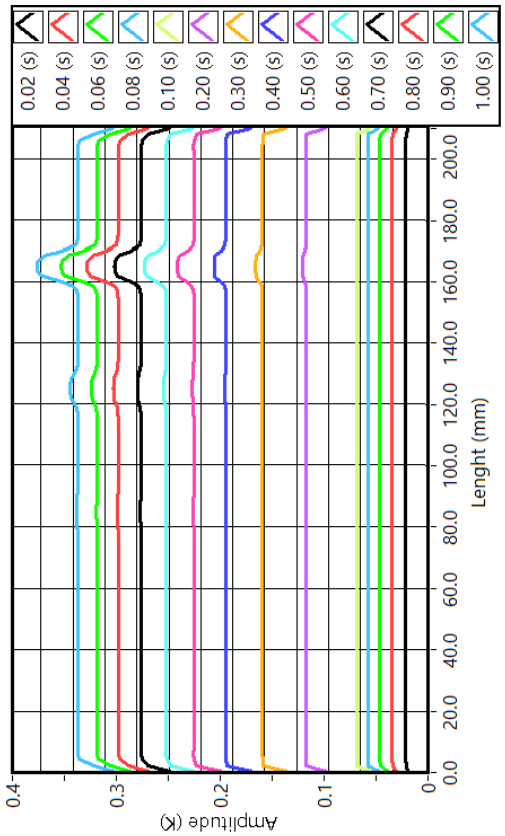

(a) Amplitude response e for stimulations from 0.02 to 1 seconds per cycle

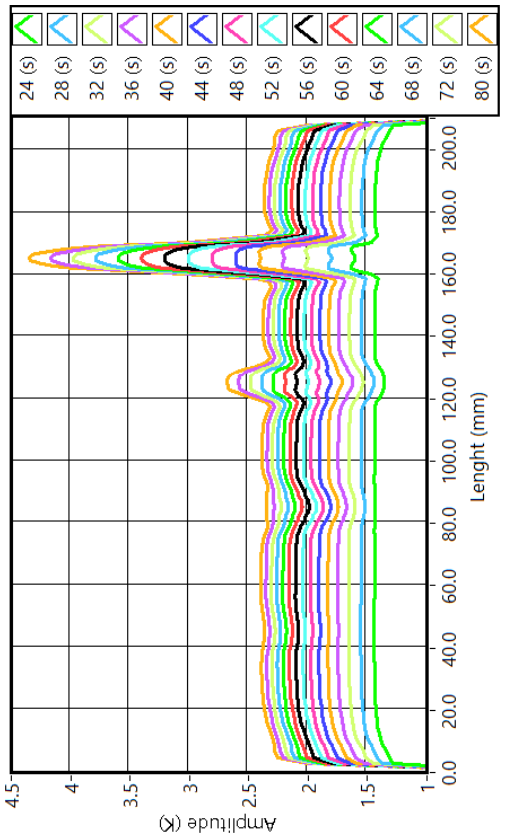

(d) Amplitude response for stimulations of 24 to 80 seconds per cycle

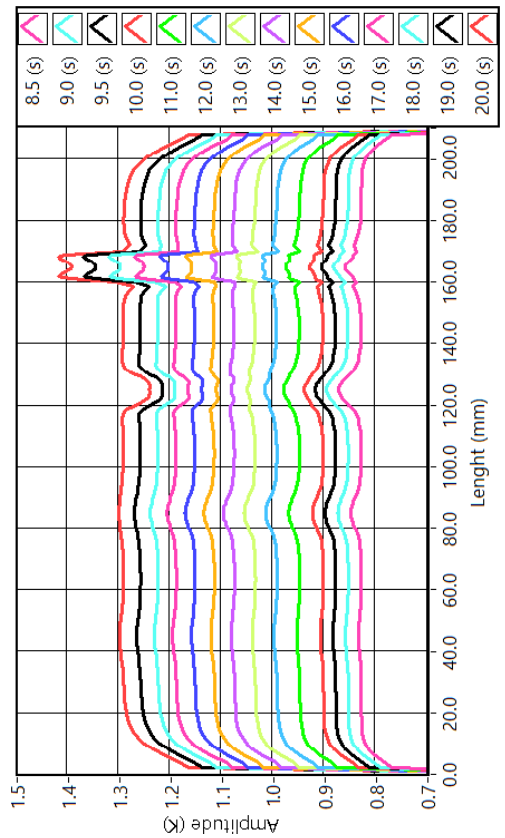

(c) Amplitude response for stimulations of 8 to 20 seconds per cycle

Figure 5.21: Amplitude responses from the stimulation surface after 15 cycles

In chapter 3.3 were presented the results from the LTT and was concluded that the most sensitive analyses was accomplished by analysing the phase data. In figure 5.22 are presented the phase profiles at the stimulation zone, for several cyclic simulations.

In figure 5.22a are presented the phase profiles for stimulations of 0.02 to 1 second per cycle. From the observations of the temperature profiles no response was expected from the faster stimulations. With a cycle time of 0.02 seconds the phase delay was considerably high, diminishing for longer cycles. The fourth slot was once again the most visible, presenting higher profile variation (increase in the phase delay) and appearing earlier (stimulation of 0.2 seconds). The third slot was visible with a stimulation of 0.4 and the first and second with stimulations of 0.5 and 1 second, respectively. It was also observed a tendency of the global phase delay to stabilize near the -2.5 rad.

In figure 5.22b it is observed a stabilization of the global phase delay at approximately -2.48 rad. In the area of the slot 4 is observed a continuous increasing of the phase delay, when compared with the neighbour values. Slot 3 is becoming well visible, even if the evolution rate is slower than slot 4. The two remaining slots are also increasingly more visible with the increasing of the stimulation period. One aspect present in all profiles is the width of the phase variation, this increases for all slots and with the stimulus duration. However this increasing is considerably far smaller than observed in the amplitude and temperature profiles.

The crescendo in the detectability of slot 4 continued to increase considerably from 8 to 20 seconds (figure 5.22c). It is observed a small reduction of the phase delay at the centre of the slot, beginning with the stimulus of 11 seconds and ending with the stimulus of 20 seconds. Slot 1, 2 and 3 present different behaviours. The phase delay decreases with the increasing of the stimulus, being most visible in slot 3 and less visible in slot 2. Slot 3 decreases its delay with a minimum for the 13 seconds stimulus, however slot 2 inverts its response (17 seconds stimulus), when comparing it to the near data.

Figure 5.22d illustrates the phase response for stimulations of 20 to 80 seconds. A small diminishing of the global phase delay is observed. The variation of phase in slot 4 are very small. The width of the phase profile in slot 4 is almost constant and the variations of its maximum are very small. Slot 3 phase variation is considerably high and is almost proportional with the time period. Slot 2 presents a new inversion of the phase response, passing through an almost non response at the 36 seconds stimulation. Slot 1 also inverts its phase response with the inversion occurring at the 48 second stimulation. The longer stimulations present an almost direct proportionality between the slot depth and its phase delay variation.

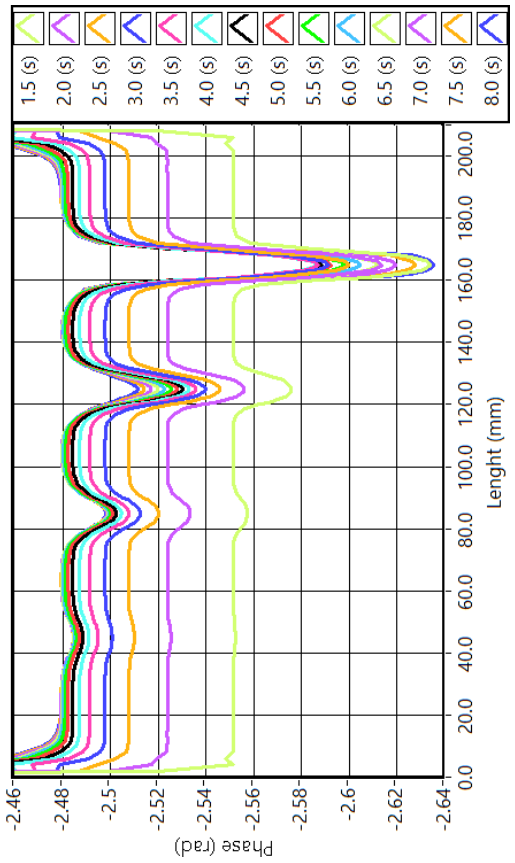

(b) Phase delay for stimulations of 1 to 8 seconds per cycle

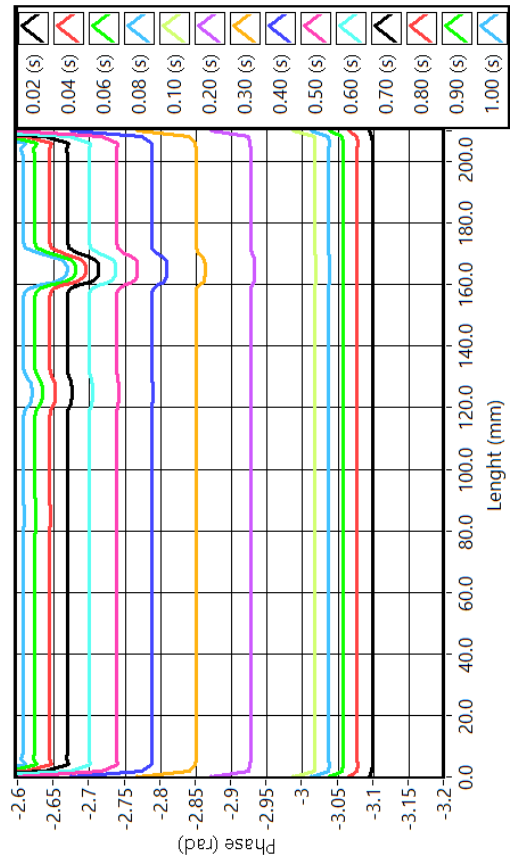

(a) Phase delay for stimulations of 0.02 to 1 seconds per cycle

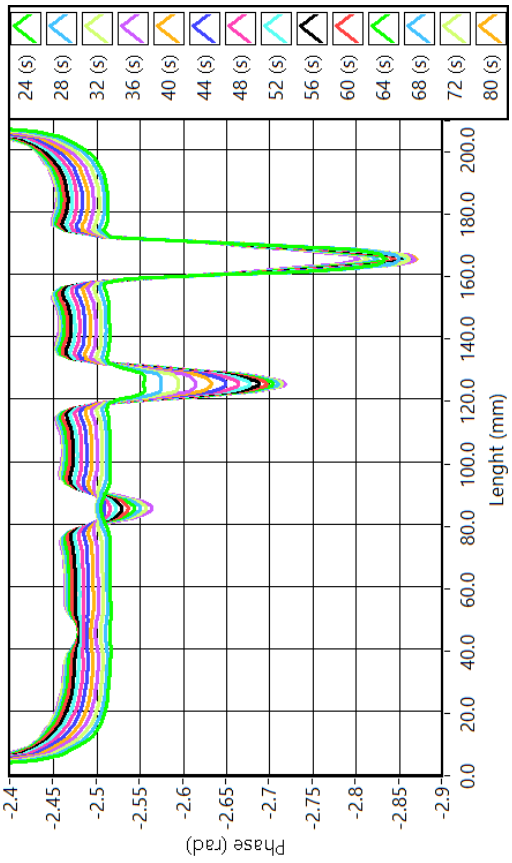

(d) Phase delay for stimulations of 20 to 80 seconds per cycle

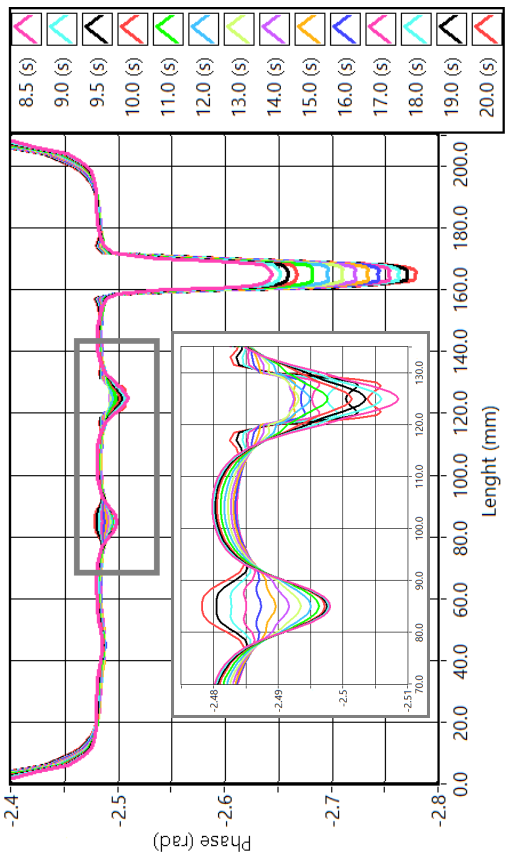

(c) Phase delay for stimulations of 8 to 20 seconds per cycle

Figure 5.22: Phase delay of the stimulation surface after 15 cycles

5.3.3 Simulation analyses

From the several results obtained, the first and main aspect to highlight is the difference between the real temperature curves and the ones obtained in the simulation. The reflected radiation prevented a direct comparison between the two sets of data. The comparison of the cycle's lower temperatures (valleys) was the selected criterion to validate the FEA parameters. The comparison of the temperature profiles, at the end of the test was used as a confirmation.

The use of a thermal image during a test that uses a cyclic stimulation may be one manner to identify some defects. This may be an important analyses if the stimulation period is near to a blind frequency. The samples used were made of PMMA having a thermal conductivity slightly lower than a common carbon fiber, but being fully isotropic. A material with low thermal conductivity is expected to increase its global temperature during a cyclic stimulation. Thus when a fast sinusoidal stimulation is applied, small temperature variations are expected. The increasing in the stimulation cycle period delivers more energy to the specimen, and thus leading to a higher temperature.

The use of longer stimulations allows the samples to present temperature evolutions that consist in negative exponential. This type of behaviour is observed in over-damped mechanical systems. Since all the tests used sinusoidal stimulations, it was not possible to separate the negative exponential from the sinusoidal response in the temperature data. When these present a constant sinusoid evolution, it indicates that the test lasted sufficient time and the temperature reached a stable value. If a longer sinusoidal stimulations is used, an exponential thermal response will appear, overlapped with the sinusoidal thermal response. An extreme long stimulation may even result in a temperature evolution very similar to warming phase of a transient stimulation. The usage of a cyclic stimulation can also be used as cumulative effect to amplify a thermal profiles and thus present different temperature patterns than the ones observed when using a constant and single stimulation.

Increasing the time period of a cyclic stimulation also increases the amount of energy received by the sample. Thinner areas receive more energy per volume, resulting in a higher temperatures and vice-versa. For long cycle periods, areas having higher temperatures and with the stimulation being in a lower instance of the cycle, these areas will start to warm its surroundings. The existing of this lateral temperature conduction (along the X axis) will lead to disperse of any temperature gradient in a transition area such as the slot boundaries. This is observed in the eight boundaries of the slots and at the profile extremities. As the cycle period increases, the time available for this lateral heat flux to become visible also increases. A higher difference between the slot temperature and the surrounding sound areas, increases the lateral heat flux and consequentially softens the temperature profile. Resulting in temperature profiles where the boundaries are difficult to identify.

For extreme long stimulations, the temperature profiles change. The lowest temperature are observed at the boundary of the slots. This is explained by the slot geometry. The slots had straight geometries, which creates a lateral surfaces that are exposed to air. These surfaces locally increase area subjected to convection, thus the boundaries of the slots present local temperature valleys appear.

The most important data is the temperature difference between the sound areas and the slots. These represent the sensibility of this technique and are presented in figure 5.23 for several cycle periods. A short stimulation delivers little energy to the sample, this manner, the temperature profiles present lower variations. Therefore the temperature amplitudes also have to be small, like in all the slots. It was observed an inversion of the amplitude response in all the other slots, except for slot 4. The amplitude response started by having higher value for shorter stimulation periods. Observing the response in slot 4, it is noticed an increase in the amplitude up to the stimulation of 3 seconds. From the 3 to 10 seconds stimulation, the amplitude decreases to a point where is almost undetected (5.23a). These two stimulations periods can be considered two inversion points and may indicate a blind frequency for this slot, even being observed a small amplitude response. The third slot started in the same manner, increasing the stimulation period would result in the increase of the amplitude response. This situation was inverted with the stimulations of 14 seconds in slot 3 and inverted again with a stimulation of 56 seconds (figure 5.23b). The second slot also started by having a higher value, inverted its response with the stimulation of 20 seconds, and with the last stimulations, it is indicated a new inversion. These inversions and null response clearly indicate a blind frequency. Unfortunately, the first slot was never clearly identified. This last aspect reveals the limitations of amplitude images. When comparing the amplitude response with the final temperature, the first slot was visible in the temperature profiles, contrary to what was initially expected.

The relation between the applied energy and the phase delay is more complex than the observed until now. The temperature response is a combination of the heat received by radiation (optical stimulation) and the heat transfer to the environment, by radiation, convection with the air and conduction with the material at the interior of the sample. The radiated heat from the sample is very small thus can be discarded. Thus, for stimulations where the amplitude is extremely small, the phase should not be considered. With the increasing in the cycle period, the sample temperature will also increase. This manner, the variations and differences inside the sample will also increase. With the increase of temperature, the heat loss by convection will also increase. In an instant where the stimulation is less than the necessary to increase the surface temperature, the heat flow will change. Meaning that the heat will not travel from the surface to the interior of the sample, but will travel from the inside to the outside of the sample. Less energy (shorter stimulation) results in less thermal dynamic by convection since the temperature difference is smaller, likewise, lower temperatures leads to very low heat flow by conduction.

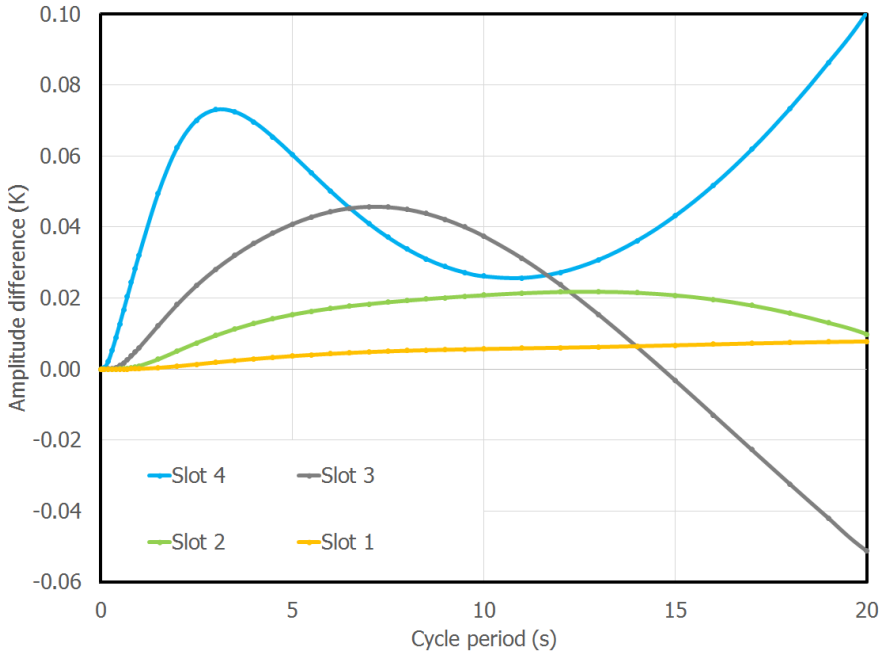

(a) Amplitude difference between the slot and its surroundings from 0.02 to 20 seconds per cycle

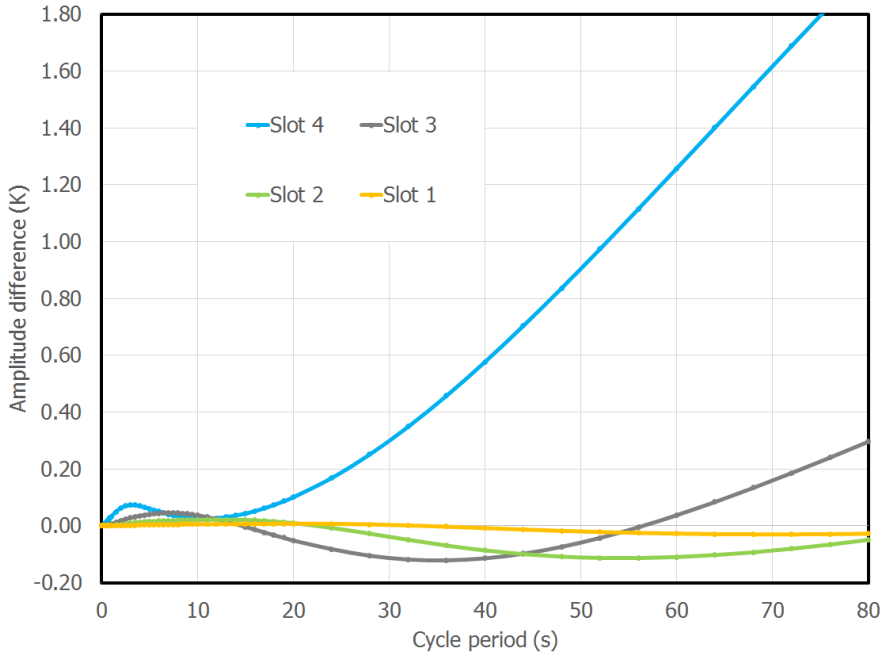

(b) Amplitude difference between the slot and its surroundings from 0.02 to 80 seconds per cycle

Figure 5.23: Amplitude difference between the slot and sound areas, for several cycle periods

Increasing the stimulation period will result in a decrease in the phase delay. This decrease will reach a minimum critical point. From this point the temperature inside the specimen will be high enough to originate a heat flow that will maintain a considerable heat flow by conduction inside the component. This behaviour exists in the slots and in the sound area.

A slot can be observed as an area with smaller thickness. Thinner area, means more heat per volume of material. Thus the inversion or referred critical point will be reached with a shorter stimulation. But an area with a higher thickness will have a higher damping factor, resulting in smaller dynamic. So, the detection and characterization of defects is accomplished by the observation of different patterns. The most relevant aspect is the different dynamics of the sound area and the possible defects, in this case the slots. In figure 5.24a and 5.24b are represented the phase differences between the slots and its surrounding sound areas for all the simulations.

The area corresponding to slot 4 is very thin, when compared with the sample thickness, and the geometry variation of the first slot is very small, this resulted in values of c very low or higher than the recommended limit. The most representative behaviour is observed for slot 2 and 3. The minimum for slot 3 was reached with a stimulation of 4.5 seconds and with the 6.5 seconds for slot 2. These represent a maximum detection for a short cycle period. The maximum reached with the stimulations of 28 and 14 seconds, for slots 2 and 3 respectively, evidences the existence of a blind frequency. For slot 3 the curve in figure 5.24b does not cross the zero axis, however it is very close. With the existence of noise in real or laboratory tests, a real blind frequency may not be observed. However, slot 2 reaches a maximum of 0.01 leading to the intersection of the zero phase delay and consequentially the existence of two blind frequencies. This maximum should be avoided and the thermal tests should be conducted with stimulations that are considerably shorter or longer. A longer stimulation will result in phase images with the contrast presented in figure 5.24b and figure 5.22.

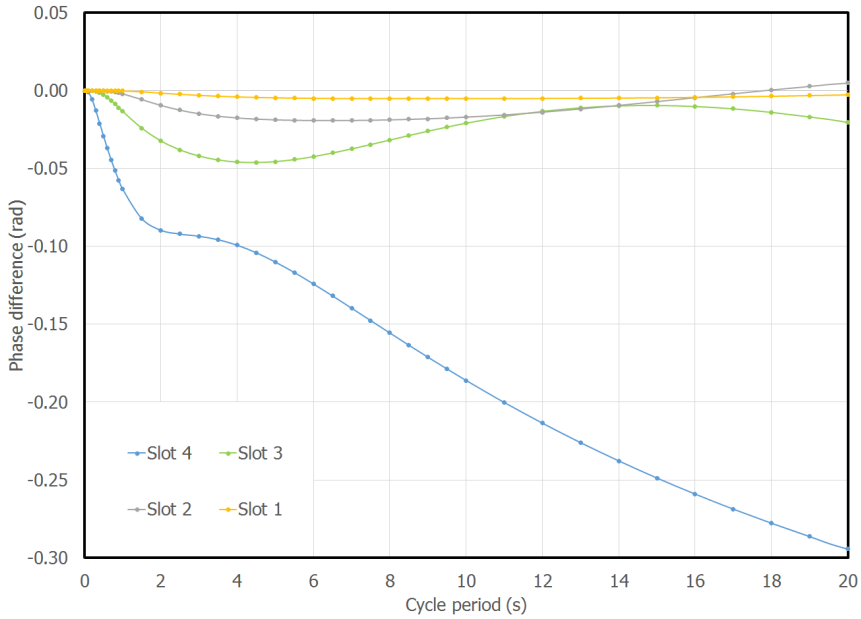

(a) Temperature difference for periods from 0.02 to 20 seconds per cycle

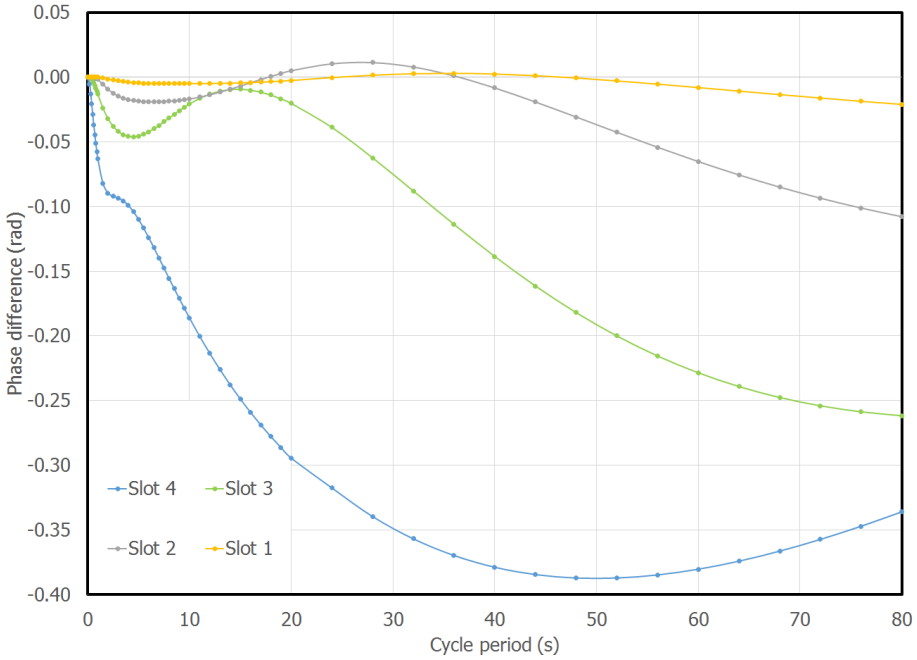

(b) Temperature difference for periods from 0.02 to 80 seconds per cycle

Figure 5.24: Phase difference between the slot and sound areas, for several cycle periods

Phase images present attenuation in their boundaries that are considerably smaller than in other tests or data types. Thus, the disadvantage of longer stimulation is the inherent duration of the global thermal test. In industrial applications, a longer stimulation means that the NDT test, and consequentially the entire maintenance or preventive operation will have a higher cost or may even became a bottleneck. One of the alternatives to reduce the test global length is to use less cycles. In figure 5.25 is represented the variation in phase as function of the number of cycles, for stimulations with 5, 28 and 80 seconds per cycle period.

To accurately calculate the phase delay and amplitude response, a higher number of measures (thermal images) is preferable. The best situation or characteristic response have been found for stimulations with periods of a few seconds. Since the majority of the cameras can reach tens of frames per second, reaching more than 100 images in a single test with a single stimulation is easily accomplished. However to accurately calculate the amplitude response, at least two cycles should be used.

The influence of the number of cycles in the phase delay can by obtained from the difference between the slots and sound area are presented in figure 5.25. For a short stimulation, like the one represented in figure 5.25a (cycle period of 5 seconds) the slots that are harder to detect require more cycles, while the deepest slots reach the maximum phase difference with 5 to 9 cycles. With a stimulation of 28 seconds presented in figure 5.25b (stimulation that introduces blind frequencies), slots 2 and 3 decrease with each cycle.

This is particularly critical for slot 2, reaching a zero phase for nine cycles, while the third slot indicates that with a few more cycles this slot would not be detected. For a stimulation of 80 seconds (figure 5.25c) the smallest slots are manly insensitive to the variation of the number of cycles. On the contrary, the third and fourth slot present some big variations. One important aspect is the fact that the forth slot presented a higher phase delay with a stimulation of 15 seconds and one cycle, when compared with the 15 cycles and a stimulation of 80 seconds per cycle, which results in a considerable shorter test. As a resume, in figure 5.26 is presented a tridimensional representation of the simulated tests and its phase variation when is used 1 up to 15 cycles.

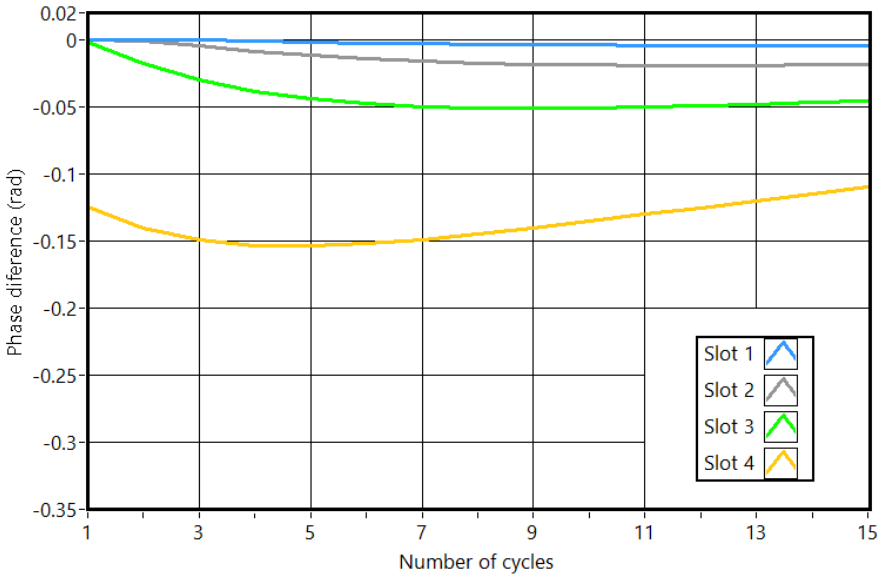

(a) Phase difference for a cycle period of 5 seconds

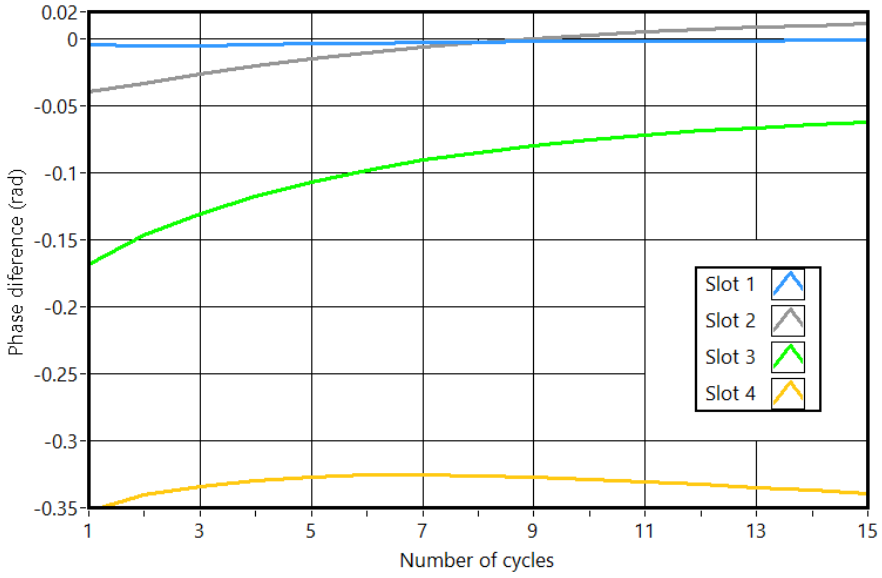

(b) Phase difference for a cycle period of 28 seconds

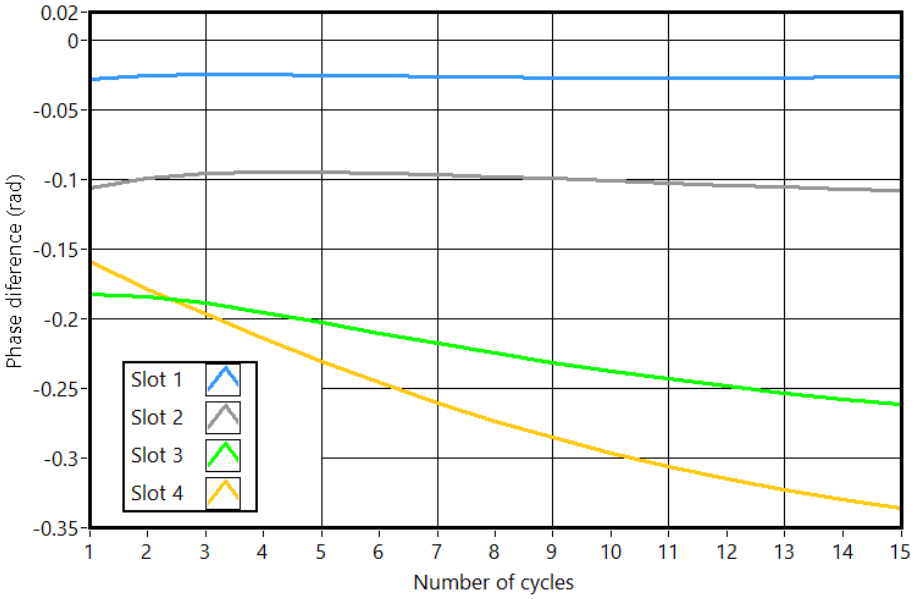

(c) Phase variation for a cycle period of 80 seconds

Figure 5.25: Phase variation trough number of cycles

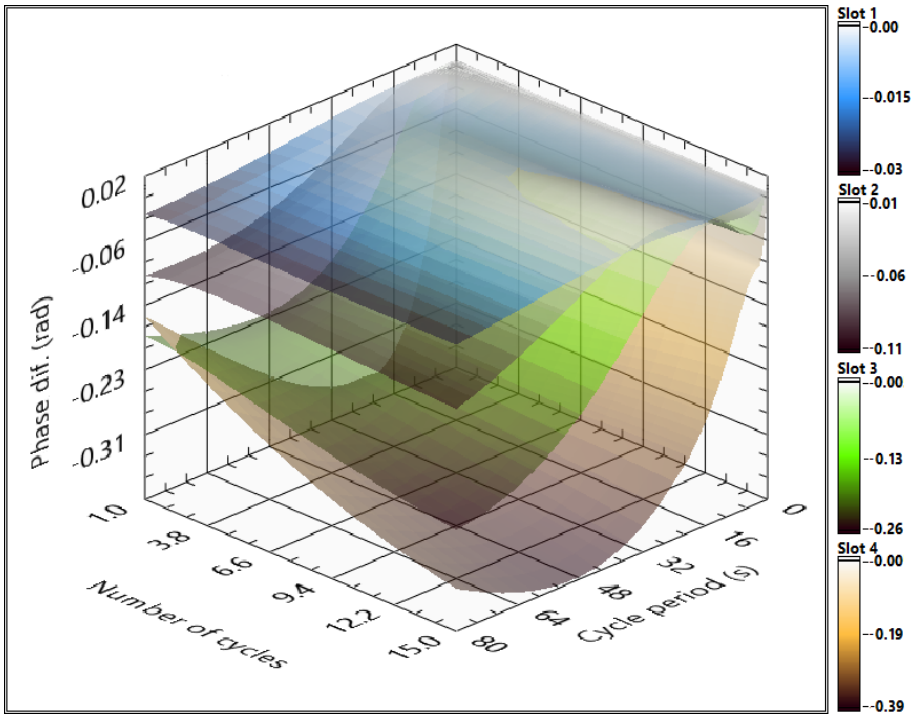

Figure 5.26: Phase difference function of cycle period, number of cycles ans for slots 1 to 4

5.3.4 Optimum settings

Similar the validation performed for the transient analyses, next will be presented the best results for the lock-in tests. Here, it will be used two different samples, one made of PMMA and another made of CFRP. The samples used are the same used to identify the optimum parameters for the transient tests, therefore they will not be described. Similar to TTT optimum settings and for similar reasons, the optimum parameters of the LTT will be defined for a geometry similar to slot 2.

Contrary to the TTT, like already referred, in chapters 3 and 4, in LTT it was not possible to identify a single image that produced the desired results. The best results were obtained when the amplitude and phase images were used. Thus, the optimal parameters will be calculated for these two types of data. It were performed several simulations for different thicknesses and cycle periods. For each simulation an amplitude and phase difference was calculated. These calculations consisted in subtracting the amplitude response in the slot area by the corresponding in the sound area. A similar process was performed for the phase.

In figure 5.27 is represented the amplitude variation for tests with different cycle periods and for samples with several thicknesses, this amplitude surface (AS) is obtained with equation B.7(this is described up front). Here, a longer stimulation will lead to higher temperature differences. The only exception is in the thicker samples and for shorter stimulations. These are important, indicating where the amplitude response will be smaller. The location of these minimums can be calculated using equation B.9. These stimulations should be avoided, if possible. Since increasing the cycle period, no positive inversion point was reached, it was identified the locations where the lower increasing rate occurs (equation 5.9). These locations (green points in figure 5.27) can be described as the ideal location to conduct the tests due to the stability in the amplitude response.

From the analyses performed in chapter 3.3, was concluded that the amplitude images do not provided the most accurate data. Despite a longer stimulation lead to a higher amplitude result, the defect boundaries will become blur. Therefore, the amplitude images are important not for the direct analyses, but to act as quality and accuracy control for the phase images. A higher amplitude response means that the temperature variations are significant and thus leading to less noise in the phase delay images. They can also act as a control preventing any false detection due to blind frequencies. Therefore the equation 5.9 indicates the ideal stimulation for the amplitude analyses. However its relevance is small, when comparing it to the importance of the ideal phase curve. However cycle periods corresponding to the minimum curve (equation B.9) should be avoided at all costs. They have the potential of presenting a zero amplitude response despite the existence of a certain defect. In equations B.7 to B.10 the variable l represents the sample thickness (in millimetres).

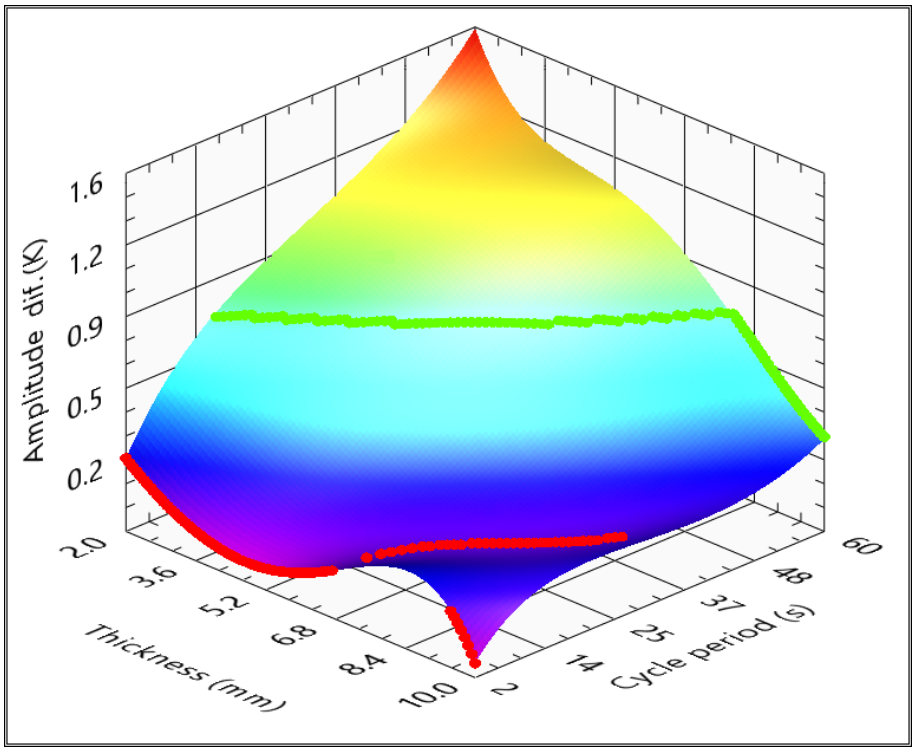

Figure 5.27: Amplitude difference function of PMMA sample thickness and cycle period

$$Cycle\,Period_{recommended}\,(s) = 4.1615 + 11.6358 \times l - 0.5648 \times l^2 \tag{5.9}$$

In previous chapters, the phase images were considered one of the most sensitive ones. Apart from the blind frequencies, these could be used to completely identify and characterize the sample results. In figure 5.28 is represented the phase difference between the reference slot and its surrounding sound area, for different sample thicknesses and cycle periods. The most important conclusion of figure 5.28 is the highlight of the minimum and maximum areas corresponding to the red and green points. Naturally, the existence of a negative area reveals the crossing of the zero axis and consequentially the presence of at least one blind frequency. This corresponds to an inversion in the phase profiles, already observed in the chapters 3.3, 4 and in this same chapter.

The surface presented in figure 5.28 can be divided in three main areas: the peak for thicker samples and short cycle periods, the valley in the diagonal of the surface and the maximum area for the thinner samples and longer stimulations. The first mentioned area is due to the usage of short stimulations. The amplitudes are very low in real and laboratory tests, thus the phase images will present very high level of noise. The area that presents a valley is a direct result from the existence of a blind frequency. From the analyses of the several slots it was concluded that a cycle period that resulted a minimum phase delay of a defect, could correspond to the exact blind frequency of another. As a result, the cycle periods and sample thicknesses of these locations should be avoided. The final area correspond to the maximum obtained for longer stimulus periods.

The maximum area indicates the presence of a higher difference in the phase profiles. These points are observed in long stimulations, for thicknesses lower than 5 millimetres. The ideal stimulations should be located here, since the phase delay is higher and present less fluctuations for a small variation of thickness or cycle period. It is observed a transition for the ideal stimulation (green points). The first conclusion is that for a sample with this thickness, the best stimulation is 2 seconds. Due to the low amplitude, the phase will have a high level of noise. Thus, the best situation is to use a longer stimulation where the amplitude response is significant, reducing the noise in the phase images. Due to the polynomial regression for the phase surface (equation B.8), a vertex appears for the thicker samples (more than 8 millimetres) and for shorter stimulations (less than 10 seconds). This was not actually observed and is a small imperfection of the polynomial regression. For these locations, the phase delay was constant and similar to the local maximum. The same was observed for the results "*behind*" the green points located at the local maximum of the thinner samples. Here the phase results also tend to stabilize near the local maximum.

The usage of LTT and its ideal parameters is highly dependable on the method used to identify and characterize the defect. The ideal parameters should take into consideration where the best results are obtained, using the phase or the amplitude images. While the phase images tend to present higher detectability and signal to noise, the amplitude response should be higher enough to enable the phase image to eliminate most of the existing noise. Overall, the best results using the phase images are obtained using equation 5.10.

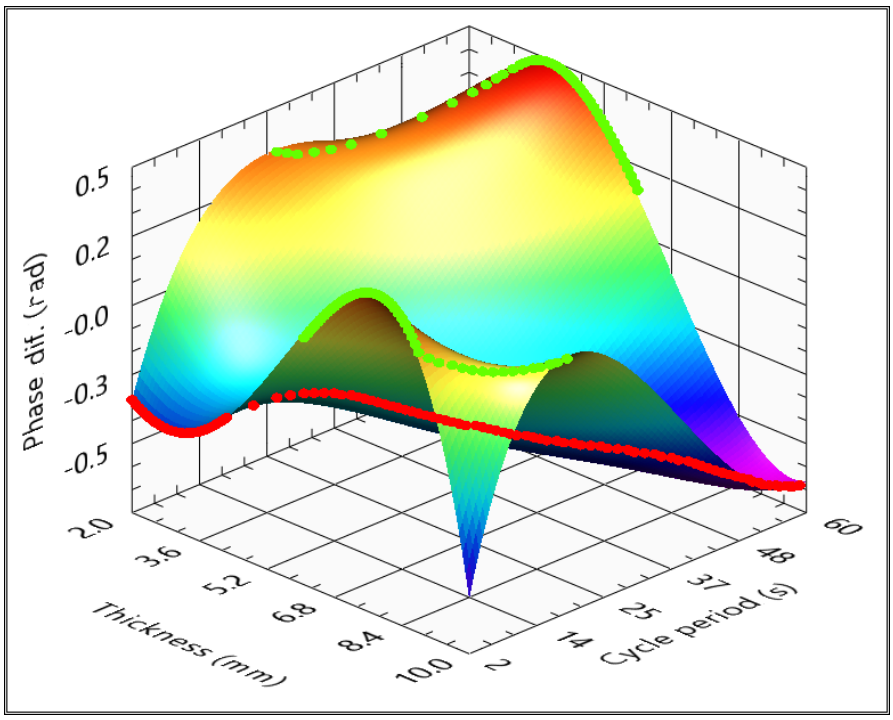

Figure 5.28: Phase difference function of the sample thickness and cycle period of PMMA samples

$$Cycle\,Period_{\,recommended}\,(s) = 3.91 - 6.40 \times l + 2.38 \times l^2 - 0.12 \times y^3 \tag{5.10}$$

Following the approach performed to TTT, the next step is to find the best parameters to conduct a LTT in CRFP. Thus, the same number of simulations was performed, for the already mentioned samples. The LTT simulations followed similar process to the one already mentioned in the TTT simulations for the CFRP samples and its corresponding parameters. Due to the CFRP thermal conductivity, the maximum cycle period was half of the used in the PMMA samples.

Figure 5.29 presents the amplitude temperature difference, similar to the other situations already presented here. These differences were calculated for the sample thicknesses and cycle periods. The amplitude difference response presents a shape that is very similar to the one observed for the PMMA simulations. Despite the maximum cycle period simulated, the correspondent amplitude response for the PMMA sample is higher than for the CFRP. This may be due to the different and higher thermal conductivity in the fiber direction (parallel to the surface) that helps to blur and reduce the superficial thermal patterns, existing in the simulated carbon fibers samples. The higher thermal conductivity decreases the temperature variations during the test. There is an area where the sample clearly does not present any phase difference (smaller cycle periods and thicker samples). This is an area that should be avoided. Here, the thermal response is so low that the noise level will not allow clear image, this limit is obtained using equation 5.11.

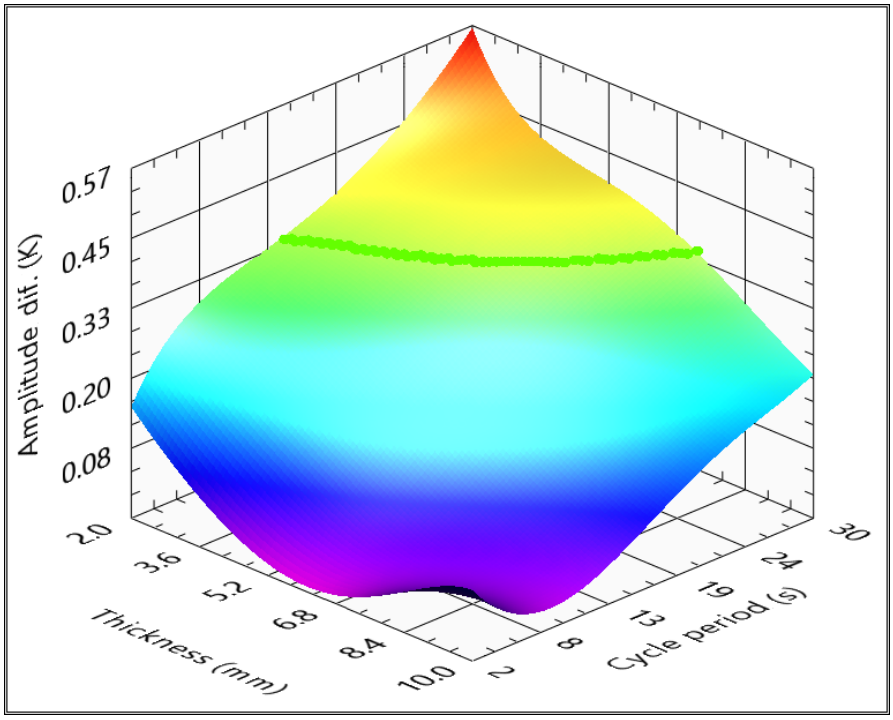

Figure 5.29: Amplitude difference function of the samples thickness and cycle period, for CFRP

$$Cycle\,Period_{minimum}\,(s) = 3.91 - 6.4 \times l + 2.38 \times l^2 - 0.12 \times l^3 \tag{5.11}$$

Finally will be described the influence of the cycle period and sample thickness for the phase response of a CFRP. The phase response for the performed simulation is represented in figure 5.30 with the corresponding surface being equation B.12. An obvious observation is the resemblance between the phase surface corresponding to the CFRP and the PMMA already discussed, apart from the phase and cycle period absolute values. Here the surface also crosses the zero phase plane, revealing the existence of blind frequencies in some situations. Here, it is also advised the usage of longer cycle periods, despite the higher values, obtained with shorter cycle periods for thicker samples. This manner the low amplitude responses will be avoided and the noise existent in the phase images will be smaller. In the aforementioned PMMA phase surface, when reaching the 5 millimetres thickness, the phase revealed the incapacity to maintain a good response. In the phase surface corresponding to the CFRP, the cycle period for which the maximum phase was observed, it is almost proportional to sample thickness. This is obvious in the best phase response given by equation 5.12. Similar to the observed in the previous described phase surface, the local lower peak observed for the sample with 10 millimetres and a cycle period of 2 seconds was not observed. This is an inaccuracy resulting from the polynomial regression. Likewise, the area "*behind*" the ideal points does not present any oscillations. This is fairly flat and with a soft decay towards the point corresponding to the 2 millimetres thickness and stimulation of 30 seconds.

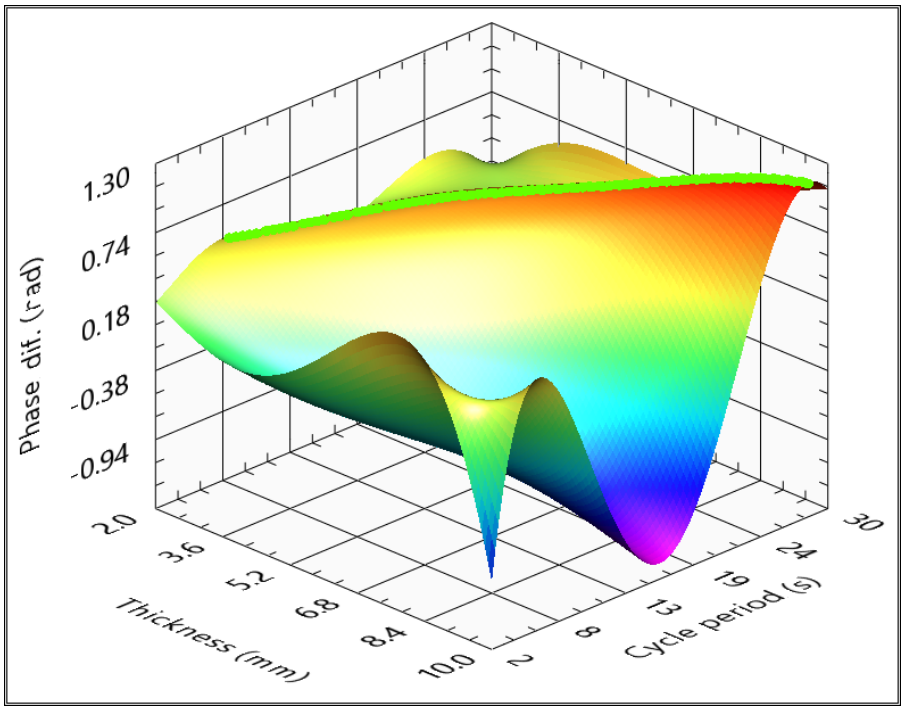

Figure 5.30: Phase difference function of the sample thickness and cycle period of CFRP samples.

$$Cycle\,Period_{recommended} = -2.5 + 5.53 \times l - 0.25 \times l^2 \tag{5.12}$$

5.4 Conclusion

After the analyses of the laboratory conditions, the Biot number was higher than the desired, however, this still allowed the sample simplification into a two dimension surface. The performed simulations were able to represent and mimic the real tests and the situations previous analysed.

Compared with results from a commercial program to perform the numeric simulations, the implementation of a finite element code in Matlab® provided an extra flexibility during the analyses and can provide important results in future works. The comparison of several different meshes prevented the usage of unnecessary elements. Consequentially, the time spent for the simulations was minimized. Without compromising the accuracy of the thermal simulations.

For the transient analyses it was possible to identify the limit and ideal conditions to perform TTT. This was accomplished for both, PMMA and CFRP samples, with various thicknesses. The ideal and limit conditions for both materials were translated into mathematical equations. The surface equation resulting from the polynomial regression easily represented the results obtained with the numeric simulations.

In the lock-in tests, the cyclic stimulation of the laboratory tests introduced an increment in the temperature that prevented the exact overlapping of the temperature evolution curves between the real tests and the simulated ones. The lock-in tests revealed several variations in the thermal patterns and temperature evolution. The temperature variations during a test can be divided in two thermal responses, one from the cyclic stimulation that presents a frequency similar to the one used by the stimulation and another corresponding to an exponential evolution. The amplitude presented a well-defined response for different stimulation periods. It was also very clear the limitation of the amplitude response as a tool to detect defects. The phase variation showed the existence of blind frequencies. Depending on the stimulation period, in some situations they can be minimized by changing the number of cycles used in the analyses. Similar to the observed laboratory tests, these two parameters are the most important when performing a LTT.

The polynomial regression obtained for the parameters surface of the phase (equations B.8 and B.12) revealed some inaccuracies compared to the results obtained by the simulations. The major errors are for the longer stimulations and thinner samples. Since these are far from the critical area of the surface, these differences are not relevant.

Chapter 6

Optimum Stimulus Validation

The third chapter presents some laboratory test and compared the several analyses alternatives. This was performed for the two main types of tests, transient and lock-in tests. In the fifth chapter, based in numeric simulations, was calculated the remaining and crucial parameter to conduct a thermal analyses, the duration of the stimulus. In this chapter, will be verified, through the realization of some key thermal tests these same recommended stimulations.

The first sub-chapter compares the results obtained for the transient thermal test. The second sub-chapter quickly evaluates the lock-in thermal tests. Finally the third sub-chapter performs a rapid comparison with a field optical technology, namely shearography.

The validation of the algorithm that identifies the ideal stimulation is performed using two different samples. The first is made of PMMA, and has four different slots, all with the thickness described in the previous chapter and used to defined recommended stimulations. The second is made of CFRP and has some different blind holes. At the end a comparison with shearography was performed using two of the samples described in chapter 3 and the one made of CFRP.

6.1 Transient test validation

6.1.1 Analyses of a sample made of PMMA

In the previous chapter were presented the equations that give the most accurate stimulation as a function of the sample thickness. In particular, equations 5.7 and B.2 provided the ideal and maximum stimulation periods. The most accurate way to validate these equations is through a series of TTT. These tests were performed using a sample similar to the one used in chapter 3. The difference was in the slots geometry. Here, all the slots have different widths, the depth was kept constant and equal to the second slot. On the contrary, they had different widths, 5.0, 7.5, 10.0 and 12.5 millimetres.

The process followed the already described steps in order to identify the sample edge and calculate averaged temperature profile. The averaged thermal profiles of transient stimulations with durations of 20, 30, 45, 60, 90 and 150 seconds are illustrated in figure 6.1.

Following the simulations and its results presented in figure 5.15, the temperature differences were expect to increase with the stimulations periods. With the 90 and 150 seconds stimulation, the temperature difference was expected to be very similar to one observed with the stimulation of 60 seconds. The major difference between the shorter and longer profiles (apart of the average temperature difference) was the definition of the slots area. This was the reason because the maximum temperature difference was not selected as the ideal stimulation period. This is easily observed for all the slots, being less visible in the ones with smaller diameter. The temperature difference observed in figure 6.1 was approximately 1 K in both situations. This is in agreement with the 0.94 K and 0.96 K obtained by using equation B.1 (PMMA response surface).

From the previous findings it was expected that a wider slot (more than 10 millimetres) did not introduced major temperature differences. For a certain width, this should not introduce significant variations in the temperature differences. By observing figure 6.1 one could verify that the temperature amplitude variations in the profiles were very similar, with the exclusion of the slot with 5 millimetres. In this case, the factor c is smaller than 2 ($c = 5/3$). While this factor was previous reported as the detection limit. A slot with a lower value (lower than 2) was clearly detected. This can be a turning point in the thermal response and consequentially in the technique detectability.

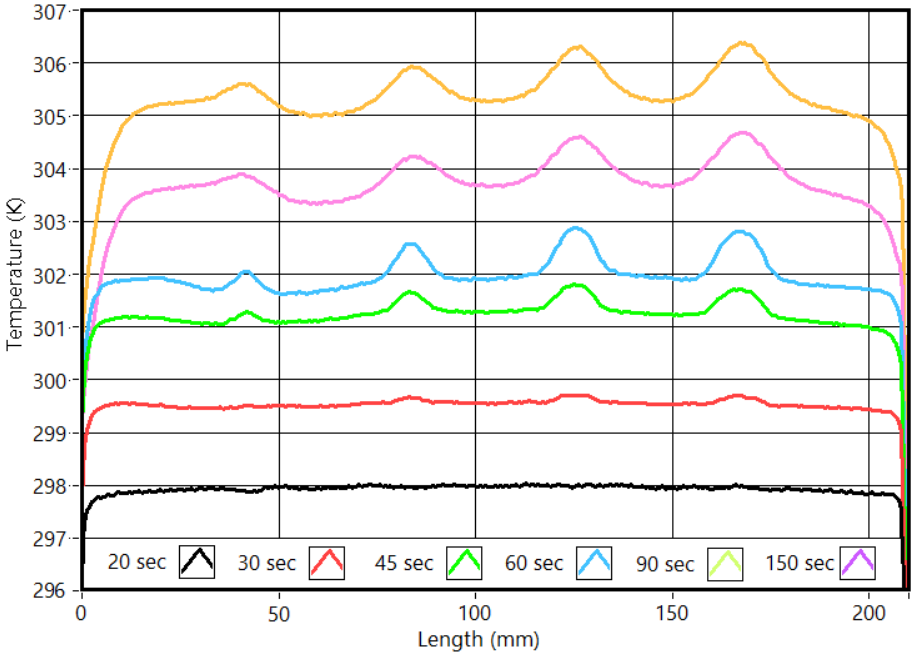

Figure 6.1: Average temperature cross section profiles (10 millimetre width)

6.1.2 Analyses of a sample made of CFRP

To evaluate the numeric simulation regarding a CFRP sample and the consequential algorithm that indicates the ideal an maximum stimulation period, a CFRP sample was build. The sample was designed to be the validation test, having a different thickness, material and slot geometry when compared with the referred so far.

The carbon fiber sample was built from the bounding of four different CFRP plates. Each was 2 millimetres thick and was formed by overlapping seven layers of carbon sheets. This resulted in a total of 28 layers of carbon sheets. For this reason the sample can be observed has a uniform mixture of carbon fiber sheets and resin, thus an isotropic sample. The first plate have three rows of holes, the second have two rows and the third one row while the forth (blue surface in figure 6.2) has no holes and was used as the front plate for the stimulation. The four plates were bound together using the same polymeric resin that was used in the bounding of the carbon sheets. The holes have the following diameters: 10, 16, 20 and 25 millimetres. The sample with all the plates bounded have $206 \times 170 \times 8$ millimetres and several blind holes. Finally the front of the sample was painted with the same black mate varnish (kameralack) from Tetenal®.

According to the results obtained in chapter 5, the ideal and maximum transient stimulation period should have 25 and 38 seconds respectively (blind holes of 4 and 6 millimetres), like results from equations 5.8 and B.5. In figure 6.3 are represented the vertical temperature profiles at the centre of the circular slots for stimulations of 7, 10, 15, 20, 25, 30, 40, 50, 60, and 90 seconds.

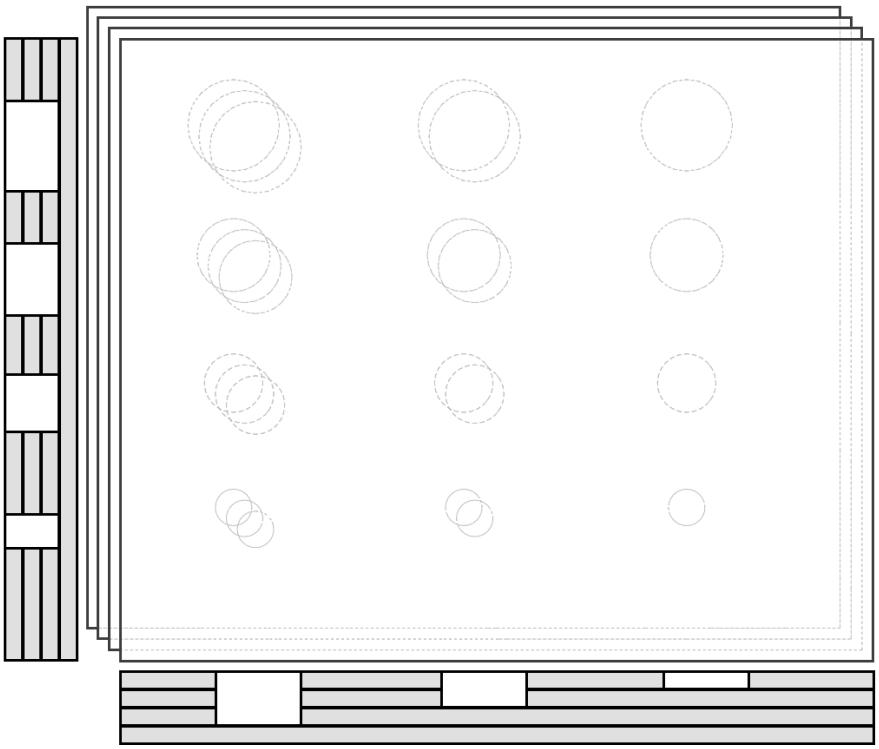

Figure 6.2: CFRP sample geometry

In figure 6.2 are represented the temperature profiles of the left side (figure 6.3a) corresponding to a hole of 6 millimetre and in the middle (figure 6.3b). The highest temperature difference between the holes and the sound area is 2.5 K. This was observed for a stimulation of 40 seconds, being very close to the one calculated, 38 seconds. The edge of the slots, were very difficult to locate in all the tests. The CFRP presented considerable different thermal conductivities in the sheets plane (X and Z axis) *vs* the through the sample (Y axis). Since the conductivity parallel to the sample surface is greater, a blurring in the boundaries was expected.

While not observed a great difference in the holes temperature for the stimulations longer than 25 seconds, the vertical mean temperature was considerably different. A stimulation that considerably increased the mean temperature will lead to results where the defects boundaries will be difficult to identify.

6.2 Lock-in test validation

6.2.1 Analyses of a sample made of PMMA

In the previous chapter were presented the best parameters to perform a lock-in thermal test, either for a PMMA or a CFRP sample. The result revealed that in some cases the usage of phase images can lead to inconclusive results. To overcome some uncertainties, the amplitude image should

always be considered in the evaluation. Following the performed analyses for the TTT, the first sample to be analysed is the one made from PMMA, with four slots, each with a different width. For this case, the optimum parameters can be obtained by the equations B.8 and 5.9.

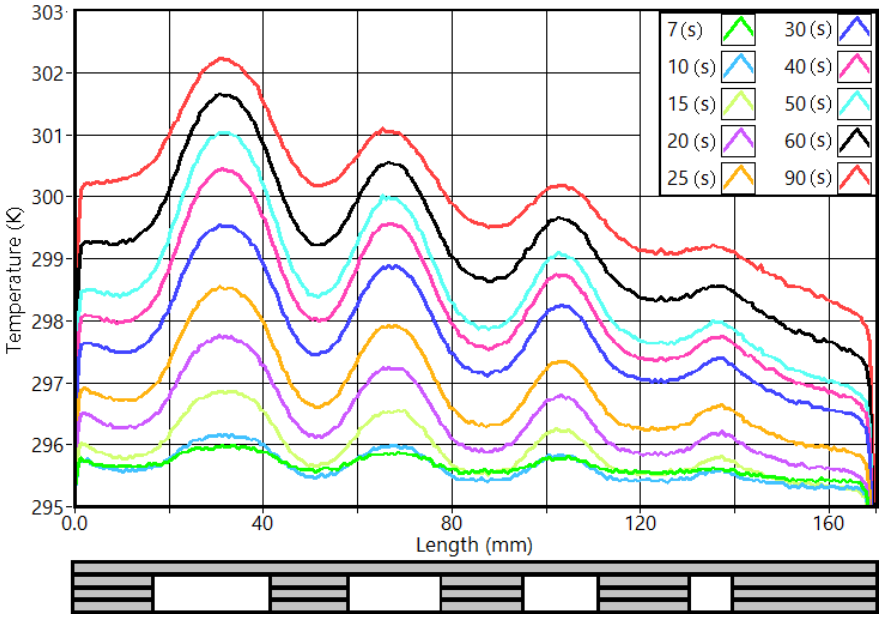

(a) Vertical temperature profiles for the deeper holes (2 mm thick)

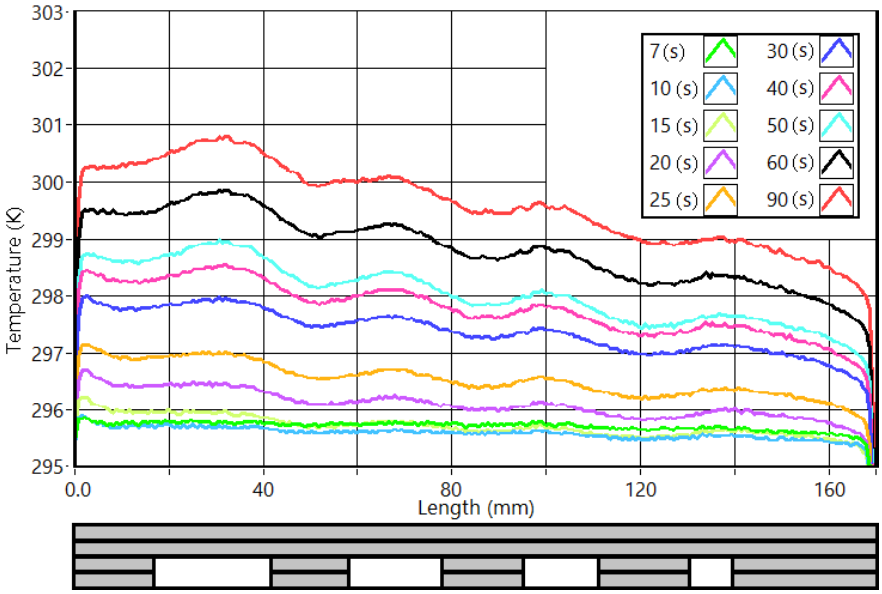

(b) Vertical temperature profiles for the middle holes (4 mm thick)

Figure 6.3: Vertical temperature profiles for the CFRP sample

In Figure 6.4 are illustrated the averaged cross-sections obtained from the tests performed. For the sample of PMMA it was obtained an ideal amplitude response of 39 seconds. By observing figure 6.4a are visible the average cross-section resulting from tests with different cycle periods.

Here is noticeable a small crescendo in the amplitude response of the slots. Along with this increase, the average amplitude response also increases with the cycle period. This was already reported and is due to the higher amount of energy received by the sample. Figure 6.4b illustrates the phase delay in the thermal tests. Like expected, the phase difference is very small (almost non-existing) for the shorter stimulation. With the increase of the cycle period, the phase response in the slots started to increase. Flowing the pattern found in the simulations and the evolution described in the previous chapter, the phase difference at the slots becomes constant. The downside of longer stimulations is fading out the boundaries. In phase profiles this is evident. Apart from the possible identification of very small defects, these LTT should be avoided.

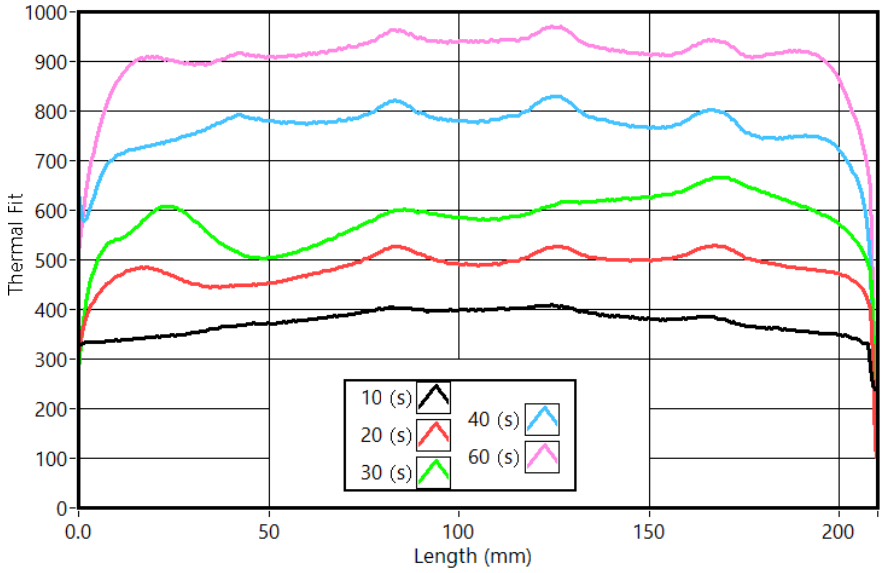

(a) Average amplitude profiles

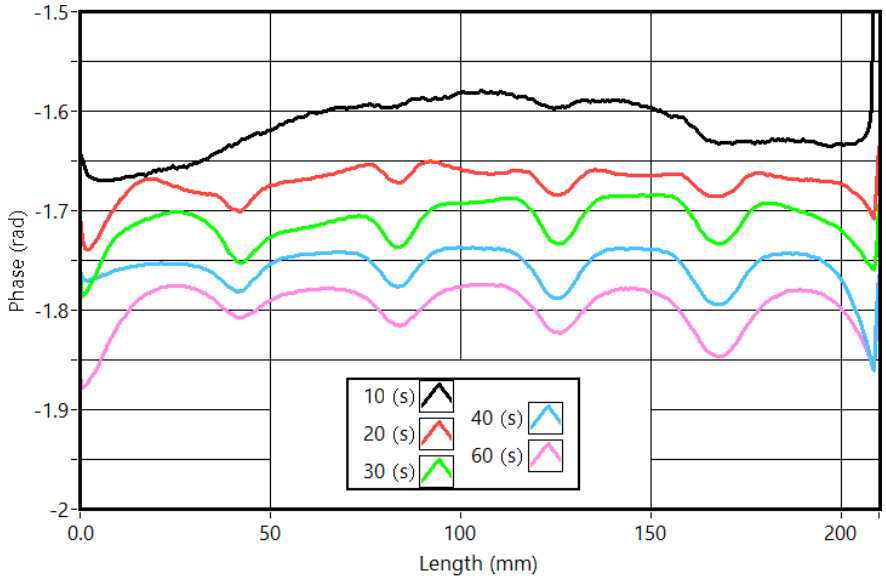

(b) Average phase profiles

Figure 6.4: Average cross section profiles from several LTT

6.2.2 Analyses of a sample made of CFRP

The last analyses refers to the CFRP sample, this being the already described in the validation section for the TTT, possessing circular holes with different diameters and depths.

Performing an analogy to the observations of the PMMA sample, the overall thermal response for the amplitude response should increase almost in a continuous manner with the cycle period. Figure 6.5 presents the vertical profiles for two sets of slots. In 6.5a are illustrated the amplitude profiles of the deeper slots. According to the pattern being described, the amplitude response in the slots should increase for longer cycle periods. This is verified in figures 6.5a and 6.5b corresponding to the slots with 2 and 4 millimetre thick. Naturally, a deeper slot and a longer cycle period lead to higher visibility of the slots in the thermal images. An important aspect is the similarity in the amplitude responses of the 20 and 30 seconds. Thus validating the recommended equation and the calculated simulation.

The phase data should also be analysed, like already observed and discussed, the phase images usually present a higher sensibility. The vertical profiles for the two sets of slots are illustrated in figures 6.6a and 6.6b. Similar to the PMMA samples and its phase, these profiles of the CFRP, present a crescendo with the cycle period. The phase delay revealed small variations for the two shorter cycles. Presenting a considerable variation for the 20 and 30 seconds profile. This follow the behaviour of the PMMA sample and the indicated by the performed simulations (chapter 5.3.4 figure 5.30). The phase delay for the cycle periods of 20 and 30 seconds are extremely similar. While this is not fully predictable from the phase difference surface equation (equation B.12) this is due to the inaccuracy of the modulated equation to accurately represent the results from the simulation.

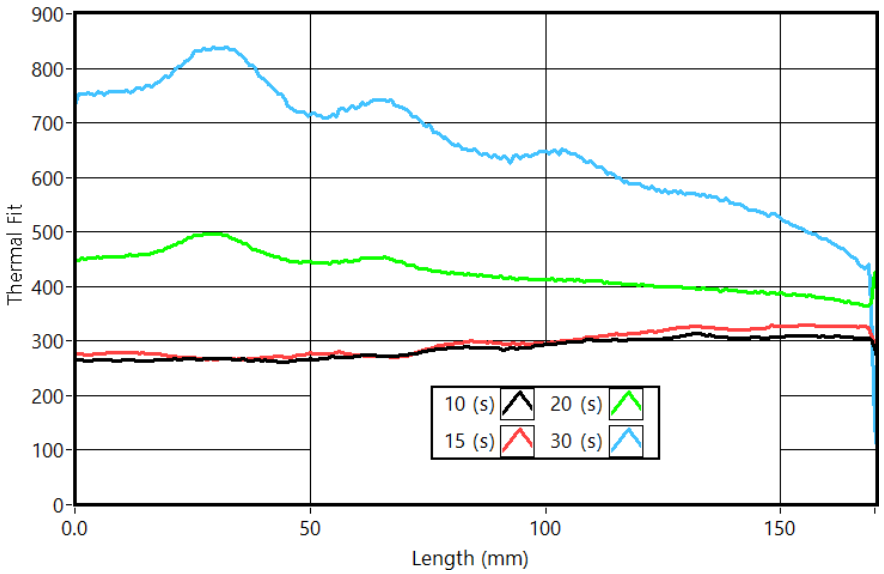

(a) Vertical amplitude profiles for the deeper slots (2 mm thick)

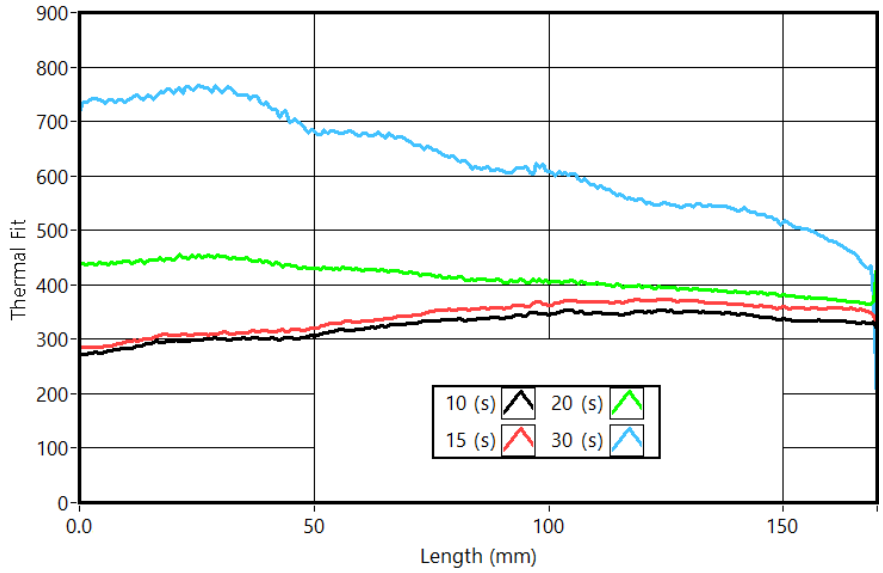

(b) Vertical temperature profiles for the deeper slots (4 mm thick)

Figure 6.5: Vertical amplitude profiles for the CFRP sample

An important aspect is the signal to noise ratio presented by the amplitude and phase. The amplitude images revealed a lower signal to noise ratio than the phase images. In some situations, the blind frequencies can result in a null response, being only visible in the amplitude response. The rapid variation in the phase profiles was predictable, this was observed as the cycle period increased from fifteen to twenty seconds. The temperature, amplitude and phase profiles definition of the boundaries was not yet quantified. The observation of the cross section profiles clearly indicated that a shorter stimulation originates a better boundary definition. From all types of data, the phase images shown to have a higher sensitivity to the stimulus and cycle period variation.

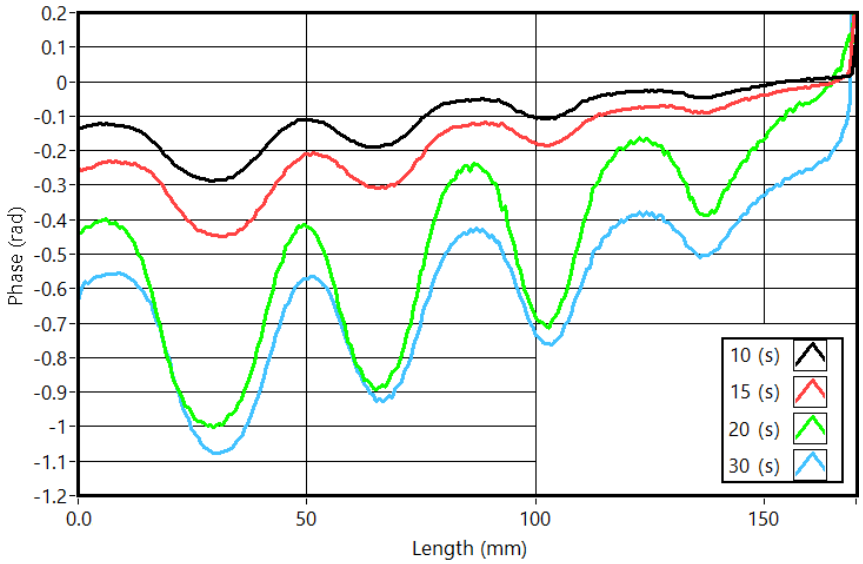

(a) Vertical phase profiles for the deeper slots (2 mm thick)

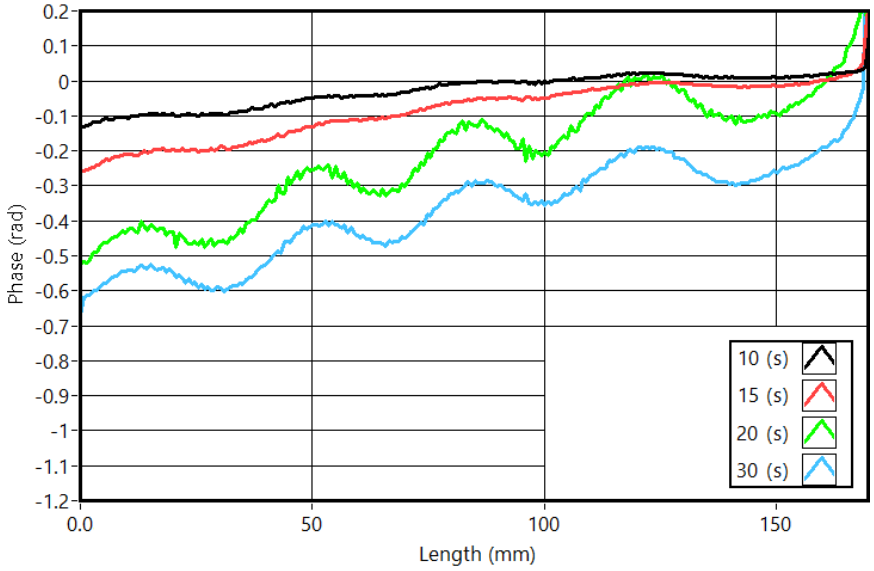

(b) Vertical phase profiles for the deeper slots (4 mm thick)

Figure 6.6: Vertical phase profiles for the CFRP sample

6.2.3 Results eliminating optical reflection

Like already mentioned, the applied stimulation is often different than a sinusoid, introducing errors in the evaluations. Along this, the objects under analyses are not perfect black bodies. Thus, during the stimulation phase part of the measured radiation is not due to the object temperature but is reflected from the stimulation source. Resuming, the radiation captured by the thermal camera (measured radiation MR) is the sum of two components, one resulting from the stimulation reflection with unknown amplitude and a phase of zero (stimulus radiation SR), and a second one corresponding to the radiation emitted by the surface of the object due to its temperature (temperature radiation TR). These radiations and their relations are represented in the figure 6.7 [1].

So far it was discussed the behaviour of the amplitude and phase of the measured radiation (MR), so, with a LTT are determined the length of MR and the angle θ. Thus, to determine the real amplitude and phase delay of the samples is required to determine another parameter, there are two alternatives. The first ones to use feedback stimulation signal and use it in the commercial program to dynamically change the value of the reflected radiation. The second one is to use data from the numeric simulation presented in chapter 5.3.

The commercial software did not permit the usage of an analogue signal in the definition of the reflected radiation. This could be overcome with the development of a custom made application to perform the lock-in thermal tests. However, this means that the reflected radiation (amplitude or phase) would have the natural noise from an analogue acquisition. Another step back is the required characterization of the reflected radiation. Since the stimulation is not a collimated light

[1] The amplitude and phase representations are merely schematic and are not in their real scale or proportionality

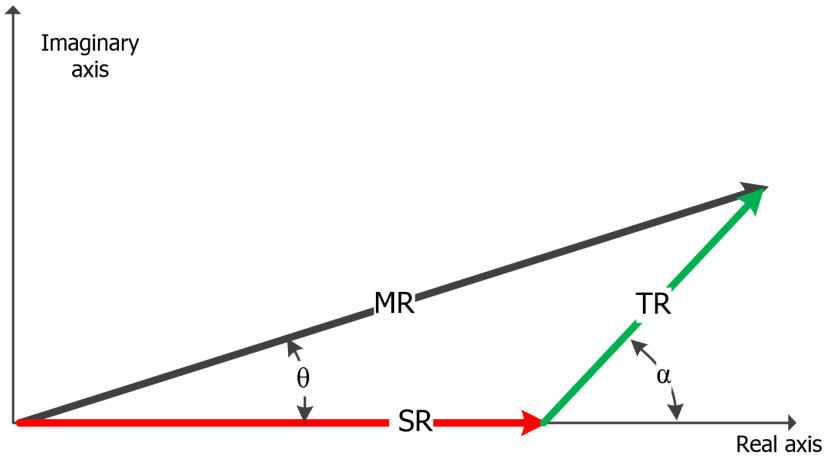

Figure 6.7: Radiation in the thermal image acquisition and their relationship

and the sample is not 100% diffuse, the reflection will have different intensities in each zone of the sample. Thus, the reflected radiation will have different amplitudes.

Another alternative is to use the data obtained in the simulations. With the temperature curves obtained with the simulations it was possible to obtain the real amplitude response without any reflection (TR), as well as the real phase delay α, these being different for each area of the sample. However, areas that are relatively nearby of each other, the difference between the reflected radiations will be small. Therefore, it is possible to subtract a sinusoidal curve (obtained from the measured radiation and then fitted to the measured temperature curves, in order to obtain a temperature curve (measured) similar to the ones simulated. The amplitude and phase was then calculated using 6.1 and 6.2.

$$\begin{aligned} A(\omega) &= |H(j\omega)| \\ \phi(\omega) &= \angle H(j\omega) \end{aligned} \tag{6.1}$$

and

$$\begin{aligned} A(\omega) &= \frac{|Y(j\omega)|}{|X(j\omega)|} \\ \phi(\omega) &= \angle Y(j\omega) - \angle X(j\omega) \end{aligned} \tag{6.2}$$

Where:

- X(jω) - system input (stimulation)
- Y(jω) - system output (temperature measurement)
- H(jω) - real system (sample temperature response)

This second approach was the selected due to its quickness of implementation and the low level of uncertainty introduced in the calculations. These uncertainties are mainly due to the noise existing in the feedback data. In figure 6.8 are presented two images corresponding to the "normal" phase obtained with the commercial software and the "new" phase image obtained with this second method proposed (figure 6.8b). In figure 6.8a is illustrated the phase image from a LTT of the CFRP sample performed with a cycle period of 15 seconds. The stimulation source was located above the sample, thus the upper part of the sample would have a more direct radiation reflection. Thus, in the image is observed a higher response in the upper part of the image, which is decreasing towards the lower part of the image. This results from a higher amplitude or SR, which decreases the measured phase (θ). In figure 6.8b this aspect is clearly not observed. Here, a greater uniformity is observed in the entire specimen, along with a clear improvement in the defect visibility. Along with an improvement in the visualization of the deeper slots (on the left part of the figure 6.8b), the slots at the centre are clearly observed, which did not happen with the common phase image (figure 6.8a). Along with the slots other defects are observed, namely possible deboundings at the periphery of the specimen resulting from the manufacturing process. In the right side of the image are becoming visible the smaller slots, even if not fully identifiable. Throughout this work, several parameters were addressed, both for TTT and for LTT. In Table 6.1 are resumed the most relevant parameters and precautions when performed a thermal test.

(a) Phase image obtained with commercial software without feedback.

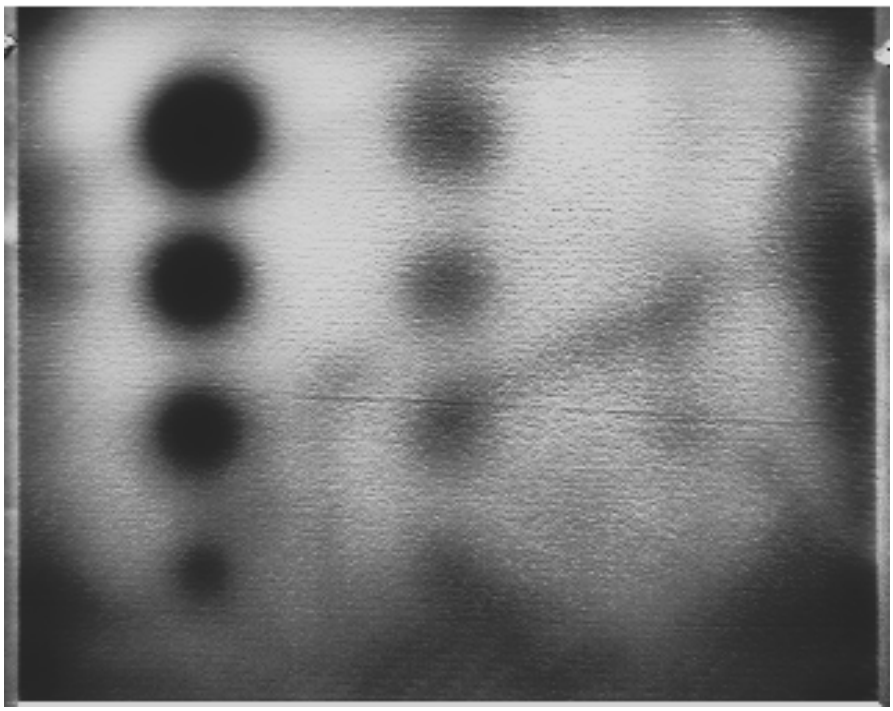

(b) Phase image obtained with alternative processing tool.

Figure 6.8: Phase images for the CFRP sample corresponding to a stimulation of 15 seconds

Table 6.1: Recommendations for Infrared thermal tests

Transient thermal tests		**Lock-in thermal tests**	
Stimulation period	Recommended (function of the nominal thickness)	Cycle period	Recommended (function of the nominal thickness)
Instant of analyzes	After the stimulation	Number of cycles	Typically 7
Sample maximum thickness	For CFRP thicknesses smaller than 5 mm produce better results	Sample maximum thickness	The recommended cycle period was calculated up-to 1m mm
Lower c coefficient	Approximately 2	Lower c coefficient	Approximately 5/3
Analyses type	Reconstruction	Analyses type	Phase images, these should be confirmed with other data due to possible blind frequencies
Precautions	Analyses has to be performed after the stimulation is 100 % off	Precautions	Errors can occur in the stimulation sinusoidal waveform, feedback sensor is advised

6.3 Comparison with shearography

Along with the validation of the developed algorithm to identify the best settings for a certain type of test and sample. It is also important to ensure that the result of the thermal tests is relevant when compared with other NDT techniques. To finalize the results obtained with thermography for the PMMA sample with slots of 10 mm width is compared with shearography. Shearography is a field image technique described in the second chapter.

The test with shearography, consisted in a small warm up similar to the performed in the transient analyses. Several tests were performed to find a set-up and protocol that delivered a good result. Since shearography measures (indirect measures) extremely small displacements, the interpretation of the results is not so clear has in the case of thermography. The best result were obtained using the phase-shift technique, with this image being presented in figure 6.9a. The pattern variation in the speckle indicates the existence of a variation in the sample position. Through the variations in the colour patterns, it is possible to identify the existence of the third and fourth slot. The second slot is partially identified and the first is not even detected. In all the slots the boundaries are hard to identify. This aspect is even more evident in the top and bottom slots.

The results from the transient analyses are presented in figure 6.9b. Here, all the slots are clearly identified, with the thermal responses being smaller for the first slot and higher for the fourth one. A soft vertical gradient is observed in both, the sound areas and the vertical slots. This is due to the natural convention existing from the sample warm-up and is not observed in the shearography image, being this almost horizontally symmetrical. This can be overcome by performing the tests with the sample in a horizontal position however, this was not performed to simulate the worst condition found in real situations.

Figure 6.9c illustrates the amplitude image of a LTT. Here the first slot is not visible. The slots boundaries are not well defined in all the situations. This was predictable since the cycle period was selected to maximize the phase results. Here is also observed a small vertical gradient in the entire sample. Like mentioned before, the amplitude response should be impermeable to frequencies different from the stimulation, like the slow convection flow. Since the stimulation was positioned above the sample, this was more reflective at the top of the sample.

Since the LTT cycle period was chosen so that the phase image revealed the best results possible, it was expected that figure 6.9d presented the best results. By comparing the first slot in all the images this is clear. The slots boundaries are also well defined, either on the slots sides, or on the extremities (top and bottom). The vertical gradient present in other images is not visible. On the downside, the sample boundaries present a small gradient. This is due to the heat loss at the boundaries with the environment.

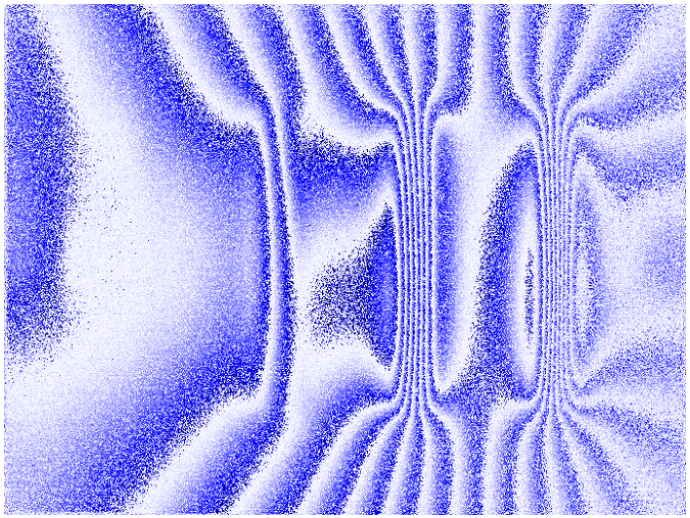

(a) Shearography phase image

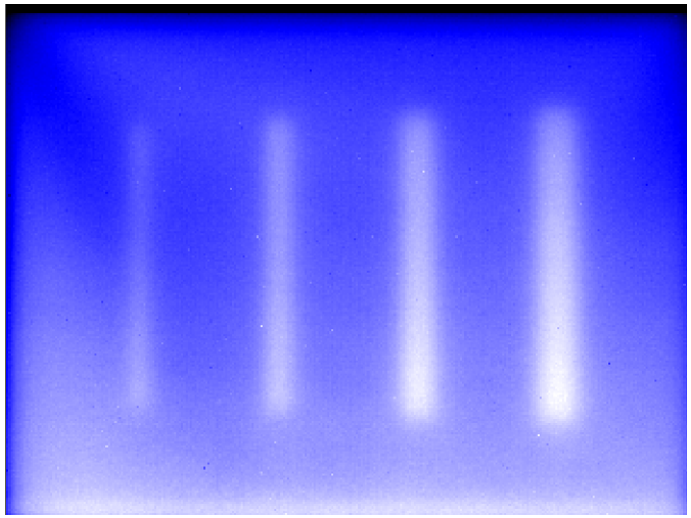

(b) Best image from the TTT

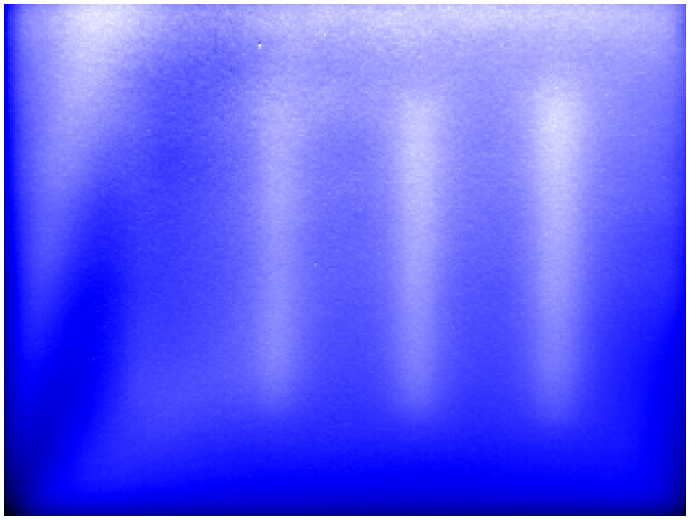

(c) Amplitude image for the ideal test

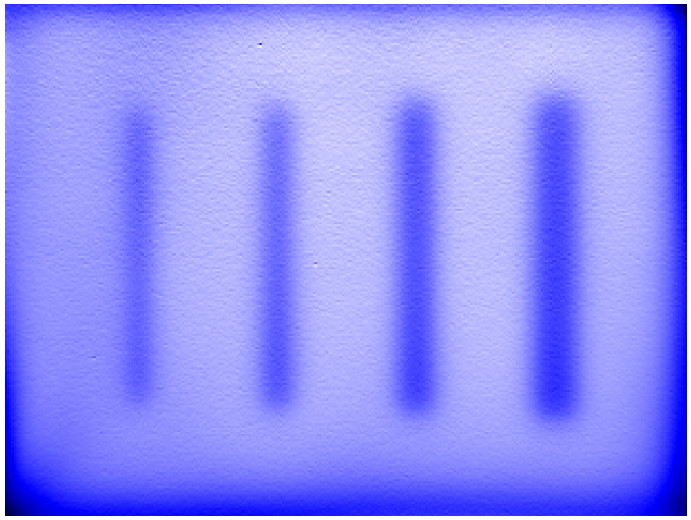

(d) Phase image from the ideal test

Figure 6.9: Images obtained by different techniques

6.4 Conclusion

After the definition of the ideal parameters for a transient and lock-in thermal analyses, the missing block was to validate the obtained results.

The TTT were initially tested in a PMMA sample. The developed algorithms for these samples were successfully tested and validated. The parallelism to a CFRP sample was also accomplished. Similar to the PMMA sample, the tests revealed a good correspondence between the TTT and the ideal parameters. To increase the confidence in the developed algorithm, the CFRP slots had a different geometry.

In parallel with an algorithm to optimize the TTT stimulation period, another one was also developed to optimize the LTT cycle period. This was tested with a different sample made from PMMA. The results from these tests revealed a dual optimum situation, already identified in the simulations. Depending on the analyses, the ideal parameters were validated. The validation process also was performed in a CFRP sample. The sample was the same used in the TTT. Like expected, the validation tests confirmed the optimum parameters described in the previous chapter.

As a conclusion of this work, comparing the images resulting from the ideal tests already described. The comparison was made between the amplitude and phase images from a LTT, a thermal image from a TTT and the result obtained from a shearography test (phase image). While the data resulting from each analyses is not comparable, the phase image revealed the best results in the majority of the observations.

This page was intentionally left blank.

Chapter 7

Conclusions

Composite materials, in particular CFRP, are vastly used in structural components in aeronautic industry due to their mechanical properties. In aeronautics, the presence of any defect in a component may result in a catastrophic event, which may be detected by non-destructive tests (NDT).

Radiographic and ultrasound testing use either ionizing radiation or are incapable of analysing large areas. Infrared thermography does not present either of these disadvantages and can produce very good and accurate results, being currently part of the standards in aeronautics, such as the ISO-10880, among others. Infrared techniques can scan large surface areas in a short time with great sensibility and accuracy.

This work intends to contribute to Infrared Non-destructive Testing (IRNDT) efficiency by recommending the test and analysing parameters that will produce the best results leading to a higher sensitivity to defects defection in composite boards. This objective was fully accomplished and correctly validated with Carbon Fiber Reinforced Polymers (CFRP) samples.

Generally, the Active Infrared Thermal Tests (AIRTT) is the correct method to detect and characterize the defects in composite materials in reflective mode. Like observed in laboratory tests, the same sample and defect can produce different results, depending on the parameters used during the test, such as: stimulation or cycle period, instant of analysis, single or cyclic stimulation, among others. Several works have been published tempting to revert the thermal images in order to geometrically define the samples and their defects. Without a guideline that defines the correct parameters, this task is almost impossible to generalize.

This work was divided into four main tasks: experimental testing of samples, simulation of thermal response, analysis of the best parameters to improve defect detection, and finally validation of results.

The laboratory tests served to evaluate the influence of several parameters in the results and as reference to the numeric simulations. The laboratory tests covered all of the most important variations and configurations possible in the infrared thermal testing. This was performed for the two most important techniques, transient and lock-in thermal testing. Transient Thermal Testing (TTT) and Lock-in Thermal Tests (LTT) were performed to identify the combinations and settings that resulted in better defect detection. During the laboratory tests an imperfection in the optical stimulation waveform was observed. It was concluded that this largely influenced the results and the technique' sensibility and accuracy. The optical stimulation revealed difficulties in providing sinusoidal stimulations with frequencies higher than 0.27 Hz. When using a transient stimulation, the optical response required near one second to stabilize. Overall the stimulation presents faster responses to raising than to falling. Two approaches were implemented: the usage of the real stimulation in the analysis and the creation of a stimulation that had higher similarities with a sinusoid through the usage of a PID controller. The usage of the stimulation feedback revealed significant improvements in the thermal images. These improvements were mirrored when a PID controller was applied to the stimulation in order to produce a real sinusoidal stimulation. It was concluded that the correct correspondence between the stimulation wave and the one used as reference in the lock-in calculus is required. Despite its importance in LTT, it was not found any literature concerning this matter. In this work only one system was tested, however most certainly other commercial systems present similar dynamic responses.

The numeric analysis of the temperature during thermal tests revealed a Biot number that required the consideration of the heat loss by convection. However, this was small enough to allow the simplification of the tridimensional volume into a simpler two dimensional shape. The performed simulations were capable of accurately mimic the laboratory tests and situations previous analysed. The only significant difference was due to the optical reflection of the stimulation, mainly in the LTT. The comparison of several mesh prevented the usage of unnecessary elements, without reducing the accuracy of the temperature simulations and its accurate representation of the temperatures observed in the laboratory tests.

In the transient test it was possible to pinpoint the limit conditions and recommend conditions to perform TTT in PMMA and CFRP samples. The validation using a different PMMA sample assured the accuracy of the entire procedure and the simulations to delimit the ideal situations to perform a TTT in a CFRP. Nonetheless, the model for the recommended parameters was validated with a sample made of CFRP with several holes instated of slots. The recommended and limit conditions for both materials were converted into mathematical equations.

During the lock-in tests, the cyclic stimulation introduced an increment in the temperature measurements that prevented the exact correspondence of the temperature during the entire test. The lock-in tests revealed several indirect variations in the thermal patterns and temperature evolution. During a test the temperature variations can be divided in two thermal responses,

an exponential evolution and a cyclic temperature variation corresponding to the optical cyclic stimulation. The amplitude presented a well-defined response for different stimulation periods. It was also evident, in some tests, the limitation of the amplitude images as a tool to detect defects. On the other side, the phase images presented evidences of blind frequencies. Depending on the stimulation period, these can be overcome by changing the number of cycles used in the analyses. With these two situations it was not possible to identify a generic ideal cycle period for the LTT.

The polynomial regression obtained for the parameters revealed some inaccuracies compared to the results obtained by the simulations. These limitations are clear and do not affect the equations of the ideal parameters since they are located in the extremities of the prediction surfaces. These errors related to oscillations were not observed for the longer stimulations and thinner samples. In the LTT was observed that the amplitude is required to have a significant value. For smaller amplitude stimulation, the temperature differences will be very low, resulting in a high level of noise in the phase images. A longer cycle period does not decrease the amplitude or phase images, however will highly decrease the boundaries identification (blurring). The parallelism between the PMMA and CFRP samples was very good despite the heterogeneity anisotropy of the last. Similar to the PMMA sample, the tests revealed a good correspondence between the TTT and its ideal parameters. To increase the assurance given by the ideal parameters, the slots in the CFRP sample had a different geometry. This increased the confidence in the developed algorithm.

At the end of the work a quick comparison among the two techniques and shearography was performed. While the data resulting from each one/of them is not comparable, the area corresponding to the sample was cropped and qualitatively compared. The phase image revealed the best results in the majority of the observations. Shearography revealed to produce images that are difficult to interpret without any gain when compared to thermography. The TTT presented better results than the amplitude image and worse than the phase. Shearography revealed to be insensitive to the vertical natural convention currents, while with thermography this was only observed in the phase data. However, the latter may result of the stimulation being applied from above the sample, resulting in a higher optical reflection in the upper sections of the sample.

7.1 Contributions

The use of Active Infrared Non-destructive Testing (AIRNDT) is becoming more common as this technology is contactless and relatively fast to operate. However, the settings used for the thermal stimulation and the timing of the image acquisition are critical to the performance of the method. Thus, the contributions of this work to the state-of-the-art are:

a) recommended stimulation and cycle period equations to be used in transient and lock-in thermal tests, for samples made from poly-methyl-meth-acrylate and from carbon fiber reinforced polymers;

b) estimation of amplitude and phase thermal response of the lock-in tests;

c) estimation of the thermal response of sample under transient or cyclic stimulation, and thus selection the most suitable;

d) database of thermal tests (transient, lock-in and thermoelastic stress tests) that can be used to evaluate other processing tools;

e) Matlab toolbox to perform numeric simulation of thermal tests with 3, 4 or 8 nodes and any desired waveform, also being possible to apply differentiated stimulations to each node;

f) light feedback device to be used in IRNDT equipment to provide optical feedback and thus improve the accuracy of the tests.

7.2 Future works

In the transient analysis it was determined the ideal stimulation period based on the cooling phase analysis. Despite the reflected radiation from the stimulation, the warming phase can also be used to identify defects. This phase of the test presents an additional advantage since it can allows the analysis to be shorter and also longer stimulations in a single test.

The temperature of the lock-in tests revealed the presence of two types of curves, an exponential and a sinusoidal wave. The lock-in processing algorithms only use the sinusoidal waves. The creation of a new analysis tool that combined the two types of information could greatly increase the accuracy of the technique.

The lock-in stimulation presented considerable errors in the sinusoidal waves created. This aspect should be tested and compared with other commercial systems. Similar results should lead to the creation of a standard equipment to measure the optical stimulation during the tests.

In this work two types of infrared thermal tests were analysed, transient and lock-in. However, flash thermography is also very popular and usually presents good results, especially with materials with high thermal conductivities. It is also very important to define the influence of the test parameters in flash thermography.

During the Lock-in tests, one of the downsides was the reflected radiation. It was shown that it is possible to remove the reflected radiation. Using the reference signal it may be possible to eliminate the temperature variations with a zero phase. A similar processing is used in Thermal Stress Tests to calculate the mechanical stress in two perpendicular directions.

In the last decades LED have evolved and are now present all-around. LEDs can deliver a high dynamic response, thus providing stimulation waves with a very precise waveform and with a narrow wavelength. These may allow the application of a transient stimulation and evaluate the warm-up phase, shutting down the stimulation for a few milliseconds to capture the thermal images without any reflected radiation. This rapid stimulation cut-down can also be used in other wave types like cyclic waveforms.

In appendix A, several Thermoelastic Stress Analysis (TSA) are presented and analysed. Despite the experimental findings these should be simulated to fully understand the temperature behaviour and improve the tests' accuracy and creation of an algorithm to determine the SIF "*in situ*".

This page was intentionally left blank.

Appendix A

Thermal Stress Analyses

A.1 Thermal stress testing

The main goal of this section is to describe the thermal patterns obtained during a common thermal stress test (TSA). A detailed emphases is given to the crack tip and progression path. The tests and consequential analyses were performed for several frequencies to access the frequency influence in the thermal pattern evolution.

A.1.1 Overview

Nowadays, structural components where weight is a critical requirement, like in the aeronautics, are usually calculated based in damage tolerance design principle. Thus, the structure must endure the appearance and evolution of small abnormalities (like cracks or certain impact related damages) until the next maintenance operation. This principle usually leads to frequent inspections operations, to minimize the danger these type of defects may represent to the safety. Today, approximately 90% of the failures in metallic structures result from fatigue or fatigue cracks, making it the most dangerous failure cause and critical issue [208]. In addition, the crack and its propagation will change the shape of the component during its life service. As a consequence, the load transferred to other components may also vary. This results in a variation in the complete structure behaviour and transferred loads, increasing the demand for technologies that can measure the stress in situ. Therefore, the early detection of cracks in structural and mechanical components is of extreme importance for the safety of the users and the complete structural integrity. Making the crack detection and monitoring, a critical phase in aeronautic maintenance procedures and standards. One of the most accepted techniques to detect and identify cracks, is linear ultrasonic evaluation [209]. Here, the reflection and refraction transmission of ultrasound waves propagation is used [210, 211]. The introduction of nonlinear ultrasonic techniques results in an even more precise detection [212, 213]. The downside is the complexity of the processing algorithms, user expertise, experience, and the difficulties in separate the real crack from its reflections.

Alternatively, one can use other relevant technologies to access defects using non-destructive image testing techniques, infrared thermography [209], with several known advantages, namely measurement without contact and the possibility of scanning large areas. The existence of any thermal alterations, due to the mechanical damage in metals is a well and established fact [214]. Therefore, one of the most promising techniques, in the field of defect detection and monitorization is infrared thermography (IRT). Crack detection using IRT can be achieved using one of several techniques, depending of the crack direction, shape, size and material [215–217]. As so, usually the best results are achieved using an external and controlled stimulation source which minimizes the uncertainties and errors in the interpretation of the results. In this case, the component to be inspected is subjected to a small increment in its local internal energy. The existence of any crack or void changes the direction of temperature flow in the interior of the component, making the changes noticeable at surface.

To characterize a fatigue crack in a component using thermography, the most effective method is to apply a load to the component and register its thermal response - thermal stress test (TSA). This consists in applying a load with specific characteristics (pattern, mean, amplitude, direction and frequency) to a component with a crack in order to assess it. In 1979 D. S. Mountain and J. M. B. Webber developed the first thermoelastic stress analyses system, the SPATE. This test was based in the reversible, adiabatic thermodynamics principle of isotropic materials [218]. In this method, a thermal imaging system was used to evaluate the presence of the stress in a certain component, using the thermoelastic properties of the material under study. The thermoelasticity of a certain material defines its temperature variation when subjected to a cyclic stress. In order to measure this phenomenon, the load should be applied with a frequency between 5 and 200 Hz [219]. The results of a TSA depend on the load average, amplitude and waveform, component mean temperature, material anisotropy and crack orientation relative to the load direction.

The existence of a crack leads to an unwanted variation in the component geometry. As a result, in the crack tip it will appear a stress concentration that tends to increase the crack itself. This localized stress is visualized by thermography as a local temperature decrease or increase, depending if the sample is subjected to tensile or compression phase of the cycle. The thermoelastic coefficient of the material links local stress with the temperature variation. Since these are usually very low, the temperature variations are very small (approximately for aluminium 50 mK), consequently, several cycles are necessary to achieve an image with enough signal to noise ratio. This image (amplitude response) is calculated using a phase lock loop algorithm, similar to the one used in lock-in thermography. The stress is then calculated using the amplitude response image for the stress value and the phase to determine the stress signal (0 to 180 degrees positive and 180 to 360 negative).

The Stress Intensity Factor (SIF) progression can represent and be correlated, for a specific material or alloy, with the crack progression rate. Thus, the remaining cycles until structure

failure, i.e. the component remaining life. Therefore one of the most important parameters in crack detection, progression and monitorization is SIF.

The current regulation to assess the fatigue crack growth measurement and data analysis is set by ASTM E 647-08 [220]. This standard describes the shape, size and test conditions for several specimens and their crack propagation conditions. Therefore, this work was developed according with the indications presented in the referred document.

The main goal of this section was to access the thermal patterns during a thermal stress test. A detailed observation is given to the crack tip and progression path. The tests and consequent analysis were performed for several frequencies in order to assess its influence in the thermal patterns.

A.1.2 Experimental protocol

To conduct the tests it was used a stress-strain testing machine from Instron ®, model ElectroPuls E1000. The test load was set to a sinusoidal profile, varying from 75 to 750 N of tensile force at a constant frequency. Two different cameras were used to monitor the specimen crack length and progression. The first was a visible camera (AT3.5) with a zoom lenses of 12.5×. The thermal camera was from FLIR™, model 7500 MWIR with a measurement waveband from 1.5 to 5.1 μm and a spatial resolution of 320x256 pixels. For all tests the acquisition frequency was adjusted to be ten times higher than the stimulation load. The specimen was made of aluminium (2219–T851) with the geometry recommended by the ASTM E 647-08 for compact specimen, figure A.1a. The sample has a thickness of 2 millimetres and the dimensions indicated in figure A.1a. For a higher and uniform emissivity, the specimen was painted with a black mate black varnish (kameralack) from Tetenal.

Emissivity is the most important parameter when conduct a quantitative infrared thermography measurement and analysis, at ambient temperature in a closed environment. Indeed, even a small error in the emissivity will lead to a large stress estimation error, since the temperature increase is only about 0.05 K. To eliminate any uncertainty, the emissivity was experimentally determined. For this, the same varnish applied to the specimen was also used in a Peltier element that was warmed and cooled until reaching a certain steady temperature. Alongside with the thermal camera, it was used a RTD sensor and a NI-9219 with a NI USB-912 carrier to measure the Peltier temperature. The emissivity was adjusted in the software to obtain the same gradient for the temperature measurements (with RTD and Thermography). This process was repeated for five different temperatures values, reaching this way the emissivity of 0.97. This procedure was performed in ambient conditions similar to the ones of the TSA tests.

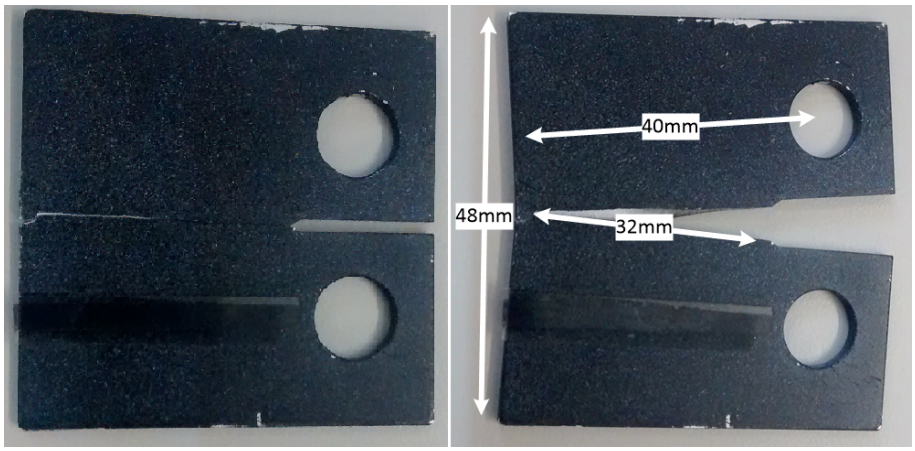

(a) Test specimen before and after rupture

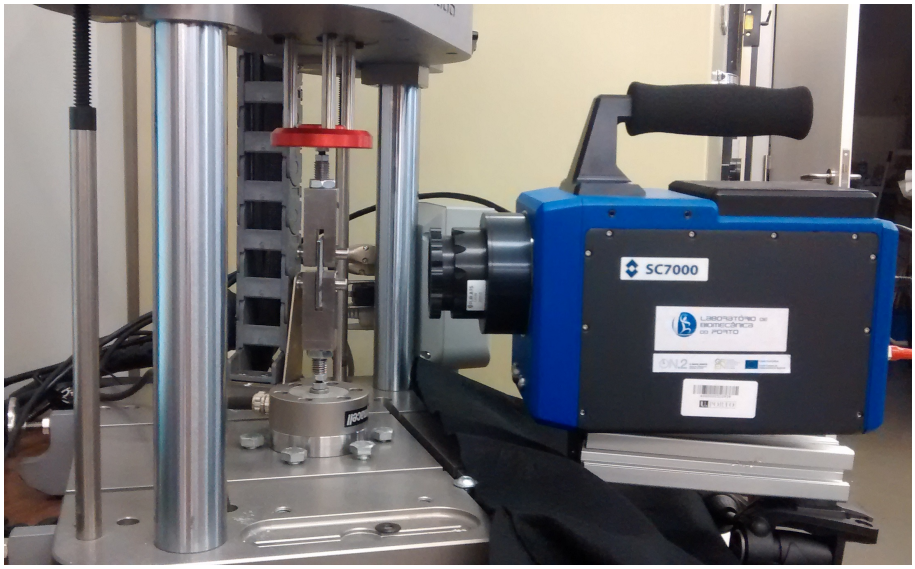

(b) Thermal camera and sample positioning

Figure A.1: Test sample and set-up

The crack length was measured at the beginning and at the end of the two sets of TSA tests. During a set of tests, the crack length and its corresponding growth rate was estimated. The estimation was based in the progression rate of another specimen, previously tested until rupture. For each measurement were used 1050 cycles for the crack progression and 200 cycles for measurement (TSA test). The crack evolution during this initial test is represented in figure A.2a. Using a third order approximation it was achieved a correlation of 0.994 between the number of cycles and the crack length (figure A.2a). Using this approximation it is possible to estimate the crack growth during one cycle. Deriving the regression equation obtained previously, it is obtained a maximum crack progression rate of approximately 0.2 μm per cycle up until the 70 000 cycles, as visible in figure A.2b. After these the crack progression during a single TSA test with 250

cycles surpasses 0.5 mm, resulting in considerable errors in the thermal measurements.

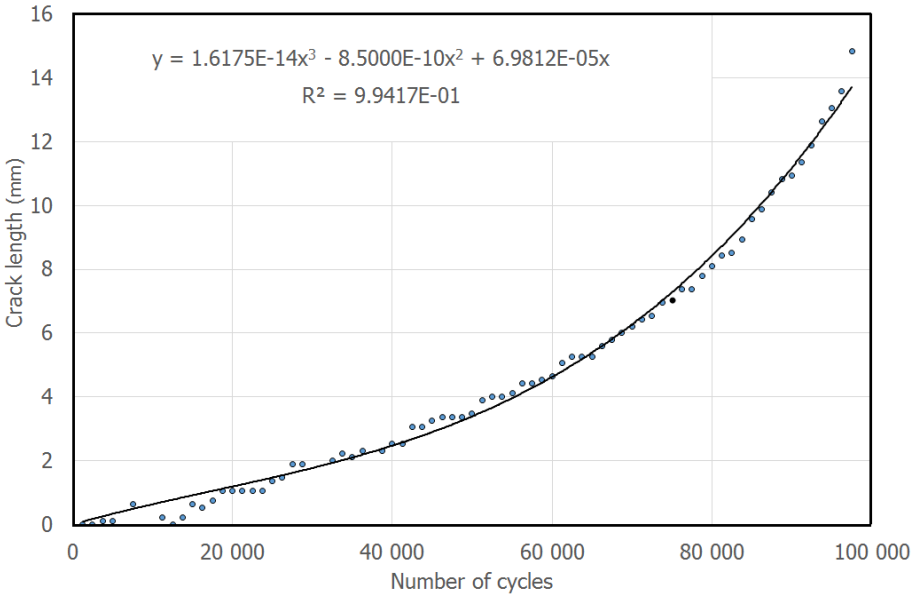

(a) Crack length during a test, up until rupture

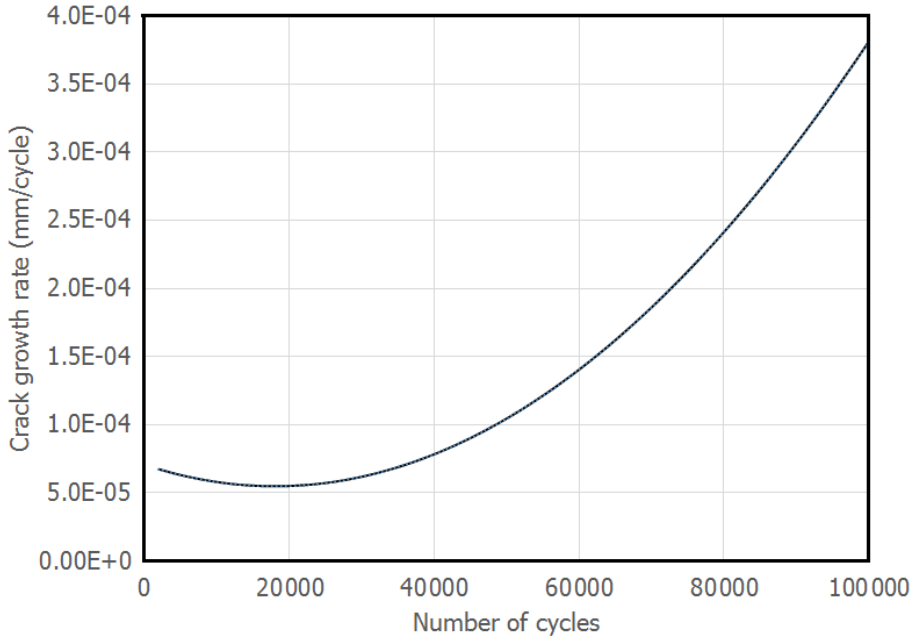

(b) Crack growth rate until rupture

Figure A.2: Crack evolution in initial tests

The specimen tests were divided into two different phases, each one corresponding to a different crack length. In each phase the crack length was monitored before and after the TSA test using the visible camera and a ruler with 4 lines/mm. During an entire phase, the specimen was subjected to several TSA tests. Each test was divided into three different steps: loading, stabilization and monitorization. In the loading step (3 seconds), a load was applied starting from 0 up to 412.5 N,

this value corresponds to the mean value of the sinusoidal load. The stabilization step served to unify the temperature in the specimen and also had a duration of 3 seconds. The monitorization step consisted in the application of a sinusoidal load, ranging from 75 to 750N at a constant frequency. To assess the frequency influence in the thermal patterns of the TSA test, several tests were performed at different frequencies: 2.5, 5, 10, 20, 30, 40, 50, 60, and 70 Hz, and thus complete one phase. The tests for each frequency consisted in a complete phase.

During the monitorization test, the thermal camera was set to acquire images at ten times the frequency of the stimulation, which had a duration of 100 cycles for each test. Since the thermal camera was not able to acquire images at 700 Hz at full frame, it was used a windowing parameter resulting in an image with 320x100 pixel (for all the tests). This, enabled a detailed monitorization of the area and path of the crack during all the tests and without changing the integration time of the camera for which it was calibrated. All the images were recorded in the computer RAM memory and analysed using the IRNDT software from Automation Technology$^{\text{Inc}}$.

The processing algorithm used to assess the stress images is based in lock-in principle. This uses a reference signal from the test machine as a reference input (100 N/V) to calculate the amplitude and phase response of each pixel. Several authors suggest values of approximately 8.2 E-6 for the aluminium thermoelastic coefficient, however, the software maker (IRNDT version 1.7 2008) indicates the value of 7.7 E-6. To confirm this coefficient, a rectangular aluminium bar with 180 x 10 x 1.5 mm was instrumented with two strain gages, one in each side, to measure the induced strain. The bar was tested using two different loads: a static and a dynamic load with several frequencies in the direction of the strain gages, while TSA tests were performed using thermography. The thermal images were analysed using a rectangular area and averaging the measured stress in that area. The selected area was selected with a distance of 2 mm from both sides of the bar and approximately 20 mm in height.

A.1.3 Results

The bar was tested to validate the setup, the equipment and the algorithm to process the data. From the bar geometry it was expected a uniform stress distribution of 22.5 MPa, which was measured with the strain gages (with a standard deviation of 1.9 MPa). The selected area used in thermography had 6×17 mm (approximately 100 pixels) for all the frequencies analysed. The results from the thermal measures, mean temperature and standard deviation are presented in A.3. This did not show any correlation between the stress (measured by thermography) and the load frequency.

The stress profile in the images was assessed using a custom script in LabVIEW$^{\text{TM}}$. This script detect the peak in the images and extract horizontal cross section that passed at the detected peak. This was possible because the thermal camera was perfectly aligned with test specimen. The stress

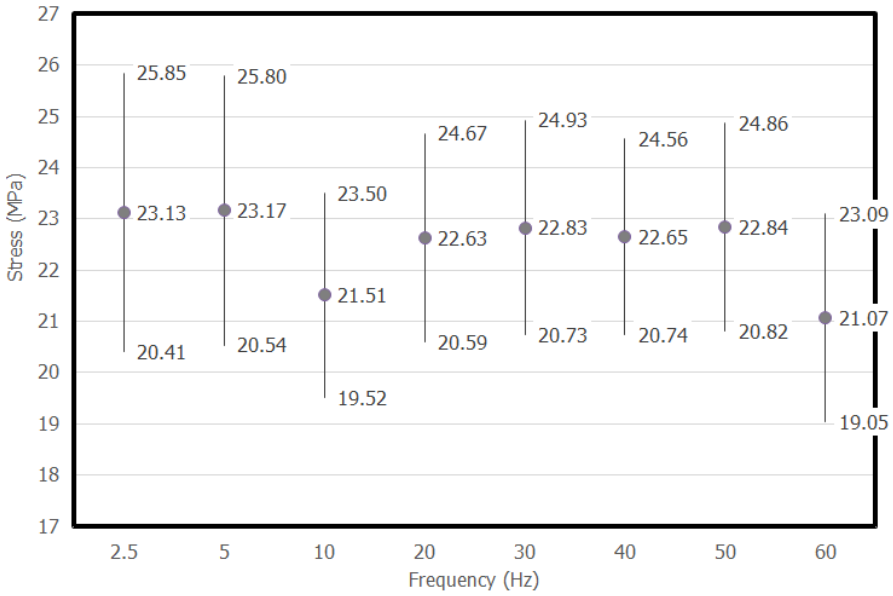

Figure A.3: Thermal results for the flat bar tests

images were all processed in this manner and the profiles were then compared and analysed.

The compact specimen CT, was tested with several frequencies, similar the ones used in the flat bar. In figure A.4a) is presented a stress image obtained by thermography that shows the area where the crack tip is located. Due to the small value of the aluminium's thermoelasticity, the temperature variations are little higher than the camera resolution. In order to improve the readings, the load is applied during several cycles and calculated the resulting amplitude. To improve the accuracy, the raw stress image obtained by thermography were filtered. It was applied a wavelet transformation, followed by a soft threshold in the approximation parameters and finally the data was reconstructed [221, 222]. An example of the filtering result is presented in figure A.4b, this image is the result of the filtering operation for the 30 Hz test (presented in figure A.4a). Figure A.4c presents a cross section that passes through the crack tip in both images, raw stress thermal image and after the filtering operation. Here, is noticed a rise in the noise level near the area of zero stress. The space resolution of the thermal camera and the small opening in the crack tip makes it difficult to pinpoint with precision the crack opening, which is the reason for the development of peak location script in LabVIEW^{TM}.

An important part of this work was to analyse the impact of different frequencies in the TSA tests. For this purpose, it were compared the stress profiles of the tests conducted for the selected frequencies at two different crack lengths.

The first aspect to highlight is the overall high similarity in the stress profiles for the different frequencies (figure A.5a and A.5c). One other important aspect is the extreme similarity in the "noise", even in the areas with higher noise near the zero stress values. Nevertheless, when

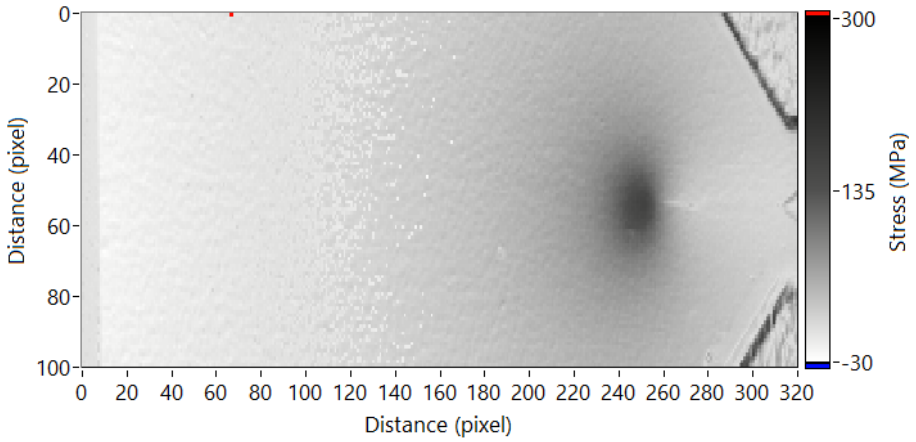

(a) Raw infrared stress image for the 30 Hz test

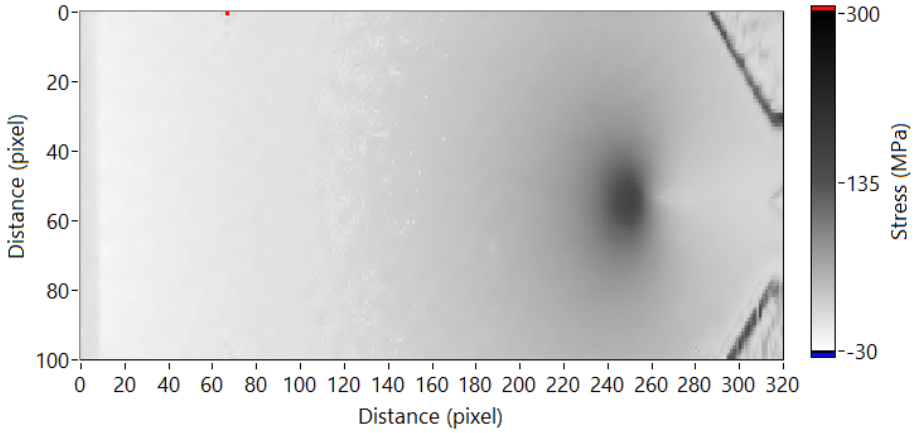

(b) Filtered infrared stress image

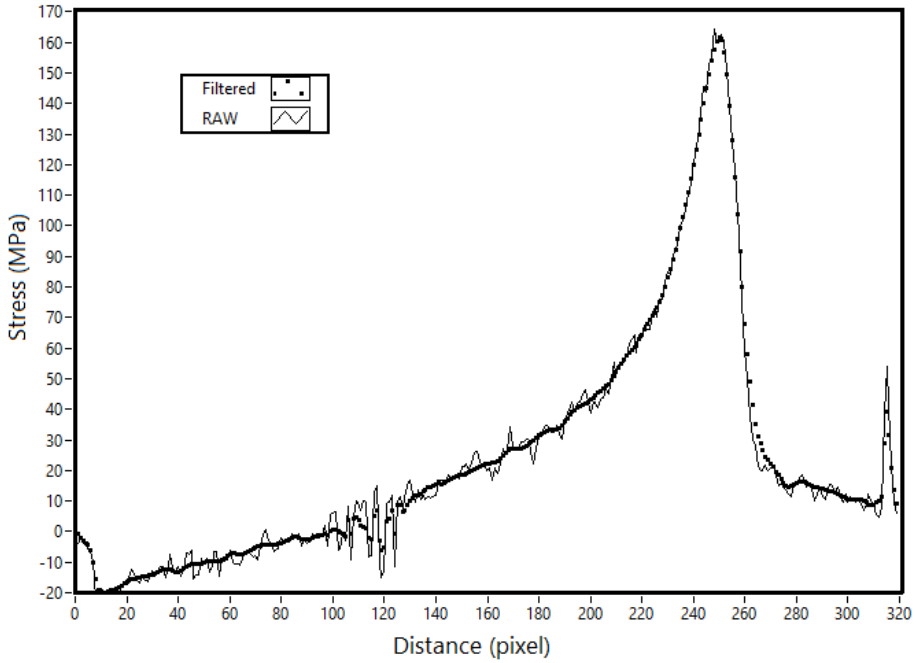

(c) Filtered and raw stress profile at the crack tip

Figure A.4: Crack thermal patterns

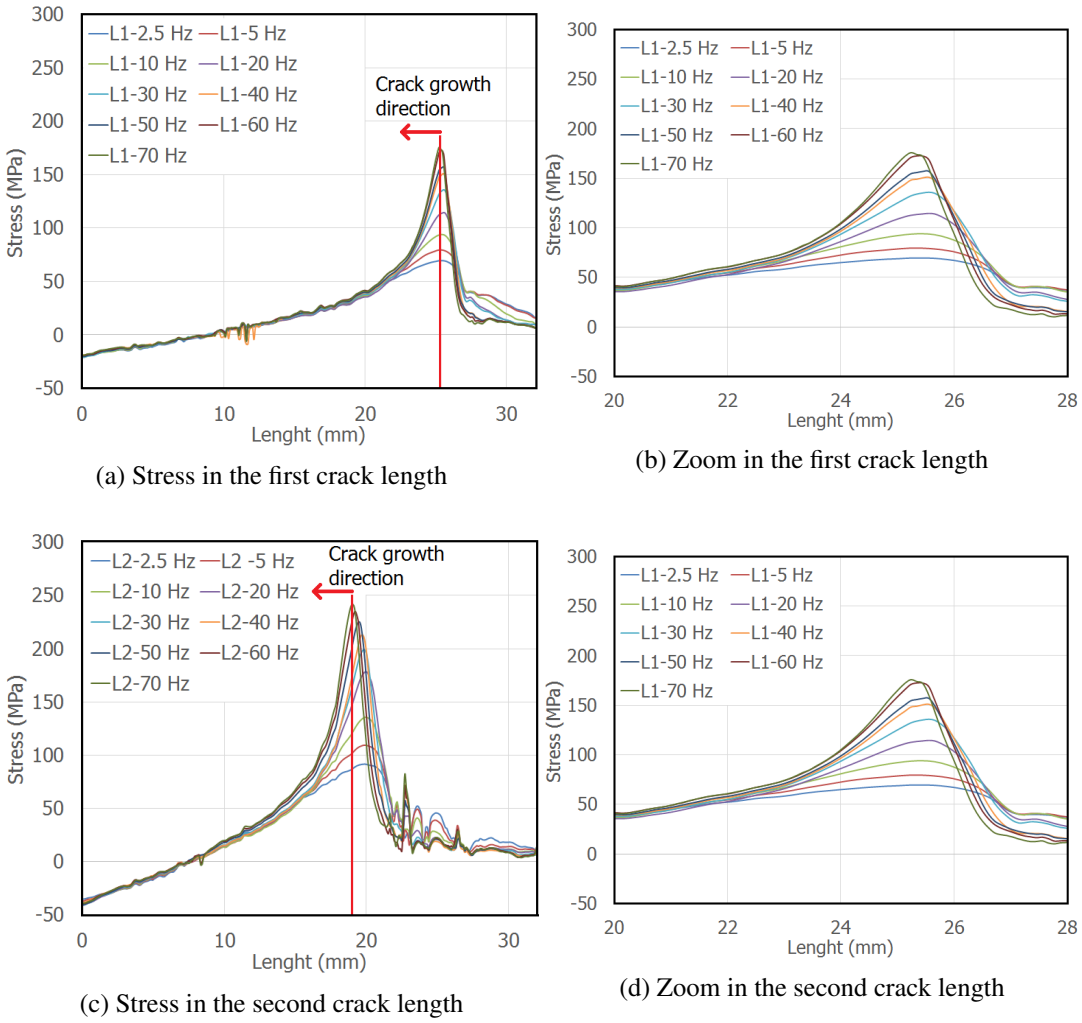

(a) Stress in the first crack length

(b) Zoom in the first crack length

(c) Stress in the second crack length

(d) Zoom in the second crack length

Figure A.5: Thermal profiles along the crack tip

approaching the crack tip, and in a small region, the curves deviate considerably among themselves. In all the tests, a higher frequency results in a higher maximum stress peak (figure A.5b and A.5d)). In the second series of tests, the difference between the stress curves from a certain frequency is higher and extends for a higher region. The location of the referred stress peak also represents a temperature peak and over the tests is moving left, in the direction of increasing the crack length, more than in the first phase.

Looking at the temperature peaks, it is observed a relation between these and the load frequencies (figure A.6). Using a power function it is possible to approximate the experimental data with a squared correlation coefficient of 0.9958 for the smaller crack and 0.9956 for the larger crack, figure A.6. The stress peaks follow a very well defined path. This is supported by the higher R square values reaching over 0.99 for both regressions.

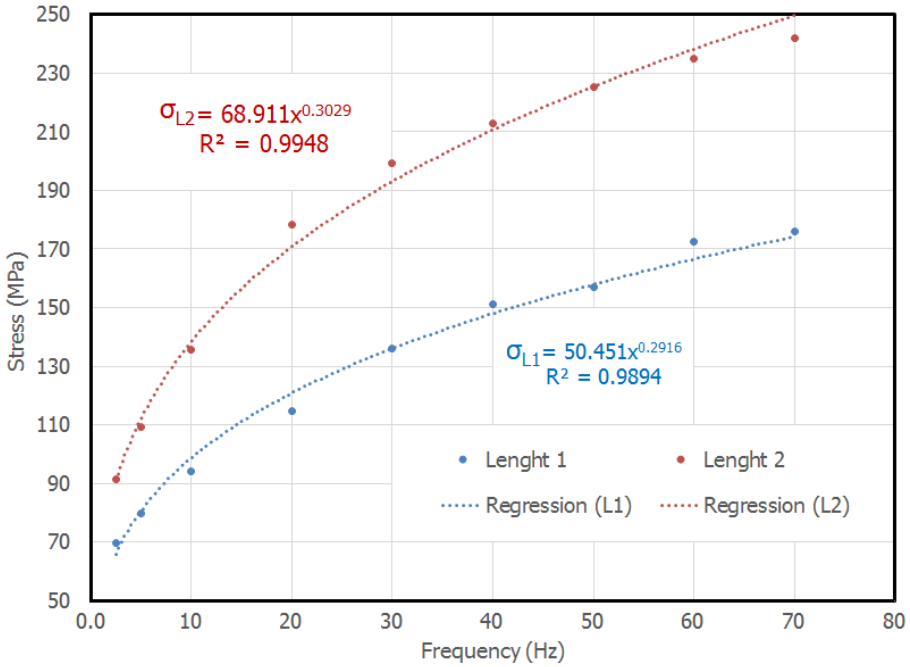

Figure A.6: Stress peaks for the tested frequencies

A.1.4 Analyses

In all the TSA test performed, it was easy to locate the area where the crack was located, as well as the specimen boundaries, important to introduce a scale in the thermal and stress images.

The stress (and temperature) profiles at the right side of the stress peak are not relevant (figure A.5). These represent the background of specimen part, depending on the instant during a loading cycle. When in the temperature and stress profiles, this part of the profile is a conjugation of both.

Due to the spatial resolution of the thermal equipment and the crack opening size, it is extremely difficult to achieve a static image that is focused in the crack tip. Viewing the crack from larger distances will lead to a poor resolution that will not permit a good and detailed image of the crack tip. On the other hand, zooming too close to the crack tip will induce errors and noise in the calculus of the stress image due to the movement of specimen resulting from the cyclic load.

The current commercial technology have a fast and very accurate processing algorithm, along with a very well documented procedure to measure a uniform stress. This was observed when the flat bar was tested, with the thermal images noise amplitude near the one of the strain gages.

Even today, the state of the art of thermal cameras still have a poor thermal resolution to calculate the stress resulting from a loading situation. Since one of the main goals of this work was to assess and characterize the stress profile at the front of the crack tip, the filtering operation reduced the noise of the curves. In the area surrounding the zero stress, is well visible an increase

in the noise due to the calculus procedure. The stress values are calculated with the thermal amplitude and signal of stress (tensile or compression) with the phase response. After a certain value, the noise in the phase image is irrelevant and therefore the only noise visible in the stress image is resulting from the thermal amplitude image. Near zero stress zones, the noise in the phase image appears and adds an extra level of noise to the calculus and then to the resulting stress image.

Due to the increase of the stress concentration factor, it was expected a very small growing of the thermal profile, at each test and mainly from the first to the second phase. This was clearly observed in the specimen tested up until rupture with a progression of approximately 1250 cycles between measurements. For each measurement were used 1050 cycles for the crack progression and 200 cycles for TSA measurements. However for the specimen tested with different frequencies, these observations were somewhat different, especially when blindly compare the results of the two phases.

When analysing figures A.5a and A.5b, particularly the increment in the stress peak values from the lower frequencies to the higher, it is obvious that this increment is not due to the increment of the crack and therefore the concentration factor. This is the first indication of the influence of the stimulation frequency in the temperature profiles. By observing the stress peak values in figure A.6 it is evident the influence of the stimulation frequency. Despite the higher number of cycles in each test (approximately 200) and therefore limiting the number of phases. The comparison between the two phases revealed correlations between the frequency and the stress peak, achieving an R2 higher than 0.989 in both sets of tests. Just with two crack lengths is extremely difficult to achieve a model between the stress profile and the stimulation frequency, and therefore more tests should be performed.

Another important aspect is the difference in the global stress profiles, presented in figure A.5. It was not observed any difference between the stress profiles. While for the second phase, for a distance of 6 millimetres, there was a considerable difference between the stress profiles, revealing a higher influence of the stimulation frequency in the stress profiles. Comparing the profiles of lower frequencies with higher frequencies, they present a stress peak with considerable different locations. Looking at the data presented in figure A.2, for approximately 2000 cycles (duration of one phase) was expected a crack progression of near 0.3 millimetres. While this may be observed in the first phase, in the second phase the difference from the 70 Hz peak and the lower frequencies exceeded 1 millimetre. This may reveal the reason for the difference in the stress peaks.

Since the specimens were made out of aluminium, they have a very high thermal conductivity. Therefore they are able to dissipate the heat variations in a fast way. Thus, when the specimen is subjected to a tensile load, the temperature will decrease and vice-versa. If a variation of the load is slow, the high conductivity of the aluminium may help to dissipate the localized increase of temperature. With the increasing in the load frequency, the material conductivity has a less

preponderant role during the cycle, since it cannot conduct the same amount of energy per cycle. As a result, for lower frequencies the temperature variations will be smoothed and lower, while for higher frequencies they will appear with higher peaks and more pronounced stress profiles.

A.1.5 TSA conclusions

It was evident that is possible to access the stress values in a metallic object, using only the temperature variations while this is subjected to a sinusoidal load. The comparison between the load measure with a strain gage and with TSA test revealed very resemble levels of amplitude and noise.

The localization of the crack tip using only thermography is very easy and can be extremely precise, like visible by the crack progression in figure A.2a.

The higher noise values in the areas near the zero stress are easily expressed by the algorithm used to calculate the stress value that overlaps the amplitude and phase data and consequentially the corresponding noise values.

The influence of the stimulation frequency is very clear. The regression between the frequency and the maximum stress has an R^2 over 0.989. This means higher frequencies will result in a higher overall thermal amplitude response. Lower frequencies will result in a smoothed temperature and consequentially stress profile. The lower frequencies also lead to a deviation of the temperature profile compared to the real stress profile, probably due to the thermal conductivity of the material.

With the present work it was not observed a stabilization of the peak stress values for the tested frequencies (the test equipment was unable the accomplish this). This way a test with higher frequencies should be performed, for frequencies over the 200 Hz in order to find a stabilization period at which the frequency does not influence the stress profiles. Thus, it may be possible to create a model to correct the usage of a non-ideal stimulation frequency. Alongside this, numeric simulations should be performed to access the internal behaviour of the specimen during the cyclic loading.

Appendix B

Equations to Predict Thermal Differences

Chapter 5 presented the numeric simulations relating the laboratory IRTT. The results from these simulations enabled the definition of several prediction surfaces function of the sample thickness (l) and the test characteristic period, stimulation Period for TTT and cycle period for LTT. The equations for these will be presented in the following pages.

B.1 Transient thermal tests

Transient Thermal Testing (TTT) uses a single squared stimulation that is characterized by the pulse width, here denominated Stimulus Period (SP). This is the most important parameter in TTT determining the energy applied to the object under analyses. Equations B.1 and B.4 predict the temperature difference of the deepest defect that this test can characterize function of the sample thickness l and the Stimulation Period (SP). The maximum SP (equations B.2 and B.5) identifies the maximum time for the stimulation. For longer stimulations the temperature difference will decrease. The recommended SP (equations B.3 and B.6) indicates the time for which the temperature difference is near the maximum and the defect blurring at its boundaries is still very low. The equations here presented refer to samples made of PMMA and CFRP, with equations B.3 and B.6 being also presented in the main text (equations 5.7 and 5.8).

B.1.1 Equations of TTT for PMMA

$$\begin{aligned} Transient\ Surface_{PMMA}(K) = {} & 0.525 + 1.52 \times 10^{-2} \times SP + 4.29 \times 10^{-2} \times l - 6.10 \times 10^{-4} \times \\ & SP^2 + 1.11 \times 10^{-2} \times SP \times l - 1.02 \times 10^{-1} \times l^2 + 3.85 \times 10^{-6} \times \\ & SP^3 + 9.29 \times 10^{-6} \times SP^2 \times l - 1.58 \times 10^{-3} \times SP \times l^2 + 1.76 \times \\ & 10^{-2} \times l^3 - 7.34 \times 10^{-9} \times SP^4 - 1.41 \times 10^{-7} \times SP^3 \times l + 1.95 \times \\ & 10^{-6} \times SP^2 \times l^2 + 6.05 \times 10^{-5} \times SP \times l^3 - 8.68 \times 10^{-4} \times l^4 \end{aligned} \tag{B.1}$$

$$Stimulus\ Period_{maximum}(s) = 35.31 - 33.58 \times l + 22.88 \times l^2 - 3.34 \times l^3 + 0.15 \times l^4 \tag{B.2}$$

$$Stimulus\ Period_{recommended}(s) = 17.74 + 3.53 \times l + 2.94 \times l^2 - 0.211 \times l^3 \tag{B.3}$$

B.1.2 Equations of TTT for CFRP

$$\begin{aligned} Transient\ Surface_{CFRP}(K) = {} & +1.17 + 9.99 \times 10^{-2} \times SP - 0.919 \times l - 2.07 \times 10^{-3} \times SP^2 - \\ & 1.1 \times 10^{-2} \times SP \times l + 0.25 \times l^2 + 1.74 \times 10^{-5} \times SP^3 + 1.50 \times \\ & 10^{-4} \times SP^2 \times l + 3.62 \times 10^{-4} \times SP \times l^2 - 2.57 \times 10^{-2} \times l^3 \\ & -6.14 \times 10^{-8} \times SP^4 - 1.86 \times 10^{-7} \times SP^3 \times l - 1.01 \times 10^{-5} \times \\ & SP^2 \times l^2 + 4.53 \times 10^{-5} \times SP \times l^3 + 8.51 \times 10^{-4} \times l^4 \end{aligned} \tag{B.4}$$

$$Stimulation\ Period_{maximum}(s) = 41.68 + 2.10 \times l - 1.25 \times l^2 + 0.11 \times l^3 \tag{B.5}$$

$$Stimulation\ Period_{recommended}(s) = 34.39 - 1.17 \times l - 0.46 \times l^2 + 0.056 \times l^3 \tag{B.6}$$

B.2 Lock-in thermal tests

Lock-in Thermal Testing (LTT) uses multiple stimulations (usually sinusoidal waveform) that are characterized by the period, here denominated Cycle Period (CP). This is the most important parameter in LTT, determining the energy and speed this is applied to the object under analyses. The LTT can be analysed using the amplitude or/and phase images. The results obtained by these can be predicted using equations B.7, B.8, B.11 and B.12. The first two graphs predict the amplitude and phase for PMMA samples, while the last ones relate CFRP objects. The LTT usually obtain better results using the phase images, however only if the amplitude presents a significant thermal difference between the defects and sound areas. Thus, is necessary that the CP has a minimum value (equations B.9 and B.13), with the recommended CP obtained by equations B.10 and B.14.

B.2.1 Equations of LTT for PMMA

$$\begin{aligned} Amplitude\,Surface_{PMMA}(K) = {} & 0.557 + 5.82\times10^{-2}\times CP - 0.339\times l - 2.73\times10^{-3}\times \\ & CP^2 + 7.98\times10^{-3}\times CP\times l + 5.27\times10^{-2}\times l^2 + 6.35\times \\ & 10^{-5}\times CP^3 + 1.28\times10^{-4}\times CP^2\times l - 1.70\times10^{-3}\times CP\times \\ & l^2 - 8.03\times10^{-3}\times l^3 - 4.38\times10^{-7}\times CP^4 - 1.26\times10^{-5}\times \\ & CP^3\times l + 1.24\times10^{-4}\times CP^2\times l^2 - 5.02\times10^{-4}\times CP\times \\ & l^3 + 1.61\times10^{-3}\times l^4 + 2.28\times10^{-9}\times CP^5 - 4.66\times10^{-9}\times \\ & CP^4\times l + 1.10\times10^{-6}\times CP^3\times l^2 - 1.31\times10^{-5}\times CP^2\times \\ & l^3 + 5.81\times10^{-5}\times CP\times l^4 - 1.08\times10^{-4}\times l^5 \end{aligned} \tag{B.7}$$

$$\begin{aligned} Phase\,Surface_{PMMA}(rad) = {} & -0.111 \times +0.139 \times \times CP - 0.337 \times l - 6.73 \times 10^{-}3 \times CP^2 - \\ & 1.38 \times 10^{-}2 \times CP \times l + 4.33 \times 10^{-}2 \times l^2 + 8.21 \times 10^{-}5 \times CP^3 + \\ & 2.06 \times 10^{-}3 \times CP^2 \times l - 7.58 \times 10^{-}3 \times CP \times l^2 + 1.22 \times 10^{-}2 \times \\ & l^3 - 3.38 \times 10^{-}7 \times CP^4 - 2.30 \times 10^{-}5 \times CP^3 \times l - 7.73 \times 10^{-}5 \times \\ & CP^2 \times l^2 + 6.70 \times 10^{-}4 \times CP \times l^3 - 1.48 \times 10^{-}3 \times l^4 + 1.16 \times \\ & 10^{-}9 \times CP^5 + 4.29 \times 10^{-}9 \times CP^4 \times l + 2.04 \times 10^{-}6 \times CP^3 \times \\ & l^2 - 1.06 \times 10^{-}5 \times CP^2 \times l^3 + 2.04 \times 10^{-}5 \times CP \times l^4 + 9.06 \times \\ & 10^{-}6 \times l^5 \end{aligned} \tag{B.8}$$

$$Cycle\,Period_{minimum}(s) = -1196 + 426.9 \times l - 50.53 \times l^2 + 2.02 \times l^3 \tag{B.9}$$

$$Cycle\,Period_{recommended}(s) = 4.16 + 11.64 \times l - 0.56 \times l^2 \tag{B.10}$$

B.2.2 Equations of LTT for CFRP

$$\begin{aligned} Amplitude\,Surface_{CFRP}(K) = {} & 0.30 + 4.38 \times 10^{-2} \times CP - 0.168 \times l - 6.06 \times 10^{-3} \times CP^2 + \\ & 1.16 \times 10^{-2} \times CP \times l + 3.06 \times 10^{-2} \times l^2 + 3.54 \times 10^{-4} \times CP^3 - \\ & 2.12 \times 10^{-4} \times CP^2 \times l - 9.91 \times 10^{-4} \times CP \times l^2 - 5.42 \times 10^{-3} \times \\ & l^3 - 7.14 \times 10^{-6} \times CP^4 - 3.63 \times 10^{-5} \times CP^3 \times l + 2.04 \times 10^{-4} \times \\ & CP^2 \times l^2 - 3.63 \times 10^{-4} \times CP \times l^3 + 7.39 \times 10^{-4} \times l^4 + 5.65 \times \\ & 10^{-}8 \times CP^5 + 4.21 \times 10^{-}7 \times CP^4 \times l - 5.58 \times 10^{-}8 \times CP^3 \times \\ & l^2 - 9.2 \times 10^{-6} \times CP^2 \times l^3 + 2.6 \times 10^{-5} \times CP \times l^4 - 3.5 \times 10^{-5} \times l^5 \end{aligned} \tag{B.11}$$

$$\begin{aligned} Phase\ Surface_{CFRP}(rad) = {} & +0.257 - 1.86\times10^{-3}\times CP - 9.34\times10^{-3}\times l - 6.71\times10^{-4}\times \\ & CP^2 + 2.96\times10^{-2}\times CP\times l - 4.25\times10^{-2}\times l^2 - 4.30\times10^{-3}\times \\ & CP^3 + 2.50\times10^{-2}\times CP^2\times l - 3.02\times10^{-2}\times CP\times l^2 - 1.58\times \\ & 10^{-2}\times l^3 + 4.92\times10^{-4}\times CP^4 - 3.01\times10^{-3}\times CP^3\times l + 5.56\times \\ & 10^{-3}\times CP^2\times l^2 - 8.79\times10^{-3}\times CP\times l^3 + 1.37\times10^{-2}\times l^4 - \\ & 1.61\times10^{-5}\times CP^5 + 5.77\times10^{-5}\times CP^4\times l + 1.59\times10^{-4}\times CP^3\times \\ & l^2 - 8.22\times10^{-4}\times CP^2\times l^3 + 1.62\times10^{-3}\times CP\times l^4 - 1.86\times \\ & 10^{-3}\times l^5 + 1.50\times10^{-7}CP^6 + 3.97\times10^{-7}\times CP^5\times l - 8.89\times \\ & 10^{-6}\times CP^4\times l^2 + 2.57\times10^{-5}\times CP^3\times l^3 - 2.13\times10^{-5}\times CP^2\times \\ & l^4 - 2.79\times10^{-5}\times CP\times l^5 + 6.44\times10^{-5}\times l^6 \end{aligned} \tag{B.12}$$

$$Cycle\ Period_{\,minimum}(s) = 3.9109 - 6.4023\times l + 2.381\times l^2 - 0.1175\times l^3 \tag{B.13}$$

$$Cycle\ Period_{\,recommended}(s) = -2.5013 + 5.5281\times l - 0.2474\times l^2 \tag{B.14}$$

This page was intentionally left blank.

Appendix C

Technical drawings

C.1 PMMA with 10 mm slots

C.2 CFRP sample

C.3 CT sample

This page was intentionally left blank.

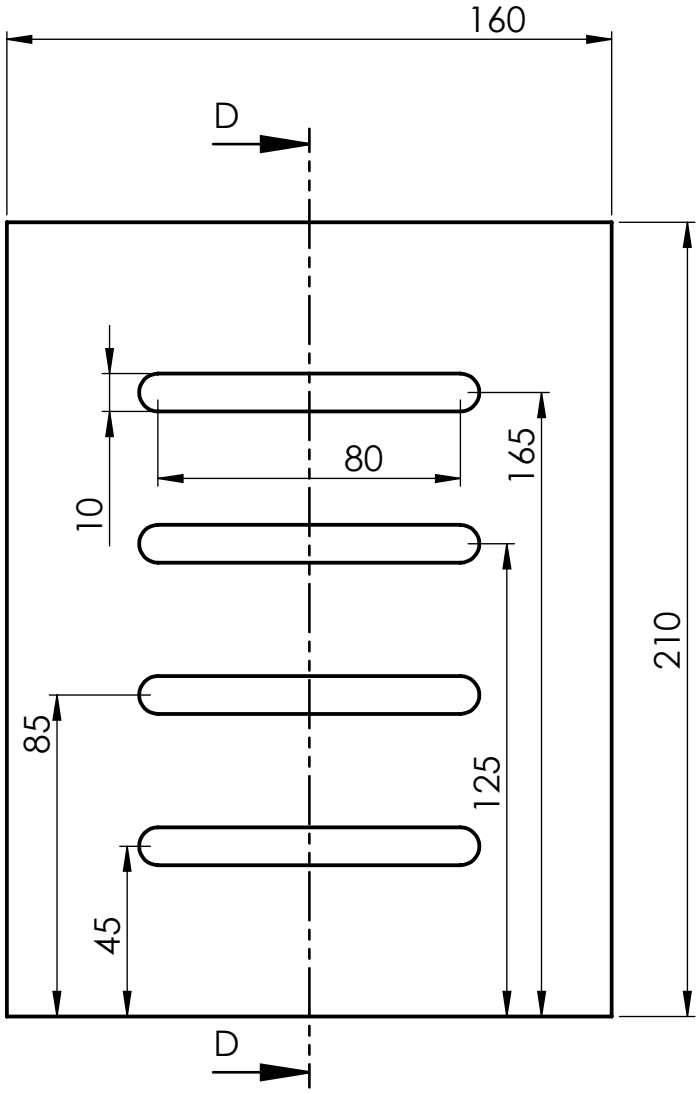

SECTION D-D

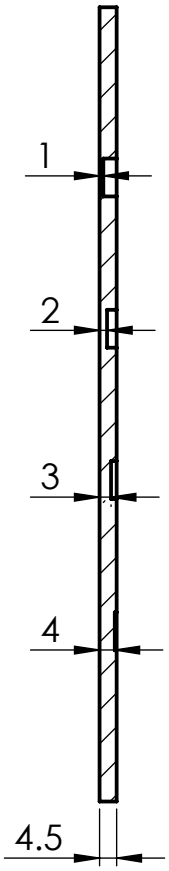

UNLESS OTHERWISE SPECIFIED: DIMENSIONS ARE IN MILLIMETERS SURFACE FINISH: TOLERANCES: LINEAR: ANGULAR:		FINISH:		DEBUR AND BREAK SHARP EDGES	DO NOT SCALE DRAWING	REVISION
	NAME	SIGNATURE	DATE		TITLE:	
DRAWN	AJRS		2/12/2015		PMMA 10 mm slots	
CHK'D	AJRS		3/12/2015			
APPV'D						
MFG						
Q.A				MATERIAL: PMMA	DWG NO. Test_Samples	A4
				WEIGHT:	SCALE:1:2	SHEET 1 OF 6

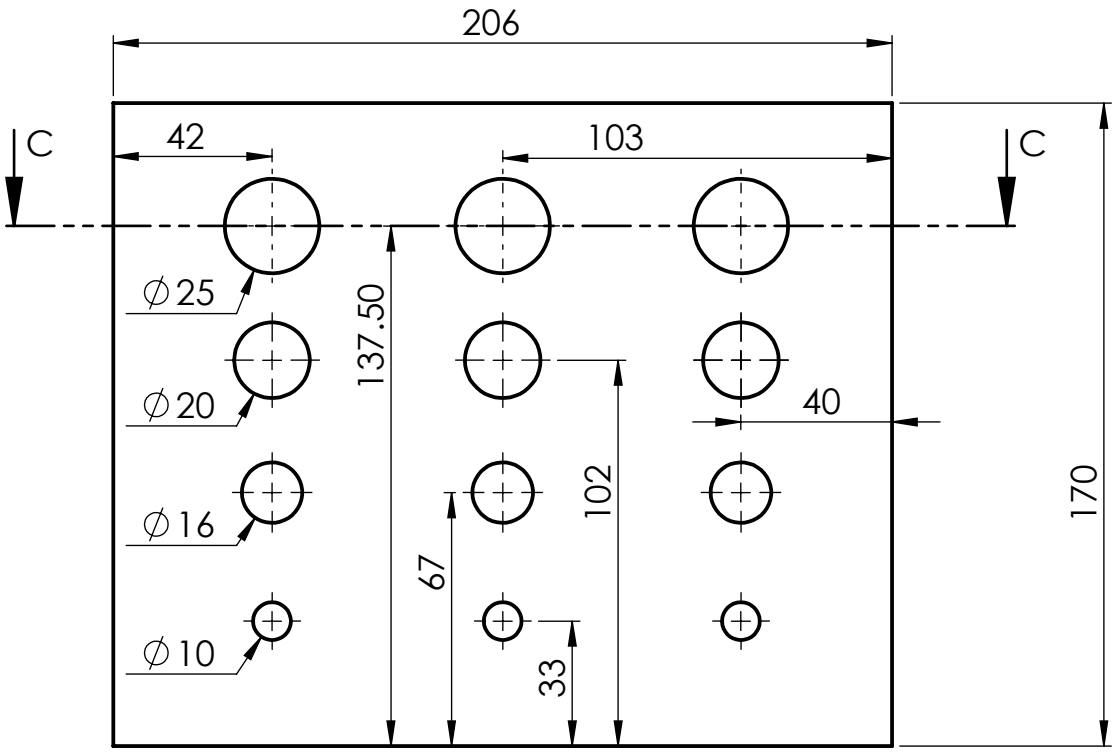

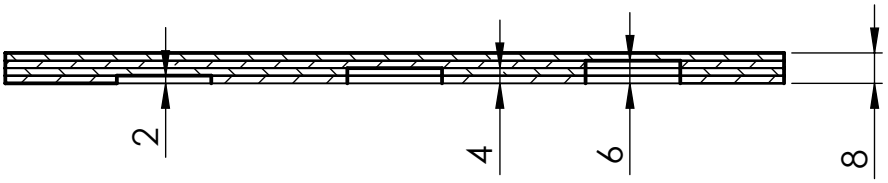

SECTION C-C

UNLESS OTHERWISE SPECIFIED: DIMENSIONS ARE IN MILLIMETERS SURFACE FINISH: TOLERANCES: LINEAR: ANGULAR:	FINISH:		DEBUR AND BREAK SHARP EDGES	DO NOT SCALE DRAWING	REVISION	
	NAME	SIGNATURE	DATE	TITLE:		
DRAWN	AJRS		2/12/2015	CFRP sample		
CHK'D	AJRS		3/12/2015			
APPV'D						
MFG						
Q.A				MATERIAL: CFRP	DWG NO. Test_Samples	A4
				WEIGHT:	SCALE:1:2	SHEET 3 OF 6

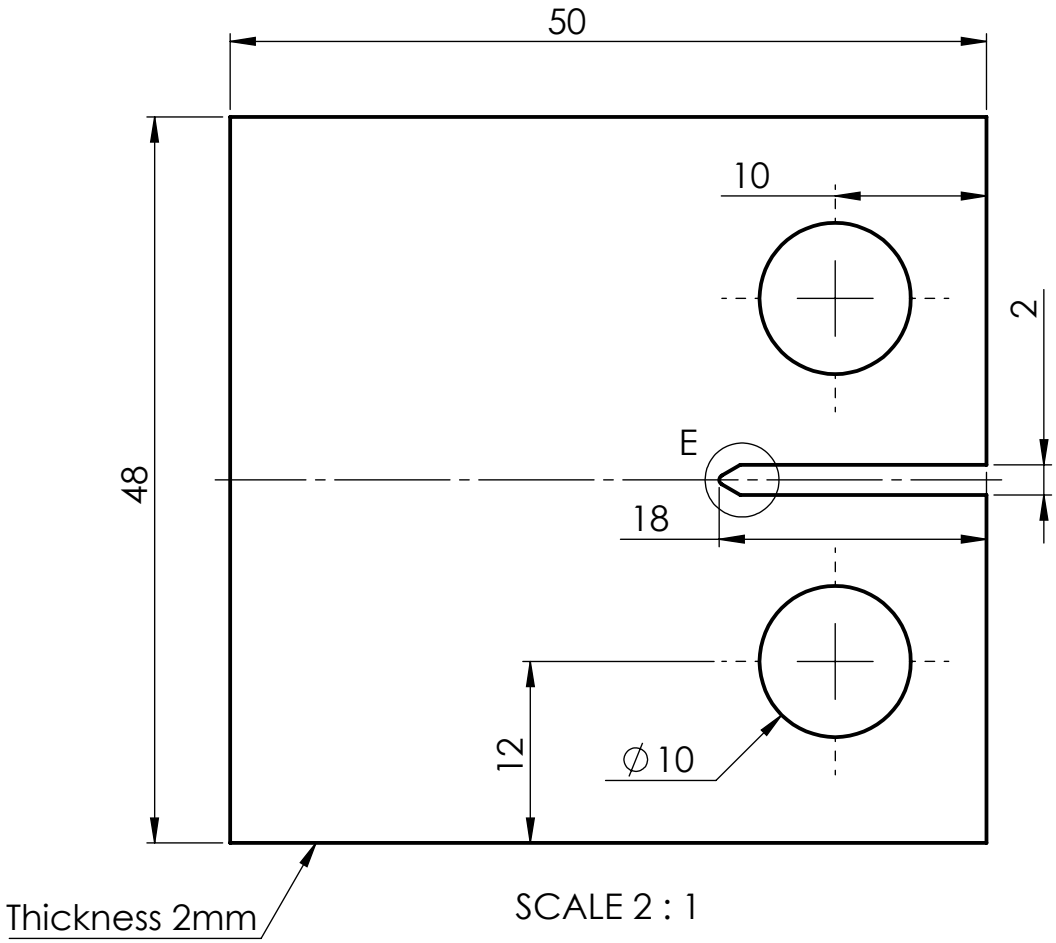

SCALE 2 : 1

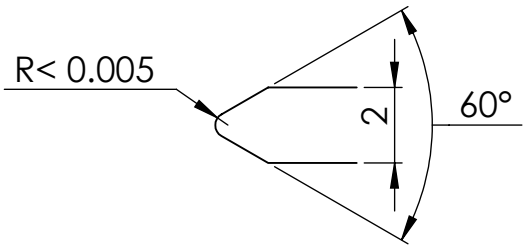

DETAIL E
SCALE 5 : 1

UNLESS OTHERWISE SPECIFIED: DIMENSIONS ARE IN MILLIMETERS SURFACE FINISH: TOLERANCES: LINEAR: ANGULAR:	FINISH:		DEBUR AND BREAK SHARP EDGES	DO NOT SCALE DRAWING	REVISION	
	NAME	SIGNATURE	DATE	TITLE:		
DRAWN			2/12/2015	CT sample		
CHK'D			3/12/2015			
APPV'D						
MFG						
Q.A				MATERIAL:	DWG NO.	A4
				Aluminum	Test_Samples	
				WEIGHT:	SCALE:1:2	SHEET 5 OF 6

References

[1] D. Hull and T.W. Clyne. *An Introduction to Composite Materials* [1]. Cambridge Solid State Science Series. Cambridge University Press, 1996. URL: https://books.google.pt/books?id=BRcdDu4bUhMC.

[2] Jayamangal Prasad. and C. G. Krishnadas Nair. *Non-Destructive Test And Evaluation Of Materials, chapters 7-9*. Tata McGraw-Hill, 2009. URL: https://books.google.com/books?id=orfm3oALLpEC.

[3] F.L. Matthews and R.D. Rawlings. *Composite Materials: Engineering and Science, chapter 1*. Taylorand Francis, 1999.

[4] F.L. Matthews and R.D. Rawlings. *Composite Materials: Engineering and Science, chapter 2*. Taylor and Francis, 1999.

[5] Valery V Vasiliev and Evgeny V Morozov. *Mechanics and Analysis of Composite Materials.(2001)*. Elsevier Science, 2001.

[6] C.T. Herakovich. *Mechanics of Fibrous Composites*. Wiley, 1997. URL: https://books.google.pt/books?id=Zj7yQwAACAAJ.

[7] Narottam P Bansal. *Handbook of ceramic composites, chapter 4*, volume 200. Springer Science & Business Media, 2006.

[8] G.J. John. Method of producing fibers from vitreous materials, July 1930. US Patent 1,769,181. URL: https://www.google.com/patents/US1769181.

[9] Narottam P Bansal. *Handbook of ceramic compositeschapter 20*, volume 200. Springer Science & Business Media, 2006.

[10] Krishan K. Chawla. *Composite Materials: Science and Engineering, chapter 7*. Materials Research and Engineering. Springer New York, 2013. URL: https://books.google.pt/books?id=ET09xfkprSkC.

[11] C. Leyens and M. Peters. *Titanium and Titanium Alloys: Fundamentals and Applications, chapter 12*. Wiley, 2006.

[1] all links in the references were consulted between July and November of 2015

[12] K. Suganuma, T. Okamoto, T. Hayami, Y. Oku, and N. Suzuki. Influence of high temperature exposure on the properties of alumina short fibre reinforced aa6061 alloy. *Journal of Materials Science*, 23(4):1317–1323, 1988. URL: http://dx.doi.org/10.1007/BF01154595, doi:10.1007/BF01154595.

[13] K.U. Kainer. European materials research society 1990 spring meeting on metal matrix composites influence of heat treatment on the properties of short-fibre-reinforced magnesium composites. *Materials Science and Engineering: A*, 135:243 – 246, 1991. URL: http://www.sciencedirect.com/science/article/pii/092150939190570D, doi:http://dx.doi.org/10.1016/0921-5093(91)90570-D.

[14] C. Leyens and M. Peters. *Titanium and Titanium Alloys: Fundamentals and Applications, chapter 1*. Wiley, 2006. URL: https://books.google.pt/books?id=Zq3xMa-IOvMC.

[15] C. Leyens and M. Peters. *Titanium and Titanium Alloys: Fundamentals and Applications, chapter 13*. Wiley, 2006.

[16] K.U. Kainer. *Metal Matrix Composites: Custom-made Materials for Automotive and Aerospace Engineering, chapter 2*. Wiley, 2006.

[17] K.U. Kainer. *Metal Matrix Composites: Custom-made Materials for Automotive and Aerospace Engineering, chapter 11*. Wiley, 2006. URL: https://books.google.pt/books?id=ILmG9jtrzTQC.

[18] S.C.D.S.C. Aeronautics, A.S.E. Board, D.E.P. Sciences, and N.R. Council. *Decadal Survey of Civil Aeronautics:: Foundation for the Future, chapter 3*. National Academies Press, 2006. URL: https://books.google.pt/books?id=0HucqzZSOkUC.

[19] Anthony Kelly. *Concise encyclopedia of composite materials*. Elsevier, 1994.

[20] R.K. Bregg. *Frontal Polymer Research, chapter 2*. Nova Science Publishers, 2006. URL: https://books.google.pt/books?id=KuzlID1l0VsC.

[21] K.V. Pochiraju, G. Tandon, and G.A. Schoeppner. *Long-Term Durability of Polymeric Matrix Composites, chapter 1*. SpringerLink : Bücher. Springer US, 2011. URL: https://books.google.pt/books?id=-Wwy71BRzgAC.

[22] N.B.C. Engineers. *The Complete Technology Book on Expanded Plastics, Polyurethane, Polyamide and Polyester Fibres, chapter 3*. NIIR Project Consultancy Services, 2006. URL: https://books.google.pt/books?id=4wK3AgAAQBAJ.

[23] L. Pilato. *Phenolic Resins: A Century of Progress, chapter 1 and 2*. SpringerLink: Springer e-Books. Springer Berlin Heidelberg, 2010. URL: https://books.google.pt/books?id=a6Hd6Trsnw8C.

[24] N. Board. *Modern Technology of Synthetic Resins & Their Applications, chapter 20*. NIIR Project Consultancy Services, 2002. URL: https://books.google.pt/books?id=wIuuAwAAQBAJ.

[25] S. Beland. *High Performance Thermoplastic Resins and Their Composites, chapter 3*. Elsevier Science, 2012.

[26] S. Beland. *High Performance Thermoplastic Resins and Their Composites, chapter 4 and 5*. Elsevier Science, 2012.

[27] S. Beland. *High Performance Thermoplastic Resins and Their Composites, chapter 2*. Elsevier Science, 2012.

[28] J.K. Fink. *Reactive Polymers Fundamentals and Applications: A Concise Guide to Industrial Polymers, chapter 11*. Plastics Design Library. Elsevier Science, 2013. URL: https://books.google.pt/books?id=T2C3diHrnFgC.

[29] G. Pritchard. *Developments in Reinforced Plastics—5: Processing and Fabrication, chapter 2*. Springer Netherlands, 2012. URL: https://books.google.pt/books?id=HzPrCAAAQBAJ.

[30] Wernfried Heilen. *Silicone Resins and Their Combinations*. European coatings literature. Vincentz Network, 2005. URL: https://books.google.pt/books?id=rQlKQSnWsrwC.

[31] F.P. Bachman. *Great Inventors and Their Inventions*. Yesterday's Classics, 2006. URL: https://books.google.pt/books?id=rBDTCtKSWfkC.

[32] Roger Bacon. Growth, structure, and properties of graphite whiskers. *Journal of applied physics*, Volume 1:283 – 290, 1960.

[33] M.S.A. Rahaman, A.F. Ismail, and A. Mustafa. A review of heat treatment on polyacrylonitrile fiber. *Polymer Degradation and Stability*, 92(8):1421 – 1432, 2007. URL: http://www.sciencedirect.com/science/article/pii/S0141391007001279, doi:http://dx.doi.org/10.1016/j.polymdegradstab.2007.03.023.

[34] ZP Wang, JS Ghotra, G Pritchard, and RG Rose. The mechanical properties of particulate-filled aramid and polyethylene laminates. *Polymer international*, 42(3):241–244, 1997.

[35] G. Pritchard Z. P. Wang, J. S. Ghotra. Mechanical properties of epoxies reinforced with chloride-treated aramid fibers. *Polymer International*, 42:241–244, 1997.

[36] Tony Calvert. *Composite Engineering Materials, Guide to Composites*. SP Systems, 2003. URL: http://www.composites.ugent.be/home_made_composites/documentation/SP_Composites_Guide.pdf.

[37] A.A.B. Baker and D.W. Kelly. *Composite Materials for Aircraft Structures, chapter 3*. AIAA education series. American Institute of Aeronautics & Astronautics, 2004. URL: https://books.google.pt/books?id=5SPAIKFmFjcC.

[38] Narottam P Bansal. *Handbook of ceramic composites, chapter 1*, volume 200. Springer Science & Business Media, 2006.

[39] Narottam P Bansal. *Handbook of ceramic composites, chapter 2*, volume 200. Springer Science & Business Media, 2006.

[40] E.J. Barbero. *Introduction to Composite Materials Design, chapter 2*. Composite Materials. Taylor & Francis, second edition edition, 2010. URL: https://books.google.pt/books?id=fZSan7b5z0IC.

[41] Sumio Iijima. Helical microtubules of graphitic carbon. *Nature*, 354, (7 November 1991):56–58, 1991.

[42] Philip G. Collins and Phaedon Avouris. Nanotubes for electrinics. *Scientific MAmerican*, 283, 6:62–71, 2000.

[43] Ernesto Joselevich Greg Y. Tseng Chin-Li Cheung Charles M. Lieber Thomas Rueckes, Kyoungha Kim. Carbon nanotube–based nonvolatile random access memory for molecular computing. *SCIENCE*, VOL:94–97, 2000.

[44] Marjan Nezafati J. B. Ferguson-Benjamin F. Schultz Zahra Bajestani-Gohari Pradeep K. Rohatgi Kyu Cho Chang-Soo Kim, Il Sohn. Prediction models for the yield strenght of particle reinforced unimodal pure magnesium metal matrix nanocomposites. *Journal of Materials Science*, 48 (12):4191–4204, 2013.

[45] W. Maziarz K. Haberko W. Pyda J. Dutkiewicz, L. Litynska and A. Kanciruk. Structure and properties of nanocomposites prepared from ball milled 6061aluminium alloy with zro nanoparticles. *Crystal Research and Technology*, 44 (10):1163–1169, 2009.

[46] E. Mohammad Sharifi, F. Karimzadeh, and M.H. Enayati. Fabrication and evaluation of mechanical and tribological properties of boron carbide reinforced aluminum matrix nanocomposites. *Materials and Design*, 32:3263–3271, 2011. doi:doi:10.1016/j.matdes.2011.02.033.

[47] M. S. de Vries-G. Gorman R. Savoy J. Vazquez & R. Beyers D. S. Bethune, C. H. Kiang. Cobalt-catalysed growth of carbon nanotubes with single-atomic-layer walls. *Nature*, 363:605 – 607, 1993. doi:10.1038/363605a0.

[48] Qiang Zhang Huanhuan Xie Weizhong Qian-Fei Wei Rufan Zhang, Yingying Zhang. Growth of half-meter long carbon nanotubes based on schulz-flory distribution. *ACS Nano*, 7:6156–61, 2013.

[49] C. R. Martin G. Che, B. B. Lakshmi and E. R. Fisher. Chemical vapor deposition based synthesis of carbon nanotubes and nanofibers using a template method. *Chemestry of Materials*, 10:260–267, 1998.

[50] X. Fan A. A. Puretzky, D. B. Geohegan and S. J. Pennycook. In situ imaging and spectroscopy of single-wall carbon nanotube synthesis by laser vaporization. *Applied physics letters*, 76 (2):182 – 184, 2000.

[51] Stuart M. Lee. *Handbook of Composite Reinforcements*. Wiley, 1992. URL: https://books.google.pt/books?id=pPirpE73tDYC.

[52] Edgar Lara-Curzio Tatsuya Hinoki and Lance L. Snead. Mechanical properties of high purity sic fiber reinforced cvi-sic matrix composites mechanical properties of high purity sic fiber-reinforced cvi-sic matrix composites. *FUSIONSCIENCEANDTECHNOLOGY*, 44:211–218, 2003.

[53] Tim Pepper. *Polyester Resins*. ASM International, USA, 2003.

[54] Yuhong Wu, Frederick J. McGarry, Bizhong Zhu, John R. Keryk, and Dimitris E. Katsoulis. Temperature effect on mechanical properties of toughened silicone resins. *Polymer Engineering & Science*, 45(11):1522–1531, 2005. URL: http://dx.doi.org/10.1002/pen.20423, doi:10.1002/pen.20423.

[55] H Heuer, M Schulze, M Pooch, S Gäbler, A Nocke, G Bardl, Ch Cherif, M Klein, R Kupke, R Vetter, et al. Review on quality assurance along the cfrp value chain–non-destructive testing of fabrics, preforms and cfrp by hf radio wave techniques. *Composites Part B: Engineering*, 77:494–501, 2015.

[56] E.A. Lloyd. Non-destructive testing of bonded joints: A case for testing laminated structures by wide-band ultrasound. *Non-Destructive Testing*, 7:331–334, 1974.

[57] P.E.E.E. Paul E. Mix. *Introduction to Nondestructive Testing: A Training Guide*. Wiley, 2005. URL: https://books.google.pt/books?id=LtlFcoeIP-UC.

[58] R.C. Anderson. *Inspection of Metals: Visual examination*. Inspection of Metals. American Society for Metals, 1983. URL: https://books.google.pt/books?id=uj1kAAAAMAAJ.

[59] Visual inspection for aircraft, federal aviation administration, U.S. department of transport, august 1997.

[60] M.W. Allgaier, P. MacIntire, S. Ness, P.O. Moore, and American Society for Nondestructive Testing. *ASNT Nondestructive Testing Handbook: Visual and Optical Testing*. Nondestructive Testing Handbook, Vol 8. American Society for Nondestructive Testing, American Society for Metals, 1993. URL: https://books.google.pt/books?id=i6geAQAAIAAJ.

[61] Lorenz PG. Expanding technology adds value to visual testing and remote visual inspection procedures. *Materials evaluation*, 55:1001 – 1004, 1997.

[62] Joseph L Switzer and Robert C Switzer. Daylight fluorescent pigment compositions, #feb# 21 1950. US Patent 2,498,592.

[63] Joseph L Switzer, Robert C Switzer, and Richard A Ward. Light-responsive fluorescent media, #sep# 22 1953. US Patent 2,653,109.

[64] Joseph L Switzer and Jr Donald W Parker. Fluorescent penetrant inspection materials and methods, #jan# 5 1960. US Patent 2,920,203.

[65] J. L. Switzer. Non-visible penetrant methods of flaw detection and apparatus therefor, #sep# 12 1967. US Patent 3,341,010.

[66] D.J. Lovejoy. {NDT} techniques: Penetration of liquids. In K.H. Jürgen BuschowRobert W. CahnMerton C. FlemingsBernhard IlschnerEdward J. KramerSubhash MahajanPatrick Veyssière, editor, *Encyclopedia of Materials: Science and Technology (Second Edition)*, pages 6024 – 6026. Elsevier, Oxford, second edition edition, 2001. URL: http://www.sciencedirect.com/science/article/pii/B0080431526010615, doi:http://dx.doi.org/10.1016/B0-08-043152-6/01061-5.

[67] Xu Guirong, Guan Xuesong, Qiao Yuliang, and Gao Yan. Analysis and innovation for penetrant testing for airplane parts. *Procedia Engineering*, 99:1438–1442, 2015.

[68] F.A.A.F.A. Administration. *Aircraft Inspection and Repair, section 5*. Skyhorse Publishing Company, Incorporated, 2013. URL: https://books.google.pt/books?id=smchAgAAQBAJ.

[69] B. Raj, T. Jayakumar, and M. Thavasimuthu. *Practical Non-destructive Testing, chapter 2*. Woodhead, 2002. URL: https://books.google.pt/books?id=qXcCKsL2IMUC.

[70] B. Raj, T. Jayakumar, and M. Thavasimuthu. *Practical Non-destructive Testing, chapter 5*. Woodhead, 2002.

[71] J. Blitz. *Electrical and Magnetic Methods of Non-destructive Testing, chapter 2*. Non-Destructive Evaluation Series. Springer Netherlands, 2 edition, 2012. ISBN-9401158185, 9789401158183.

[72] W. T. Cui L. J. Yang and S. W. Gao. Magnetic flux leakage field within the detector unit optimization based on comsol. In *Proceedings of the 2015 International Conference on Testing and Measurement Techniques (TMTA 2015)*, volume 1, pages 271 –275, 2015. DOI - 10.1201/b18470-63.

[73] J. Gauthier, T.W. Krause, and D.L. Atherton. Measurement of residual stress in steel using the magnetic barkhausen noise technique. *{NDT} & E International*, 31(1):23 –

31, 1998. URL: http://www.sciencedirect.com/science/article/pii/S0963869597000236, doi:http://dx.doi.org/10.1016/S0963-8695(97)00023-6.

[74] A. Niku-Lari. *Residual Stresses: Technology — Applications — Effects, chapter 3*. Elsevier Science, 2014. URL: https://books.google.pt/books?id=PyGjBQAAQBAJ.

[75] W.H. Cubberly, R. Bakerjian, and Society of Manufacturing Engineers. *Tool and Manufacturing Engineers Handbook Desk Edition, chapter 13*. Desk Edition. Society of Manufacturing Engineers, 1989. URL: https://books.google.pt/books?id=NRXnXmFRjWYC.

[76] T.J. Kinsella. *ASNT Level III Study Guide Radiographic Testing Method*. American Society for Nondestructive Testing, 2004. URL: https://books.google.pt/books?id=MId1PQAACAAJ.

[77] C.U. Grosse and M. Ohtsu. *Acoustic Emission Testing, chapter 7*. Springer Berlin Heidelberg, 2008. URL: https://books.google.pt/books?id=HxsJ39eEg20C.

[78] C.U. Grosse and M. Ohtsu. *Acoustic Emission Testing, Part B*. Springer Berlin Heidelberg, 2008.

[79] Alan G. Beattie. Acoustic emission non-destructive testing of structures using source location techniques. Technical report, Sandia National Laboratories, California, United States, 2013.

[80] O. Svelto. *Principles of Lasers*. Springer US, fourth edition, 1998. URL: https://books.google.pt/books?id=ioywRI5W2HEC.

[81] K. Thyagarajan and A. Ghatak. *Lasers: Fundamentals and Applications*. Graduate Texts in Physics. Springer US, 2010. URL: https://books.google.pt/books?id=z13wEOBwn1wC.

[82] A. Donges and R. Noll. *Laser Measurement Technology: Fundamentals and Applications*. Springer Series in Optical Sciences. Springer Berlin Heidelberg, 2014.

[83] A. Fahr. *Aeronautical Applications of Non-destructive Testing:*. DEStech Publications, Incorporated, 2013. URL: https://books.google.pt/books?id=65hQAgAAQBAJ.

[84] M.A.P. Vaz P.M.S.T. Castro V. Richter-Trummer, P.M.G.P. Moreira. Methodology for in situ stress intensity factor determination on cracked structures by digital image correlation. *International Journal of Structural Integrity*, 1(14):344–357, 2010.

[85] M.P. Norton and D.G. Karczub. *Fundamentals of Noise and Vibration Analysis for Engineers, chapter 1*. Cambridge University Press, 2003. URL: https://books.google.pt/books?id=jDeRCSqtev4C.

[86] C. Scheffer and P. Girdhar. *Practical Machinery Vibration Analysis and Predictive Maintenance, chapter 5*. Practical Machinery Vibration Analysis and Predictive Maintenance. Elsevier Science, 2004. URL: https://books.google.pt/books?id=tAvTO1t2mwkC.

[87] A. Brandt. *Noise and Vibration Analysis: Signal Analysis and Experimental Procedures, chapter 7*. EngineeringPro collection. Wiley, 2011. URL: https://books.google.pt/books?id=-1DSxrlhL5sC.

[88] ASTM D999 - 08(2015), standard test methods for vibration testing of shipping containers, astm international, 2015.

[89] Chung-Bang Yun Daniel J. Inman Seunghee Parka, Jong-Jae Lee. A built-in active sensing system-based structural health monitoring technique using statistical pattern recognition. *Journal of Mechanical Science and Technology*, 21:896 902, 2007.

[90] Norman F. Hunter Hoon Sohn, Charles R. Farrar and Keith Worden. Structural health monitoring using statistical pattern recognition techniques. *Journal of Dynamic Systems, Measurement, and Control | Volume 123 |*, 123 (4):706–711, 2001.

[91] P. Burrascano, S. Callegari, A. Montisci, M. Ricci, and M. Versaci. *Ultrasonic Nondestructive Evaluation Systems: Industrial Application Issues, Part IV*. EBL-Schweitzer. Springer International Publishing, 2014. URL: https://books.google.pt/books?id=4HS1BQAAQBAJ.

[92] V.A. Krasilnikov. *Sound and Ultrasound Waves in Air, Water and Solid Bodies*. NASA technical translation. National Science Foundation, Washington, 1963. URL: https://books.google.pt/books?id=aFrTTp6VN7cC.

[93] R.N. Thurston, A.D. Pierce, and E.P. Papadakis. *Reference for Modern Instrumentation, Techniques, and Technology: Ultrasonic Instruments and Devices I, chapter 3*. Physical Acoustics. Elsevier Science, 1998. URL: https://books.google.pt/books?id=bm_ErZB4KvMC.

[94] J. Blitz and G. Simpson. *Ultrasonic Methods of Non-destructive Testing*. Non-Destructive Evaluation Series. Springer Netherlands, 1995. URL: https://books.google.pt/books?id=d3WWect9zQEC.

[95] X Maldague. Nondestructive evaluation of materials by infrared thermography. *Springer-Verlag*, 1993. doi:10.1007/978-1-4471-1995-1.

[96] Xavier Maldague. *Trends in Optical Nondestructive Testing*. Elsevier, 2000.

[97] Michael Vollmer and Klaus-Peter Möllmann. *Infrared thermal imaging: fundamentals, research and applications*. John Wiley & Sons, 2010.

[98] N. Sullivan. *Temperature*. Measure up! Marshall Cavendish Benchmark, 2006. URL: https://books.google.pt/books?id=UMNV9IiQV_wC.

[99] John G Webster. *Measurement, Instrumentation, and Sensors Handbook, section 6*. Chapman & Hall/CRCnetBASE, 1999.

[100] Dictionary.com unabridged, Aug 2015. (thermo). URL: http://dictionary.reference.com/browse/thermo-.

[101] Dictionary.com unabridged, Aug 2015. (graphy). URL: http://dictionary.reference.com/browse/graphy.

[102] S. Ashforth-Frost K. Jambunathan T. L Chan. Calibrating for viewing angle effect during heat transfer measurements on a curved surface. *International Journal of heat and mass transfer*, 44:2209–2223, 2001.

[103] B Konda Reddy and C Balaji. Bayesian estimation of heat flux and thermal diffusivity using liquid crystal thermography. *International Journal of Thermal Sciences*, 87:31–48, 2015.

[104] EFJ Ring. The discovery of infrared radiation in 1800. *Imaging Science Journal*, 48(1):1–8, 2000.

[105] S. Chomet G. Gaussorgues. *Infrared thermography*. Chapman & Hali, 1994.

[106] Otwin Breitenstein, Wilhelm Warta, and Martin Langenkamp. *Lock-in thermography: Basics and use for evaluating electronic devices and materials*, volume 10. Springer Science & Business Media, 2010.

[107] Gunter Gauglitz and Tuan Vo-Dinh. *Handbook of Spectroscopy: Volume 1 and 2*. Wiley VCH, 2002.

[108] J. Byrnes. *Unexploded Ordnance Detection and Mitigation, chapter 2*. NATO Science for Peace and Security Series B: Physics and Biophysics. Springer Netherlands, 2008. URL: https://books.google.pt/books?id=B_KLtHJbgvAC.

[109] Antonio Rogalski. *Infrared Detectors, Second Edition*. CRC press, 2010. URL: https://books.google.pt/books?id=0VUJSafhaK0C&lpg=PP1&dq=detectors&hl=pt-PT&pg=PP1#v=onepage&q=detectors&f=false.

[110] FLIR. *Altair Reference Guide*. FLIR Systems, 2014. URL: http://www.flir.eu/corporate/display/?id=42241.

[111] Christian Monte and Jörg Hollandt. The measurement of directional spectral emissivity in the temperature range from 80 c to 500 c at the physikalisch-technische bundesanstalt. *High Temperatures–High Pressures*, 39(2), 2010.

[112] F. Nicodemus. Directional reflectance and emissivity of an opaque surface. *Appl. Opt.*, 4:767–775, 1965.

[113] "Chang-Da Wen". Investigation of steel emissivity behaviors: Examination of multispectral radiation thermometry (mrt) emissivity models. *International Journal of Heat and Mass Transfer*, 53:2035–2043, 2010. doi:doi:10.1016/j.ijheatmasstransfer.2009.12.053.

[114] S Henke, Detlef Karstädt, Klaus-Peter Möllmann, Frank Pinno, and Michael Vollmer. Identification and suppression of thermal reflections in infrared thermal imaging. *Inframation Proc*, 5:287–98, 2004.

[115] Dominique Guilhem, Roger Reichle, and Hélène Roche. Reflections and surface temperature measurements in experimental fusion reactors Tore-Supra, JET and ITER. *Quantitative InfraRed Thermography Journal*, 3(2):155–168, 2006.

[116] U. Platt and J. Stutz. *Differential Optical Absorption Spectroscopy: Principles and Applications*. Physics of Earth and Space Environments. Springer Berlin Heidelberg, 2008. URL: https://books.google.pt/books?id=y90g9yF1QncC.

[117] Kleespies TJ. McMillin LM, Crone LJ. Atmospheric transmittance of an absorbing gas. 5. improvements to the optran approach. *Appl Opt. 1995 Dec 20;34(36):8396-9. doi: 10.1364/AO.34.008396.*, 10:8396–8405, 1995.

[118] WANG Wei-hua WANG Chong. Summarization on atmospheric transmittance of infrared radiation. *Equipment Environmental Engineering 2011-04*, 01, 2011.

[119] ASTM Standard. G173-03, standard tables for reference solar spectral irradiances: direct normal and hemispherical on 37-degree tilted surface, 2003.

[120] David P DeWitt and Gene D Nutter. *Theory and practice of radiation thermometry*. Wiley Online Library, 1988.

[121] Jean Dumoulin and Vincent Boucher. Infrared thermography system for transport infrastructures survey with inline local atmospheric parameter measurements and offline model for radiation attenuation evaluations. *Journal of Applied Remote Sensing*, 8(1):084978, 2014. URL: http://dx.doi.org/10.1117/1.JRS.8.084978, doi:10.1117/1.JRS.8.084978.

[122] F Hengstberger. *Absolute Radiometry: Electrically Calibrated Thermal Detectors of Optical Radiation*. Elsevier, 2012.

[123] Ermanno Grinzato. Humidity and air temperature measurement by quantitative infrared thermography. *Quantitative InfraRed Thermography Journal*, 7(1):55–72, 2010.

[124] Waldemar Minkina and Sebastian Dudzik. *Infrared thermography: errors and uncertainties*. John Wiley & Sons, 2009.

[125] Nelson Wilbur Pech-May, Arantza Mendioroz, and Agustín Salazar. Simultaneous measurement of the in-plane and in-depth thermal diffusivity of solids using pulsed infrared thermography with focused illumination. *NDT & E International*, 77:28–34, 2016.

[126] Liu Junyan, Wang Fei, Liu Yang, and Wang Yang. Inverse methodology for identification the thermal diffusivity and subsurface defect of cfrp composite by lock-in thermographic phase (litp) profile reconstruction. *Composite Structures*, 138:214–226, 2016.

[127] Pablo Rodrigues Muniz, Robson da Silva Magalhães, Shirley Peroni Neves Cani, and Clainer Bravin Donadel. Non-contact measurement of angle of view between the inspected surface and the thermal imager. *Infrared Physics & Technology*, 72:77–83, 2015.

[128] Pablo R Muniz, Shirley PN Cani, and Robson da S Magalhaes. Influence of field of view of thermal imagers and angle of view on temperature measurements by infrared thermovision. *Sensors Journal, IEEE*, 14(3):729–733, 2014.

[129] Paul M. Kodzwa Jr A E John K. Eaton. Angular effects on thermochromic liquid crystal thermography. *Experimental fluids*, 43:929–937, 2007.

[130] WT Chiu, PW Lin, HY Chiou, WS Lee, CN Lee, YY Yang, HM Lee, MS Hsieh, CJ Hu, YS Ho, et al. Infrared thermography to mass-screen suspected sars patients with fever. *Asia-Pacific Journal of Public Health*, 17(1):26–28, 2005.

[131] E.Y.-K. Ng. A review of thermography as promising non-invasive detection modality for breast tumor. *International Journal of Thermal Sciences*, 48(5):849 – 859, 2009. URL: http://www.sciencedirect.com/science/article/pii/S129007290800149X, doi:http://dx.doi.org/10.1016/j.ijthermalsci.2008.06.015.

[132] Ying-Chieh Chou and Leehter Yao. Automatic diagnostic system of electrical equipment using infrared thermography. In *Soft Computing and Pattern Recognition, 2009. SOCPAR'09. International Conference of*, pages 155–160. IEEE, 2009.

[133] Toshimitsu Ishii Terumi Inagaki and Toshikatsu Iwamoto. On the ndt and e for the diagnosis of defects using infrared thermography. *NDT & E International*, 32(5):247 – 257, 1999. URL: http://www.sciencedirect.com/science/article/pii/S0963869598000590, doi:http://dx.doi.org/10.1016/S0963-8695(98)00059-0.

[134] Amir M. Alani, Morteza Aboutalebi, and Gokhan Kilic. Integrated health assessment strategy using {NDT} for reinforced concrete bridges. *{NDT} & E International*, 61:80 – 94, 2014. URL: http://www.sciencedirect.com/science/article/pii/

S0963869513001333, doi:http://dx.doi.org/10.1016/j.ndteint.2013.10.001.

[135] S. Laguela, J. Martínez, J. Armesto, and P. Arias. Energy efficiency studies through 3d laser scanning and thermographic technologies. *Energy and Buildings*, 43(6):1216 – 1221, 2011. URL: http://www.sciencedirect.com/science/article/pii/S0378778811000041, doi:http://dx.doi.org/10.1016/j.enbuild.2010.12.031.

[136] Ji B Holliday D Hu Y, Cao W. Thermography-based virtual MPPT scheme for improving PV energy efficiency under partial shading conditions. *IEEE Transactions on Power Electronics*, 29:5667–5672, 2014.

[137] X.P.V. Maldague. Introduction to NDT by active infrared thermography. *Materials Evaluation*, 60:1–3, 2002.

[138] and Jing Zhou, Ning Tao, Lichun Feng, and Cunlin Zhang. Absolute peak slope time based thickness measurement using pulsed thermography. *Infrared Physics & Technology*, 55:200 – 204, 2012. doi:doi:10.1016/j.infrared.2012.01.005.

[139] Petros Christou Angeliki Kylili, Paris A. Fokaides and Soteris A. Kalogirou. Infrared thermography (irt) applications for building diagnostics: A review. *Applied Energy*, 134:531–549, 2014. doi:doi:10.1016/j.apenergy.2014.08.005.

[140] D.P. Almond N.P. Avdelidis, B.C. Hawtin. Transient thermography in the assessment of defects of aircraft composits.pdf. *NDT&E International*, 36:433–439, 2003.

[141] J. G. Sun. Analysis of pulsed thermography methods for defect depth prediction. *Journal of Heat Transfer*, 128:329–338, 2005.

[142] O. Breitenstein, W. Warta, and M. Langenkamp. *Lock-in Thermography: Basics and Use for Evaluating Electronic Devices and Materials*. Springer Series in Advanced Microelectronics. Springer Berlin Heidelberg, 2013. URL: https://books.google.pt/books?id=1ETtCAAAQBAJ.

[143] T. Proulx. *Thermomechanics and Infra-Red Imaging, Volume 7: Proceedings of the 2011 Annual Conference on Experimental and Applied Mechanics*. Conference Proceedings of the Society for Experimental Mechanics Series. Springer New York, 2011. URL: https://books.google.pt/books?id=pEzFoRh307wC.

[144] X.P.V. Maldague. *Nondestructive Evaluation of Materials by Infrared Thermography, chapter 2*. Springer London, 2012. URL: https://books.google.pt/books?id=6MHcBwAAQBAJ.

[145] Inc FLIR Systems. Ndt in composite materials with flash, transient, and lock-in thermography, Dezember 2011. URL: http://www.flir.com/science/content/?id=67277.

[146] Marc Genest, Clemente Ibarra-Castanedo, Jean-Marc Piau, Stéphane Guibert, Mirela Susa, Abdelhakim Bendada, Xavier Maldague, and Abbas Fahr. Comparison of thermography techniques for inspection of cf-18 honeycomb structures. In *Aircraft Aging 2007 Conference*, page 14, 2007.

[147] R. Sorrentino and G. Bianchi. *Microwave and RF Engineering, chapter 1 and 2*. Microwave and Optical Engineering. Wiley, 2010. URL: https://books.google.com/books?id=y_tYmSjpYkQC.

[148] J.R. Pardo, J. Cernicharo, and E. Serabyn. Atmospheric transmission at microwaves (atm): an improved model for millimeter/submillimeter applications. *Antennas and Propagation, IEEE Transactions on*, 49(12):1683–1694, Dec 2001. doi:10.1109/8.982447.

[149] Keo Sam-Ang, Defer Didier, Breaban Florin, and Brachelet Franck. Comparison between microwave infrared thermography and co 2 laser infrared thermography in defect detection in applications with cfrp. *Materials Sciences and Applications*, 2013:600–605, 2013.

[150] R Plum and T Ummenhofer. Ultrasound excited thermography of load bearing members used in constructional steelwork. In *Proceedings of 9th International Conference on Quantitative Infrared Thermography (QIRT08), Krakow (Poland)*, 2008.

[151] Krishnendu Chatterjee, Suneet Tuli, Simon G Pickering, and Darryl P Almond. A comparison of the pulsed, lock-in and frequency modulated thermography nondestructive evaluation techniques. *NDT & E International*, 44(7):655–667, 2011.

[152] Jeounghak Park Heesang Park, Manyong Choi and Wontae Kim. A study on detection of micro-cracks in the dissimilar metal weld through ultrasound infrared thermography. *Infrared Physics & Technology*, 62:124–131, 2014. doi:doi:10.1016/j.infrared.2013.10.006.

[153] Liu Junyan, Liu Liqiang, and Wang Yang. Experimental study on active infrared thermography as a ndi tool for carbon-carbon composites. *Composites:Part B*, 45:138–147, 2013.

[154] Sam Ang Keo, Franck Brachelet, Florin Breaban, and Didier Defer. Defect detection in cfrp by infrared thermography with co 2 laser excitation compared to conventional lock-in infrared thermography. *Composites Part B: Engineering*, 69:1–5, 2015.

[155] Sam Ang Keo, Franck Brachelet, Florin Breaban, and Didier Defer. Steel detection in reinforced concrete wall by microwave infrared thermography. *NDT&E International*, 62:172–177, 2014. doi:doi:10.1016/j.ndteint.2013.12.002.

[156] Jia Liu, Gui Yun Tian, Bin Gao, WenWei Ren, and Jin Song Meng. Investigation of thermal imaging sampling frequency for eddy current pulsed thermography. *NDT&E International*, 62:85–92, 2014. doi:doi:10.1016/j.ndteint.2013.11.009.

[157] Jeremy Renshaw, John C. Chen, Stephen D. Holland, and R. Bruce Thompson. The sources of heat generation in vibrothermography. *NDT&E International*, 44:736–739, 2011. doi:doi:10.1016/j.ndteint.2011.07.012.

[158] R.H. Kingston. *Detection of Optical and Infrared Radiation, chapter 1*. Springer Series in Optical Sciences. Springer Berlin Heidelberg, 2013. URL: https://books.google.pt/books?id=oB2hBwAAQBAJ.

[159] S. Dudzik. Analysis of the accuracy of a neural algorithm for defect depth estimation using pca processing from active thermography data. *Infrared Physics & Technology*, 56:1–7, 2013. doi:doi:10.1016/j.infrared.2012.08.006.

[160] Zhi Zeng, Chunguang Li, Ning Tao, Lichun Feng, and Cunlin Zhang. Depth prediction of non-air interface defect using pulsed thermography. *NDT&E International*, 48:39–45, 2012. doi:doi:10.1016/j.ndteint.2012.02.008.

[161] HI Ringermacher, RJ Archacki Jr, and WA Veronesi. Nondestructive testing: transient depth thermography: Us, 5711603.

[162] Miguel Lizaranzu, Alberto Lario, Agustín Chiminelli, and Ibán Amenabar. Non-destructive testing of composite materials by means of active thermography-based tools. *Infrared Physics & Technology*, 71:113–120, 2015.

[163] Mercedes Reischel Henrik Steinfurth Mathias Röllig Christiane Maierhofer, Philipp Myrach and Matthias Kunert. Characterizing damage in cfrp structures using flash thermography in reflection and transmission configurations. *Composites: Part B*, 57:35–46, 2014. doi:doi:10.1016/j.compositesb.2013.09.036.

[164] Sebastian Dudzik. Characterization of material defects using active thermography and an artificial neural network. *Metrology and measurement systems*, xx:491–500, 2013.

[165] Masashi Ishikawa, Hiroshi Hatta, Yoshio Habuka, Ryo Fukui, and Shin Utsunomiya. Detecting deeper defects using pulse phase thermography. *Infrared Physics & Technology*, 57:42–49, 2013. doi:doi:10.1016/j.infrared.2012.11.009.

[166] Roberto Montanini. Quantitative determination of subsurface defects in a reference specimen made of plexiglas by means of lock-in and pulse phase infrared thermography. *Infrared Physics & Technology*, 53:363–371, 2010. doi:doi:10.1016/j.infrared.2010.07.002.

[167] V. Feuillet, L. Ibos, M. Fois, J. Dumoulin, and Y. Candau. Defect detection and characterization in composite materials using square pulse thermography coupled with singular value decomposition analysis and thermal quadrupole modeling. *NDT&E International*, 51:58–67, 2012. doi:doi:10.1016/j.ndteint.2012.06.003.

[168] Christiane Maierhofer, Mathias Röllig, Karsten Ehrig, Dietmar Meinel, and Gilbert Céspedes-Gonzales. Validation of flash thermography using computed tomography for characterizing inhomogeneities and defects in cfrp structures. *Composites Part B: Engineering*, 64:175–186, 2014.

[169] Steven M Shepard. System for generating thermographic images using thermographic signal reconstruction, #may# 25 2010. US Patent 7,724,925.

[170] S Grys, W Minkina, and L Vokorokos. Automated characterisation of subsurface defects by active ir thermographic testing–discussion of step heating duration and defect depth determination. *Infrared Physics & Technology*, 68:84–91, 2015.

[171] Xavier P. Maldague. *Theory and Practice of Infrared Technology for Nondestructive Testing*. Wiley-Interscience, 1 edition, April 2001.

[172] Automation technology GmbH. *IR-NDT Manual english*. Automation technology GmbH, 2008.

[173] D. Lu J. Hewitt D. Bates, G. Smith. Rapid thermal non-destructive testing of aircraft components. *Composites: Part B*, 31:175–185, 2000.

[174] G. Giorleo, C. Meola, and A. Squillace. Analysis of defective carbon-epoxy by means of lock-in thermography. *Research in Nondestructive Evaluation*, 12:241–250, 2000.

[175] Gerd Busse Datong Wu. Lock-in thermography for nondestructive evaluation of materials. *Revue Générale de Thermique*, 37:693–703, 1998.

[176] Jeonghak Park Wontae Kim Koungsuk Kim Manyong Choi, Kisoo Kang. Quantitative determination of a subsurface defect of reference specimen by lock-in infrared thermography. *NDT&E International*, 41:119–124, 2008. doi:10.1016/j.ndteint.2007.08.006.

[177] A Gleiter, G Riegert, Th Zweschper, and G Busse. Ultrasound lock-in thermography for advanced depth resolved defect selective imaging. *Insight-Non-Destructive Testing and Condition Monitoring*, 49(5):272–274, 2007.

[178] Otwin Breitenstein, JP Rakotoniaina, F Altmann, T Riediger, and M Gradhand. New developments in ir lock-in thermography. In *Proc. 30th ISTFA*, pages 595–599, 2004.

[179] Khalid Muzaffar, Suneet Tuli, and Shiban Koul. Beam width estimation of microwave antennas using lock-in infrared thermography. *Infrared Physics & Technology*, 72:244–248, 2015.

[180] Raphael Danjoux Jean Louis Beaudoin, Etienne Merienne and Michel Egee. Numerical system for infrared scanners and application to the subsurface control of materials by photothermal radiometry. 590:285–292, 1986.

[181] P.K. Kuo, Z.J. Feng, T. Ahmed, L.D. Favro, R.L. Thomas, and J. Hartikainen. Parallel thermal wave imaging using a vector lock-in video technique. In Peter Hess and Josef Pelzl, editors, *Photoacoustic and Photothermal Phenomena*, volume 58 of *Springer Series in Optical Sciences*, pages 415–418. Springer Berlin Heidelberg, 1988.

[182] S Quek, Darryl P Almond, L Nelson, and T Barden. A novel and robust thermal wave signal reconstruction technique for defect detection in lock-in thermography. *Measurement Science & Technology*, 16(5):1223–1233, May 2005. URL: http://opus.bath.ac.uk/1996/, doi:10.1088/0957-0233/16/5/024.

[183] Krishnendu Chatterjee and Suneet Tuli. Prediction of blind frequency in lock-in thermography using electro-thermal model based numerical simulation. *Journal of Applied Physics*, 114(17), 2013. URL: http://scitation.aip.org/content/aip/journal/jap/114/17/10.1063/1.4828480, doi:http://dx.doi.org/10.1063/1.4828480.

[184] Clemente Ibarra-Castanedo and Xavier P. V. Maldague. Interactive methodology for optimized defect characterization by quantitative pulsed phase thermography. *Research in Nondestructive Evaluation*, 16(4):175–193, 2005. URL: http://dx.doi.org/10.1080/09349840500351846, arXiv:http://dx.doi.org/10.1080/09349840500351846, doi:10.1080/09349840500351846.

[185] Patty RR. Bennett CA Jr. Thermal wave interferometry: a potential application of the photoacoustic effect. *Applied optics*, 21:49–54, 1982.

[186] D Sharath, M Menaka, and B Venkatraman. Effect of defect size on defect depth quantification in pulsed thermography. *Measurement Science and Technology*, 24(12):125205, 2013. URL: http://stacks.iop.org/0957-0233/24/i=12/a=125205.

[187] Sharath Delanthabettu, Murugesan Menaka, Balasubramanian Venkatraman, and Baldev Raj. Defect depth quantification using lock-in thermography. *Quantitative InfraRed Thermography Journal*, (ahead-of-print):1–16, 2015.

[188] G.S Padhi, M.A McCarthy, and C.T McCarthy. Boljat: a tool for designing composite bolted joints using three-dimensional finite element analysis. *Composites Part A: Applied Science and Manufacturing*, 33(11):1573 – 1584, 2002. URL: http://www.sciencedirect.com/science/article/pii/S1359835X02001136, doi:http://dx.doi.org/10.1016/S1359-835X(02)00113-6.

[189] C Zoecke, A Langmeier, and W Arnold. Size retrieval of defects in composite material with lockin thermography. In *Journal of Physics: Conference Series*, volume 214, page 012093. IOP Publishing, 2010.

[190] M.J. Assael, S. Botsios, K. Gialou, and I.N. Metaxa. Thermal conductivity of polymethyl methacrylate (pmma) and borosilicate crown glass bk7. *International Journal of Thermophysics*, 26(5):1595–1605, 2005. URL: http://dx.doi.org/10.1007/s10765-005-8106-5, doi:10.1007/s10765-005-8106-5.

[191] D.R.O.Y. CHOUDHURY. *MODERN CONTROL ENGINEERING*. PHI Learning, 2005. URL: https://books.google.pt/books?id=_l3JtXcL98IC.

[192] Stuart W. Churchill and Humbert H.S. Chu. Correlating equations for laminar and turbulent free convection from a vertical plate. *International Journal of Heat and Mass Transfer*, 18(11):1323 – 1329, 1975. URL: http://www.sciencedirect.com/science/article/pii/0017931075902434, doi:http://dx.doi.org/10.1016/0017-9310(75)90243-4.

[193] A.J.M. Ferreira. *Problemas de elementos finitos em Matlab*. Fundacao Calouste Gulbenkian, 2010. URL: https://books.google.pt/books?id=tdfTcQAACAAJ.

[194] G. Allaire. *Numerical Analysis and Optimization: An Introduction to Mathematical Modelling and Numerical Simulation*. Numerical Mathematics and Scientific Computation. Oxford University Press, 2007. URL: https://books.google.pt/books?id=QFsZAQAAIAAJ.

[195] N. Ozisik. *Finite Difference Methods in Heat Transfer*. Heat Transfer. Taylor & Francis, 1994. URL: https://books.google.pt/books?id=M-Jun14kdxcC.

[196] F. Moukalled, L. Mangani, and M. Darwish. *The Finite Volume Method in Computational Fluid Dynamics: An Advanced Introduction with OpenFOAM and Matlab*. Fluid Mechanics and Its Applications. Springer International Publishing, 2015. URL: https://books.google.pt/books?id=GYRgCgAAQBAJ.

[197] Qing Fang, Takuya Tsuchiya, and Tetsuro Yamamoto. Finite difference, finite element and finite volume methods applied to two-point boundary value problems. *Journal of Computational and Applied Mathematics*, 139(1):9 – 19, 2002. URL: http://www.sciencedirect.com/science/article/pii/S0377042701003922, doi:http://dx.doi.org/10.1016/S0377-0427(01)00392-2.

[198] E.G. Thompson. *An introduction to the finite element method: theory, programming, and applications*. John Wiley, 2004. URL: https://books.google.pt/books?id=VmkeAQAAIAAJ.

[199] E.G. Thompson. *An Introduction to the Finite Element Method: Theory, Programming, and Applications*. John Wiley, 2005. URL: https://books.google.com/books?id=8TK-QgAACAAJ.

[200] Sun-Jeong Kim, Chang-Hun Kim, and David Levin. Surface simplification using a discrete curvature norm. *Computers & Graphics*, 26(5):657 – 663, 2002. URL: http://www.sciencedirect.com/science/article/pii/S0097849302001218, doi:http://dx.doi.org/10.1016/S0097-8493(02)00121-8.

[201] P. Cignoni, C. Montani, and R. Scopigno. A comparison of mesh simplification algorithms. *Computers & Graphics*, 22(1):37 – 54, 1998. URL: http://www.sciencedirect.com/science/article/pii/S0097849397000824, doi:http://dx.doi.org/10.1016/S0097-8493(97)00082-4.

[202] Clemente Ibarra-Castanedo and Xavier P Maldague. Defect depth retrieval from pulsed phase thermographic data on plexiglas and aluminum samples. In *Defense and Security*, pages 348–356. International Society for Optics and Photonics, 2004.

[203] Tian Tian and Kevin D. Cole. Anisotropic thermal conductivity measurement of carbon-fiber/epoxy composite materials. *International Journal of Heat and Mass Transfer*, 55(23–24):6530 – 6537, 2012. URL: http://www.sciencedirect.com/science/article/pii/S0017931012004905, doi:http://dx.doi.org/10.1016/j.ijheatmasstransfer.2012.06.059.

[204] Tomohiro Yokozeki, Yutaka Iwahori, Shin Ishiwata, and Kiyoshi Enomoto. Mechanical properties of cfrp laminates manufactured from unidirectional prepregs using cscnt-dispersed epoxy. *Composites Part A: Applied Science and Manufacturing*, 38(10):2121 – 2130, 2007. URL: http://www.sciencedirect.com/science/article/pii/S1359835X07001108, doi:http://dx.doi.org/10.1016/j.compositesa.2007.07.002.

[205] Naveed A Siddiqui, Ricky SC Woo, Jang-Kyo Kim, Christopher CK Leung, and Arshad Munir. Mode i interlaminar fracture behavior and mechanical properties of cfrps with nanoclay-filled epoxy matrix. *Composites Part A: Applied science and manufacturing*, 38(2):449–460, 2007.

[206] Seungjin Han and D.D.L. Chung. Increasing the through-thickness thermal conductivity of carbon fiber polymer–matrix composite by curing pressure increase and filler incorporation. *Composites Science and Technology*, 71(16):1944 – 1952, 2011. URL: http://www.sciencedirect.com/science/article/pii/S0266353811003381, doi:http://dx.doi.org/10.1016/j.compscitech.2011.09.011.

[207] Junnfeng Liang, Mrinal C Saha, and M Cengiz Altan. Effect of carbon nanofibers on thermal conductivity of carbon fiber reinforced composites. *Procedia Engineering*, 56:814–820, 2013.

[208] F. C. Campbell. *elements of metallurgy and engineering alloys*. ASM International, USA, 2008.

[209] Yuhua Cheng, Yiming Deng, Jing Cao, Xin Xiong, Libing Bai, and Zhaojun Li. Multi-wave and hybrid imaging techniques: A new direction for nondestructive testing and structural health monitoring. *Sensors*, 13(12):16146–16190, 2013.

[210] SB Kim and H Sohn. Continuous fatigue crack monitoring without baseline data. *Fatigue & Fracture of Engineering Materials & Structures*, 31(8):644–659, 2008.

[211] M Ryles, FH Ngau, I McDonald, and WJ Staszewski. Comparative study of nonlinear acoustic and lamb wave techniques for fatigue crack detection in metallic structures. *Fatigue & Fracture of Engineering Materials & Structures*, 31(8):674–683, 2008.

[212] Simon V Walker, Jin-Yeon Kim, Jianmin Qu, and Laurence J Jacobs. Fatigue damage evaluation in a36 steel using nonlinear rayleigh surface waves. *NDT & E International*, 48:10–15, 2012.

[213] Chao Zhou, Ming Hong, Zhongqing Su, Qiang Wang, and Li Cheng. Evaluation of fatigue cracks using nonlinearities of acousto-ultrasonic waves acquired by an active sensor network. *Smart Materials and Structures*, 22(1):015018, 2013.

[214] XD Li, H Zhang, DL Wu, X Liu, and JY Liu. Adopting lock-in infrared thermography technique for rapid determination of fatigue limit of aluminum alloy riveted component and affection to determined result caused by initial stress. *International Journal of Fatigue*, 36(1):18–23, 2012.

[215] Yun-Kyu An, Ji Min Kim, and Hoon Sohn. Laser lock-in thermography for detection of surface-breaking fatigue cracks on uncoated steel structures. *NDT & E International*, 65:54–63, 2014.

[216] Xingwang Guo and Vladimir Vavilov. Crack detection in aluminum parts by using ultrasound-excited infrared thermography. *Infrared Physics & Technology*, 61:149–156, 2013.

[217] Ben Weekes, Darryl P Almond, Peter Cawley, and Tim Barden. Eddy-current induced thermography—probability of detection study of small fatigue cracks in steel, titanium and nickel-based superalloy. *NDT & E International*, 49:47–56, 2012.

[218] D. S. Mountain and J. M. B. Webber. Stress pattern analysis by thermal emission (spate). volume 0164, pages 189–196, 1979. URL: http://dx.doi.org/10.1117/12.965516, doi:10.1117/12.965516.

[219] Robert E. Rowlands Richard J. Greene, Eann A. Patterson. *springer handbook of experimental solid mechanics*. springer, 2008.

[220] ASTM International. Standard test method for measurement of fatigue crack growth rates, 2011.

[221] David L. Donoho. De-noising by soft-thresholding - information theory, ieee transactions on. *IEEE Transactions on Information Theory*, 41:613 – 627, 1995.

[222] Yu Zhang, Yuanyuan Wang, and Weiqi Wang. Denoising quadrature doppler signals from bi-directional flow using the wavelet frame. *Ultrasonics, Ferroelectrics and Frequency Control, IEEE Transactions on*, 50(5):561–564, 2003.